PhD Thesis

# *Development of Stimuli-Responsive Suprasomes for Therapeutics, Temporal Catalysis and Communication*

*A dissertation submitted to the*
*Indian Institute of Technology Guwahati*
*as partial fulfilment for the Degree of*
*Doctor of Philosophy in Chemistry*

*By*

*Biswa Mohan Prusty*


*Department of Chemistry*
*Indian Institute of Technology Guwahati*
*Guwahati 781039, Assam, India*


*Jay Jaggannath…*

# *Declaration*

*21st November, 2025*

*I hereby declare that the thesis entitled* ***"Development of Stimuli-Responsive Suprasomes for Therapeutics, Temporal Catalysis and Communication"*** *is compilation of research work which was carried out by me under the supervision of Prof. Debasis Manna, Department of Chemistry, Indian Institute of Technology Guwahati. This thesis has been submitted by me to the Department of Chemistry, Indian Institute of Technology Guwahati, for the award of the degree of Doctor of Philosophy. In keeping with the general practice of reporting scientific observations, due acknowledgements have been made wherever the work described is based on the findings of other investigators. I further declare that this work has not been submitted anywhere else for any degree, diploma, associateship or membership etc. of any Institute or University to the best of my knowledge.*

Biswa Mohan Prusty

(Biswa Mohan Prusty)

भारतीय प्रौद्योगिकी संस्थान गुवाहाटी
Indian Institute of Technology Guwahati

Prof. Debasis Manna
Department of Chemistry
Phone: +91-0361-258-2325
Fax: +91-0361-258-2349
E-mail: dmanna@iitg.ac.in

*21st November, 2025*

# *To whom it may concern*

*This is to certify that the thesis entitled* ***"Development of Stimuli-Responsive Suprasomes for Therapeutics, Temporal Catalysis and Communication"*** *being submitted by Mr. Biswa Mohan Prusty (Roll No. 206122017) for the award of PhD degree in Chemistry to the Indian Institute of Technology Guwahati, is genuinely his own research work which was carried out by him. The information and data reported by him are completely his original findings. He has meticulously carried out the investigations and also followed the guidelines of my laboratory. Neither this thesis nor any part of it has been submitted for the award of any degree/diploma to anywhere before.*

***Prof. Debasis Manna***

# *Contents*

# Acknowledgements

*This dissertation is a consequence of endless support and encouragement by numerous well-wishers'. I would like to acknowledge each of them for helping me to reach the milestone in my life.*

*Prior to all, I would like to convey my sincere gratefulness to my supervising guide, Prof. Debasis Manna who introduced me to the splendid world of science. His consistent guidance, encouragement and scholarly inputs have enriched me a lot for shining in science. I am truly honoured and blessed to have been a part of his research group. Apart from research, his thoughts and ideas about life paved the way to me a better person in future. Thank you, Sir, for being my Mentor.*

*My sincere and heartfelt thanks to my collaborators, Prof. Sachin Kumar (Dept. of BSBE, IIT Guwahati, India), Prof. Mathias Winterhalter (School of Science, Constructor University, Germany), Nandan Haloi (Department of Biochemistry and Biophysics, Science for Life, Laboratory, Stockholm University, Tomtebodavägen 23, Solna, Sweden) for their constructive support in my research.*

*I would also like to thank my doctoral committee members Prof. Biplab Mondal, Prof. Kalyan Raidongia, and Prof. Manish Kumar for their valuable suggestions and consistent evaluation of my research works.*

*I would like to express my gratitude to all the faculty and staff members of Department of Chemistry for their continuous support. Also, I am immensely thankful to Department of Chemistry and CIF (IIT Guwahati) for allowing me to use the sophisticated instrument facility. A special mention in this note of acknowledgement will certainly be of CSIR India for providing me the scholarship.*

*I would also like to acknowledge all my past and present lab members including Dr. Nirmalya Pradhan, Dr. Nasim Akhtar, Dr. Subhasis Dey, Dr. Oindrila Biswas, Dr. Anjali Patel, Dr. Sribash Das, Mrs. Priyanka Mazumder, Ms. Soumya Srimayee, Dr. Gunanka Hazarika, Ms. Niku Moni Das, Ms. Rama Karn, Mr. Mrinal Kanti Kar, Mr. Rahul Kumar, Ms. Suravi Chouhan, Mr. Joydip Pal, Mr. Pritam Kumar Mohanta, Ms. Ritama Mukherjee, Mr. Yousuf SK, and Mr. Soumajit Saha, for providing me a healthy and friendly atmosphere in the lab.*

*I extend my sincere thanks to all of my friends, especially Mr. Biswaranjan Sahoo and Mr. Siba Prasad Behera for their constant mental support during my lows. A special*

*thanks to my friend philosopher and guide, Dr. Aryaman Pattanaik, for his constant help, guidance and encouragement. Also, I am thankful to my friends Om Prakash, Mayur and Sushant for being a constant company during my Ph. D. journey.*

*Last but not the least, my Ph. D. endeavours would not have been accomplished without acknowledging my loving family and mother, Ms. Malati Manjari Prusty. Their endless love, continuous support and blessings boost me up to cross the hurdles of my career. I express my deepest gratitude to my family members (my uncles, aunts, cousin brothers and sisters, Chintu, Guduli, Guguli, Tikina, Chinkun). A heartfelt gratitude for my loved one, Mamun, for standing by me through all my highs and lows, and for walking with me into the future.*

*Thank you all for being a memorable part of my Ph. D. career.*

***Mr. Biswa Mohan Prusty***

# Abstract

This thesis, "Development of Stimuli-Responsive Suprasomes for Therapeutics, Temporal Catalysis and Communication," explores the development of various types of suprasomes with different stimuli-responsive and multifaceted applications, including therapeutics, catalysis, information storage, and inter-vesicle communication. It has been organised into five chapters, based on the experimental results obtained during my doctoral research.

**Chapter 1** describes the principle of supramolecular self-assembly and emphasises the development of suprasomes as adaptable synthetic compartments. This chapter examines the constraints of conventional drug delivery systems, including liposomes and polymersomes, and highlights the benefits of suprasomes, particularly their facile and reversible assembly and disassembly.

**Chapter 2** discusses the development of an anionic suprasome that exhibits facile assembly and stimuli-responsive ($Zn^{2+}$ and $H^{+}$) disassembly. This stimuli-responsive behaviour was utilised to showcase tunable antibacterial activity as well as antibiotic delivery to desired target sites.

**Chapter 3** illustrates the creation of a supramolecular $Zn^{2+}$ ion channel and the subsequent construction of a stimuli-responsive suprasome incorporating the ionophore and β-CD, which facilitates the delivery of the ionophore triggered by $Zn^{2+}$ and exhibits remarkable antibacterial efficacy through $Zn^{2+}$-mediated excessive ROS generation.

**Chapter 4** discusses the dynamic suprasome and the stimuli-triggered conversion to supracube, which demonstrates temporal regulation of esterase activity and shows $Zn^{2+}$ ionophore-mediated chemical communication. This highlights the importance of transient supramolecular assembly for modulating important activities.

**Chapter 5** provides a vivid explanation of the design and development of a temporally gated, dual-responsive (light and $Zn^{2+}$) suprasome for capturing optical signals, temporal information, and intervesicle communication.

# List of Abbreviation

| | |
|---|---|
| ADME | Absorption, Distribution, Metabolism, Excretion |
| AFM | Atomic Force Microscopy |
| CAC | Critical Aggregation Constant |
| CD | Circular Dichroism |
| $CDCl_3$ | Deuterated Chloroform |
| CFSE | Carboxyfluorescein succinimidyl ester |
| CLSM | Confocal Laser Scanning Microscopy |
| CQ | Clioquinol |
| CQE | Clioquinol Ester Derivative |
| Cys | Cysteine |
| DCC | Dynamic Combinatorial Chemistry |
| DCM | Dichloromethane |
| DDS | Drug Delivery System |
| DFT | Density Functional Theory |
| $d_H$ | Hydrodynamic Diameters |
| DLS | Dynamic Light Scattering |
| DMAB | Dimethylaminobenzaldehyde |
| DMF | Dimethylformamide |
| DMSO | Dimethyl sulfoxide |
| Dox | Doxorubicin |
| DPPC | Phospholipid dipalmitoylphosphatidylcholine |
| $EC_{50}$ | Half maximal effective concentration |
| EDC.HCl | *N*-Ethyl-N′-(3-dimethylaminopropyl)carbodiimide hydrochloride |
| EDTA | Ethylenediaminetetraacetic Acid |
| EDTAE | Ethylenediaminetetraacetate Ester |
| EtOAc | Ethyl Acetate |
| FESEM | Field Emission Scanning Electron Microscopy |
| FETEM | Field Emission Transmission Electron Microscopy |
| GSH | Glutathione |
| $H_2O$ | Water |

| | |
|---|---|
| $H_2O_2$ | Hydrogen Peroxide |
| $H_3PO_4$ | Phosphoric Acid |
| HAase | Hyaluronidase |
| HBTU | (2-(1H-benzotriazol-1-yl)-1,1,3,3-tetramethyluronium hexafluorophosphate |
| HCl | Hydrochloric Acid |
| HEPES | 4-(2-hydroxyethyl)-1-piperazineethanesulfonic acid |
| His | Histidine |
| HOBt | Hydroxybenzotriazole |
| HPLC | High Performance Liquid Chromatography |
| HRMS | High-Resolution Mass Spectrometry |
| HSA | Human Serum Albumin |
| $IC_{50}$ | Half maximal inhibitory concentration |
| IPTG | Isopropyl β-D-1-thiogalactopyranoside |
| ITC | Isothermal Titration Calorimetry |
| $K_a$ | Association Rate |
| $K_{cat}$ | Turnover Number |
| KCl | Potassium Chloride |
| $K_d$ | Binding Affinity |
| $K_D$ | Dissociation Constant |
| KOH | Potassium Hydroxide |
| KPB | Potassium Phosphate Buffer |
| MALDI-TOF | Matrix Assisted Laser Desorption Ionization-Time Of Flight |
| MD | Molecular Dynamic |
| MeOH | Methanol |
| MOPS | 3-(*N*-morpholino)propanesulfonic acid |
| MSNPs | Mesoporous Silica Nanoparticles. |
| MTT | 3-(4,5-dimethylthiazol-2-yl)-2,5-diphenyl tetrazolium bromide |
| $N_2$ | Nitrogen |
| $Na_2S_2O_4$ | Sodium Dithionite |
| NaCl | Sodium Chloride |
| NaOle | Sodium Oleate |
| NAs | Nano-aggregates |

| | |
|---|---|
| NMR | Nuclear Magnetic Resonance |
| $O_2$ | Oxygen |
| OD | Optical Density |
| PBS | Phosphate-Buffered Saline |
| PDB | Protein Data Bank |
| PDT | Photodynamic Therapy |
| PEG | Polyethylene Glycol |
| RBC | Red Blood Cells |
| ROS | Reactive Oxygen Species |
| RPM | Revolutions Per Minute |
| STDP | Spike-Timing-Dependent Plasticity |
| TCA | Trichloroacetic Acid |
| TFA | Trifluoroacetic Acid |
| THF | Tetrahydrofuran |
| TLC | Thin Layer Chromatography |
| Tris | Tris(hydroxymethyl)aminomethane |
| UV-Vis | Ultraviolet–visible |
| β-CD | β-cyclodextrin |
| $\lambda_{em}$ | Emission Wavelength |
| $\lambda_{ex}$ | Excitation Wavelength |

**For symbols/units**

| | |
|---|---|
| α | Alpha |
| Å | Angstrom |
| atm | Atmosphere |
| β | Beta |
| C | Celsius |
| *J* | Coupling Constant |
| ° | Degree |
| *δ* | Delta |
| Hz | Hertz |
| K | Kelvin |
| MHz | Megahertz |
| *m* | Meta |
| µg | Microgram |
| µM | Micromolar |

| | |
|---|---|
| mL | Millilitre |
| mV | Mili Volt |
| min | Minute |
| nM | Nanomolar |
| *o* | Ortho |
| *p* | Para |
| ppm | Parts per million |
| % | Percent |
| π | Pi |
| s | Second |

## *Chapter 1*

### Introduction to Supramolecular Assembly and Suprasomes

Supramolecular self-assembly-based compartmentalisation is a core principle of life, facilitating coordinated spatial and temporal regulation of biochemical processes.[1] Key cellular processes, such as nutrient uptake, enzymatic cascades, energy conversion, and signal transduction, depend on membranes and organelles that spatially isolate reactions, control molecular distribution, and permit regulated communication between compartments.[2] Such spatial and functional separation not only augments efficiency but also introduces regulation and adaptability, which are essential features of living systems. Replicating such compartmentalised behaviour in synthetic constructs has been a fundamental goal in supramolecular chemistry, synthetic biology, and systems chemistry, since it offers tremendous potential to understand the origins of cellular complexity and to engineer life-like artificial systems.

Recent research has witnessed significant advances in designing artificial supramolecular compartments. Liposomes, being assembled from phospholipid bilayers, have been extensively used as model membranes for drug delivery systems.[3, 4] Similarly, polymersomes, assembled by the block copolymers, offer superior mechanical tunability and stability. Similar conditions include peptide-based vesicles, emulsions, and coacervates, each providing unique advantages for replicating biological compartmentalisation.[5, 6] Although they suffer from critical drawbacks, these systems have delivered key insights and practical applications. Lipid vesicles are not only biocompatible but also exhibit limited stability; once disrupted, their reassembly is difficult and rarely reversible. Introducing functional moieties into lipids typically requires sophisticated chemical modification, making the development of stimuli-responsive liposomes synthetically challenging. Polymersomes, although more robust, often exhibit excessive stability, which hinders their reversible disassembly and responsiveness to dynamic stimuli. In general, within many of these systems, assembly and disassembly are either irreversible or often demand harsh conditions, which constrain their ability to closely mimic the dynamic and reversible behaviours of living compartments.

These difficulties pose great challenges for the development of synthetic compartments that combine facile assembly, disassembly, dynamic reversibility, and customised functionalisation. In this context, suprasomes, self-assembled vesicles generated through host–guest interactions with amphiphilic moieties, have emerged as potential platforms.[7] Unlike

liposomes or polymersomes, suprasomes are assembled by simply mixing host and guest under mild conditions, without tedious synthetic effort. As their assembly is driven by non-covalent interactions, it offers facile assembly, disassembly, and reassembly under controlled stimuli. This reversibility sets them apart from conventional lipid-based supramolecular compartments, which often lack such adaptive control. Additionally, suprasomes are highly customisable: a simple variation of the amphiphiles leads to the incorporation of desired properties, such as responsiveness to different environmental cues (pH, metal ions, redox environment, light), as well as transient functional roles in catalysis, drug delivery, or molecular communication. Thus, suprasomes offer a versatile and experimentally accessible platform for engineering stimuli-responsive, reversible compartments that can cater to multiple fields of research.

Despite such fundamental and functional advantages, current suprasome research still leaves key gaps unaddressed. Most reported supramolecular assemblies focus on static structural properties or simple cargo encapsulation and release strategies.[7] However, biological compartments function dynamically with transient active or inactive sessions, often operated by time-gated signals within narrow time windows.[8] Biological activities such as coordinated enzyme cascades, neurotransmitter-based inter-neuron communication, and long-term potentiation in neurons exemplify how temporally gated inputs are key to sophisticated outcomes that are necessary for the complex operation of living cells.[9, 10] Engineering suprasomes with such complex attributes so that it responds to stimuli in a reversible and temporally gated manner, enabling growth, differentiation, catalysis, and inter-compartmental communication.

**Aim of the Thesis**

To address these challenging research gaps, this thesis explores the design and development of suprasomal systems that merge reversible assembly–disassembly with stimuli-responsive and temporally controlled tunable properties. **Chapter 2** discusses the development of anionic suprasomes capable of stimuli-responsive disassembly for drug delivery and tunable antibacterial activity, establishing them as a versatile drug delivery vehicle. **Chapter 3** extends this concept by introducing synthetic supramolecular nanochannels and suprasome-mediated $Zn^{2+}$ ionophore delivery, providing a simplistic model for ion transport and subsequent antibacterial activity. In **Chapter 4**, exploration of transient catalysis regulation demonstrated that suprasomes can undergo $Zn^{2+}$-driven differentiation into supracubes, showcasing reversible growth–decay dynamics and ion transport regulation. Finally, **Chapter 5** presents a

dual-stimuli-responsive suprasomal system that integrates photoisomerisation and metal coordination to achieve temporally gated transformations, leading to subsequent optical signal generation, as well as temporal information storage and inter-vesicular communication.

Ultimately, our work establishes suprasomes as one of the distinguished supramolecular constructs due to their facile assembly, functionalisation, and capability for reversible and temporally gated transformations and activities. To address the limitations of traditional vesicular systems and explore unexplored areas, this work contributes to bridge the gap between static synthetic assemblies and the adaptive behaviour of living systems.

---

## Chapter 2

**Stimuli-Responsive Assembly and Disassembly of Anionic Suprasomes with Tunable Antibacterial Activity**

The traditional liposome-based drug delivery systems can be designed smartly to cater to different requirements, such as stimuli-responsive behaviour to different environmental cues, such as pH, metal ions, GSH, light, heat, etc.[11] But to achieve this, a stimuli-responsive lipid needs to be synthesised, which usually requires rigorous multistep synthesis with difficult, low-yield synthetic steps involved in between. Secondly, stimuli trigger an irreversible chemical change in the lipid, as well as an irreversible structural modification in the liposome, causing its subsequent disruption and drug release. Additionally, traditional liposomes lack tunability in size and long-term stability. Overall, these classical systems encounter significant challenges due to laborious synthetic pathways leading to irreversible chemical and structural changes in response to stimuli, as well as inadequate stability and size modulation characteristics. To tackle these multifaceted challenges, we considered using suprasomes due to their ease of construction and stimulus-responsive disassembly characteristics.

This second chapter details the development of innovative host–guest complexation-based suprasomes constructed from anionic sodium oleate (NaOle) and cationic benzimidazolium amphiphiles (C12mbm) mediated by β-cyclodextrin (β-CD). The suprasomal vesicles exhibit a negative surface charge (~−25 mV) and variable dimensions (~300–500 nm), which ensures colloidal stability and favourable encapsulation conditions for both hydrophilic and hydrophobic pharmaceuticals. Dynamic light scattering (DLS), isothermal titration calorimetry (ITC), zeta potential, atomic force microscopy (AFM), and transmission electron microscopy

(TEM) validate the micelle-to-vesicle transition induced by β-CD concentration, enabling precise control over size and assembly.

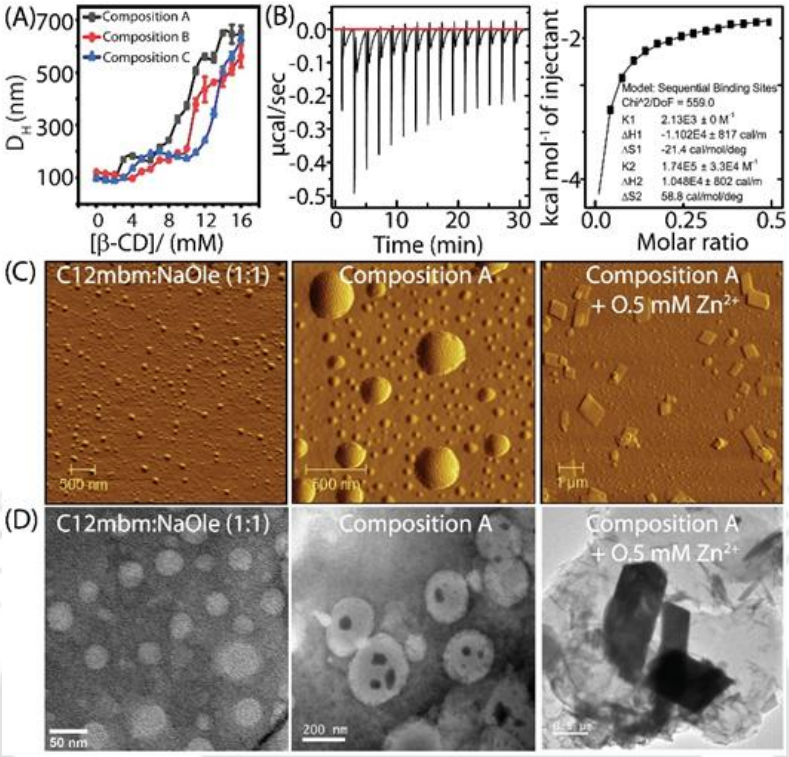


**Figure I.** (A) Variation of $D_H$ values of the suprasomes against different concentrations of β-CD. (B) ITC measurements of the mixture of C12mbm and NaOle (1: 1) with β-CD. Representative (C) AFM and (D) TEM images of the aggregates after different treatments.

Moreover, the suprasomes have demonstrated stimuli-responsive disassembly in the presence of $Zn^{2+}$ ions or an acidic environment, leading to the release of the therapeutic cargo, including free C12mbm amphiphiles and tetracycline, due to vesicle disruption. The $Zn^{2+}$-triggered disassembly of suprasomes have shown enhanced antibacterial activity against Gram-positive bacteria, such as Staphylococcus aureus. In addition, tetracycline-loaded suprasomes exhibit an MIC value of 15 nM, which is 280-fold greater than that of free tetracycline.

Structurally, the self-assembled suprasome reduces the intrinsic antibacterial activity of free C12mbm by masking the cationic headgroups, while $Zn^{2+}$ stimulation restores and amplifies its potency. These vesicles also demonstrate biocompatibility and selectivity, resulting in low haemolytic activity and reduced toxicity for red blood cells and human cell lines. A membrane disruption assay, conducted via fluorescence measurement, structural and functional analysis, and FESEM, demonstrated the mechanism of bacterial membrane damage caused by the released amphiphilic agents.

This chapter demonstrates the development of multi-stimuli-responsive suprasomal DDS showcasing size tunability, biocompatibility, facile functionalisation, and controlled cargo release. This suprasome has futuristic application as a next-generation DDS capable of imparting antimicrobial effect with the ability to respond to pathological microenvironments rich in $Zn^{2+}$ or acidic pH. Such brilliant suprasomes offer a versatile, highly effective approach for improving therapeutic outcomes while minimising toxicity.

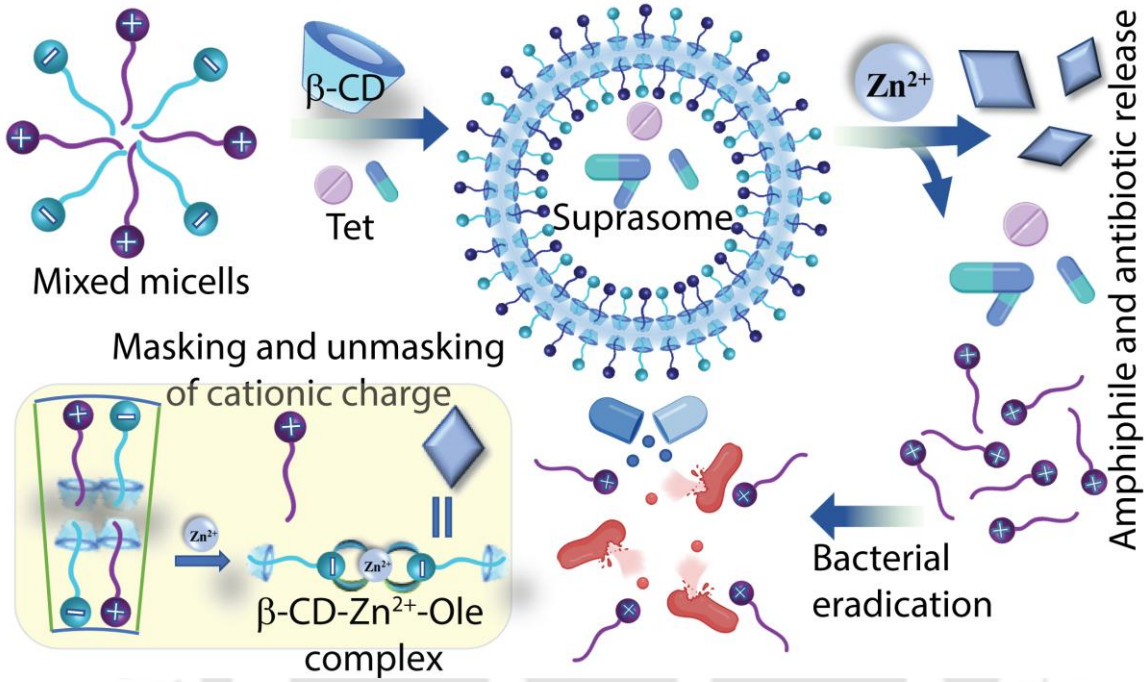


**Figure II.** Schematic representation of the stimuli-regulated assembly and disassembly of suprasomes and their tunable antibacterial activity.

---

***Chapter 3***

**Supramolecular Nanochannels: Suprasome-Mediated Delivery of Ionophore to Regulate Transmembrane $Zn^{2+}$ Ion Transport**

Supramolecular ion channels for selective ion transport across lipid bilayer membranes have represented a central and rigorous subject of investigation in chemistry, both historically and presently. Only the methodology for achieving it has evolved in recent decades. Initially, Tabushi and colleagues created the first synthetic ion channel capable of facilitating the transport of metal ions ($Co^{2+}$) across a lipid bilayer membrane by supramolecular assembly. In the last decade, small molecule-based supramolecular nanochannels have garnered significant attention due to their enhanced efficacy and facile manoeuvrability in fields such as cutting-

edge therapeutics and artificial cell biology. Although these small-molecule self-assembled ion channels have significant advantages, they face severe unaddressed challenges. Firstly, due to their inherent hydrophobic nature, the delivery of ionophores, along with unfavourable pharmacokinetic and pharmacodynamic characteristics, poses a key challenge in ionophore research. Despite this, no prior attempts have been made to deliver these hydrophobic ionophores in a stimulus-responsive manner, where their release and reassembly into a supramolecular ion channel can be controlled via a stimulus trigger. Furthermore, efforts to develop therapeutics based on divalent ion channels for bacterial eradication remain exceptionally scarce, presenting a promising yet largely untapped avenue for innovation.

This chapter details the design and synthesis of effective bis(vinylbenzimidazole)phenol derivatives intended to self-assemble inside lipid bilayers, creating supramolecular nanochannels that selectively facilitate the transit of $Zn^{2+}$ ions across membranes. To achieve such multifaceted objectives, a library of bis(benzimidazole)phenol and bis(vinylbenzimidazole)phenol derivatives was designed and synthesised, starting from p-cresol, as described in the synthetic scheme below. Desired structural modifications led to the installation of both phenolic and benzimidazole moieties, which are necessary for coordinating $Zn^{2+}$ ions while maintaining optimal lipophilicity for entry into the hydrophobic lipid bilayer membrane. Further, a morphology analysis using FESEM confirmed nanorod-like self-assemblies of the potent derivative only in hydrophobic environments. This reflected its intrinsic ability to assemble into ordered structures through noncovalent interactions, forming membrane-embedded channels. Such preliminary observations established the molecular foundation required for the development of a supramolecular $Zn^{2+}$ selective ion channel across lipid bilayers.

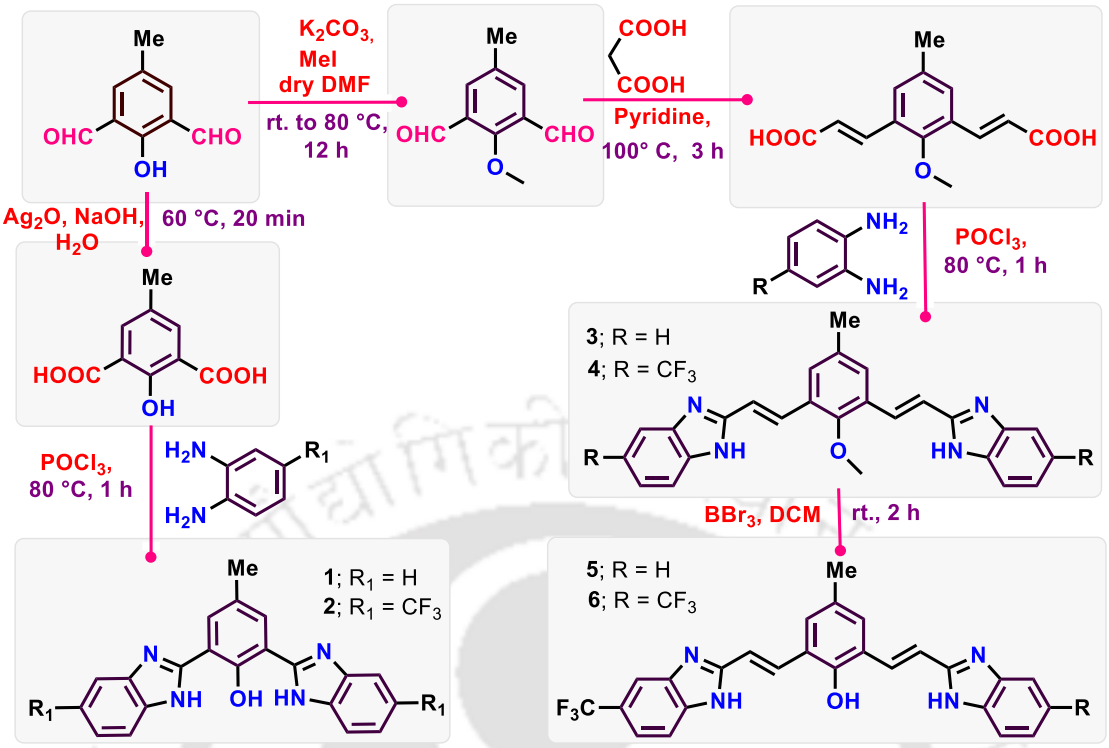


**Scheme I.** Synthetic routes to bis(benzimidazole)phenols and bis(vinylbenzimidazole) phenols.

Fluorescence kinetics-based screening and concentration-dependent transport studies using MgG-loaded liposomes confirmed the potent compound for $Zn^{2+}$ transport across the lipid bilayer membrane. Further mechanistic studies confirmed that the synthetic ionophores demonstrated optimal lipophilicity and binding affinity for $Zn^{2+}$, facilitating efficient and selective transmembrane transport through an electrogenic route, as validated by real-time fluorescence-based transport experiments. Since BLM-based (Black Lipid Membrane) electrophysiological studies are considered the benchmark for examining channel formation across lipid bilayers, we performed these experiments accordingly. These electrophysiology studies confirmed the formation of transient supramolecular channels that selectively pass $Zn^{2+}$ across the lipid bilayer. This established the fulfilment of our first objective for this chapter.

To tackle the unaddressed challenges related to the delivery of hydrophobic ionophores, the ionophore was rationally and carefully designed with a benzimidazole moiety present symmetrically at both ends of the potent compound. The strategic installation of the benzimidazole moiety was due to its well-known ability to form host-guest complexes with β-CD. The interaction of a potent ionophore and β-CD led to the formation of a suprasome, as validated through ITC, FESEM, and UV-Vis absorbance studies. The suprasomal assemblies

possess variable sizes and considerable stability, undergoing stimuli-responsive disintegration upon exposure to $Zn^{2+}$ ions. Such a stimuli-responsive ionophore release mechanism enables the release and self-assembly of functional nanochannels, effectively modulating ionic transport only at the desired site. Accordingly, our second goal in this chapter was achieved.

Going forward, our objective was to explore divalent metal ion channel-forming therapeutics as potential next-generation antibiotics. Based on our antibacterial studies, we observed that potent ionophores, when combined with $Zn^{2+}$, cause excessive internalisation of $Zn^{2+}$ and subsequently produce ROS inside bacterial cells. This demonstrated that the disruption of metal ion homeostasis can lead to potent bactericidal effects against both Gram-positive and Gram-negative bacteria, as well as drug-resistant species. Minimal membrane depolarisation and haemolytic toxicity tests, as well as mechanistic evaluations using fluorescent dyes, demonstrate that intracellular oxidative stress, rather than membrane rupture, is the primary source of the antibacterial activity.

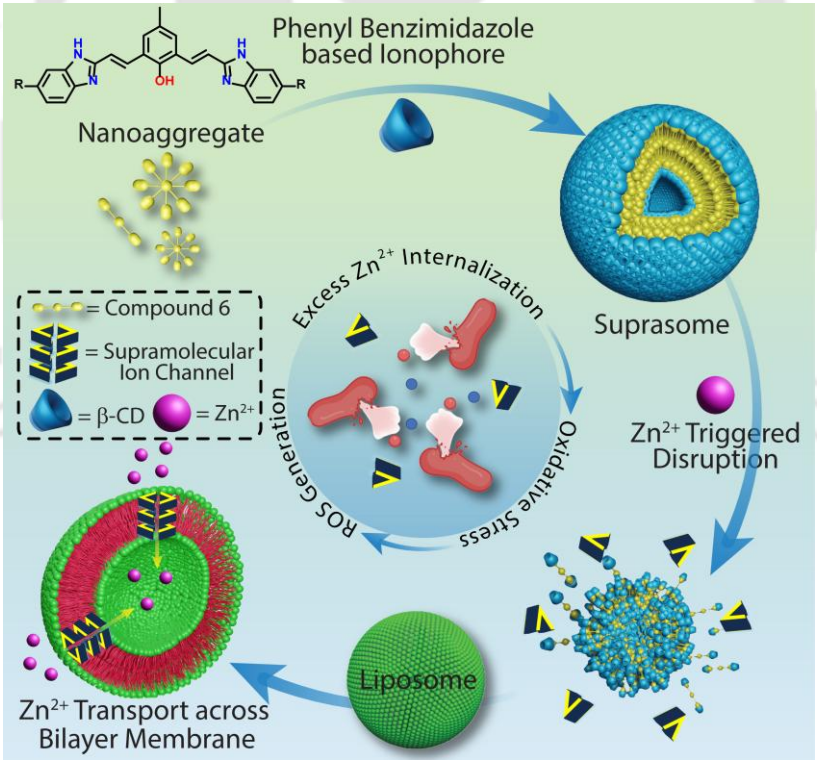


**Figure III.** Schematic representation of suprasomal assembly of the potent ion transporter with β-CD through dynamic host-guest interactions and $Zn^{2+}$ ions mediated disassembly of suprasomes to release the ion transporter.

To advance suprasome-based delivery approaches for emerging ion transport therapies, this chapter integrates multiple disciplines, including microbiological assessment, biophysical

characterisation, chemical synthesis, and supramolecular chemistry. The findings establish a strong foundation for the controlled regulation of metal ion transport, with potential applications in combating infectious diseases and beyond.

---

## Chapter 4

### Temporally Controlled Interconversion Between Suprasome and Supracube Structures to Regulate Catalytic Activities

Systems chemistry has emerged as a vibrant field that investigates how interacting molecules give rise to collective behaviours and emergent properties beyond those of individual components. Phenomena such as synchronisation, autocatalysis, and self-replication exemplify how intricate molecular networks can mimic hallmarks of living systems. Central to this discipline is the study of far-from-equilibrium states, where continuous energy input sustains dynamic processes that are analogous to those found in biology.

Important strategies such as autocatalytic networks, dynamic combinatorial chemistry (DCC) for adaptive molecular selection, and compartmentalisation through self-assembled membranes or coacervates have provided valuable insights into how life-like organisation might emerge from chemistry. Yet, despite these advances, several important questions remain open. These include the challenge of programming molecular assemblies to perform increasingly complex functions, the need to establish design rules for robust far-from-equilibrium behaviour, and the difficulty of engineering chemical systems that integrate multiple stimuli in ways reminiscent of cellular decision-making.

Equally important are challenges along the temporal dimension. These include achieving stimulus-triggered compartment growth and differentiation, establishing reliable strategies for temporal stability control, developing programmable time-gated catalysis, and extending such temporally regulated catalysis toward intervesicle communication to enable networks of chemical compartments that interact like primitive communities. Addressing these gaps requires new molecular architectures and design principles. In this chapter, we build on these foundations to explore chemical stimuli-triggered growth and differentiation of supramolecular compartments, as well as their utilisation of temporally gated catalysis, offering an approach

toward temporally regulated intervesicle communication, advancing the scope and arena of synthetic chemical biology.

The current scenario in protocell research and artificial cell engineering requires sophisticated, compartmentalised assemblies that display controlled growth, differentiation, and regulated catalytic activity. In the ongoing chapter, we illustrate the formation of supramolecular, compartmentalised systems exhibiting metastable, stimuli-responsive properties, drawing inspiration from the function of fundamental compartments as catalytic centres in early chemical evolution.

Amphiphilic assemblies of 6-(hydrazineylidenemethyl) picolinaldehyde oxime (AHPO) and dodecyl trimethylammonium bromide (DTAB) formed nano-assemblies ($D_H \approx 200$ nm), which, upon interaction with β-CD as a host-guest complex, enlarged into larger suprasomes ($D_H \approx$ 1000 nm). FESEM and ITC measurements confirmed the role of entropy-driven β-CD interactions in facilitating suprasome formation. The suprasomes underwent structural differentiation into cube-like supracubes ($D_H \approx 2500$ nm) upon addition of $Zn^{2+}$, as confirmed by FESEM, DLS, and TEM-SAED analysis. The polycrystalline morphology of supracubes suggests a highly ordered supramolecular arrangement driven by AHPO–$Zn^{2+}$ complexation and hydrophobic host–guest interactions with β-CD.

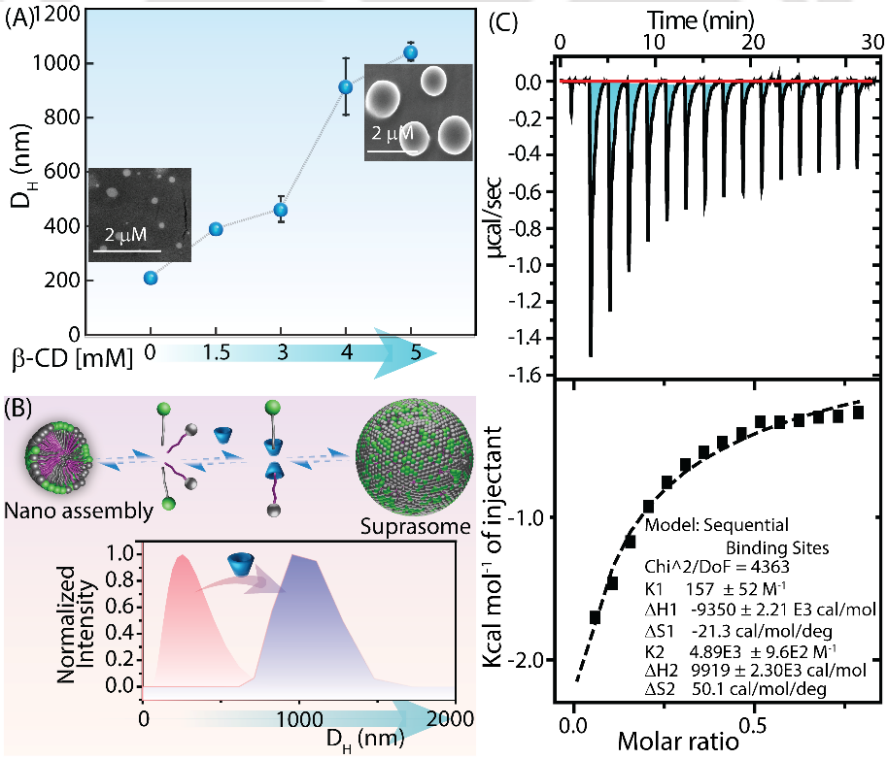

**Figure IV.** (A) Variation of hydrodynamic diameter ($D_H$) during nanoassembly to suprasome transition upon increasing β-CD concentration; inset: representative FESEM images of nanoassemblies and suprasomes. (B) Plausible suprasome growth mechanism; inset: $D_H$ distribution of nanoassemblies and suprasomes. (C) ITC profile of DTAB–AHPO (1:1) with β-CD.

The supracubes exhibited esterase-like catalytic activity by hydrolysing the proionophore clioquinol ester (CQE) into the active form of clioquinol (CQ). Through fluorescence quenching, HPLC analysis, and kinetic studies, the catalytic process was validated, which revealed a rate of $2.78 \times 10^{-8}$ M/s. $Zn^{2+}$-mediated activation of the pyridine-oxime moiety of AHPO resulted in catalytic activity, which reduced its pKa, promoting oximate formation as the active catalyst. Catalytic activation in a transient manner highlights the role of supracubes as dynamic functional compartments.

EDTA or its ester derivative (EDTAE) was introduced into the system to regulate the lifetime of the catalytically active compartments. $Zn^{2+}$ was captured by EDTA, triggering the reversal of supracubes back to suprasomes and turning off the catalytic efficiency of the system. Thus, the introduction of EDTAE as a negative feedback regulator enabled programmed temporal control. EDTAE was hydrolysed by the supracubes to gradually release EDTA, sequestering $Zn^{2+}$, which limited the supracubes' lifetime to ~ 6 hours. This reversible switching of compartmentalised structures, along with catalytic activity, has been shown to continue over multiple cycles with fresh $Zn^{2+}$ fuelling.

Thereafter, we performed inter-compartmental communication by coupling suprasome-to-supracube differentiation with ion transport in a separate secondary vesicular compartment. The catalytically released CQ from CQE activates $Zn^{2+}$ ion transport across lipid membranes, which is monitored using magnesium green (MgG, $\lambda_{ex}$ = 506 nm, $\lambda_{em}$ = 531 nm) assays. Hence, this system highlights the ability of transient compartments to mediate chemical communication through catalytic differentiation.

In conclusion, this work demonstrates the design of stimuli-responsive supramolecular self-assembly capable of performing transient structural differentiation, catalytic activity, and feedback-controlled lifetimes. Such systems mimic life-like behaviour of growth, functional activation, and decay, thereby offering a framework for developing programmable artificial cell models, ionophore-based therapeutics, and dissipative supramolecular architectures.

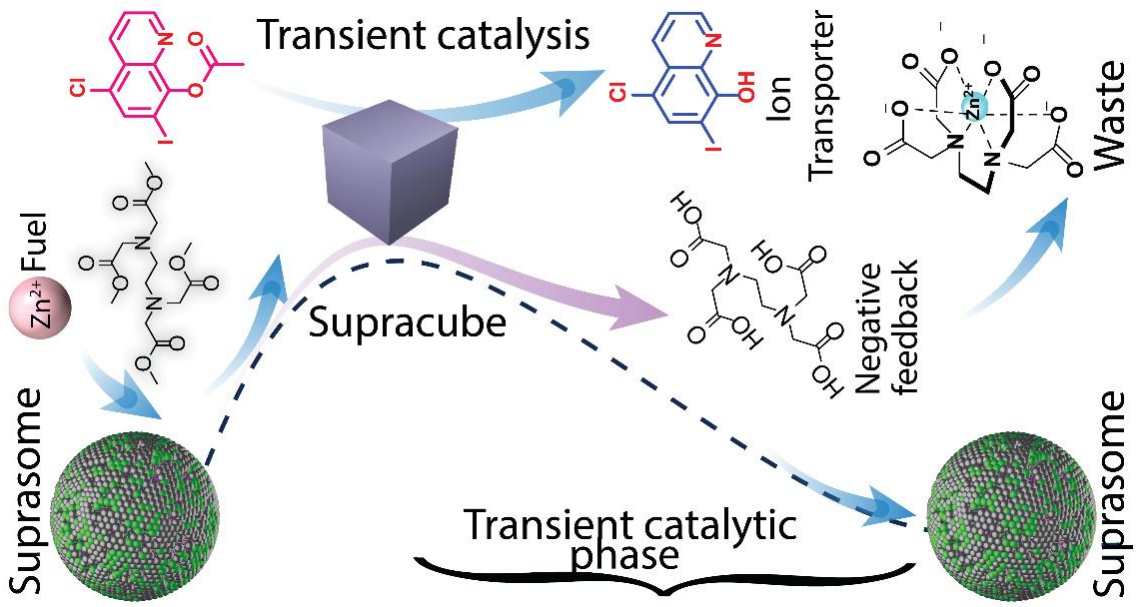


**Figure V.** Schematic representation of the suprasome-supracube interconversion of compartmentalised structures with transient catalytic activity, with $Zn^{2+}$ as a chemical stimulus and EDTA as a negative feedback controller.

---

*Chapter 5*

**Stimuli-Responsive Dynamic Supramolecular Assemblies: Temporally Gated Catalysis for Photonic Memory Formation and Intervesicle Communication**

Over the past decade, multi-stimuli responsive systems have garnered significant attention in supramolecular chemistry research. This multi-signal responsive behaviour provides a unique logic-gated system that demonstrates the development of complex decision-making in response to environmental cues, like living systems do. We know that nature is the mother of all sciences. A notable example is the living systems that demonstrate the next step of multi-stimulus responsiveness, where the relative timing of the stimulus treatment affects the output. Such outputs typically involve cascading biochemical reactions that activate or deactivate solely based on the availability of time-gated stimuli. Emulating such temporally gated, multi-stimuli-responsive behaviour will open a new doorway in supramolecular chemistry, as it will deliver unique chemical systems that not only capture chemical information but also encode temporal information. Initial attempts by Lapteva and co-workers have demonstrated that such temporally logic-gated behaviour can be implemented in DNA strand displacement, leading to

temporally gated output, which can be utilised for developing smart decision-making futuristic devices that respond to chemical stimuli, along with their relative timing of treatment. Although initial attempts have been made with DNA strands, there have been almost no attempts to develop supramolecular systems with such chemical and temporal gating behaviour. In tandem, such systems can provide a unique opportunity for futuristic applications, such as the development of optical and temporal memory, as well as temporally gated inter-vesicle communication. Addressing these gaps requires new molecular architectures and design principles. In this chapter, we build on the foundations of the suprasomal platform, offering an approach toward temporally gated, multi-input chemical behaviours that echo memory and decision-making processes in biology.

A spiropyran-based amphiphile (ASP) with a hydrophobic C12 chain and Tween 20 was co-assembled to form the system. The presence of entropy-driven host-guest interactions with β-cyclodextrin caused the nanoassemblies ($D_H$ ~185 nm) to reorganise into suprasomes (~1200 nm), as verified by DLS, FESEM, and ITC. The process of ASP undergoing reversible photoisomerisation to its merocyanine form (AMC) was triggered by exposure to UV light (365 nm), resulting in suprasome shrinkage (~400-500 nm).

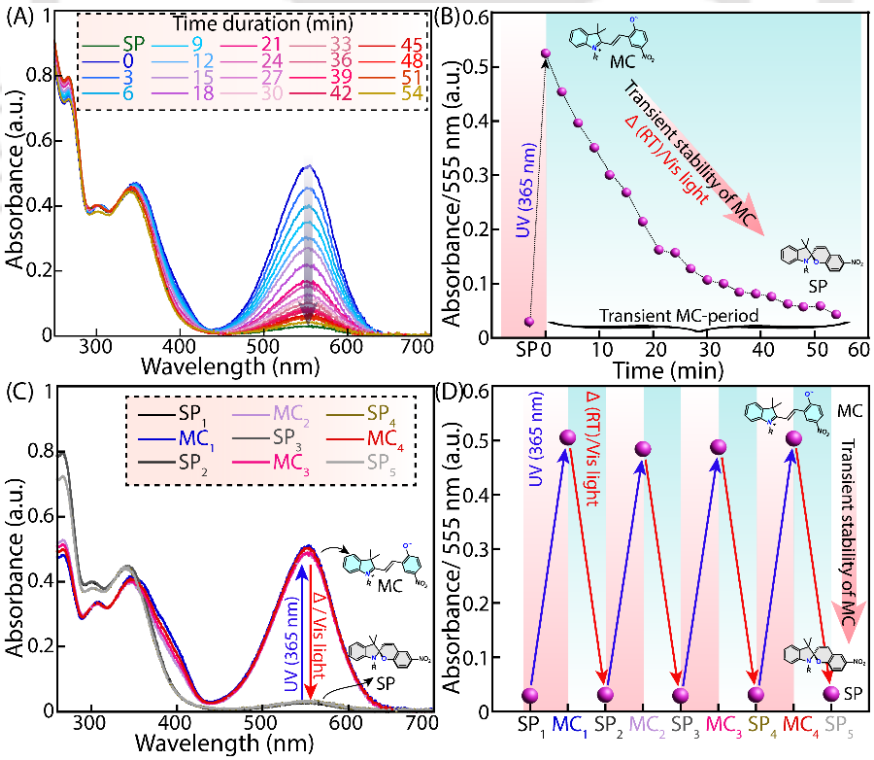


**Figure VI.** (A) UV-Vis absorbance spectra demonstrating the conversion of AMC to ASP under dark and ambient conditions in aqueous medium. (B) Time-dependent absorbance decay

during conversion of AMC to ASP. (C) Absorbance changes during ASP to AMC photoisomerisation under UV light and reversal under dark and ambient conditions in aqueous medium. (D) Reversible ASP-AMC conversion for multiple cycles in aqueous medium.

This compact state returned to its previous suprasome shape after approximately 45 minutes of metastability. In this short time frame, the interaction of $Zn^{2+}$ with the MC form caused a non-equilibrium change into nanosheet morphologies (~3500 nm), which cannot be accessed unless the two stimuli occur at the same time. When the MC was heated to its ASP state, absorbance tests confirmed the complexation between MC and $Zn^{2+}$, and a morphological reversal to suprasomes occurred. This created a synthetic version of biological temporal gating, where structural development required concomitant dual inputs (light + $Zn^{2+}$) within a short time frame.

This temporally confined dual-input logic was utilised to generate functional outputs. The ester hydrolysis catalysed by HMPO-$Zn^{2+}$ complexes could only produce fluorescent HPTS when dual inputs were simultaneously applied to suprasomes that contained both HMPO ((1E,1E)-6-((E)-(hydroxyimino)methyl)picolinaldehyde oxime) and AHPTS (acyl-8-hydroxy-1,3,6-pyrene-trisulfonic acid). A photonic memory module, the gated optical output (>90% conversion), recorded the existence and time of input events.

We also managed to design communication between vesicles. Initiator suprasomes were loaded with CQE (a proionophore) and HMPO, whereas effector liposomes contained $Zn^{2+}$-sensitive MgG dye. The suprasomes generated active CQ through HMPO-$Zn^{2+}$ catalysis when light and $Zn^{2+}$ inputs occurred simultaneously. This allowed $Zn^{2+}$ to be transported into effector vesicles, resulting in fluorescence readouts. Consistent inputs release gated ion fluxes, a process analogous to neural signalling.

EDTAE (ester derivative of EDTA) and HMPO were externally localised to encode both optical and temporal information, whereas AHPTS was enclosed within suprasomes. The hydrolysis of EDTAE by suprasomes produced EDTA, gradually reducing free $Zn^{2+}$ levels, thereby guaranteeing that both $Zn^{2+}$ availability and MC-state suprasomes were present only over brief intervals. Experiments utilising multi-well plate layouts revealed that fluorescence manifested just at the spatial-temporal intersections of light and $Zn^{2+}$ application, establishing a synthetic framework for encoding information regarding both the "where" and "when" of input events.

Collectively, this suprasomal construct demonstrates reversible light-triggered shrinkage, temporally confined structural differentiation, catalytic activation, and inter-compartmental communication. This chemical system replicates essential features of synaptic plasticity by combining transitory optical and chemical inputs, including simultaneous stimulus response, gated ion transport, and potentiation-like photonic memory. This study develops a flexible supramolecular framework for constructing time-gated artificial compartments, which are utilised in information storage, synthetic biology, and artificial cell engineering.

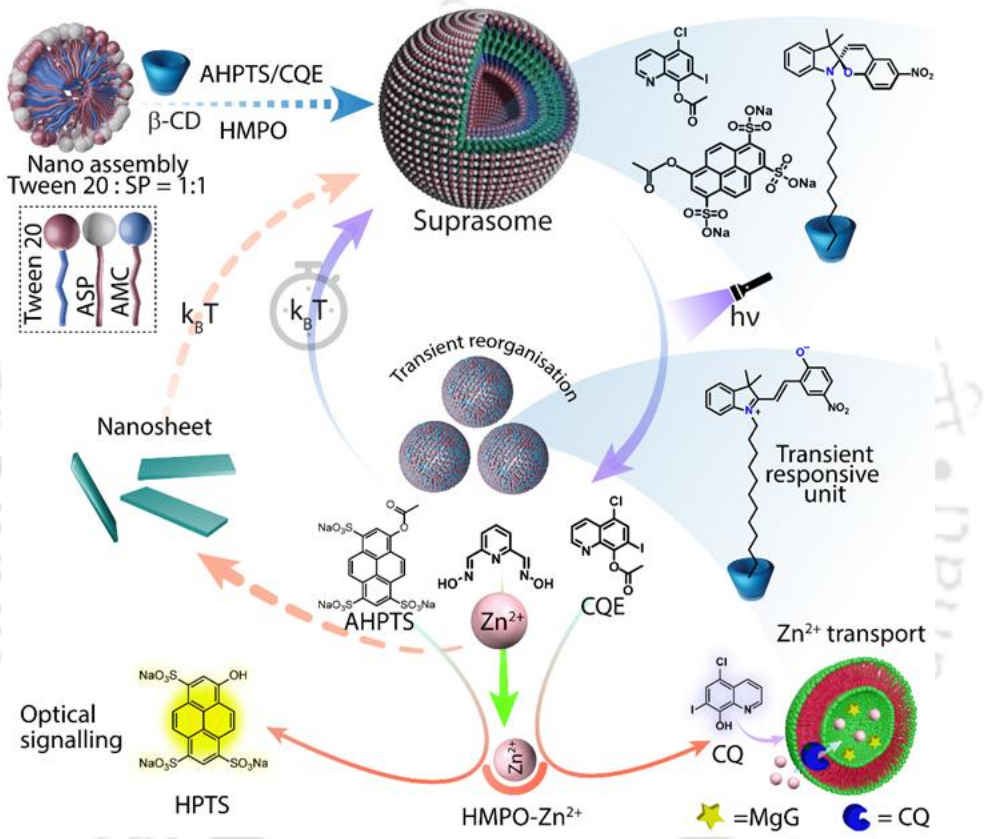


**Figure VII.** Schematic representation of photo-induced transient suprasome shrinkage and time-confined $Zn^{2+}$ triggering, which activates structural transformation accompanied by catalytic activation for subsequent optical output and $Zn^{2+}$ transport, thereby achieving key concepts such as signal transduction and intravesicular molecular communication.

---

## Conclusions

Through the course of this thesis, we have envisioned and showcased that suprasomes can serve as versatile platforms for diverse functionalities ranging from stimuli-responsive drug delivery

to inter-vesicle communication and temporally gated photonic memory storage, thereby establishing artificial supramolecular systems capable of adaptive, decision-making behaviour that offers a glimpse into the future of intelligent soft matter.

At the onset, **Chapter 1** describes the origin, speciality, fundamental benefits, as well as the non-covalent forces behind supramolecular host-guest chemistry. Additionally, a comprehensive discussion on recent trends in suprasomes and their applications in the field of drug delivery is also a crucial component. The use of β-CD as a host to develop a suprasome that delivers antibiotics upon stimulation by $Zn^{2+}$ is explained in **Chapter 2**. This approach showcases tunable antibacterial properties. **Chapter 3** addressed a significant research gap in the delivery of ion transporters, new-age therapeutics for multiple diseases, and the development of supramolecular ion channel-based therapeutics (for divalent metal ions, such as $Zn^{2+}$). Going forward, **Chapter 4** explores a suprasomal synthetic construct that converts into a supracube upon exposure to a $Zn^{2+}$ chemical stimulus. This structural transformation is transient in nature and associated with a catalytic esterase activity that can be utilised for controlling ion transport activity in another liposome, achieving a key concept of chemical communication. **Chapter 5** explores a unique suprasome that highlights how nature-inspired, temporally gated, multistimuli-responsive behaviour can be utilised for temporal and photonic memory storage and inter-vesicle communication. This thesis, as a whole, revolves around the suprasome as its centre and covers its multifaceted applications, ranging from drug delivery to temporal catalysis, photonic memory storage, and inter-vesicle communication.

---

## Future Prospects

In this thesis, we have explored different possibilities that can be achieved through stimuli-responsive suprasomes. Targeted therapeutics, ionophore delivery, developing supramolecular ion channels, stimuli-triggered temporal catalysis, and temporally gated photonic memory storage are some of the aspects we have explored in our work. The fundamental concept of suprasome can be leveraged for the advancement of synthetic chemical biology, artificial cells, communication networks, and biomedical applications.

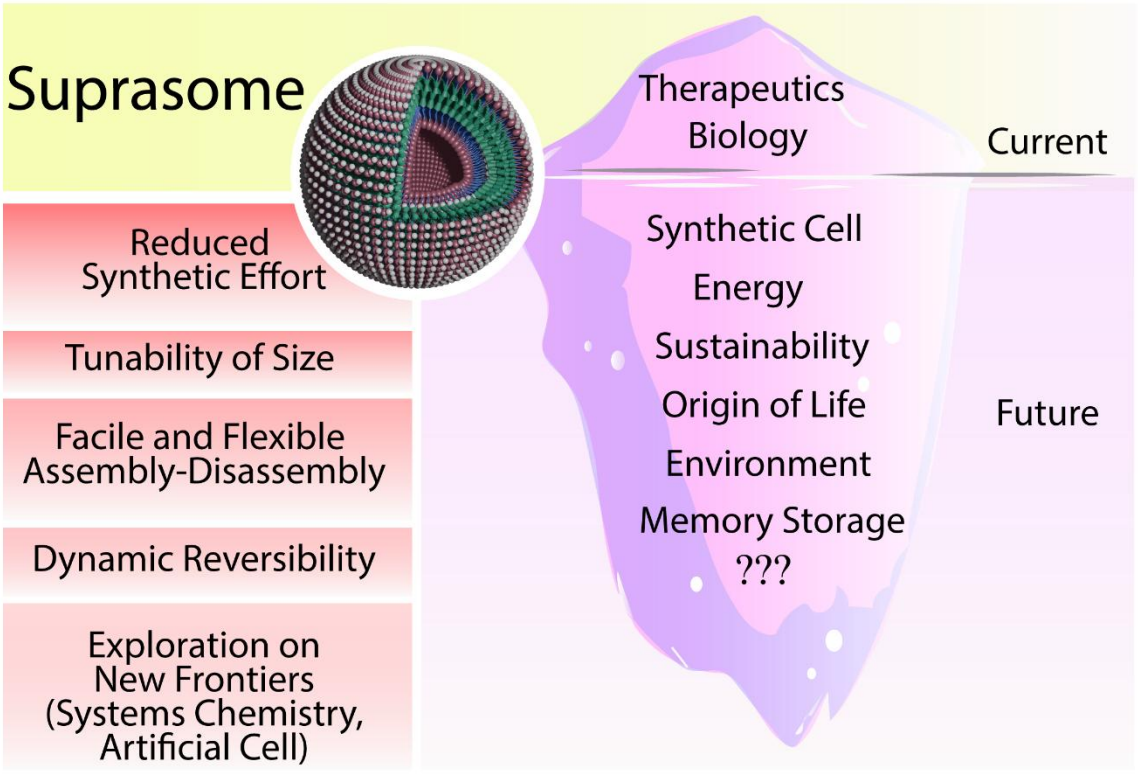


**Figure VIII.** Key advantages of the suprasome, along with its current applications and future scope.

To achieve an artificial cellular network and an advanced synthetic cellular system, it is crucial to integrate insights from diverse research domains. In this thesis, we have taken a small initiative toward this goal by coupling ion transport with suprasome-based stimuli-responsive assembly, disassembly, and reassembly strategies, thereby enabling intervesicle communication and temporally gated photonic memory storage. Such innovative developments reflect initial yet substantial breakthroughs in the evolution of next-generation artificial cells. In pursuit of future advancements, sustained innovations depend on close interdisciplinary synergistic collaboration across multiple disciplines, including supramolecular and systems chemistry, synthetic ion channels, signal transduction, and intervesicle communication. Collectively, this field is emerging as a multifaceted platform capable of resolving challenges spanning therapeutics, catalysis, energy, environmental sustainability, and the fundamental understanding of life's origins.

---

**References:**

1. Wang, Y.; Lovrak, M.; Liu, Q.; Maity, C.; le Sage, V. A.; Guo, X.; Eelkema, R.; van Esch, J. H., Hierarchically compartmentalised supramolecular gels through multilevel self-sorting. *J. Am. Chem. Soc.* **2018,** *141* (7), 2847-2851.

2. Bar-Peled, L.; Kory, N., Principles and functions of metabolic compartmentalisation. *Nat. Metab.* **2022,** *4* (10), 1232-1244.

3. Chelliah, R.; Rubab, M.; Vijayalakshmi, S.; Karuvelan, M.; Barathikannan, K.; Oh, D.-H., Liposomes for drug delivery: Classification, therapeutic applications, and limitations. *Next Nanotech.* **2025,** *8*, 100209.

4. Pattni, B. S.; Chupin, V. V.; Torchilin, V. P., New developments in liposomal drug delivery. *Chem. Rev.* **2015,** *115* (19), 10938-10966.

5. Zhu, Y.; Cao, S.; Huo, M.; van Hest, J. C.; Che, H., Recent advances in permeable polymersomes: fabrication, responsiveness, and applications. *Chem. Sci.* **2023,** *14* (27), 7411-7437.

6. Abbas, M.; Lipiński, W. P.; Wang, J.; Spruijt, E., Peptide-based coacervates as biomimetic protocells. *Chem. Soc. Rev.* **2021,** *50* (6), 3690-3705.

7. Yang, K.; Hua, B.; Qi, S.; Bai, B.; Yu, C.; Huang, F.; Yu, G., Suprasomes based on host–guest molecular recognition: an excellent alternative to liposomes in cancer theranostics. *Angew. Chem. Int. Ed.* **2022,** *134* (52), e202213572.

8. Chaudhuri, A.; Bhattacharya, B.; Gowrishankar, K.; Mayor, S.; Rao, M., Spatiotemporal regulation of chemical reactions by active cytoskeletal remodeling. *Proc. Natl. Acad. Sci. U.S.A.* **2011,** *108* (36), 14825-14830.

9. Moody, E.; Obexer, R.; Nickl, F.; Spiess, R.; Lovelock, S., An enzyme cascade enables production of therapeutic oligonucleotides in a single operation. *Science* **2023,** *380* (6650), 1150-1154.

10. Citri, A.; Malenka, R. C., Synaptic plasticity: multiple forms, functions, and mechanisms. *Neuropsychopharmacology* **2008,** *33* (1), 18-41.

11. Kashiwada, A.; Taoka, N.; Chijimi, Y.; Noguchi, K.; Shigematsu, K.; Miura, M.; Suzuki, T., Weakly acidic pH-responsive liposomal content release induced by histidine-modified agents. *Org. Biomol. Chem.* **2024,** *22* (14), 2844-2850.

# Chapter 1

# Introduction to Supramolecular Assembly and Suprasomes

### 1.1. What is Supramolecular Chemistry?

The Nobel laureate Jean-Marie Lehn has given a statement about supramolecular chemistry: " It is chemistry beyond the molecule."[1] This branch of chemistry is associated with the organisation of multiple molecules into complex architectures through a network of non-covalent interactions like hydrogen bonding, π–π stacking, Van der Waals forces, electrostatic interaction, metal-ligand co-ordination, and hydrophobic effects. Classical molecular chemistry primarily focuses on covalent bonds within individual molecules, whereas supramolecular chemistry extends beyond this, exploring dynamic self-assembly, association, and recognition among molecules that impart new properties and functions distinct from those of their individual constituents.

The importance of supramolecular chemistry is best illustrated by the nature that surrounds us. The fundamentals of life itself are rooted in supramolecular principles, which involve the encoding and decoding of genetic information through precise molecular recognition in genetic material, specifically DNA. Additionally, the folding and assembly of proteins through vast non-covalent interactions, compartmentalisation, and communication inherent to cellular membranes and organelles are processes that rely completely on the beautiful orchestration of supramolecular forces.

In the context of origins, the dawn of life on Earth is now thought to have depended critically on the formation of molecular assemblies with functional capabilities, assemblies able to encapsulate, protect, and process information or chemical energy before the emergence of complex biomolecules.[2] Current scientific discourse increasingly defines these primordial processes as examples of supramolecular organisation, where noncovalent bonds mediated the earliest steps of self-assembly, catalysis, and compartmentalisation that are considered prerequisites for life.[3] So, the concept of supramolecular provides a reference for us to understand not only the evolutionary progression of matter from inanimate to animate form but also the sophisticated molecular machinery of contemporary biology.

Thus, supramolecular chemistry is a vast field within the scientific research arena through which we understand the collective function, communication, and adaptivity of molecules, revealing fundamental insights into both the complexity of living systems and the origins of life itself.

## 1.2. Origin in Nature: Exemplars of Supramolecular Assembly

The principles of supramolecular chemistry fundamentally govern the evolution and progression of living beings on Earth. It unravels the beauty of non-covalent forces, which form the basis of structural organisation, function, and molecular recognition that make supramolecular self-assembly a pivotal step in understanding biological complexity. Here are a few quintessential examples that illustrate the same point.

### 1.2.1. DNA: The Quintessential Supramolecular Assembly

The basis of all living beings lies in DNA, which has a double helical structure, illustrating nature's dependence on the supramolecular principle.[4] The precision of genetic coding and transmission is regulated by complementary base pairing through hydrogen bonds: adenine-thymine (A–T, two hydrogen bonds) and guanine-cytosine (G–C, three hydrogen bonds).[4] These directed and reversible interactions allow for exact identification of purine and pyrimidine bases, facilitating replication and transfer of genetic information. Going beyond the standard paradigm of Watson-Crick pairing, nucleic acid bases engage in vast hydrogen bonding motifs, facilitating the formation of complex supramolecular structures like G-quadruplexes and i-motifs, all of which play roles in gene regulation, chromosome organisation, and nanostructure engineering.[5, 6] The two- and three-dimensional nanostructures of DNA have been created on the basis of the self-assembly property, which highlights its function as a programmable scaffold at molecular and material levels.

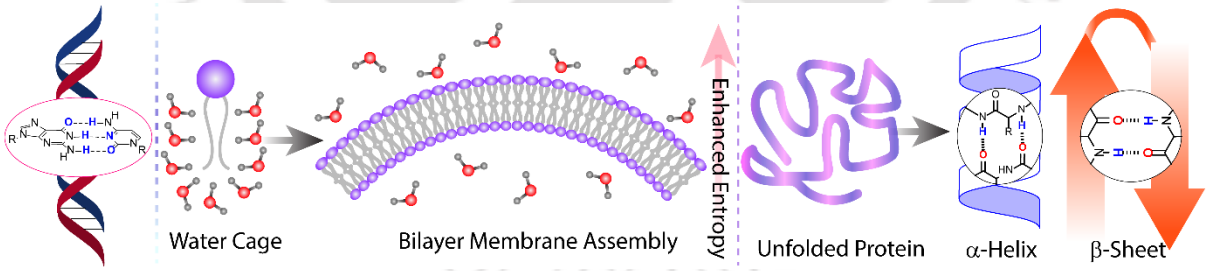


**Figure 1.1** Schematic representation of different supramolecular self-assembly in nature, such as the DNA helix, bilayer lipid membrane, and protein folding.

### 1.2.2. Hydrophobic Assembly and Cellular Compartmentalisation

Formation of lipid bilayer structures is another basic example of supramolecular self-assembly, which forms the boundaries of cells and organelles. When amphiphilic lipid molecules are introduced into a hydrophilic environment, the hydrophobic force due to non-polar tails drives them to aggregate in a patterned arrangement, repelling water, while polar headgroups remain

exposed to the solvent.[7] This is an entropy-driven process where large amphiphilic molecules assemble in a hydrophilic environment, maximising overall disorder. Spontaneous compartmentalisation and selective permeability of solutes across a semipermeable membrane rely on the basis of the hydrophobic effect. These supramolecularly assembled bilayers are the primary reason for segregation, communication, and metabolic reactions essential for the cell's sustainability.

### 1.2.3. Protein Folding: Multifaceted Noncovalent Cooperation

Protein folding is another example of the arrangement of non-covalent interactions, such as hydrogen bonding, π-π interactions, and hydrophobic effects, which transform linear non-active amino acid polymers into sophisticated, biologically active sites that facilitate important physiological cellular phenomena. The key steps involve (i) burying of nonpolar side chains in the protein core due to hydrophobic force, (ii) hydrogen bonding driving and stabilising the secondary structures (α-helices, β-sheets) for giving precise conformational structure and flexibility, and (iii) π-π stacking and salt bridges (ionic and hydrogen bond combinations) providing additional stability and specificity for tertiary and quaternary conformations.[8] If any of these weak interactions stop playing their role, then it can result in inactive or misfolded proteins that could lead to mutation, disrupted metabolic activity, and hormonal imbalance, causing hazardous health issues.

### 1.2.4. Supramolecular Recognition and Catalysis

The capacity of proteins and indeed all biological systems to discriminate substrates and effect transformations hinges on noncovalent molecular recognition. The interplay of hydrogen bonding, the Van der Waals force, and electrostatic interactions mediates ligand-to-protein binding, which is the basis of the lock-and-key model, thereby enabling an active enzymatic site for catalytic conversion with precision and selectivity.

Altogether, the formation of the double helical DNA pair to the cellular membrane, protein folding, and its active function as an enzymatic substrate are the core examples of subtle and cooperative supramolecular interactions. The sophisticated molecular machinery that enables it to store, process, and transmit information, allowing it to self-organise and adapt to its surroundings, would not have been possible without non-covalent forces or interactions. Thus, supramolecular chemistry provides us with a valuable tool for understanding nature and biology, which could lead to evolutionary solutions for existing biological complications and the engineering of advanced biotechnological tools.

### 1.3. Key Features Provided by Supramolecular Assemblies

Supramolecular assemblies play a fundamental role in biology due to the distinctive characteristics provided by noncovalent molecular organisation. These characteristics jointly support the adaptability, selectivity, and reactivity necessary for essential biological functions.

#### 1.3.1. Molecular Recognition and Selectivity

The ability to selectively and precisely recognise molecules is a fundamental property of supramolecular interactions. This selectivity enables proteins, organelles, and cells to accurately identify and interact with their respective counterparts in a dynamic system. For example, immune cells, such as macrophages, utilise surface-bound lectins to selectively recognise bacterial sugars, enabling the precise targeting and eradication of pathogens.[9] Enzymes utilise the supramolecular recognition method to bind at specific substrate sites, ensuring optimal biochemical catalysis performance critical for sustaining cells and organelles.

#### 1.3.2. Dynamic and Reversible Behaviour

Self-assemblies resulting from supramolecular host-guest interactions provide the dynamism and reversibility that are key necessities for developing smart, stimuli-responsive systems. Such dynamic reversibility is attributable to the noncovalent interactions delivering moderate strength that lies in a local potential energy minimum, unlike covalent bonds, where it's a global minimum with high binding energy. In contrast to covalent bonds, supramolecular interactions can swiftly reorganise, dissociate, and reconstruct in response to fluctuating environments, a characteristic essential for life-like processes. The dynamic assembly and

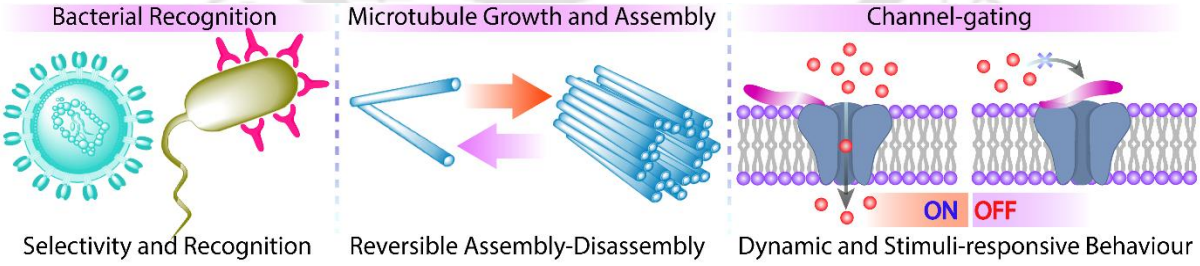


**Figure 1.2** Schematic representation of key attributes of supramolecular self-assembly observed in nature.

disassembly of microtubules during the cell cycle is one such beautiful example where this dynamicity is of tremendous utility. Polymerisation and depolymerisation of such large supramolecular polymers are essential steps for controlling key events, such as cell growth and division.[10] In tandem, these filaments also work as a walking path for motor proteins like

kinesin by using transient binding and release events to walk along the filaments and transport cargo.

### 1.3.3. Stimuli-Responsiveness and Controllability

Another significant advantage of supramolecular organisation is its sensitivity towards stimuli. The facile reversibility of weaker (non-covalent) interactions enables the formation of assemblies that can be easily regulated by environmental cues, such as pH, ionic strength, and redox conditions. The most common examples include ion channels and transporters, which are sensitive to electrical or chemical stimuli, modulating the ion flux across the bilayer and enabling various physiological processes. This triggered, opening-and-closing nature of channels allows specific stimuli to facilitate cell-to-cell communication, signal transduction, and other coordinated biological responses across tissues and organs.

### 1.3.4. Emergent Properties and Systems-Level Effects

This supramolecular self-assembly system exhibits emergent properties that differ from those of its individual components. For example, the collective behaviour of assemblies such as actin filaments, ribosomes, and lipid rafts allows complex functions in signalling, metabolism, osmotic regulation, and tissue organisation. These new properties of the system arise from hierarchical self-assembly, cooperative non-covalent networking, and its capacity for reconfiguration that is dependent on the surrounding environment.

To be precise, the important features of supramolecular assembly are its recognition ability, dynamic and reversible binding, sensitivity towards external stimuli, and emergent properties that contribute to stability and adaptivity, which explains why nature chooses supramolecular organisation as its universal strategy. These functions not only enhance precise biological function but also inspire the design of advanced materials and nanodevices for futuristic development in science.

## 1.4. Fundamental Forces Governing Supramolecular Assembly

It is essential to discuss the fundamental forces that underlie the molecular basis of such supramolecular assemblies. Having a basic understanding of these driving forces enables the design and development of assemblies with desired properties that cater to our needs in fields such as therapeutics, drug delivery, and biotechnology. The following sections discuss these noncovalent forces, their nature, categories, and key prerequisites for developing these forces to meet the demand.

### 1.4.1. Hydrogen Bonding

One of the most important non-covalent interactions, or forces, commonly observed in supramolecular assemblies is hydrogen bonding. It is characterised by a hydrogen atom covalently bonded to an electronegative atom or group (like O, N, or C=C) and attracted to another electronegative atom. Its moderate strength and directionality make it possible for large-scale organisation in both biological and material prospects. The genetic blueprint of all organisms is encoded in the DNA double helix, where the two strands are interconnected by complementary hydrogen bonds between base pairs. Adenine pairs with thymine (two hydrogen bonds), and guanine pairs with cytosine (three hydrogen bonds). The specificity and reversibility of these connections enable accurate replication and transfer of genetic information.[12] In the absence of hydrogen bonding, the double helical structure and biological heredity would collapse.

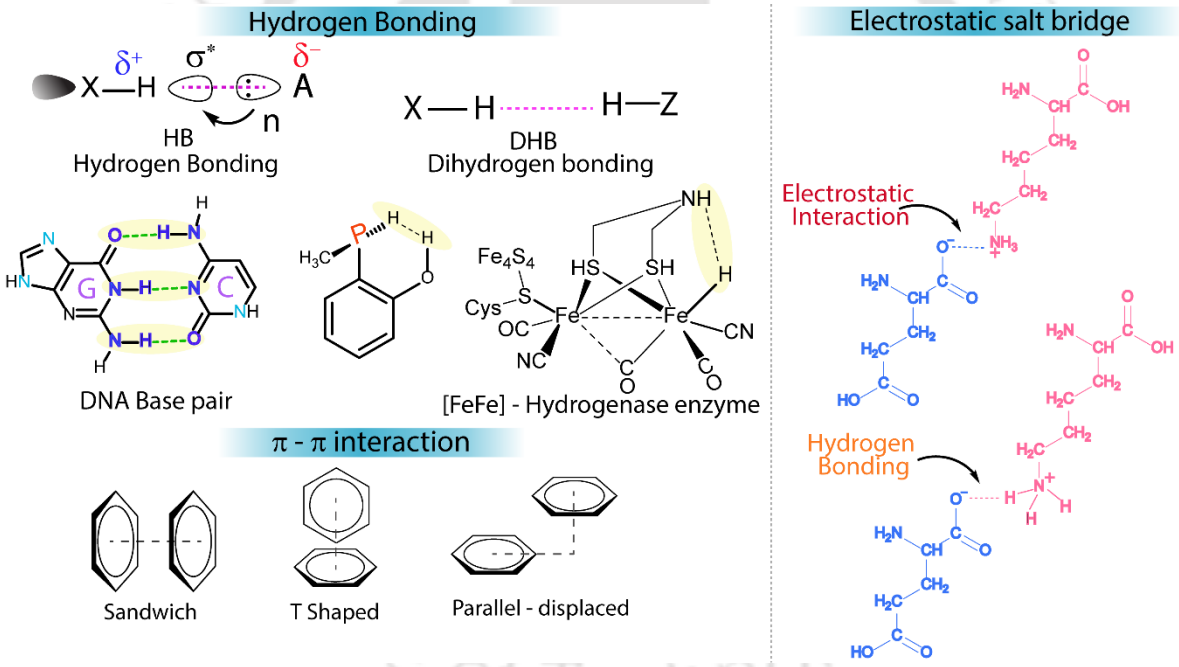


**Figure 1.3** Different noncovalent forces occurring in nature that drive supramolecular assembly formation.

Another facet of H-bonding that has received very limited attention is dihydrogen bonding. Such specialised bonds further demonstrate their key role and intricate necessity, as they provide functional flexibility at crucial occasions. A compelling natural example is observed in [FeFe]-hydrogenase enzymes, where the reversible conversion of protons and electrons to molecular hydrogen is catalysed. A stunning natural example is found in [FeFe]-hydrogenase enzymes, which catalyse the reversible conversion of protons and electrons to molecular

hydrogen. A distinct dihydrogen interaction (N–H···H–Fe) arises within the catalytic H-cluster, which uniquely facilitates highly effective proton/hydride relay at the active reaction site. Within this configuration, the aminodithiolate-bound proton (donor) interacts with a hydridic hydrogen (acceptor) at an Fe centre, functioning as a dynamic catalytic hub within biological energy conversion pathways.[13, 14] Interference with this supramolecular relay disrupts its operational functionality, emphasising the critical importance of such unique dihydrogen bonding.

### 1.4.2. Protein Salt Bridges

Salt bridges are another class of noncovalent interactions involving the coulombic force of attraction between acidic (Asp/Glu) and basic (Lys/Arg) residues.[15] It's a unique combination of electrostatic attraction between positively and negatively charged species and hydrogen bonding between acids and bases. They deliver the required rigidity and stability to the tertiary and quaternary structures of hyperthermophilic proteins and enzyme complexes, especially for adaptation to extreme environments.[16] Apart from other noncovalent forces, salt bridges provide the strongest binding force among residues. A network of such coulombic interactions ensures extreme rigidity and conformational stability, preventing thermal denaturation of proteins. Although this provides the desired stability at higher temperatures, an appropriate balance between stability and catalytic flexibility is usually maintained through various other noncovalent interactions, ensuring the protein's proper functionality at normal temperatures.

### 1.4.3. π–π Stacking Interactions

An attractive noncovalent force is formed between the pi electron clouds of aromatic or planar molecules, known as π–π stacking. The arrangement of electrons allows for regions of positive and negative charges, leading to attraction between the planar molecules that typically stack upon each other in a different manner. Parallel-displaced (offset) stacking, face-to-face (sandwich) stacking, and edge-to-face (T-shaped) stacking are a few types of stacking observed in the simple phenyl system, in order of their stability.[17] Apart from H-bonding, these pi stacking interactions play a pivotal role in protein folding and mostly in maintaining the integrity and flexibility of the DNA double helix by stacking interactions between adjacent aromatic bases. These interactions confer attributes such as resistance to denaturation and conformational disruption, which are essential for maintaining genetic fidelity and repair.

### 1.4.4. Hydrophobic Interactions

Hydrophobic interactions result from the tendency of nonpolar molecular segments to cluster together in aqueous environments, minimising the disruption of water's hydrogen-bonded network. This entropically driven force drives both compartmentalisation (membrane formation) and macromolecular folding. The spontaneous self-assembly of amphiphilic lipids into bilayer membranes is governed by hydrophobic effects, forming the essential boundaries of all cells. In globular proteins, hydrophobic residues aggregate to form tightly packed cores; without this driving force, proteins would remain extended, misfolded, and biologically inactive, as is starkly demonstrated in myoglobin and other essential enzymes.[18]

### 1.4.5. Additional Noncovalent Forces

Cation–π, dipole–dipole, and metal coordination interactions supplement the above, enriching the spectrum of recognition, assembly, and regulatory possibilities available to supramolecular systems. For instance, cation–π interactions are crucial in neurotransmitter binding within synaptic proteins, and metal–ligand coordination underlies the function of metalloproteins and enzymes.[19]

In summary, the coordinated organisation of hydrogen bonding (classic and dual), salt bridges, π–π stacking, hydrophobic effects, and additional noncovalent forces forms the bedrock of supramolecular assembly. The absence of any one of these interactions precludes the formation of nature's most fundamental and advanced molecular architectures, from DNA replication to catalytic energy conversion, defining both the essence of living systems and the inspiration for artificial supramolecular design. A detailed discussion of these forces is presented here, as knowledge about their fine-tuned modulation can enable the development of systems that mimic natural complexity or create improved systems to address challenges in various fields of research.

## 1.5. Key Applications of Supramolecular Assembly in Nature

Before discussing artificial supramolecular systems, it's essential to understand that these crucial interactions form the fundamental basis for many complex biological processes, which are pivotal to sustaining life. Selectivity, reversibility, and stimulus-responsiveness are key attributes of complex assemblies in cells that enable a range of functions, including molecular recognition, selective catalysis, and dynamic signal transduction and communication. Having a thorough mechanistic understanding of such natural supramolecular systems and their mode

of action is intellectually very compelling. Additionally, it inspires the development of artificial systems, such as suprasomes, that not only attempt to emulate key biological concepts but also offer simple solutions to challenging problems in therapeutics, synthetic chemical biology, and materials science.

### 1.5.1. Selective and Stimuli-Responsive Ion/Small Molecule Transport

Ion channels, ion pumps, or aquaporins represent a beautiful example where amino acids self-assemble in a way that the outer part is hydrophobic, allowing them to remain inside the lipid membrane for transport activity. Furthermore, the delicate balance of different noncovalent interactions results in a precise arrangement of amino acids that fold to form pores. These pores selectively recognise, bind, and allow smooth passage of hydrophilic ion molecules essential for cell survival.[20] Selective and reversible binding of the $O_2$ molecule by the heme prosthetic group in haemoglobin represents another crucial activity in our body. This illustrates how supramolecular interactions facilitate the efficient capture of $O_2$ at the lungs and its delivery to metabolically active, oxygen-requiring tissues.[21] Such examples deeply inspire researchers to develop artificial supramolecular systems that can deliver therapeutics in a stimuli-responsive manner to diseased sites such as cancer and bacterial infections. Furthermore, these platforms can address challenges faced by modern therapeutics, enabling the overcoming of off-target effects, enhancing delivery specificity, and responding adaptively to disease-associated stimuli.

### 1.5.2. Immune Defence and Detoxification

Immune defence mechanisms in our body also rely on supramolecular assembly and molecular recognition. Among biological systems, lectins provide the most illustrative example. These host proteins recognise bacterial surface sugars through noncovalent interactions (glycan-lectin recognition) and bind to them, thereby blocking pathogen adhesion and facilitating pathogen identification.[22] They act as molecular flags for the immune defence system, promoting phagocytosis of selective foreign elements. The destruction process by immune cells marks another key supramolecular event. In this regard, defensin proteins are one exemplary case. These host peptides recognise and assemble into pores within the bacterial membrane, causing membrane disintegration and leakage, which ultimately leads to the destruction of the bacterium.[23] This demonstrates a coordinated series of supramolecular events, like recognition, blockage, and channel-based membrane leakage, that can be employed to tackle pathogens. Once again, nature reveals itself as the ultimate innovator, offering timeless principles that guide human creativity and scientific advancement.

### 1.5.3. Transient Assemblies in Catalysis and Energy Regulation

Owing to the moderate stability of supramolecular assembly, they provide unique transient functionalities essential for dynamic activities in biology. Enzyme-substrate complexes and metabolons are key examples where a dynamic binding event facilitates substrate channelling, optimising the efficiency of catalysis and minimising side reactions. In the exemplary case of metabolons, glycolytic enzymes transiently assemble into a larger enzyme complex, where they work in harmony to facilitate the efficient and direct transfer of metabolic intermediates from one enzyme to the next.[24] These showcase a molecular factory at the cellular level, which not only showcases intricate supramolecular coordination but also displays stimulus-responsive functional activity in response to oxygen level and energy demand in the cell.

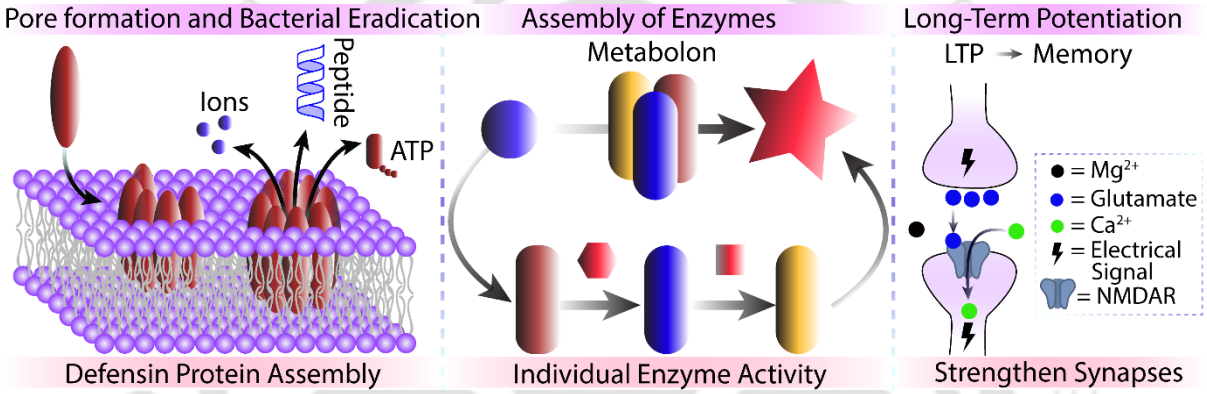


**Figure 1.4.** Schematic representation of important applications of supramolecular assembly in biology.

### 1.5.4. Supramolecular Control of Neural Communication and Memory Formation

Real-time inter-neuron communication and long-term plasticity are key functionalities in neurons that require coordinated activity, with supramolecular interaction being the driving force. SNARE protein assemblies and scaffolding proteins display synaptic vesicle docking and neurotransmitter release that are key to interneuron communication. These crucial events are the outcome of calcium-regulated supramolecular interactions, showcasing the importance of metal-responsive supramolecular platforms.[25] Long-term potentiation (LTP), also known as the cellular currency of memory, is carried out through temporally gated complex supramolecular and biochemical events that encode memory traces with plasticity of synaptic strength.[26] This demonstrates how the relative timing of triggers in a multi-stimuli supramolecular event can affect the result and can be utilised even to develop artificial memory through chemical and supramolecular platforms.

In summary, detailed analysis and discussion on the aforementioned functionalities of supramolecular assemblies not only simplifies complex biological phenomena but also offers an indispensable blueprint for the design and development of artificial supramolecular platforms. These emerging supramolecular templates, such as suprasomes, exploit foundational principles, including dynamic stimuli-responsiveness, molecular recognition, and transient activity, to emulate biological concepts and utilise them to address modern-day challenges in therapeutics, synthetic biology, and materials science.

## 1.6. Suprasomes and Their Biological Inspirations: Expanding the Frontiers of Supramolecular Assembly

Biological processes ranging from intercellular communication and signal transmission-transduction to memory formation are mostly complex, reversible, and dynamic in nature, where supramolecular interaction serves as the molecular foundation for it. Their noncovalent interactions enable the desired assembly and disassembly of a functional architecture in response to specific stimuli. The suprasomes, a synthetic supramolecular vesicle, draw their inspiration from such dynamic natural processes to offer innovative synthetic platforms that can emulate biological functions. Furthermore, assembly-disassembly dynamics, stimulus-responsiveness, reversibility, and selectivity are key controllables that need to be carefully integrated into the suprasomal system to harness the desired property from the designed suprasome. Hence, it's crucial to have a detailed discussion about its design principles.

## 1.7. Concept and Design of Suprasomes

Inspired by such biological sophistication, synthetic supramolecular systems have been developed to mimic these dynamic assembly–disassembly behaviours. Among these, suprasomes stand out as hierarchically organised, vesicular superstructures that are self-assembled from amphiphilic molecules coordinated by noncovalent host–guest interactions. These assemblies display multiple layers of supramolecular order, composed of bilayer vesicles similar to liposomes or polymersomes, wherein functional host–guest pairs dictate responsiveness to external stimuli such as pH, ions, light, and redox potential.

To achieve the desired responsiveness to stimuli, it is necessary to choose a suitable host-guest pair that assembles to form a dynamic complex mimicking the structure of a lipid, with a defined hydrophilic and hydrophobic part. This provides a flexible, detachable platform that self-assembles into a spherical liposome-like structure in aqueous media known as a suprasome. Researchers in recent times have explored a lot of such host-guest pairs, that have

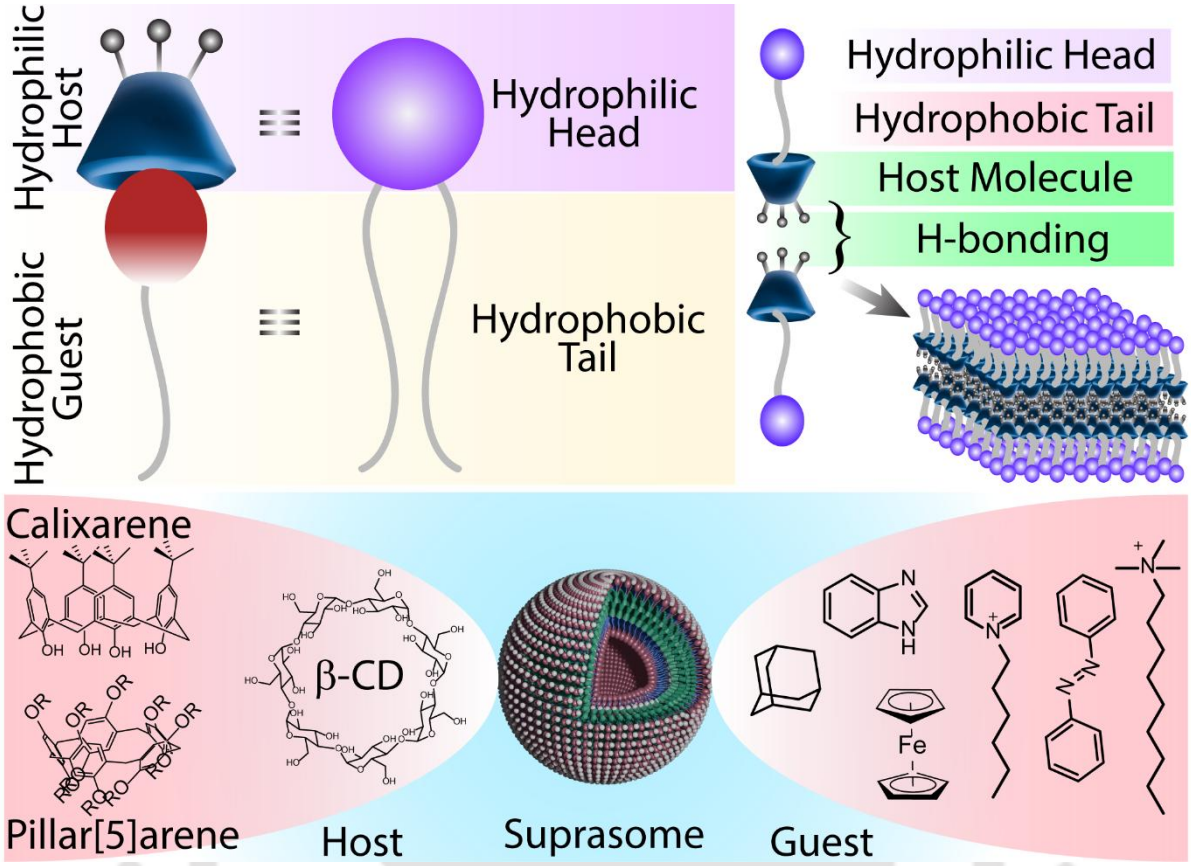


**Figure 1.5** Schematic representation of a host-guest complex mimicking lipid structure and forming a bilayer membrane. A few examples of host and guest molecules for the design and development of a suprasome.

been exploited for the development of multifunctional materials for applications in the fields of drug delivery, signal transduction, and synthetic chemical biology. A few important ones have been discussed below.

### 1.7.1. Suitable Host–Guest Chemistry for Suprasome Assembly

The appropriate selection of host-guest pairings plays a pivotal role in modulating the physical and chemical properties of the suprasome. This matchmaking not only provides the desired stability, functionality, and stimulus responsiveness but also a versatile, transient nature that meets suitable requirements. Here are a few commonly explored host-guest pairs that are popular in supramolecular research.

- Cyclodextrin–Adamantane (CD–Ad): This is one of the notable host-guest pairs where the hydrophobic cavity of cyclodextrin provides extremely strong binding affinity, hence serving as a stable self-assembled system. Along with stability, these systems also exhibit dynamic, reversible inclusion of adamantane derivatives. The dynamic

nature is further exploited for its facile assembly and disassembly, where competitive guest and enzyme triggers, such as amylase, are mostly explored ones.[27]

- Cucurbit[n]uril–Ammonium Pairs (CB[n]–$NH_3^+$): Unlike the above one, here the host provides high affinity towards the hydrophilic and cationic ammonium group. This provides an opportunity to utilise charged surfactant molecules for suprasome formation. This provides the necessary robustness as well as responsiveness to ionic conditions. Also, owing to their positive surface charge, such systems can be modulated to target negatively charged bacterial surfaces, which are crucial in current-generation DDS.[28]
- Calixarene–Viologen or Ferrocenium Complexes: Such systems are very popular for their assembly and disassembly cycles, which are manoeuvred by altering the redox environment. Additionally, ATP-analogue responsiveness renders them suitable candidates for mimicking biological platforms as well as application in medicine.[29]
- Pillar[n]arene–Pyridinium Systems: This host-guest pair is pH sensitive, making them suitable candidates for developing responsive materials that can be activated at the diseased site of acidic pH (cancer and bacterial infection).[30]

Having explored the range of macrocyclic host–guest systems from cyclodextrin–adamantane and cucurbit[n]uril–ammonium to calixarene–viologen and pillararene–pyridinium combinations, it becomes clear that the rich repertoire of supramolecular self-assembly architectures is rooted in the principles of selective, reversible, and stimuli-responsive molecular recognition.

### 1.7.2. Suitable Assembly-Disassembly Strategy

The binding affinity of such a host-guest pair should be optimal for the requirement, as this is one of the key parameters that affects its dynamic behaviour, responsiveness, stability, and selectivity to other chemical or biochemical stimuli, thereby influencing its utility for various purposes. A low binding affinity between the host-guest pair will render the assembly extremely dynamic, as well as its disassembly very facile, as the domain of molecules matching or overpowering the affinity will be large and easily available in real-world systems. Again, the strongest binding guest partner might make the complex difficult to disassemble, requiring multiple stimuli or stronger chemical stimuli. For such cases, a careful design and chemical modification of the host or guest are required that will be responsive to external stimuli (such

as light, metal ions, pH, etc.), displaying a self-assembly that can be reversibly controlled through these external stimuli. This strategy, along with the available literature, will be discussed in the following section. The last one is the type of host-guest pair whose affinity lies in an optimal sweet spot where its assembly is shielded from most guests in a natural environment, leaving few selective molecules of higher affinity that are capable of disassembling it as a competitive guest or host molecule. Hence, providing selective responsiveness is necessary to cater to targeted stimuli and responsiveness. There are examples where adamantane derivatives have been used as competitive guests to disassemble the self-assembly.[31] Simultaneously, α-CD in place of β-CD has been used as a competitive host to disrupt the azobenzene-β-CD host-guest pair.[32] Thus, different strategies that were previously utilised for self-assembly disruption can be utilised for the disassembly of suprasomes and regulate their subsequent activity and functionalities.

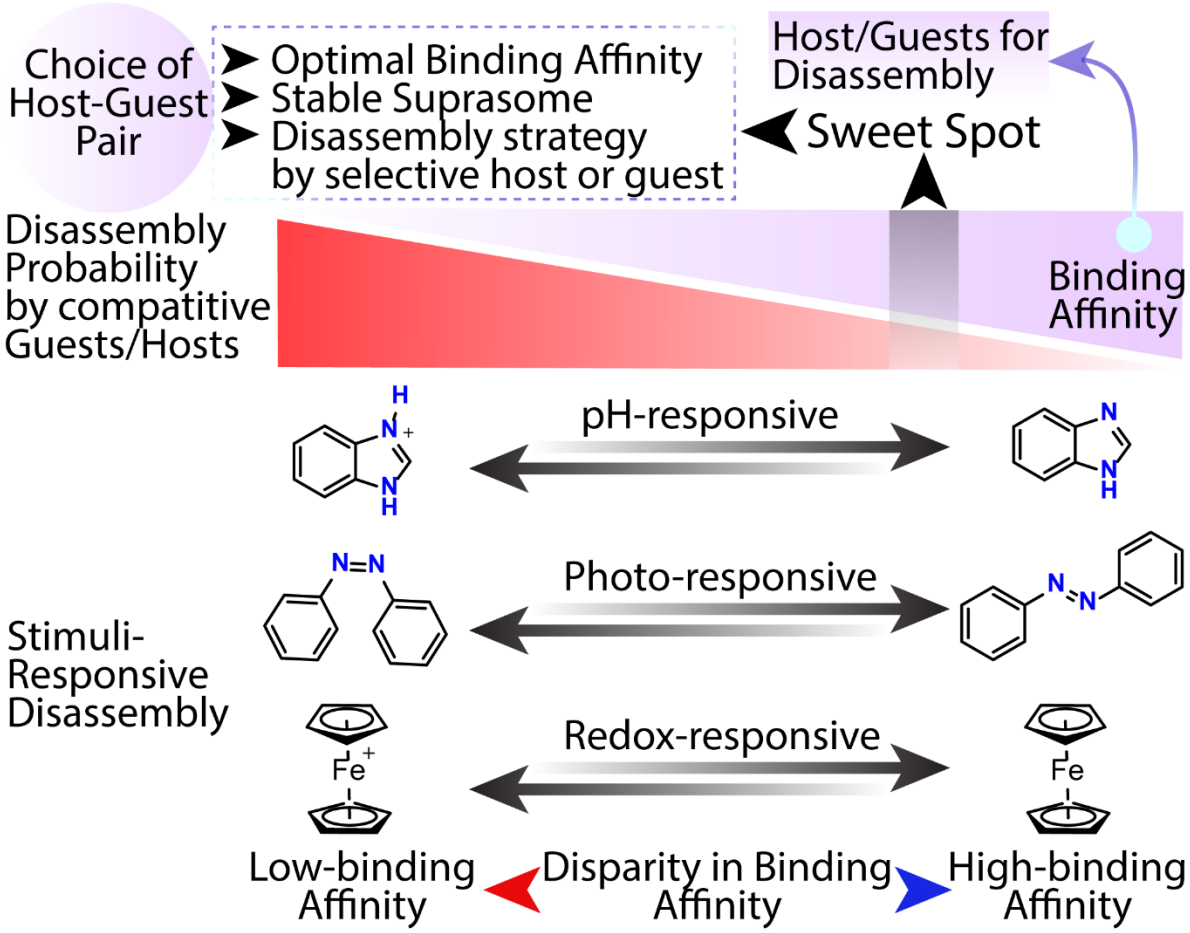


**Figure 1.6** Choice of suitable host-guest for smooth assembly into suprasome and appropriate disassembly strategies.

To develop external stimuli-responsive self-assembly, such as a photoresponsive or pH-responsive system, two strategies are typically employed: modifying the host or modifying the guest. Researchers have mostly stuck to modifying the guest with a photoresponsive group, such as diazo benzene, that acts as a host in trans form and disassembles in its cis form. This strategy is guest-specific and provides a spatiotemporal control over the assembly.[33]

Similarly, the benzimidazole group displays remarkable disparity in binding affinities towards β-CD in its protonated and deprotonated states. Such a disparity in affinity, operating in a pH-dependent manner, has been exploited for constructing pH-responsive self-assemblies. Specifically, the protonated form of benzimidazole with β-CD has a binding constant of 80–300 $M^{-1}$, while for the deprotonated (neutral) form it is around 500–1033 $M^{-1}$, reflecting that such variations in affinity offer potential for effective application in pH-responsive behaviour. As demonstrated by Huan Meng *et al.*, the β-cyclodextrin/benzimidazole supramolecular nanovalve assembly promoted pH-sensitive release of the drug from mesoporous silica nanoparticles (MSNPs). pH-mediated variation of affinity between benzimidazole and β-CD was used as a governing mechanism in this work.[34] The supramolecular assembly maintains its stable integrity at physiological pH, whereas it dissociates under a highly acidic endosomal environment. Operating via this mechanism, the system enabled the selective release of doxorubicin inside THP-1 and KB-31 cells, thereby laying the groundwork for an adaptive, pH-controlled delivery system and nuclear targeting.

Researchers have recently developed innovative tandem stimuli-responsive disassembly strategies that integrate sequential enzymatic and biomolecular recognition events to achieve precise spatiotemporal control over supramolecular behaviour in biological environments. Wang *et al.* demonstrated a tandem stimuli-responsive supramolecular assembly designed using guanidinium-modified calix[5]arene (GC5A 6C) and eosin Y-modified hyaluronic acid (EY HA), aiming to achieve successively programmable and tumor-specific phototheranostics. The unique operational principle employs a dual lock and key mechanism, where hyaluronidase (HAase) serves as the primary molecular key for unlocking the cleavage event of HA chains and dismantling the polymeric assembly, while adenosine triphosphate (ATP) acts as the secondary key to competitively displace EY from the GC5A 6C cavity, culminating in fluorescence recovery and renewal of photodynamic activity. This presented a unique tandem trigger design that enables precise, stepwise activation and controlled release of the photosensitiser EY exclusively in the tumor microenvironment, where high levels of β-galactosidase and ATP coexist. Through this study, an innovative, multi-responsive strategy

was presented for precision imaging and photoactivated therapy, introducing a tunable and generalisable interface for future phototheranostic applications.[35]

Bing Jiang *et al.* reported a redox-responsive self-assembly system based on a ferrocene-functionalised β-cyclodextrin derivative (βCD-EG-Fc). The reduced βCD-EG-Fc formed intermolecular host–guest inclusion complexes between the β-CD and Fc units, leading to network-like aggregates that evolved into vesicles over time, primarily stabilised by hydrogen bonding. Fc oxidation to ferrocenium ($Fc^+$) leads to disruption of host–guest, resulting in cationic vesicles without any host-guest pairing. Bidirectional switching between assembled states was achieved through a reversible $Fc/Fc^+$ redox process, exhibiting tunable supramolecular assembly and disassembly. Through this work, a molecular-level understanding of redox-driven supramolecular transformations lays the foundation for designing stimuli-responsive materials.[36]

Crucially, these engineered host–guest motifs do more than merely assemble vesicular nanostructures: they empower suprasomes to recapitulate fundamental biological functions. Judicious selection and stimuli-responsive host–guest pairs establish synthetic analogues of natural supramolecular assemblies, providing precise cargo loading and unloading, triggered ion transport, pore-mediated antibacterial action, transient catalytic regulation, and even information storage or chemical signalling reminiscent of neural processes. The upcoming section describes how suprasomes bridge the gap between basic molecular self-assembly and the sophisticated, organised activities observed in biological systems, demonstrating their capacity for mimicking natural functions across delivery, sensing, catalysis, and cellular communication.

### 1.8. Advantages of Suprasomes over Traditional Synthetic Vesicular Systems

Historically, vesicular self-assemblies have received considerable attention for therapeutic delivery systems. Over the period, drug delivery systems (DDS) have undergone evolution from simple micellar self-assemblies to liposomes, polymerosomes, and, more recently, advanced to third-generation suprasomes. Due to their distinct advantages over traditional systems, suprasomes have rapidly gained widespread acceptance in the scientific community. Traditional liposomes and polymerosomes often require laborious and complex synthetic routes, and the design of stimuli-responsive variants typically demands additional multistep synthesis, frequently involving harmful chemicals or metal ions.

On the other hand, suprasomes exemplify significant advancements within the areas of supramolecular chemistry and drug delivery research. Simple assembly of suprasomes is possible through the integration of compatible host–guest systems, where self-assembling processes give rise to the intended vesicular construct. Their inherent ability to self-assemble and disassemble dynamically arises from their dependence on supramolecular forces rather than covalent bonds, a feature that provides reversibility and modular tunability. Beyond that, the straightforward incorporation of stimuli-responsive moieties into suprasomal architectures enables effortless tailoring of stimulus sensitivity without extensive synthetic effort.

Therefore, the emergence of stimuli-responsive suprasomal vesicles represents an uncomplicated, flexible, and sustainable approach. This built-in multidimensionality nurtures suprasomes as the cutting-edge DDS platform, with applications and impact extending far beyond therapeutic delivery, a frontier our present work seeks to explore. Apart from this, suprasomes provide adaptable control over their diverse functional properties such as vesicle size, surface charge, robustness, stability, etc., in comparison to their conventional counterparts (liposomes, polymerosomes). Fine-tuning of host-guest complexation ratios can regulate their size and surface zeta potential.

One more critical strength resides in the dynamic nature of these assemblies, which facilitates the reversible function necessary to achieve state-of-the-art vesicle formulations, demanding advanced traits such as transient activity, catalysis, and temporally gated multistimuli-responsiveness. Such unique behaviour is crucial not only for advanced drug delivery applications but also for the development of synthetic cells, envisioned as foundational elements in synthetic chemical biology aimed at addressing cellular and molecular-level challenges.

### 1.9. Suprasome-based Drug Delivery Systems

Contemporary findings firmly establish the potential of suprasomes as multifunctional, biomimetic nano-systems across domains, particularly in precision delivery, stimulus-responsive systems, and programmable therapeutic strategies. Suprasomes, assembled through non-covalent host–guest interactions, overcome key foundational obstacles encountered by traditional vesicular drug delivery platforms, such as liposomes and polymersomes, particularly concerning the challenges of functionalisation intricacy and sensitivity to stimuli. A concise overview of recent suprasome literature is presented here to offer a perspective on validated strategies and their application scope. Moreover, it will reveal uncharted territories

and key knowledge gaps demanding dedicated exploration and evaluation by the scientific community.

Yang et al. developed suprasomes assembled through pillararene-based host–guest interactions, allowing them to encapsulate the anticancer drug cisplatin.[37] Their synthetic suprasomal platform exhibits photothermal activity: near-infrared light serves as a trigger for accurate drug release, yielding successful tumor clearance with pronounced metastasis inhibition. This strategy integrates photothermal treatment and chemotherapeutic intervention using a flexible nanostructured platform, offering user-friendly and multifunctional assembly–disassembly techniques and the capacity to cooperatively improve anticancer efficacy through programmable spatiotemporal drug release strategies.

Through their recent work, Zhang, Z., et al. have shown how a suprasome can be smartly designed to undergo reversible structural transformation by sensing the redox environment in its surroundings. They reported that their suprasomal system achieved precise loading and radiometric delivery of therapeutic combinations, as it can load multiple drug combinations. In the tumour's hypoxic microenvironmental region, the guest molecule undergoes degradation, resulting in the separation of hydrophilic and hydrophobic domains and subsequently inducing suprasome disassembly in response to local environmental cues. Through this design, they have created a platform that can cater to combination therapy, as it can deliver multiple drug molecules in a desired ratio, which is crucial in the treatment of cancer-like diseases. Additionally, the design serves hypoxia-responsive delivery, establishing suprasomes as easily customisable therapeutic carriers that can serve the needs of new-generation therapeutics.[38]

All the examples above are directly relevant, as they demonstrate the field's rapid shift toward suprasome-centric systems that bridge advanced stimulus-responsiveness, precise molecular recognition, cargo delivery, and collective dynamic behaviour. Collectively, these studies validate suprasomes as the leading paradigm for multifunctional, controllable, and bioinspired nanoplatforms. Remaining challenges, such as integrating multiple functionalities within a single suprasome, creating a coordinated behaviour of assemblies, and exploring uncharted horizons, are at the heart of this thesis and represent the frontier for future suprasome research. Previous literature clearly suggests that suprasomes have only been explored for drug delivery purposes, while they have tremendous potential in the fields of synthetic chemical biology, artificial cells, intervesicle communication, emergent collective properties, and systems chemistry.

### 1.10. Key Research Gaps and Solutions

To the best of our knowledge, the utility of suprasomes is extensively limited to drug delivery applications. Despite significant progress in supramolecular chemistry and the development of suprasomal platforms, several critical challenges persist in authentically emulating the multifunctional complexity of biological systems. Much like the transition from liposome to suprasome, contemporary suprasome research should leap forward by emulating principles from nature and biology. In this regard, modern synthetic suprasome platforms lack the integrated capability to combine reversibility, precise spatiotemporal control, coordinated multistimuli response, and emergent collective behaviours that are intrinsic to life-like processes, such as signal transduction and cellular communication. Hence, through this thesis, we have attempted to address such multifaceted research needs, which include (1) reversible and stimuli-responsive suprasomes, (2) suprasomal ionophore delivery, (3) suprasomes and systems chemistry, and (4) time-gated multistimuli-responsive suprasomes. A brief discussion focusing on challenges, expanding research frontiers, and the attempted solutions is outlined here.

- Reversible and stimuli-responsive suprasome – Traditional drug delivery systems always required tedious and labour-intensive synthesis of lipid molecules. Any stimuli-responsive system (such as GSH-responsive) needs lipid synthesis that adds further challenges. Moreover, they exhibited irreversible structural/chemical changes upon stimulus treatment, lacking reversibility, long-term stability, and smooth customisability of physical characteristics such as size and surface charge. To address this, we developed a metal-responsive suprasome that delivers the required antibiotics when triggered by $Zn^{2+}$ and exhibits its own antibacterial properties, demonstrating the concept of triggered display of antibacterial properties.
- Suprasomal ionophore delivery – Modern therapeutics, such as ion transporters, face the severe challenge of poor deliverability and bioavailability due to their inherent hydrophobic nature. Although research on ion transporters and channels is on the rise, their delivery issue has remained largely unnoticed by researchers. Additionally, very limited work has been done on divalent metal ion-selective ion channels that can eradicate bacteria. Hence, we formulated a one-step solution with a suprasome where the ionophore behaves as a guest. This suprasome disassembles with a $Zn^{2+}$ trigger, releasing the ionophore that enters the bacterial membrane and forms a $Zn^{2+}$ ion

channel, ultimately causing their death due to excessive internalisation of $Zn^{2+}$. An inspiration was drawn from defensin proteins, which kill pathogens via a pore-formation strategy.

- Suprasomes and systems chemistry – Looking at the confined research of suprasomes on drug delivery systems, we tried to push the boundaries of system chemistry. Developing a suprasomal system that mimics life-like processes such as growth, differentiation, temporally active catalysis, and intervesicle communication will be of crucial importance for research on artificial cells. To address this, we developed a suprasome-supracube system that displays temporal activation of catalysis.
- Time-gated multistimuli-responsive suprasome – Another uncharted territory is the development of a multistimuli-responsive supramolecular assembly. Simultaneously, a system where the relative timing of stimulus treatment plays a pivotal role in affecting the outcome. Such systems are critical to develop systems with smart decision-making ability and mimic biological processes such as interneuron communication and memory storage as an outcome. Hence, we explored light and metal ions as orthogonal time-gated stimuli to develop suprasomes with a temporal gating nature. Additionally, this property was utilised for optical signal generation, photonic memory, and inter-vesicular communication.

### 1.11. Future Scope

This thesis lays the groundwork for the development of next-generation suprasomal materials with genuine biomimetic potential. This kind of construct is set to impact various domains including therapeutics, artificial information processing, energy, sustainability, agriculture, origin of life studies, and environmental management. Much like the visible tip of an iceberg, the discovered functions of supramolecular assemblies are just a fraction of their vast prospective capabilities, with substantial unexplored potential awaiting discovery beneath the surface.

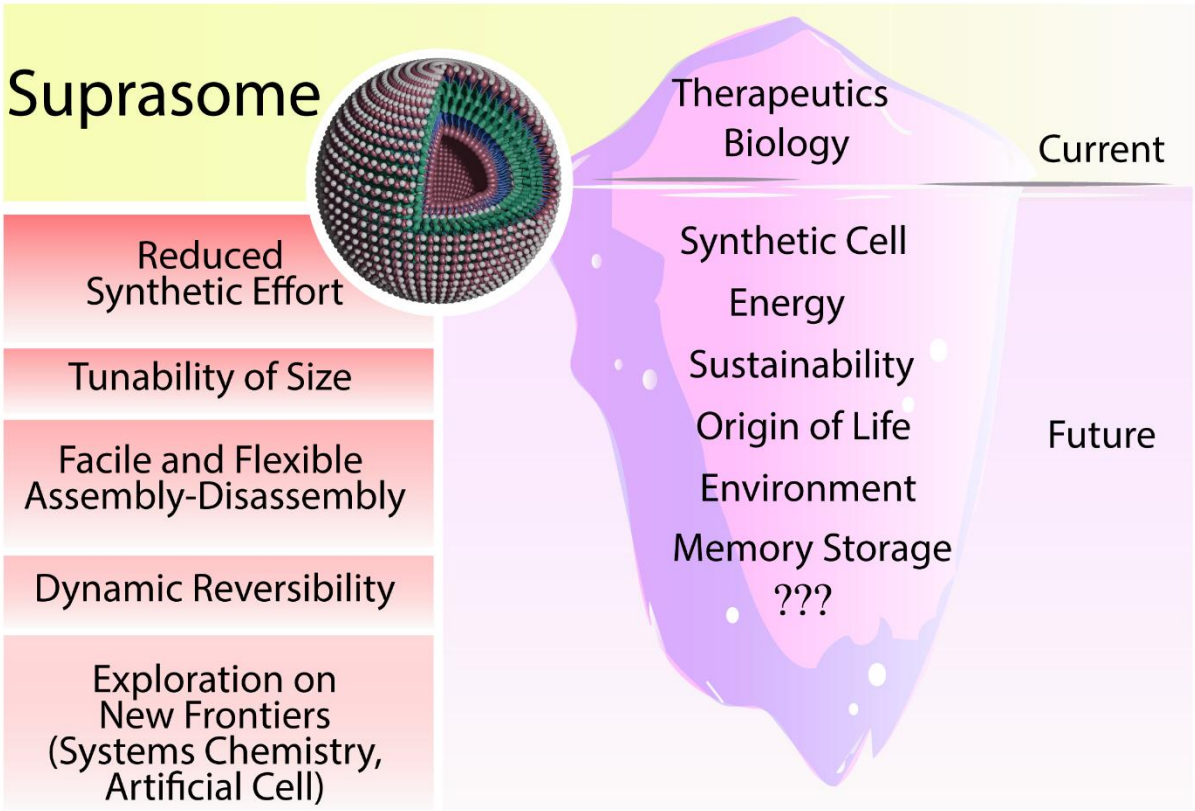


**Figure 1.7** Advantages of Suprasome over traditional vesicular systems such as liposomes and polymerosomes and future prospects of suprasome research.

**1.12 References:**

1. Lehn, J.-M., From supramolecular chemistry towards constitutional dynamic chemistry and adaptive chemistry. *Chem. Soc. Rev.* **2007,** *36* (2), 151-160.

2. Krishnamurthy, R.; Hud, N. V., Introduction: Chemical evolution and the origins of life. Rev., C., Ed. ACS Publications: 2020; Vol. 120, pp 4613-4615.

3. Lehn, J.-M., Towards complex matter: supramolecular chemistry and self-organisation. *Eur. Rev.* **2009,** *17* (2), 263-280.

4. Yan, X.; Zou, K.; Cao, J.; Li, X.; Zhao, Z.; Li, Z.; Wu, A.; Liang, W.; Mo, Y.; Jiang, Y., Single-handed supramolecular double helix of homochiral bis (N-amidothiourea) supported by double crossed C− I··· S halogen bonds. *Nat. Commun.* **2019,** *10* (1), 3610.

5. Yang, L.; Tan, X.; Wang, Z.; Zhang, X., Supramolecular polymers: historical development, preparation, characterization, and functions. *Chem. Rev.* **2015,** *115* (15), 7196-7239.

6. de La Rosa, V. R.; Woisel, P.; Hoogenboom, R., Supramolecular control over thermoresponsive polymers. *Mater. Today.* **2016,** *19* (1), 44-55.

7. Maibaum, L.; Dinner, A. R.; Chandler, D., Micelle formation and the hydrophobic effect. *J. Phys. Chem. B.* **2004,** *108* (21), 6778-6781.

8. Ben-Naim, A., Hydrophobic—Hydrophilic Forces in Protein Folding. ACS Publications: 1994.

9. Mnich, M. E.; Van Dalen, R.; Van Sorge, N. M., C-type lectin receptors in host defence against bacterial pathogens. *Front. Cell. Infect. Microbiol.* **2020,** *10*, 309.

10. Desai, A.; Mitchison, T. J., Microtubule polymerization dynamics. *Annu. Rev. Cell Dev. Biol.* **1997,** *13* (1), 83-117.

11. Hille, B., Ion Channels of Excitable Membranes. 3rd Sinauer. **2001**.

12. Bell, S. P.; Dutta, A., DNA replication in eukaryotic cells. *Annu. Rev. Biochem.* **2002,** *71* (1), 333-374.

13. Senger, M.; Eichmann, V.; Laun, K.; Duan, J.; Wittkamp, F.; Knör, G. n.; Apfel, U.-P.; Happe, T.; Winkler, M.; Heberle, J., How [FeFe]-hydrogenase facilitates bidirectional proton transfer. *J. Am. Chem. Soc.* **2019,** *141* (43), 17394-17403.

14. Huynh, M. T.; Wang, W.; Rauchfuss, T. B.; Hammes-Schiffer, S., Computational investigation of [FeFe]-hydrogenase models: characterization of singly and doubly protonated intermediates and mechanistic insights. *Inorg. Chem.* **2014,** *53* (19), 10301-10311.

15. Donald, J. E.; Kulp, D. W.; DeGrado, W. F., Salt bridges: Geometrically specific, designable interactions. *Proteins: Struct., Funct., Bioinf.* **2011,** *79* (3), 898-915.

16. Elcock, A. H., The stability of salt bridges at high temperatures: implications for hyperthermophilic proteins. *J. Mol. Biol.* **1998,** *284* (2), 489-502.

17. Huber, R. G.; Margreiter, M. A.; Fuchs, J. E.; von Grafenstein, S.; Tautermann, C. S.; Liedl, K. R.; Fox, T. J. J. o. c. i.; modeling, Heteroaromatic π-stacking energy landscapes. **2014,** *54* (5), 1371-1379.

18. Narita, M.; Narita, M.; Itsuno, Y.; Itsuno, S., Autonomous sequences in myoglobin emerging from x-ray structure of holomyoglobin. *ACS Omega.* **2019,** *4* (1), 992-999.

19. Li, Y.; Tian, R.; Zou, Y.; Wang, T.; Liu, J., Strategies and Applications for Supramolecular Protein Self-Assembly. *Chem. - Eur. J.* **2024,** *30* (66), e202402624.

20. Ryan, M. J.; Gao, L.; Valiyaveetil, F. I.; Kananenka, A. A.; Zanni, M. T., Water inside the selectivity filter of a K+ ion channel: Structural heterogeneity, picosecond dynamics, and hydrogen bonding. *J. Am. Chem. Soc.* **2024,** *146* (2), 1543-1553.

21. Perutz, M. F., Stereochemistry of cooperative effects in haemoglobin: haem–haem interaction and the problem of allostery. *Nature.* **1970,** *228* (5273), 726-734.

22. Wesener, D. A.; Dugan, A.; Kiessling, L. L., Recognition of microbial glycans by soluble human lectins. *Curr. Opin. Struct. Biol.* **2017,** *44*, 168-178.

23. Fu, J.; Zong, X.; Jin, M.; Min, J.; Wang, F.; Wang, Y., Mechanisms and regulation of defensins in host defence. *Signal Transduct. Target. Ther.* **2023,** *8* (1), 300.

24. Menard, L.; Maughan, D.; Vigoreaux, J., The structural and functional coordination of glycolytic enzymes in muscle: evidence of a metabolon? *Biology.* **2014,** *3* (3), 623-644.

25. Bera, M.; Grushin, K.; Kalyana Sundaram, R. V.; Hinzen, J. S.; Chen, J.; Chatterjee, A.; Radhakrishnan, A.; Lee, S.; Padmanarayana, M.; Coleman, J., Two successive oligomeric Munc13 assemblies scaffold vesicle docking and SNARE assembly to support neurotransmitter release. *Nat. Commun.* **2025,** *16* (1), 7222.

26. Kim, K.; Lakhanpal, G.; Lu, H. E.; Khan, M.; Suzuki, A.; Hayashi, M. K.; Narayanan, R.; Luyben, T. T.; Matsuda, T.; Nagai, T., A temporary gating of actin remodeling during synaptic plasticity consists of the interplay between the kinase and structural functions of CaMKII. *Neuron.* **2015,** *87* (4), 813-826.

27. Paolino, M.; Ennen, F.; Lamponi, S.; Cernescu, M.; Voit, B.; Cappelli, A.; Appelhans, D.; Komber, H., Cyclodextrin-adamantane host–guest interactions on the surface of biocompatible adamantyl-modified glycodendrimers. *Macromolecules.* **2013,** *46* (9), 3215-3227.

28. Márquez, C.; Hudgins, R. R.; Nau, W. M., Mechanism of host− guest complexation by cucurbituril. *J. Am. Chem. Soc.* **2004,** *126* (18), 5806-5816.

29. Sun, X.; Li, S.; Qin, Y.; Li, Y.; Zhu, Y.; Wang, L., Macrocycle/ferrocene complexation-mediated smart supramolecular gel materials and their applications. *Chem. Commun.* **2025**.

30. Ogoshi, T.; Yamagishi, T.-a.; Nakamoto, Y., Pillar-shaped macrocyclic hosts pillar [n] arenes: new key players for supramolecular chemistry. *Chem. Rev.* **2016,** *116* (14), 7937-8002.

31. Gao, B.; Wang, G.; Li, B.; Wu, L., Self-Inclusion and Dissociation of a Bridging β-Cyclodextrin Triplet. *ACS Omega.* **2020,** *5* (14), 8127-8136.

32. Liu, R.; Zhang, Y.; Feng, P., Multiresponsive supramolecular nanogated ensembles. *J. Am. Chem. Soc.* **2009,** *131* (42), 15128-15129.

33. Zhang, J.; Zhou, Z.-H.; Li, L.; Luo, Y.-L.; Xu, F.; Chen, Y., Dual stimuli-responsive supramolecular self-assemblies based on the host–guest interaction between β-cyclodextrin and azobenzene for cellular drug release. *Mol. Pharm.* **2020,** *17* (4), 1100-1113.

34. Meng, H.; Xue, M.; Xia, T.; Zhao, Y.-L.; Tamanoi, F.; Stoddart, J. F.; Zink, J. I.; Nel, A. E., Autonomous in vitro anticancer drug release from mesoporous silica nanoparticles by pH-sensitive nanovalves. *J. Am. Chem. Soc.* **2010,** *132* (36), 12690-12697.

35. Gao, J.; Yu, H.; Chen, F.-Y.; Hu, X.-Y.; Wang, Y.; Guo, D.-S., A hyaluronidase/atp tandem stimuli-responsive supramolecular assembly. *Chem. Commun.* **2019,** *55* (95), 14387-14390.

36. Jiang, B.; Guo, H.; Zhao, L.; Xu, B.; Wang, C.; Liu, C.; Fan, H., Fabrication of a β-cyclodextrin-based self-assembly containing a redox-responsive ferrocene. *Soft Matter.* **2020,** *16* (1), 125-131.

37. Yang, K.; Hua, B.; Qi, S.; Bai, B.; Yu, C.; Huang, F.; Yu, G., Suprasomes based on host–guest molecular recognition: an excellent alternative to liposomes in cancer theranostics. *Angew. Chem. - Int. Ed.* **2022,** *134* (52), e202213572.

38. Zhang, Z.; Yue, Y. X.; Xu, L.; Wang, Y.; Geng, W. C.; Li, J. J.; Kong, X. l.; Zhao, X.; Zheng, Y.; Zhao, Y., Macrocyclic-Amphiphile-Based Self-Assembled Nanoparticles for Ratiometric Delivery of Therapeutic Combinations to Tumors. *Adv. Mater.* **2021,** *33* (12), 2007719.

# Chapter 2

# Stimuli-responsive assembly and disassembly of anionic suprasomes with tunable antibacterial activity

**2.1 Background and Objective of the Current Work**

The transition of micelle to vesicle and other soluble aggregates is of great importance for vesicle-based drug delivery applications.[1, 2] The micelles-to-vesicle transition could effectively encapsulate drug molecules within its hollow cavities. The vesicle-to-other-aggregates transition could release the encapsulated drug molecules. Liposomes, the first-generation vesicle-based drug delivery system (DDS), demonstrated superior therapeutic performance and have been approved for clinical use in treating cancer and other diseases. However, the poor stability and challenges in the functionalisation of natural lipids failed to meet the requirements in the clinic. Although polymersomes overcome these limitations, poor biodegradation and immunotoxicity also restrict their clinical applications. Suprasomes, the supramolecular assembly of amphiphiles and host molecules, could be considered potential vesicle-based DDS. Structural simplicity, facile functionalisation, ease of construction, stability, biodegradability, and stimuli-responsiveness are the key advantages of suprasomes.[3] The stimuli-mediated transitions could also provide suprasomes with the desired size and properties for drug delivery and other applications.[3-5] Hence, stimuli-responsive suprasomes are considered a very attractive vesicle-based DDS. Suprasomes have the capability to encapsulate both hydrophobic and hydrophilic drugs, shielding them from degradation, lowering unwanted cytotoxicity, and reducing drug overexposure to restrict drug resistance and release them with specific stimuli.[2-4, 6] Suprasomes could also be easily disassembled into small molecules that could be easily defecated out of the body, leading to reduced toxicity of exogenous DDSs.[3] Cyclodextrins (CDs), pillararene, cucurbit[8]uril (CB[8]), and other host molecules have drawn significant interest in this supramolecular aggregate transition due to their ability to form host-guest complexes with amphiphiles. Recent studies reported that the mixture of various cationic and anionic (catanionic) amphiphiles in the presence of β-CD showed micelle-vesicle transition.[2, 3, 7, 8] Suprasomes of pillar[5]arene and BODIPY-containing methylimidazolium moiety showed excellent cisplatin encapsulation and delivery efficacy.[3] The dynamic nature of host-guest recognition could allow facile construction of suprasomes with theranostic properties. The installation of theragnostic moieties on host or guest molecules is crucial for their applications. Therefore, developing suitable suprasomes with a stimulus-regulated, stepwise transition from micelle to vesicle to other aggregates is of great interest.

Various cationic amphiphiles, including ammonium and sulfonium compounds, imidazolium, and benzimidazolium-containing compounds, exhibit strong antibacterial activity. However, due to prolonged exposure, most of these cationic amphiphiles also show strong cytotoxicity and antibacterial resistance.[9, 10] Owing to the biocompatibility and higher affinity for phosphate, imidazolium, and benzimidazolium-based compounds/polymers have been used in various biological applications, including drug delivery and antibacterial agents.[11] Hence, imidazolium and benzimidazolium amphiphiles could be potential antibacterial agents. The larger cationic head group and aromatic nature of benzimidazolium-based compounds may also promote facile partitioning and disorder in the membrane.[12] Therefore, we hypothesise that β-CD-mediated masking of benzimidazolium amphiphiles in the presence of anionic amphiphiles, followed by stimuli-regulated re-exposure of the benzimidazolium amphiphile, could enhance antibacterial efficacy, reducing cytotoxicity and unwanted exposure to bacterial cells. In addition, the β-CD-mediated suprasomes formation could also be useful in encapsulating and delivering commercial antibiotics in a regulated manner.

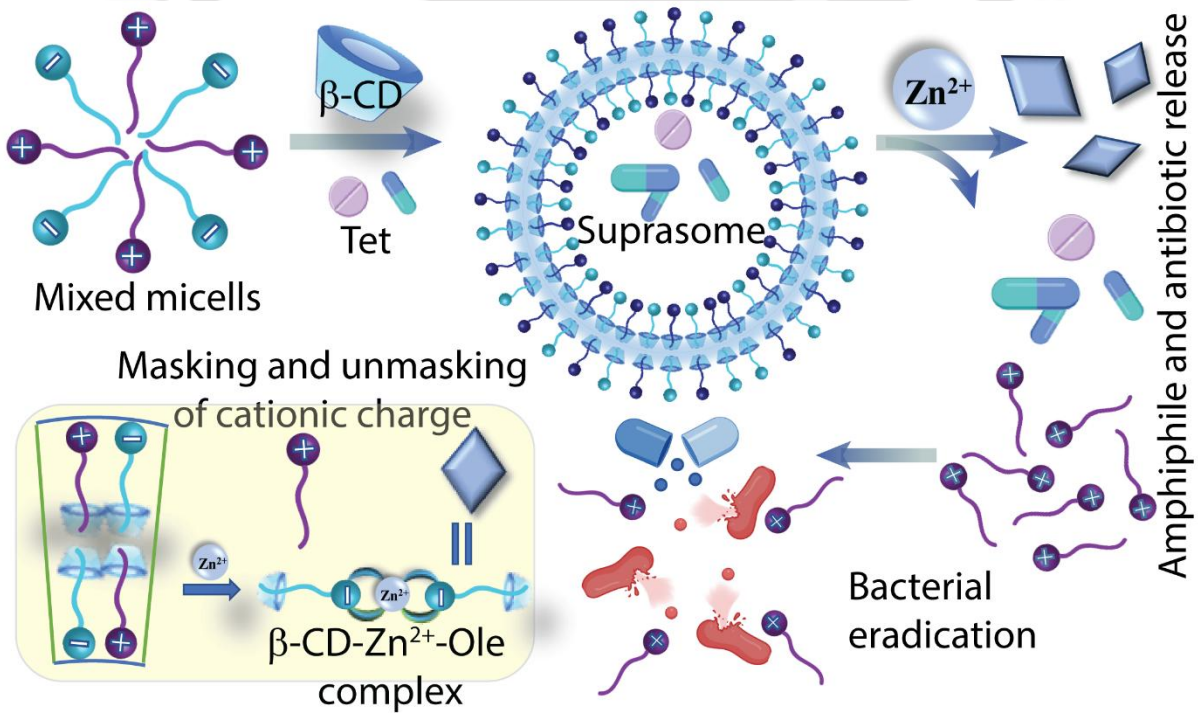


**Scheme 2.1** Schematic representation of the stimuli-regulated assembly and disassembly of suprasomes and their antibacterial activity.

Herein, we report the β-CD-mediated transition of micelles to suprasomes of a mixture of 1-dodecyl-3-methyl-1H-benzo[d]imidazol-3-ium (C12Mbm) with sodium oleate (NaOle). The C12Mbm showed strong antibacterial activity against Gram-positive bacteria. However, the suprasome showed reduced antibacterial activity. In comparison, the $Zn^{2+}$ ion-mediated disruption of suprasomes to rhombic aggregates provides more potent antibacterial activities. The presence of $Zn^{2+}$ ion not only stimulates the disruption of suprasomes due to its complexation with NaOle but also releases the C12Mbm and encapsulated tetracycline in a controlled manner.

## 2.2 Results and Discussions

### 2.2.1 Formation of Host-Guest Complex

The synthesised cationic amphiphiles C12Mbm and 1-dodecyl-3-methyl-4,5-dihydro-1H-imidazol-3-ium (C12mim) and anionic amphiphiles NaOle were used to construct the catanionic system, and β-CD acts as a host to construct suprasomes. The aggregation patterns of these amphiphiles in aqueous media were monitored by measuring their hydrodynamic diameter ($D_H$). The cationic C12Mbm (1 mM) and anionic NaOle (1 mM) amphiphiles showed average $D_H$ values of 221 and 137 nm, respectively (Fig. 2.3). The mixture of C12Mbm (1 mM) and NaOle (1-5 mM) in various ratios showed average $D_H$ values of 97-122 nm (PDI ≤ 0.4) (Figure 2.4 – 2.7). Molecular interactions between the cationic C12mim or C12Mbm and the anionic NaOle amphiphiles could drive surface adsorption and the formation of mixed micelles.[7] However, the lower $D_H$ value of these mixed micelles could be due to the size of the polar headgroup of C12mim or C12Mbm, which significantly affects their molecular interaction with NaOle. Meanwhile, a significant change in average $D_H$ values was observed when the concentration of β-CD was >10 mM for the 1:1 mixture of C12Mbm and NaOle ($D_H$ >500 nm; PDI ≤ 0.4) (Figure 2.2 A and Table 2.2). Similar changes in average $D_H$ values were observed for the other combination of C12Mbm and NaOle. The DLS measurements also revealed that the variation of C12Mbm and NaOle mixture of 1:2 or 1:5 ratios (C/C) required a higher concentration of β-CD to attain micelle-vesicle transition, which could be due to the higher concentration of NaOle in the solution. The β-CD also showed similar changes in average $D_H$ values for C12mim and NaOle mixture. Hence, the DLS measurements

revealed that the size of vesicles also could be tuned by varying the concentrations of β-CD.

### 2.2.2 Investigation of the Properties of the Suprasome

To characterise the host-guest complex, several experiments were performed. The surface zeta potential (ξ) of the aggregates was increased after the addition of β-CD, suggesting the formation of larger aggregates (large sizes have small ξ values and vice versa). The ξ values without (-90 to -45 mV) or with β-CD (-25 mV) suggest that the soluble aggregates are electrically stabilised (Figure 2.8). This observation is consistent with the stability of the vesicles over the longer period, as evidenced by minimal alteration in the $D_H$ values and no formation of any visible precipitate (Figure 2.9 and 2.10). The DLS measurements revealed that the composition A of C12Mbm, NaOle, and β-CD (composition A= C12mbm: NaOle: β-CD (1: 1: 10)) forms negatively charged vesicles with a diameter of approximately 350 nm and ζ-potential values of -25 mV. The size of the majority of commercially available liposome formulations for administering antibiotics typically ranges from 100 to 400 nm.[3] Vesicles of these sizes have also shown optimal drug delivery applications due to an ideal balance between encapsulation volume and gravitational coagulation, ensuring both efficient drug encapsulation and long-term stability.[13] Hence, this composition was selected for further studies.

The isothermal titration calorimetric (ITC) measurements revealed the interaction of C12Mbm, NaOle, and a 1:1 mixture of C12Mbm and NaOle with β-CD (Figure 2.1B and 2.13). This host-guest complexation was driven by a favourable enthalpy change and a positive entropy change. The β-CD-mediated transition of micelle-vesicles was also investigated using morphology analysis techniques, including atomic force microscopy (AFM) and transmission electron microscopy (TEM). The AFM and TEM images illustrate the micellar arrangements of the C12Mbm and NaOle (1:1) mixture, with a diameter of 50-100 nm. The addition of 10 mM β-CD resulted in the formation of vesicles with a diameter of 200-350 nm (Figure 2.1C and 2.1D). Hence, DLS, ITC measurements, and morphology analyses revealed that the β-CD-mediated formation of suprasomes of the C12Mbm and NaOle mixture could encapsulate desired drug molecules within the hydrophilic core or the hydrophobic layers.

The presence of carboxylate groups on the surface of these suprasomes could promote metal ion-induced disruption and release of cationic C12Mbm and encapsulated drug molecules.[14] Among these, $Zn^{2+}$ and $Cu^{2+}$ ions show antibacterial activities; hence, susceptibility of the suprasomes was performed with these metal ions. The DLS measurements showed an increase in $D_H$ values (Figure 2.14A). This increase in particle size is attributed to modifications in the characteristics of self-assembly of amphiphiles by metal ions, which may lead to fusion or reorganisation into other forms of other soluble or insoluble aggregates. Concurrently, the zeta potential measurements showed an increase in ξ value from -25 to -12 mV due to the complexation of carboxylate with the metal ions and removal of fatty acid from vesicles (Figure 2.14B). The complexation of the carboxylate with the metal ions, which masks the negatively charged head group, increases the ξ values. Similar effects on the $D_H$ and ξ values were observed for suprasomes in an acidic medium (final pH 6.0), indicating that the acidic medium could also act as a stimulus to disrupt the suprasomes (Figure 2.14C).

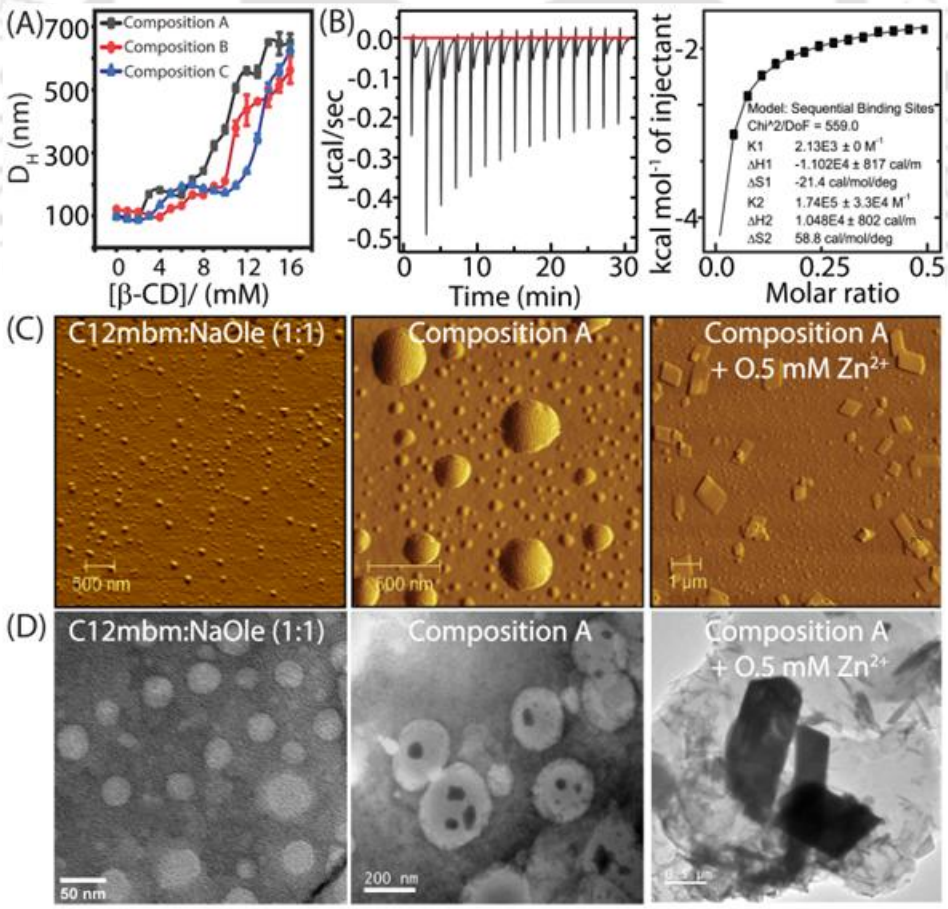


**Figure 2.1** (A) Variation of $D_H$ values of the suprasomes against different concentrations of β-CD. (B) ITC measurements of the mixture of C12Mbm and NaOle

(1:1) with β-CD. Representative (C) AFM and (D) TEM images of the aggregates after different treatments.

The metal ion-induced disruption of vesicles was additionally investigated using a polarity-sensitive fluorescent dye, Nile Red (NR). The fluorescence measurements revealed quenching of the NR fluorescence when vesicles were treated with $Zn^{2+}$ and dilute HCl, suggesting the disruption of vesicular arrangements and release of NR dye to the aqueous medium (Figure 2.18). The absorbance studies showed that the suprasomes have an encapsulation efficacy of around 50% for tetracycline. The time-dependent release profile indicated a significant acceleration in the tetracycline release efficacy in the presence of $Zn^{2+}$ ions (500 μM) and acidic medium (pH 6.0), indicating $Zn^{2+}$ ions and acidic environment act as stimuli for tetracycline release, suggesting a tunable drug release efficacy of suprasome under pathogenic conditions (Fig. 2.2A and 2.19).[15] Such environments hold significant promise for these suprasome-based DDSs.

### 2.2.3 Antibacterial Studies

The antibacterial studies demonstrated that C12Mbm exhibits stronger antibacterial activity than C12mim against *Staphylococcus aureus* (*S. aureus*; MTCC-96), with minimum inhibitory concentrations (MICs) of 2.5 and 6.5 μM, respectively. The activity of C12Mbm was increased by 3 to 4-fold in the presence of $Cu^{2+}$ and $Zn^{2+}$ ions (250 μM). However, the C12mim showed no alteration in MIC values in the presence of $Zn^{2+}$ ions. These metal ions are known to play a crucial role in bacterial growth and metabolism, serving as a stimulus to trigger the release of drugs.[14] The C12Mbm showed moderate antibacterial activity against Methicillin-Resistant *Staphylococcus aureus* (MRSA; ATCC-33592) and Gram-negative *Escherichia coli* (*E. coli*; MTCC-1687) strains with MIC values of 10 and 20 μM, respectively, and their activity was also not significantly altered in the presence of $Zn^{2+}$ ions (Table 2.4). Interestingly, the suprasomes of composition A showed 20-fold stronger activity in the presence of $Zn^{2+}$ (composition A= C12mbm: NaOle: β-CD (1: 1: 10)). The suprasomes of compositions B and C showed around 10-fold activity enhancement, but C12mim-containing suprasomes (composition D) showed no change in antibacterial activities in the presence of $Zn^{2+}$ (composition B= C12mbm: NaOle: β-CD (1: 2: 10), composition C= C12mbm: NaOle: β-CD (1: 5: 10), composition D= C12mim: NaOle: β-CD (1: 1: 10)). The suprasomes showed moderate activity differences even in the presence of $Cu^{2+}$. Hence,

further antibacterial studies were carried out in the presence of $Zn^{2+}$. The calculated MIC values suggest that the formation of suprasomes reduces the inherent antibacterial activity, which could be due to the masking of the cationic benzimidazolium headgroup of C12Mbm. We postulate that this enhancement of antibacterial activity may be attributed to the disruptive effect of $Zn^{2+}$ on suprasomes, leading to the release of C12Mbm into the surrounding aqueous medium, and also to the presence of $Zn^{2+}$. Hence, the investigation of MIC values shed light on the potential use of C12Mbm and $Zn^{2+}$ as potent antibacterial agents, suggesting a promising avenue for the development of novel therapeutic strategies against bacterial infections.

**Table 2.1** Calculated MIC values of the additives against *S. aureus*.

| | **MIC values (μM)** | | |
|---|---|---|---|
| | | $Zn^{2+}$ (250 μM) | $Cu^{2+}$ (250 μM) |
| C12Mbm | 2.50 ± 0.50 | 0.62 ± 0.15 | 0.78 ± 0.17 |
| C12mim | 6.25 ± 1.25 | 6.25 ± 1.25 | 6.25 ± 1.25 |
| Composition A | 6.25 ± 1.25 | 0.31 ± 0.07 | 5.00 ± 2.50 |
| Composition B | 12.50 ± 1.25 | 1.25 ± 0.15 | 5.00 ± 2.50 |
| Composition C | 12.50 ± 1.25 | 1.25 ± 0.15 | 10.00 ± 2.50 |
| Composition D | 9.50 ± 1.50 | 8.00 ± 1.50 | 8.00 ± 1.50 |
| $CuCl_2$ | 5000 ± 500 | - | - |
| $ZnCl_2$ | 1560 ± 390 | - | - |
| Tet | 4.20 ± 0.50 | - | - |
| Tet@composition A | - | 0.10 ± 0.02<br>0.015 ± 0.007[a] | - |

Further analysis revealed that the antibacterial activity of suprasomes, both in the absence and presence of $Zn^{2+}$, could be attributed to the abundance of free C12Mbm under the experimental conditions (Fig. 2.2B). (composition A= C12mbm: NaOle: β-CD (1: 1: 10), composition B= C12mbm: NaOle: β-CD (1: 2: 10), composition C= C12mbm: NaOle: β-CD (1: 5: 10), composition D= C12mim: NaOle: β-CD (1: 1: 10)).

Tetracycline works as an antibacterial agent by binding to the 30S subunit of the bacterial ribosome, causing inhibition of bacterial protein synthesis rather than targeting

the membrane.[16] Therefore, tetracycline-encapsulated vesicles could act as a double-edged sword in fighting against bacteria. The MIC value of tetracycline-loaded suprasomes was found to be 15 nM, over 280-fold improvement in tetracycline activity (MIC = 4.2 μM) (Table 2.1). The field-emission scanning electron microscopic (FESEM) analyses revealed a conspicuous alteration in the morphology of *S. aureus* cells, indicating the bactericidal properties of C12Mbm through its disruptive effect on the bacterial membrane (Figure 2.23). The haemolysis assay revealed that suprasomes with higher oleate content induced haemolysis in the presence of $Zn^{2+}$, possibly due to the inherent haemolytic activity of oleate (Figure 2.24-2.26). Consequently, suprasomes of composition A could be ideal DDSs, as they exhibit compatibility with red blood cells (RBCs). The cell viability assay revealed that the $IC_{50}$ value of C12Mbm was 12.57 μM; however, NaOle showed very low cytotoxicity against HEK293 cells (Figure 2.27). The propidium iodide (PI) uptake assay with C12Mbm revealed both dose- and time-dependent increases in PI fluorescence intensity, suggesting an enhancement of fluorescence in damaged or dying cells (Figure 2.29). The 3,3′-dipropylthiadicarbocyanine iodide ($DiSC_3(5)$)-assisted membrane depolarization analysis suggested C12Mbm-mediated membrane depolarization activity, which induces membrane damage-mediated bactericidal activity (Figure 2.28).[6, 16, 17] The C12Mbm-mediated membrane damage activity was also evidenced by the absence of

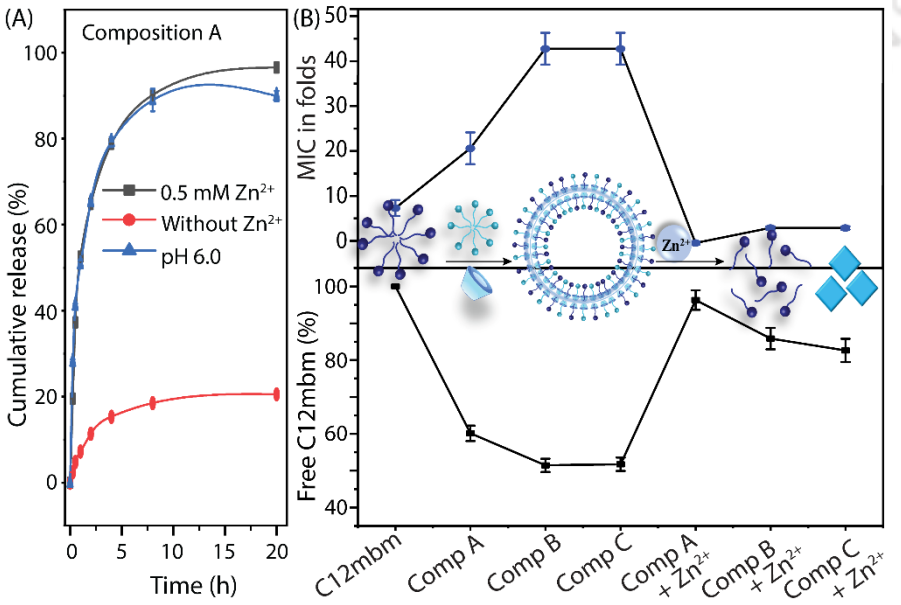

**Figure 2.2** (A) Tetracycline release profiles in the presence of $Zn^{2+}$ and acidic environment. (B) The relation between free C12Mbm in the solution and the antibacterial activities of different additives against *S. aureus*.

carboxyfluorescein succinimidyl ester (CFSE) fluorescence in live and dead cell assay (Figure 2.29). The lower intensity of CFDA-SE in C12Mbm-treated cells suggested the formation of membrane-compromised *S. aureus cells*. Such a $Zn^{2+}$-stimulated suprasome-based DDS could play a crucial role in triggering drug release under various pathological conditions, including breast cancer cells containing a 19-fold higher $Zn^{2+}$ concentration than healthy cells[18] or prostate epithelial cells with $Zn^{2+}$ concentrations of 800-1500 μM.[19] Otherwise, bacterial-infected sites with low pH could also trigger drug release.

## 2.3 Summary

In conclusion, we developed host-guest complexation-based suprasomes to deliver cationic amphiphiles and antibiotics. The β-CD-mediated formation of suprasomes with negative surface potential from the mixed micelles of C12Mbm and NaOle could also release the encapsulated cargos in a stimuli-responsive manner in the presence of $Zn^{2+}$ or an acidic environment. The superior activity of tetracycline-encapsulated suprasomes in the presence of $Zn^{2+}$ ions could be due to the combined effect of C12Mbm, tetracycline, and $Zn^{2+}$ ions against Gram-positive *S. aureus* bacterial cells. The haemolytic assays showed that the selected formulation has lower toxicity against RBCs. Therefore, the multi-stimuli-regulated step-wise transition of micelles, suprasomes, and other aggregates is of great interest in drug delivery. In addition, facile functionalisation and stimuli-responsiveness could enable suprasomes to serve as next-generation DDSs for combating bacterial infections, cancer, and other diseases.

## 2.4 Experimental Section

### 2.4.1 General Information

The benzimidazole, 1-bromododecane, methyl iodide, propidium iodide, carboxyfluorescein, and diacetate-succinamide ester (CFDA-SE) were purchased from Sigma-Aldrich. The dialysis membrane-110 and all the bacterial culture media were procured from Himedia. Tetracycline and β-cyclodextrin (β-CD) were purchased from TCI. Benzimidazolium and imidazolium derivatives were purified by column chromatography and thin-layer chromatography (TLC).

The $^{13}C$ NMR and $^{1}H$ NMR were recorded at 600 MHz with a Bruker spectrometer to observe the chemical shift, and for this purpose, DMSO-$d_6$ and $CDCl_3$ were used as the internal solvent. Multiplicities of the NMR spectra were reported as m (multiplet), d (doublet), s (singlet).

### 2.4.2 Synthesis and Characterization of Amphiphiles

#### 2.4.2.1 Synthesis of 1-dodecyl-3-methyl-1*H*-benzo[d]imidazol-3-ium iodide (C12Mbm)

To a stirring solution of benzimidazole (1 mmol) in $CH_3CN$, KOH was added (1 mmol), and the reaction mixture was continued to stir for 1-2 h at room temperature. After that, 1-bromododecane (2 mmol) was added, and the reaction mixture was heated under reflux conditions for 24 hours. The progress of the reaction was monitored by TLC. After maximum

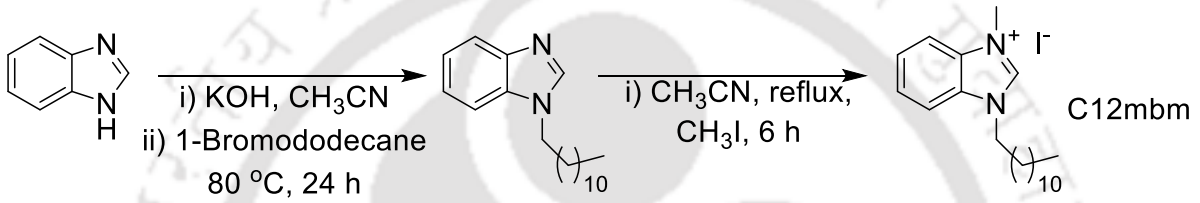


**Scheme 2.2** Synthetic routes to 1-dodecyl-3-methyl-1*H*-benzo[d]imidazol-3-ium iodide (C12Mbm).

consumption of benzimidazole, the reaction mixture was cooled down to room temperature, and unused KOH was removed by filtration. Then the organic solvent was removed under reduced pressure to yield an oily crude product. The mixture was purified through silica gel column chromatography with a solvent gradient system of 5–15% ethyl acetate in hexane to afford 1-dodecyl-1*H*-benzo[d]imidazole in a yield of 67%. After that, to a stirring solution of 1-dodecyl-1*H*-benzo[d]imidazole (1 mmol) in acetonitrile (inert condition), iodomethane (3 mmol) was added and refluxed until maximum consumption of 1-dodecyl-1*H*-benzo[d]imidazole (6 h). The progress of the reaction was monitored by TLC. Then the organic solvent was removed under reduced pressure to result 83% yield of C12Mbm. The 1-dodecyl-1*H*-benzo[d]imidazole was characterized by HRMS (ESI), $^{1}H$ NMR, and $^{13}C$ NMR analysis. **$^{1}H$ NMR (400 MHz, $CDCl_3$):** $\delta_{ppm}$ 7.88 (s, 1H), 7.82-7.80 (m, 1H), 7.41-7.38 (m, 1H), 7.32-7.29 (m, 1H), 7.28-7.25 (m, 1H), 4.15 (t, $J$ = 7.1 Hz, 2H), 1.86 (m, $J$ = 7.2 Hz, 2H), 1.32 (br, 4H), 1.24 (br, 4H), 0.88 (t, $J$ = 6.8 Hz, 3H). **$^{13}C$ NMR (126 MHz, $CDCl_3$):** $\delta_{ppm}$ 143.87, 142.91, 133.83, 122.77, 122.00, 120.36, 109.66, 45.12, 31.90, 29.82, 29.59, 29.51, 29.42, 29.32, 29.10, 26.83, 22.68, 14.11; **HRMS** (ESI) m/z: calculated for $C_{19}H_{30}N_2$ $[M+H]^+$: **287.2482, found 287.2463.**

The C12Mbm was characterized by HRMS (ESI), $^{1}$H NMR, and $^{13}$C NMR analysis. **$^{1}$H NMR (500 MHz, CDCl$_3$):** $\delta_{ppm}$ 11.07 (s, 1H), 7.73-7.70 (m, 4H), 4.57 (t, *J* = 7.5 Hz, 2H), 4.31 (s, 3H), 2.11-2.05 (m, 2H), 1.47-1.41 (m, 2H), 1.40-1.34 (m, 2H), 1.25 (br, 14H), 0.88 (t, *J* = 7.5 Hz, 3H). **$^{13}$C NMR (151 MHz, CDCl$_3$):** $\delta_{ppm}$ 142.37, 132.07, 131.16, 127.40, 127.38, 112.92, 112.88, 47.80, 33.93, 31.90, 29.59, 29.50, 29.38, 29.33, 29.03, 26.61, 22.69, 14.13; HRMS (ESI) m/z: calculated for C20H33N2 $[M]^+$ : 301.2641, found 301.2638.

### 2.4.2.2 Synthesis of 1-dodecyl-3-methyl-1*H*-benzo[d]imidazol-3-ium iodide (C12mim)

To a stirring solution of imidazole (1 mmol) in $CH_3CN$, KOH was added (1 mmol), and the reaction mixture was continued to stir for 1-2 h at room temperature. After that, 1-bromododecane (2 mmol) was added, and the reaction mixture was heated under reflux conditions for 24 hours. The progress of the reaction was monitored by TLC. After maximum consumption of imidazole, the reaction mixture was cooled down to room temperature, and unused KOH was removed by filtration. Then the organic solvent was removed under reduced pressure to yield an oily crude product. The mixture was purified through a silica gel column

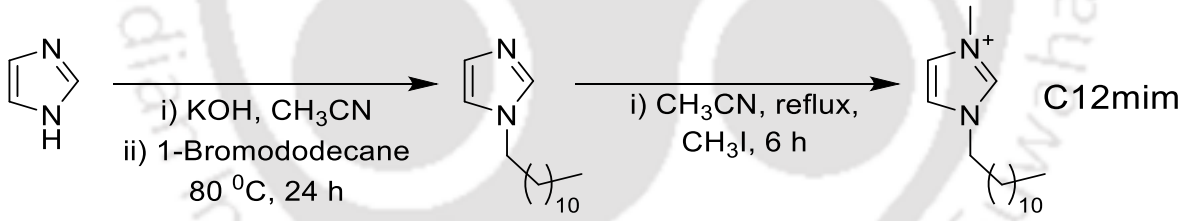


**Scheme 2.2** Synthetic routes to 1-dodecyl-3-methyl-1*H*-benzo[d]imidazol-3-ium iodide (C12mim).

chromatography with a solvent gradient system of 5–15% ethyl acetate in hexane to afford 1-dodecyl-1*H*-imidazole resulting in a yield of 71%. Thereafter, to a stirring solution of 1-dodecyl-1*H*-imidazole (1 mmol) in acetonitrile (inert condition), iodomethane (3 mmol) was added and refluxed until maximum consumption of 1-dodecyl-1*H*-imidazole. The progress of the reaction was monitored by TLC. Then the organic solvent was removed under reduced pressure to result C12mim in 89% yield. The 1-dodecyl-1*H*-imidazole was characterized by HRMS (ESI), $^{1}$H NMR, and $^{13}$C NMR analysis. **$^{1}$H NMR (500 MHz, CDCl$_3$):** $\delta_{ppm}$ 7.45 (s, 1H), 7.05 (s, 1H), 6.90 (s, 1H), 3.91 (t, J = 7.3 Hz, 2H), 1.79-1.74 (m, 2H), 1.29 (br, 4H), 1.25 (br, 14H), 0.88 (t, J = 6.8 Hz, 3H). **$^{13}$C NMR (126 MHz, CDCl$_3$):** $\delta_{ppm}$ 136.94, 123.65, 121.99,

77.32, 77.07, 76.82, 50.34, 37.18, 31.89, 30.24, 29.58, 29.49, 29.37, 29.31, 28.98, 26.26, 22.66, 14.11; **HRMS** (ESI) m/z: calculated for C15H28N2 $[M+H]^+$: 237.2325, found 237.2301.

The C12mim was characterized by HRMS (ESI), $^1$H NMR, and $^{13}$C NMR analysis. **$^1$H NMR (126 MHz, $CDCl_3$):** $\delta_{ppm}$ 10.03 (s, 1H), 7.51 (s, 1H), 7.39 (s, 1H), 4.32 (t, J = 7.5 Hz, 2H), 4.13 (s, 3H), 1.93 (p, J = 7.4 Hz, 2H), 1.35-1.33 (br, 4H), 1.25 (br, 14H), 0.88 (t, J = 6.8 Hz, 3H). **$^{13}$C NMR (151 MHz, $CDCl_3$):** $\delta_{ppm}$ 136.94, 123.65, 121.99, 77.32, 77.07, 76.82, 50.34, 37.18, 31.89, 30.24, 29.58, 29.49, 29.37, 29.31, 28.98, 26.26, 22.66, 14.11; **HRMS** (ESI) m/z: calculated for C16H31N2 $[M+H]^+$: **252.2560, found 252.2531.**

#### 2.4.2.3 Synthesis of Sodium Oleate

To a stirring solution of oleic acid in ethanol, NaOH was added and stirred for 4-5 h at room temperature. A white precipitate was formed, which was filtered and washed with ethanol to remove excess oleic acid. The filtered white precipitate was dried to get sodium oleate (NaOle).

### 2.4.3 Formation of Micelle and Suprasomes

C12Mbm (1 mM) and NaOle (1 mM) were added to 1 mL of water in a clean vial and sonicated and vortexed for 15 min to form the micelles. Micelles were also prepared at different ratios of C12Mbm and NaOle, such as 1:1 (Composition A), 1:2 (Composition B), and 1:5 (Composition C). Then, different concentrations of β-CD were added to the micellar system, vortexed for 5 min, and kept in the shaker at 180 rpm for 1 h to allow the conversion from micelles to suprasomes.

### 2.4.4 Measurements of Hydrodynamic Diameters

Micelles were prepared in different compositions, and 1 mM β-CD was added to it and kept in the shaker at 180 rpm for 1 h, and then the hydrodynamic diameter was measured using Zetasizer Nano ZS90 (Malvern, Westborough, MA) instrument at 25 °C. β-CD concentration was increased by 1 mM after each measurement, and the same procedure was repeated to measure the hydrodynamic diameter of the suprasomes formed. A similar procedure was followed to measure the effect of β-CD concentration on the zeta potential of the suprasomes. These measurements were performed for all the compositions.

**Table 2.2** Selected compositions of the additives for further studies.

| Compositions | Additives (molar ratio) |
|---|---|
| Composition A | C12Mbm: NaOle: β-CD (1: 1: 10) |

| | |
|---|---|
| Composition B | C12Mbm : NaOle: β-CD (1 : 2: 10) |
| Composition C | C12Mbm : NaOle: β-CD (1 : 5: 10) |
| Composition D | C12mim : NaOle: β-CD (1 : 1: 10) |

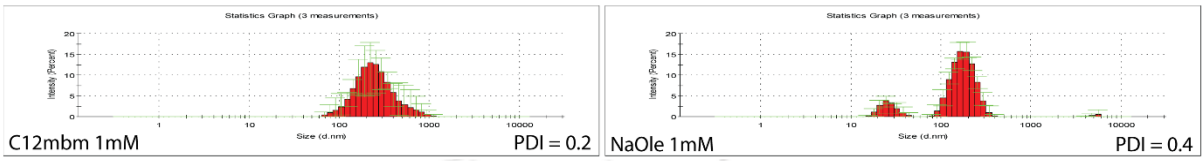


**Figure 2.3** Hydrodynamic diameters ($D_H$) of only C12Mbm and NaOle.

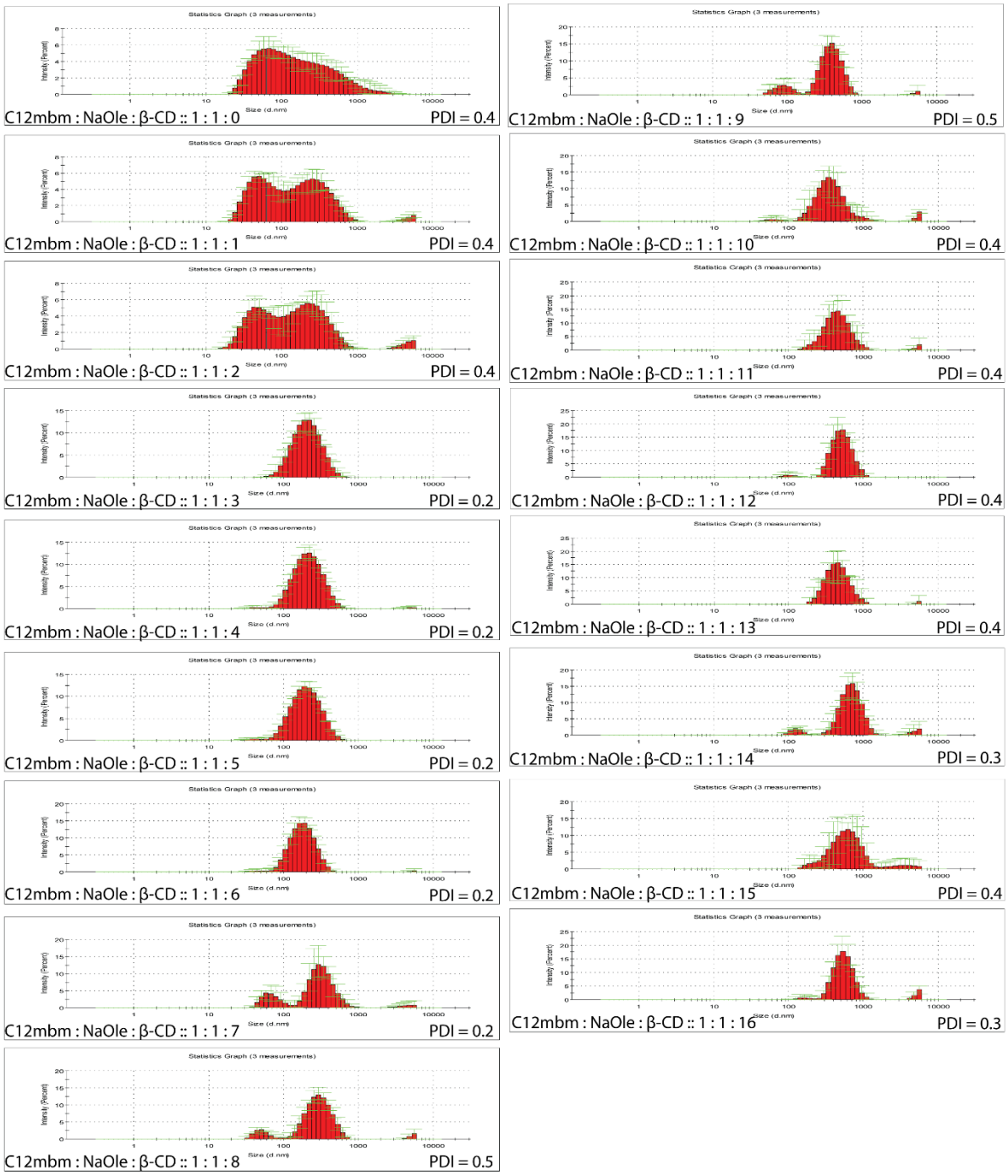


**Figure 2.4** Variation of hydrodynamic diameter of the C12Mbm and NaOle (1: 1, C/C) at different concentrations of β-CD.

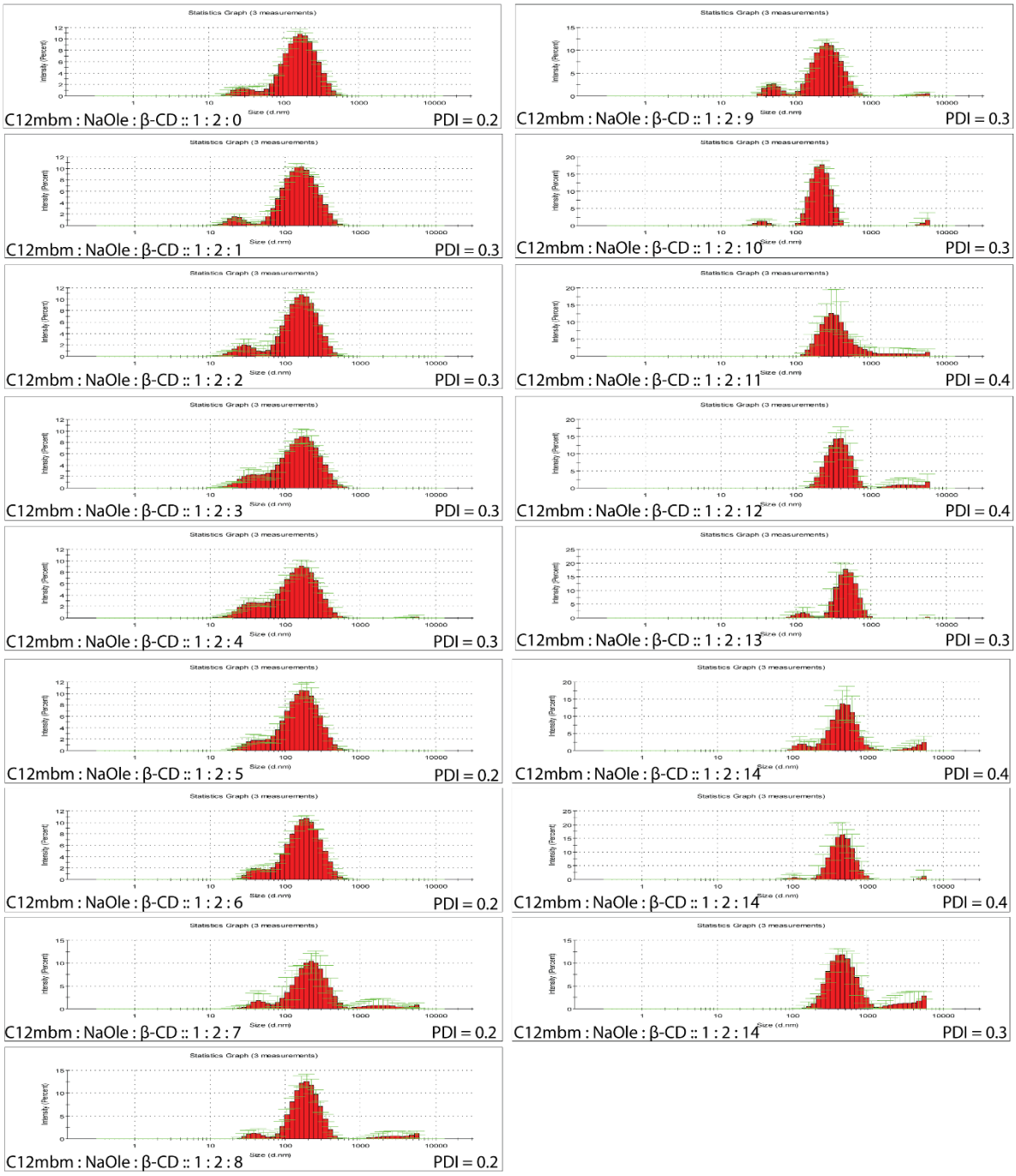


**Figure 2.5** Variation of hydrodynamic diameter of the C12Mbm and NaOle (1: 2, C/C) at different concentrations of β-CD.

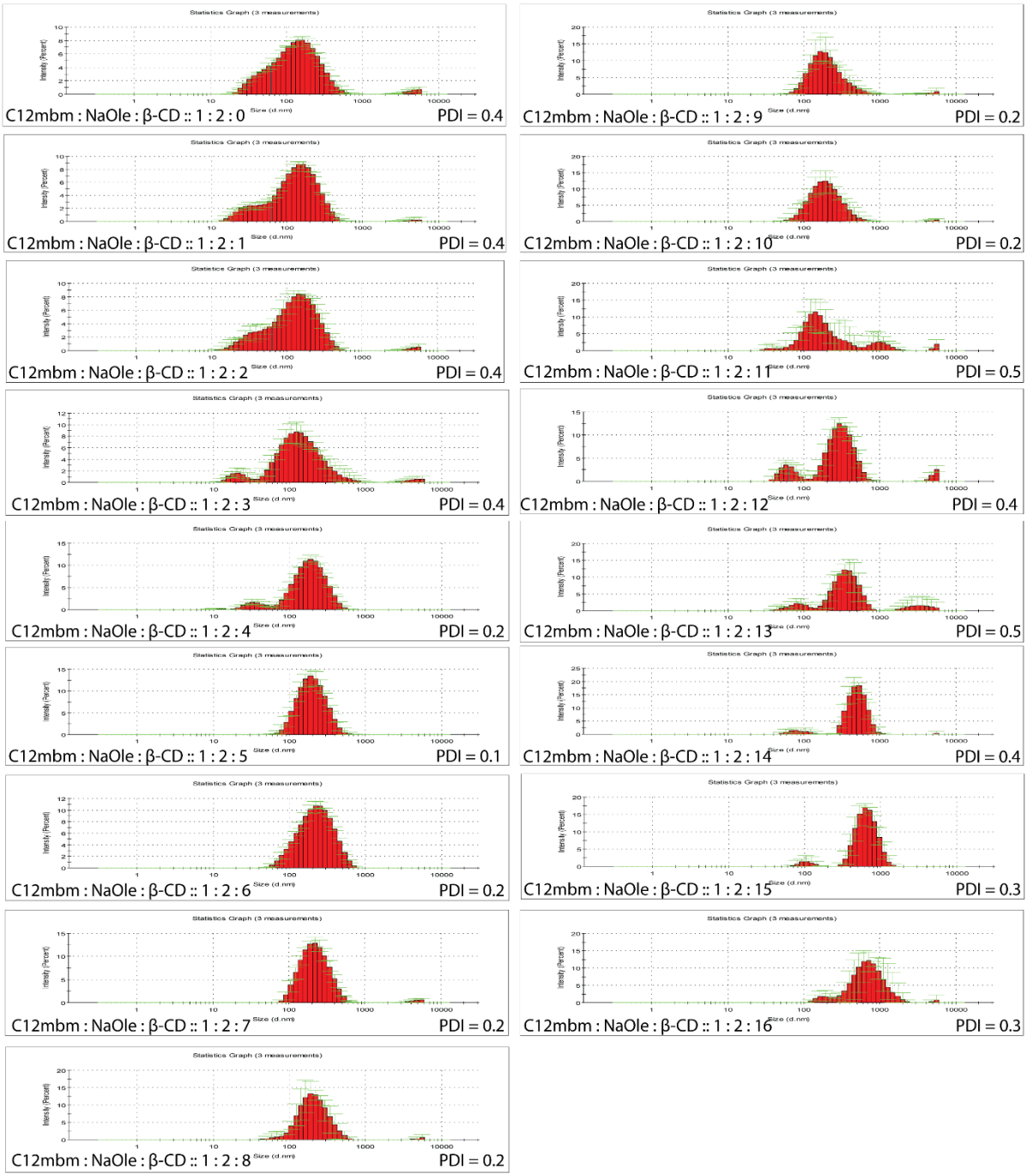


**Figure 2.6** Variation of hydrodynamic diameter of the C12Mbm and NaOle (1: 5, C/C) at different concentrations of β-CD.

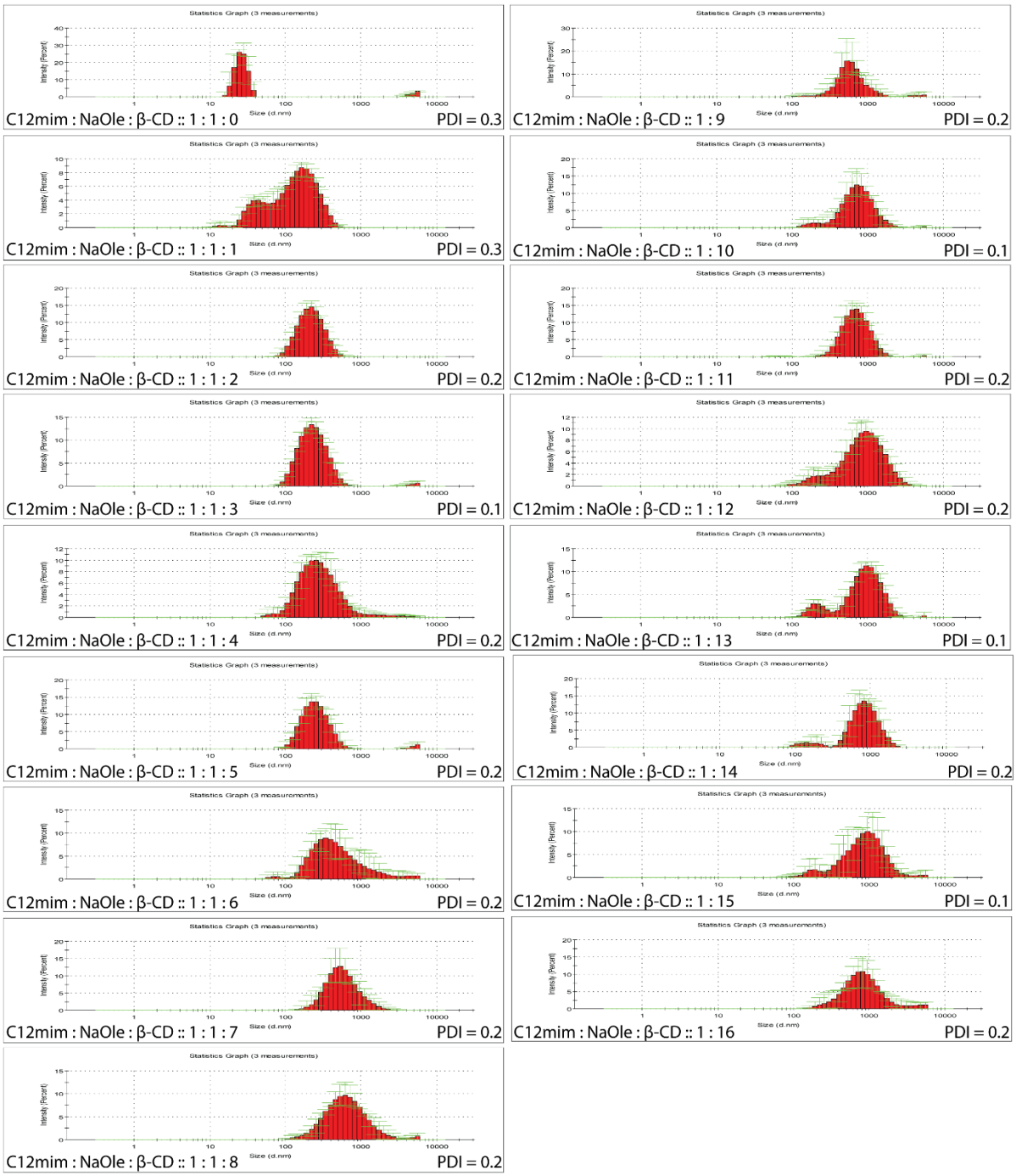


**Figure 2.7** Variation of hydrodynamic diameter of the C12mim and NaOle (1: 1, C/C) at different concentrations of β-CD.

**Table 2.3** Variation of hydrodynamic diameter of the soluble aggregates at different concentrations of β-CD.

| [β-CD]/ (mM) | Hydrodynamic diameter (nm) | | | |
|---|---|---|---|---|
| | (C12Mbm : NaOle :: 1 mM : 1 mM) | (C12Mbm : NaOle :: 1 mM : 2 mM) | (C12Mbm : NaOle :: 1 mM : 5 mM) | (C12mim : NaOle :: 1 mM : 1 mM) |
| 0 | 98.47 ± 1.9 (PDI = 0.4) | 121.63 ± 1.6 (PDI = 0.2) | 97.52 ± 0.5 (PDI = 0.4) | 28.97 ± 2.7 (PDI = 0.3) |
| 1 | 94.25 ± 1.6 (PDI = 0.4) | 115.70 ± 0.8 (PDI = 0.3) | 90.16 ± 2.0 (PDI = 0.4) | 93.64 ± 1.7 (PDI = 0.3) |
| 2 | 94.09 ± 1.4 (PDI = 0.4) | 112.30 ± 0.5 (PDI = 0.3) | 87.63 ± 0.9 (PDI = 0.4) | 189.06 ± 3.9 (PDI = 0.2) |
| 3 | 169.43 ± 1.2 (PDI = 0.2) | 102.36 ± 2.2 (PDI = 0.3) | 99.23 ± 0.4 (PDI = 0.4) | 213.70 ± 2.0 (PDI = 0.1) |
| 4 | 182.06 ± 0.8 (PDI = 0.2) | 97.71 ± 1.8 (PDI = 0.3) | 134.76 ± 1.7 (PDI = 0.2) | 233.26 ± 0.6 (PDI = 0.2) |
| 5 | 171.76 ± 2.9 (PDI = 0.2) | 123.86 ± 1.0 (PDI = 0.2) | 171.03 ± 1.3 (PDI = 0.1) | 240.03 ± 4.1 (PDI = 0.2) |
| 6 | 167.50 ± 3.8 (PDI = 0.2) | 133.60 ± 1.6 (PDI = 0.2) | 192.36 ± 1.9 (PDI = 0.2) | 360.33 ± 8.0 (PDI = 0.2) |
| 7 | 215.83 ± 7.7 (PDI = 0.2) | 167.26 ± 0.4 (PDI = 0.4) | 198.26 ± 2.7 (PDI = 0.2) | 498.30 ± 17.9 (PDI = 0.2) |
| 8 | 243.26 ± 1.7 (PDI = 0.5) | 167.46 ± 3.5 (PDI = 0.3) | 185.73 ± 6.5 (PDI = 0.2) | 546.73 ± 21.9 (PDI = 0.2) |
| 9 | 322.63 ± 12.5 (PDI = 0.5) | 194.63 ± 1.7 (PDI = 0.3) | 180.23 ± 3.5 (PDI = 0.2) | 562.13 ± 10.6 (PDI = 0.2) |
| 10 | 374.06 ± 11.5 (PDI = 0.4) | 211.06 ± 3.2 (PDI = 0.3) | 173.56 ± 3.8 (PDI = 0.2) | 600.00 ± 2.4 (PDI = 0.1) |
| 11 | 505.50 ± 11.8 (PDI = 0.4) | 378.43 ± 22.7 (PDI = 0.4) | 195.96 ± 6.5 (PDI = 0.5) | 612.23 ± 12.8 (PDI = 0.2) |
| 12 | 560.33 ± 10.1 (PDI = 0.4) | 435.40 ± 48.3 (PDI = 0.4) | 241.53 ± 4.6 (PDI = 0.4) | 647.60 ± 7.1 (PDI = 0.2) |
| 13 | 556.90 ± 17.5 | 462.93 ± 6.2 | 346.43 ± 13.9 | 665.36 ± 3.1 |

| | (PDI = 0.4) | (PDI = 0.3) | (PDI = 0.5) | (PDI = 0.1) |
|---|---|---|---|---|
| 14 | 650.70 ± 7.2<br>(PDI = 0.3) | 476.10 ± 29.5<br>(PDI = 0.4) | 507.50 ± 14.0<br>(PDI = 0.4) | 654.36 ± 15.4<br>(PDI = 0.2) |
| 15 | 645.90 ± 35.1<br>(PDI = 0.4) | 513.13 ± 20.3<br>(PDI = 0.4) | 562.90 ± 15.5<br>(PDI = 0.3) | 646.86 ± 12.9<br>(PDI = 0.1) |
| 16 | 649.70 ± 27.4<br>(PDI = 0.3) | 562.56 ± 42.2<br>(PDI = 0.3) | 627.16 ± 13.7<br>(PDI = 0.3) | 672.50 ± 24.5<br>(PDI = 0.2) |

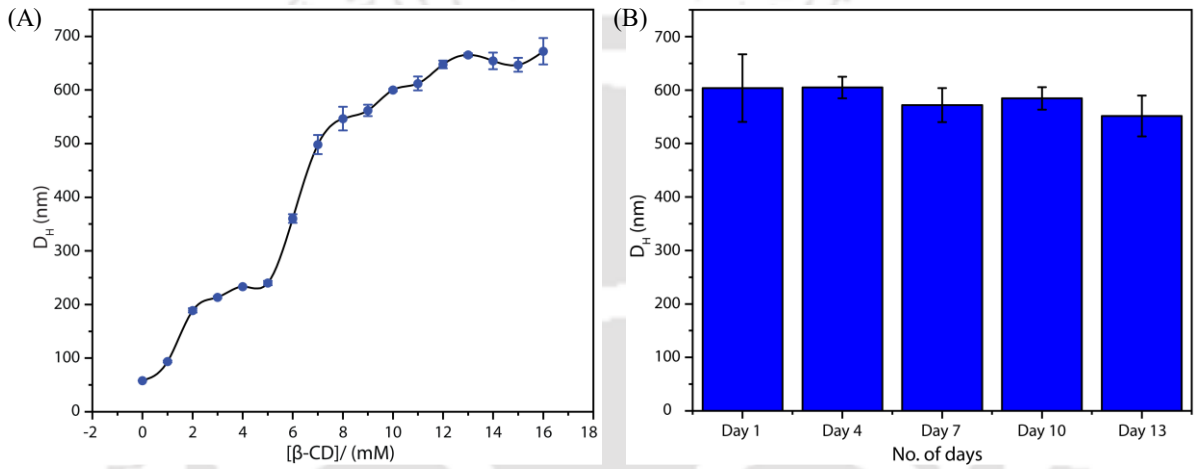


**Figure 2.8** (A) Variation of hydrodynamic diameter of C12mim:NaOle :: 1:1 system with β-CD addition. (B) Stability of composition D over 13 days.

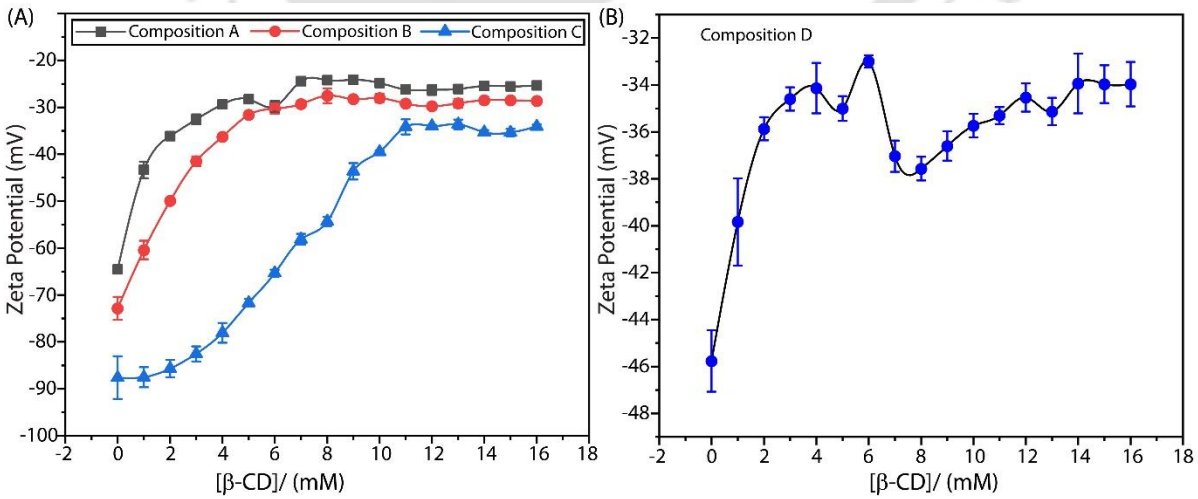


**Figure 2.9** Variation of zeta potential of different catanionic systems across different concentrations of β-CD.

### 2.4.5 Stability of Suprasomes

As previously noted, suprasomes containing 10 mM of β-CD were prepared. After each day, the hydrodynamic diameter was tested to determine if there had been any size growth, which would indicate aggregation. Thus, a stable hydrodynamic diameter over several days indicated the stability of composition A.

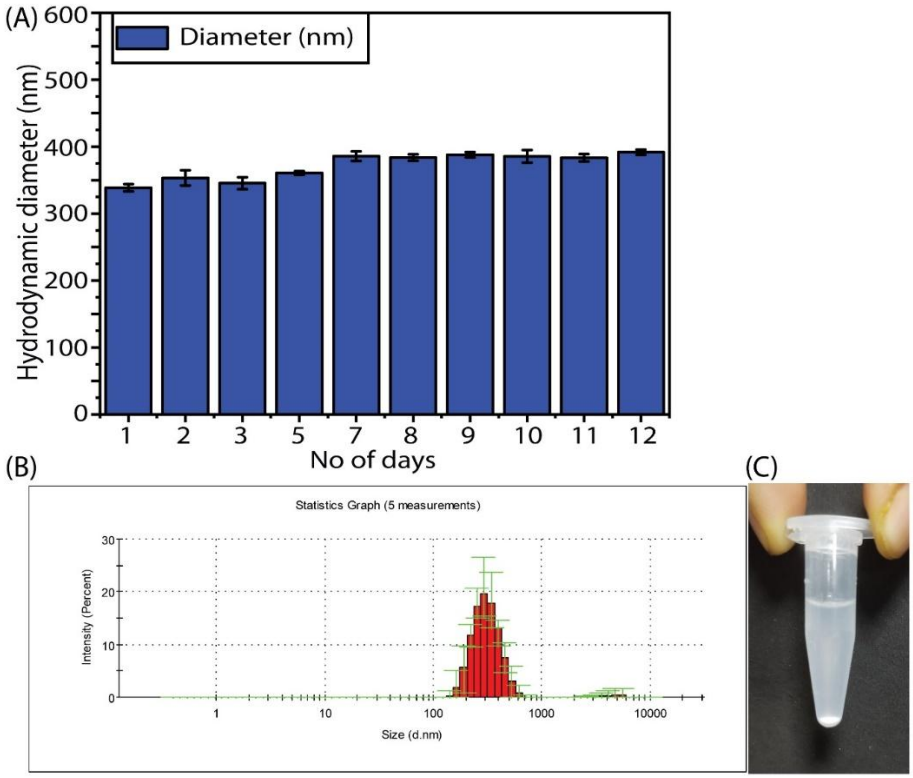


**Figure 2.10** (A) Variation of hydrodynamic diameter of the soluble aggregates on different days. (B) Hydrodynamic diameter measurement of the upper solution of composition A after 3 months. (C) Visual observation of composition A after 3 months.

**Note:** The β-CD-mediated aggregate transition was also observed visually. The aqueous solutions of C12Mbm and NaOle without or with a low concentration of β-CD were transparent at room temperature. However, the solution appeared slightly blueish when the concentration of β-CD was >8 mM, suggesting the increase in the size of the soluble aggregates, which shows light scattering properties (Fig. 2.3). We hypothesise that this change in average $D_H$ values of the catanionic amphiphiles in the presence of β-CD could be due to micelles-vesicle transition.[7, 20]

### 2.4.5.1 Stability in PBS Buffer, LB Media, and in 5% Blood Serum

The stability of suprasomes in PBS buffer (pH 7.4), LB media, and blood serum was also investigated by DLS measurements. PBS and LB media of 1/3$^{rd}$ volume were added to the suprasome solution, keeping β-CD concentration fixed at 10 μM, and the $D_H$ values were measured using DLS till 24 h. The suprasomal solutions were also prepared in PBS solution completely, and the $D_H$ were measured over time, suggesting stability of the system as the $D_H$ remained almost constant over 24h. Additionally, we also performed stability tests in blood serum. In this case, stability was observed till 6 h, and eventually, the size started to increase, suggesting a destabilisation over a longer time period of 24 h. We would like to mention that careful integration of polyethylene glycol (PEG) can definitely add longer stability to our suprasomal system, as it has a well-established reputation for increasing the circulation time of liposomes in the bloodstream, leading to the formation of stealth liposomes.

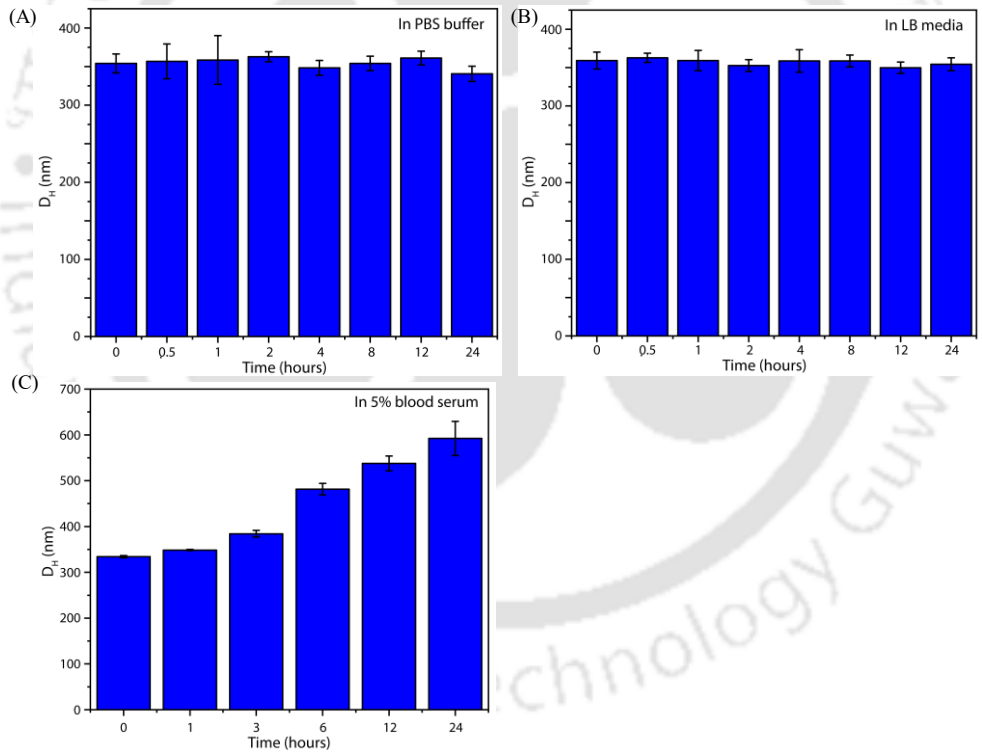


**Figure 2.11** Stability of composition A in PBS buffer (A), LB media (B), and in 5% blood serum (C).

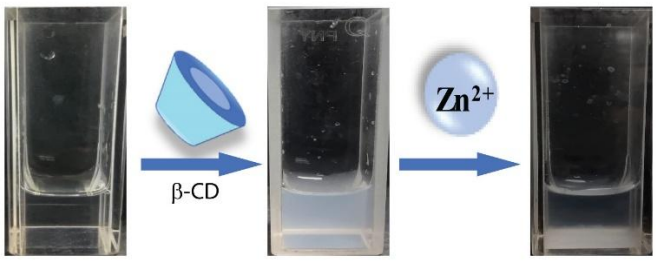


**Figure 2.12** Visual Change in aggregate transition after β-CD and $Zn^{2+}$.

### 2.4.6 Isothermal Titration Calorimetry Measurements

The interaction of β-CD with mixed micelles (C12Mbm and oleate) was investigated by isothermal titration calorimetry (ITC) measurements. The heat change induced by this interaction was measured at 28 °C (301 K) and a stirring speed of 350 rpm using an ITC-200 microcalorimeter from Microcal (Northampton, MA, USA). The β-CD (0.6 mM) solution was titrated against a 2 mM solution of C12Mbm and NaOle (1:1) mixture. The titration method involved 15 injections (2 μL of each) of the titrant (C12Mbm and NaOle mixture) into the sample cell containing β-CD (200 μL), performed at 2-minute intervals with continuous stirring. The thermodynamic parameters were determined using a machine running the Microcal Origin 7.0 software. The ΔH and ΔS values were obtained using a nonlinear least-squares fit of the data. Gibbs free energy (ΔG) was calculated by using the Gibbs equation: $\Delta G = \Delta H - T\Delta S$. The ΔH and ΔS values suggested that this process is enthalpy-driven.

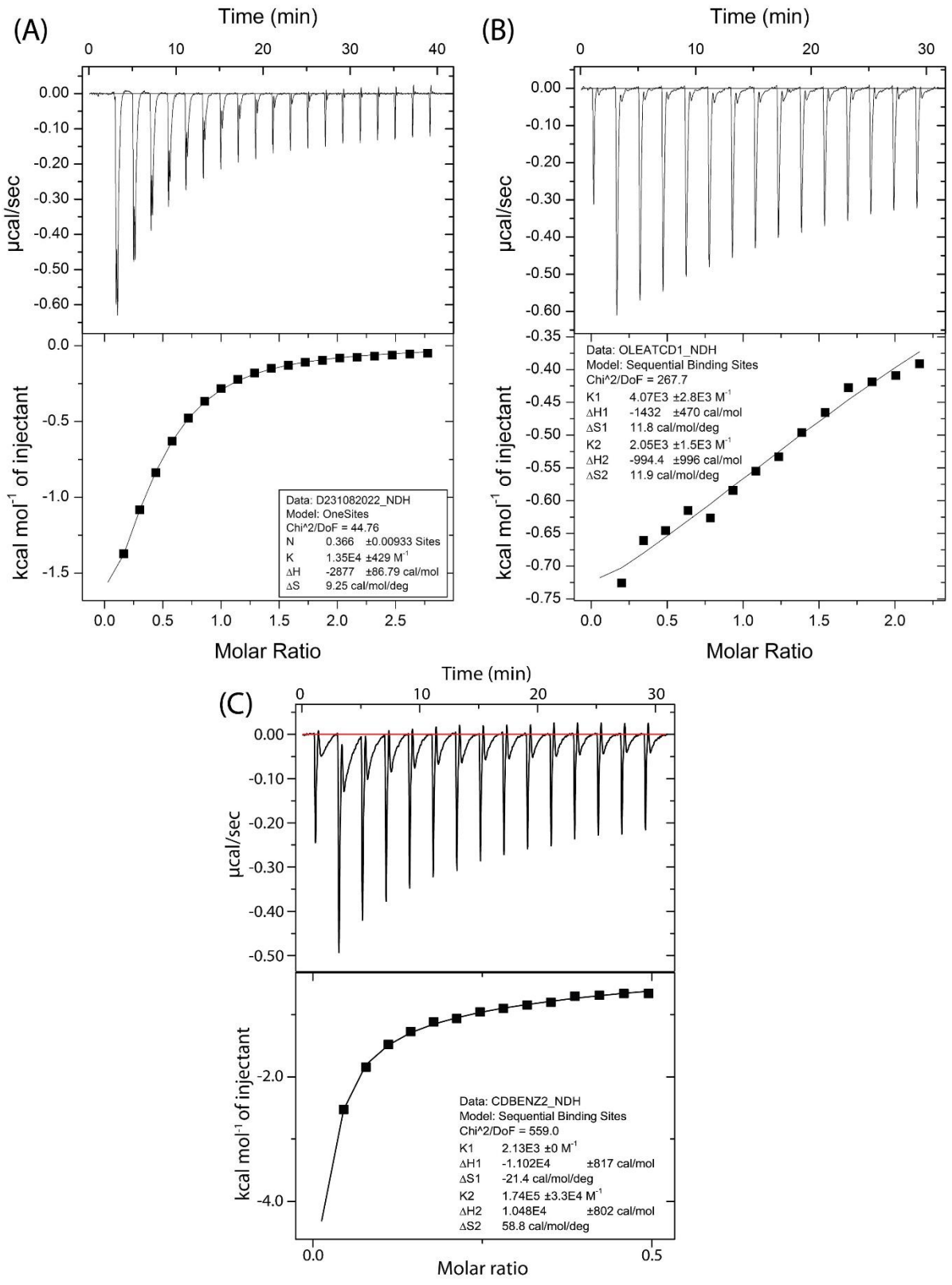


**Figure 2.13** ITC measurements of the mixture of only C12Mbm (A), only NaOle (B) and a mixture of C12Mbm and NaOle (1:1) (C) against β-CD.

### 2.4.7 Morphology Studies of Micelles and Suprasomes by TEM and AFM Analyses

Micelles and suprasomes solutions were prepared as mentioned above, and FETEM samples were prepared by the drop-cast method. For TEM investigations, 10 µL solution of composition A was placed onto a carbon-coated copper grid and allowed to settle for 5 minutes. After gently blotting the grid with filter paper, the grid was allowed to dry at room temperature for 10 minutes. The grid was then filled with 10 µL of a 2% uranyl acetate solution (in water) and left to dry for an additional minute at room temperature. The grid was dried overnight at room temperature after the excess uranyl acetate solution was absorbed using tissue paper. A JEOL JEM 2100 transmission electron microscope was used to record the images.

For AFM analysis, the samples were prepared by drop-casting 5 µL of micelles and suprasomes solutions onto a silicon wafer. The solution was then allowed to settle for 5 min and soaked with tissue paper. The silicon wafer was dried overnight at room temperature. The AFM images were recorded to determine the morphology of nanoaggregates formed. The samples were imaged by Asylum AFM AC 240 TS-R3 silicon cantilever probes. Topographic images, amplitude, and phase images of the samples were obtained and analysed by standard AC mode imaging. The Herts model was used to calculate the nanomechanical measurements.

### 2.4.8 Effect of Metal Ions on Hydrodynamic Diameter and Surface Potential

Suprasomes with composition C12Mbm (1 mM), NaOle (1 mM), and β-CD (10 mM) were prepared. The formation of suprasomes of size ~300 nm was confirmed through DLS measurement. Divalent metal ions, such as $Zn^{2+}$, $Cu^{2+}$, and HCl, were added to the suprasome solution at different concentrations (100 µM, 250 µM, 500 µM, 750 µM, and 1000 µM) and mixed thoroughly. The hydrodynamic diameters of the nanoaggregates were measured using DLS. The observed increase in size suggested disruption of suprasomes upon trigger and formation of another nanoaggregate.[21] A similar procedure was followed to measure the change in zeta potential upon the addition of divalent metal ions.

**Note:** Initially, we visualised the formation of a precipitate and a clear solution from the cloudy vesicle solution after adding divalent metals, which suggests the disruption of vesicles (Fig. 2.14).

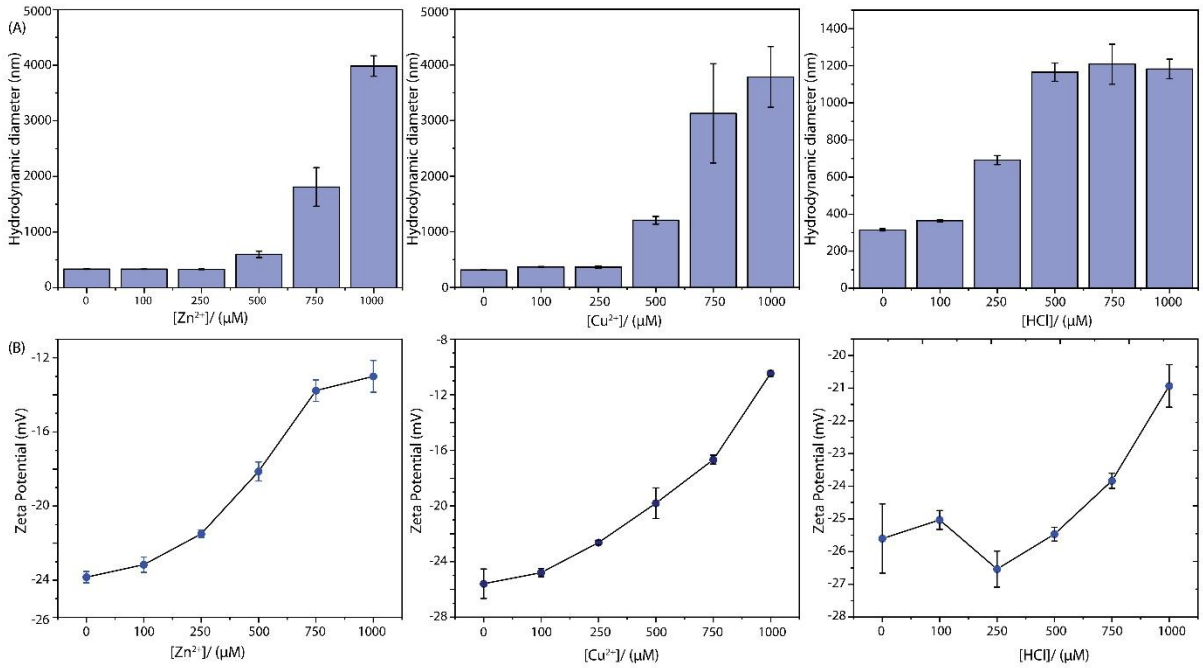


**Figure 2.14** Variation of (A) hydrodynamic diameter and (B) zeta potential of the suprasomes after treatments with different concentrations of $Zn^{2+}$, $Cu^{2+}$, and HCl.

### 2.4.9 Morphology Studies of Nanoaggregates After $Zn^{2+}$ Addition

The solutions of suprasomes were prepared as mentioned above. To the suprasome solution, $ZnCl_2$ (0.5-1 mM) was added and mixed thoroughly for 10 min. After 15 minutes, the FETEM and AFM samples were prepared from the above solutions.

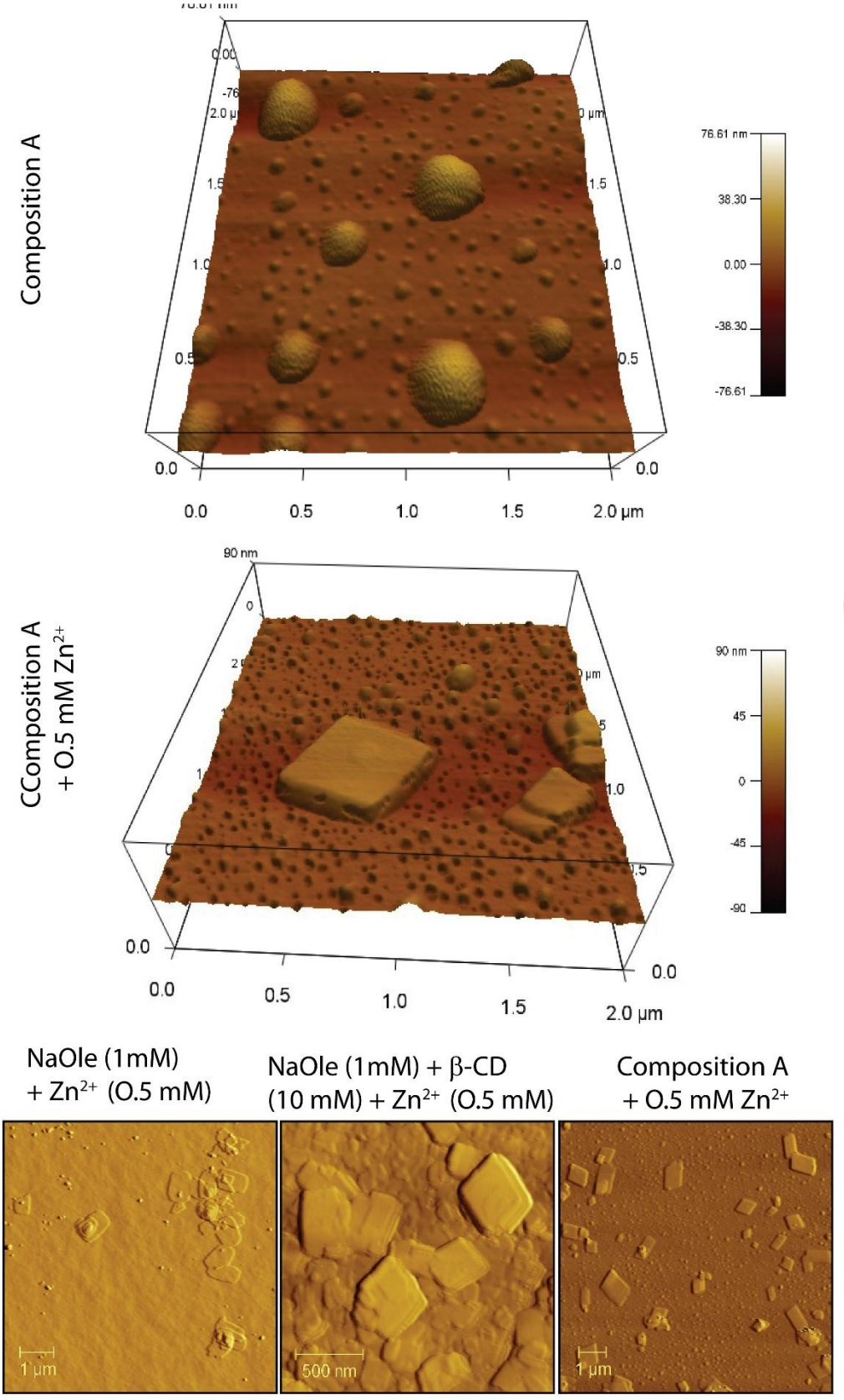


**Figure 2.15** Change in morphology of suprasomes (AFM images) after $Zn^{2+}$ treatments.

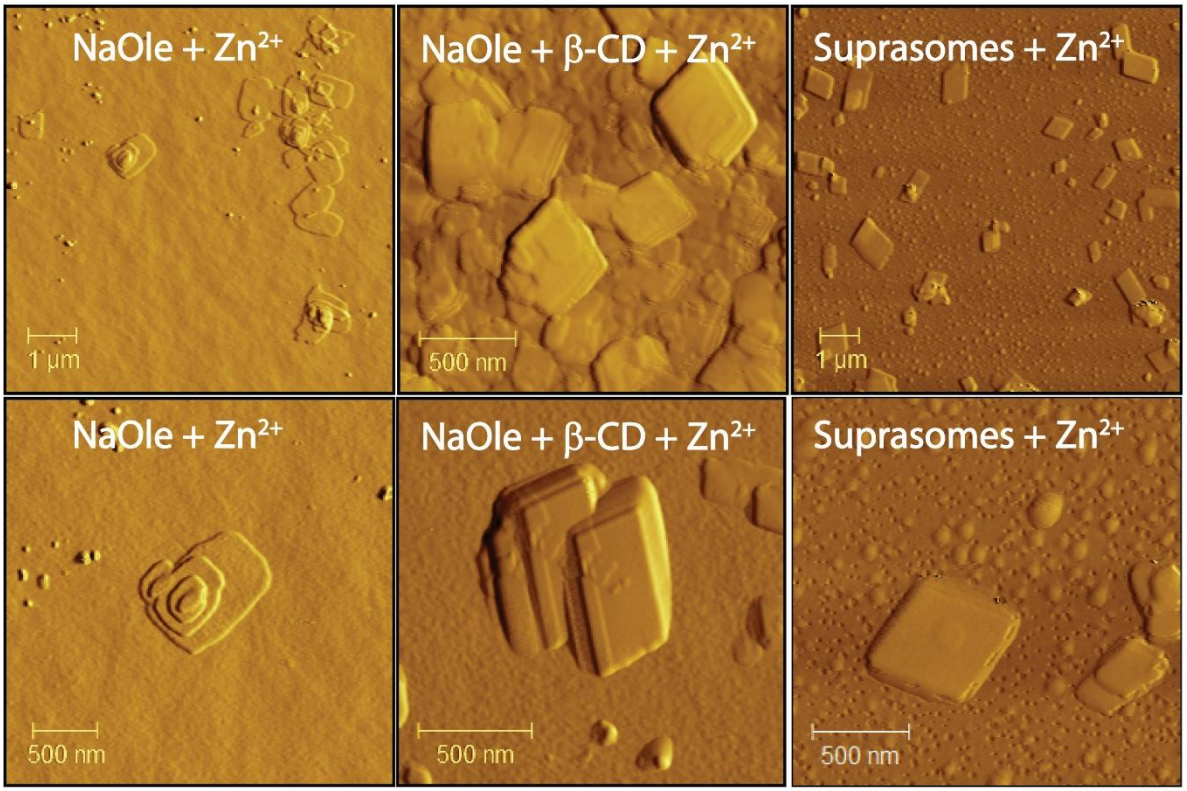


**Figure 2.16** Change in morphology of NaOle, NaOle + β-CD, and suprasomes after $Zn^{2+}$ treatments.

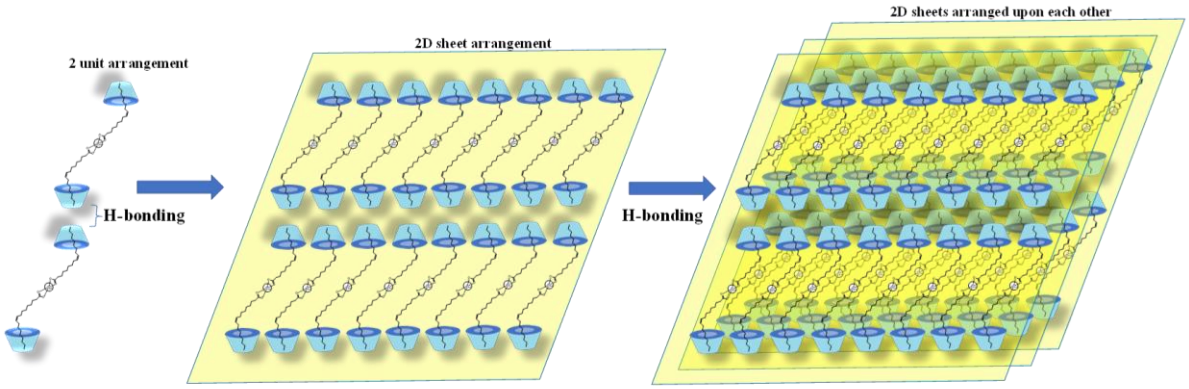


**Figure 2.17** Probable molecular arrangements of β-CD-$Zn^{2+}$-Oleate with the rhombic structure.

**Note:** To investigate the origin of rhombic structures following $Zn^{2+}$ addition to suprasomes, we performed control experiments of NaOle. The addition of $Zn^{2+}$ to NaOle solution resulted in rectangular structures with rounded corners. The addition of $Zn^{2+}$ to the mixture of NaOle and β-CD showed rhombic structures which is comparable to those previously observed in

$Zn^{2+}$-mediated suprasome disruption. These observations indicate that the rhombic structures could be developed from the proper crystalline arrangement of β-CD encapsulated zinc oleate.

### 2.4.10 Nile Red-based Kinetics Experiment

Micellar solutions were prepared in an aqueous medium using 1 mM of C12Mbm and 1 mM of NaOle, as mentioned above. Nile red was introduced to the mixture at a final concentration of 100 mM, followed by the addition of β-CD (10 mM). The solution was subjected to vortexing for 10 minutes, and then it was shaken overnight at 180 rpm, room temperature, to induce the formation of suprasomes containing Nile red, which was subsequently utilised for the kinetics experiment.

In the kinetics experiment, a 2 mL solution of the suprasomes containing Nile red was exposed to metal ion ($Zn^{2+}$) and acid (HCl) triggers, each at a final concentration of 5 mM, resulting in the swift disruption of the suprasomes. The solution was stirred using a magnetic stirrer till 800 s, and then the stirrer was stopped. The addition of metal and acid triggers caused a decrease in the fluorescence intensity of Nile red ($\lambda_{ex}$ = 550 nm, $\lambda_{em}$ = 645 nm), as evidenced by a decrease in the fluorescence signal at 645 nm, suggesting the release of Nile red from the hydrophobic bilayer to the aqueous solution. After adding the metal ions, larger aggregates were observed to have formed, causing a decrease in the fluorescence intensity of the solution. After the stirrer was turned off, these larger aggregates settled gradually, leading to a further decline in the fluorescence intensity of the suprasome solutions.

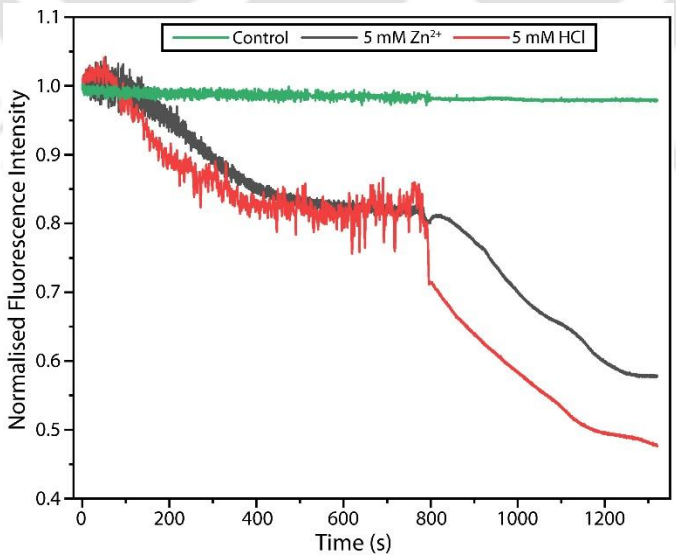


**Figure 2.18** Stimuli-responsive disruption of suprasomes was investigated by time-dependent Nile red assay.

**Note:** The NR dye has the propensity to get encapsulated within the hydrophobic layers and shows a high fluorescence signal. The disruption of vesicles could lead to the release of NR dye to the aqueous environment and the quenching of the fluorescence signal. This solvatochromic effect serves as an indicator of vesicle disintegration. The low quenching of NR fluorescence intensity after metal addition could be due to the incorporation of NR into other aggregates or within the cavity of the β-CD. A control experiment of NR in the presence of β-CD showed an enhancement of fluorescence intensity. The real-time kinetics experiment with Nile red also revealed the release of solvatochromic dye into an aqueous medium, which significantly reduces fluorescence intensity.

### 2.4.11 Drug Encapsulation and Release Studies

Tetracycline was used as a model drug to investigate the encapsulation efficacy and release profile of the suprasomes. Tetracycline was added to a micellar solution of C12Mbm (1 mM) and NaOle (1 mM) at various concentrations (50 µM, 200 µM, 400 µM, 800 µM). For improved drug encapsulation, while the suprasomes were developed from micelles, β-CD (10 mM) was added to the solution, sonicated, and then vortexed for 5 min. The solution was maintained overnight in a shaker at 180 rpm. Ultrafiltration tubes with a 10 kDa cut-off were used to separate the suprasomes formed, and the drug present in the remaining solution was measured using UV-Vis spectroscopic analysis. This gave us the drug encapsulation efficiency of the suprasomes.

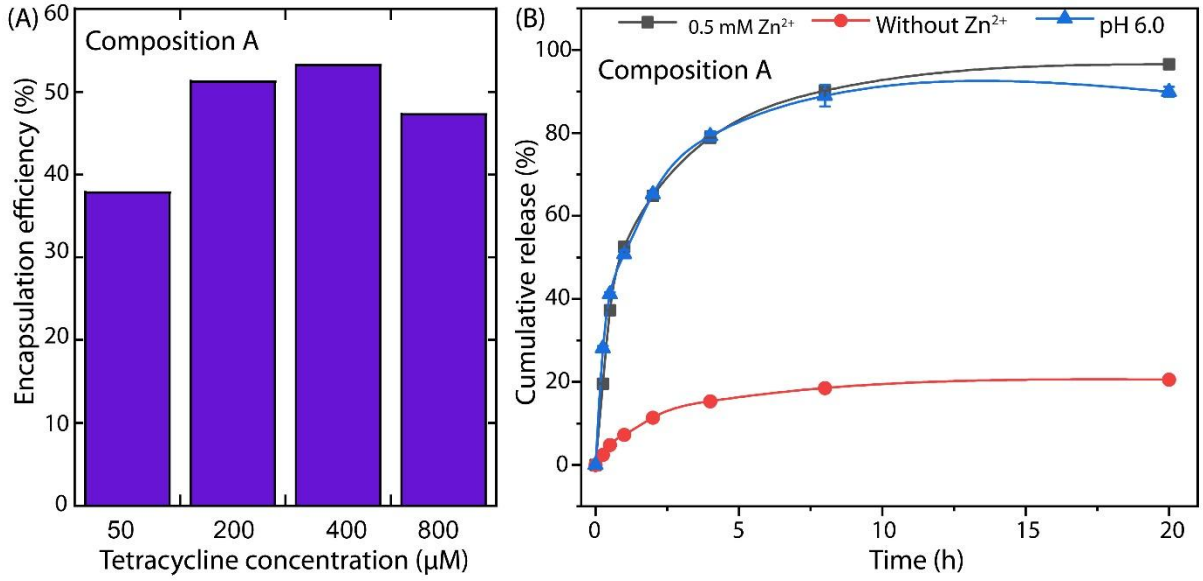


**Figure 2.19** Tetracycline encapsulation efficacy (A) and release profiles (B) of suprasomes of composition A.

Tetracycline (400 µM) was used for encapsulation in the suprasomes, as mentioned above, and dialyzed against an aqueous solution in a dialysis bag for 4-6 hours until no further excess drug release occurred. Then the dialysis bag was placed in a 40 mL aqueous solution with 0.5 mM $Zn^{2+}$ concentration. At different time intervals, 600 µL solution was removed for measurement and replaced with a fresh aqueous solution. The drug release profile was also measured in the presence of PBS buffer at pH 6.0 following the above procedure.

**Note:** Recent findings revealed that bacterial infections induce low pH environments at bacterial-infected sites, facilitating site-selective drug release.[15] This observation suggests that our suprasome-based DDSs might exhibit effectiveness in bacterial-infected regions characterized by a low pH environment.

### 2.4.12 Antimicrobial Activity Assessment

The antimicrobial activity of the additives (C12Mbm, C12mim, and various compositions) was evaluated using the microbroth dilution method against the Gram-positive bacterial strain

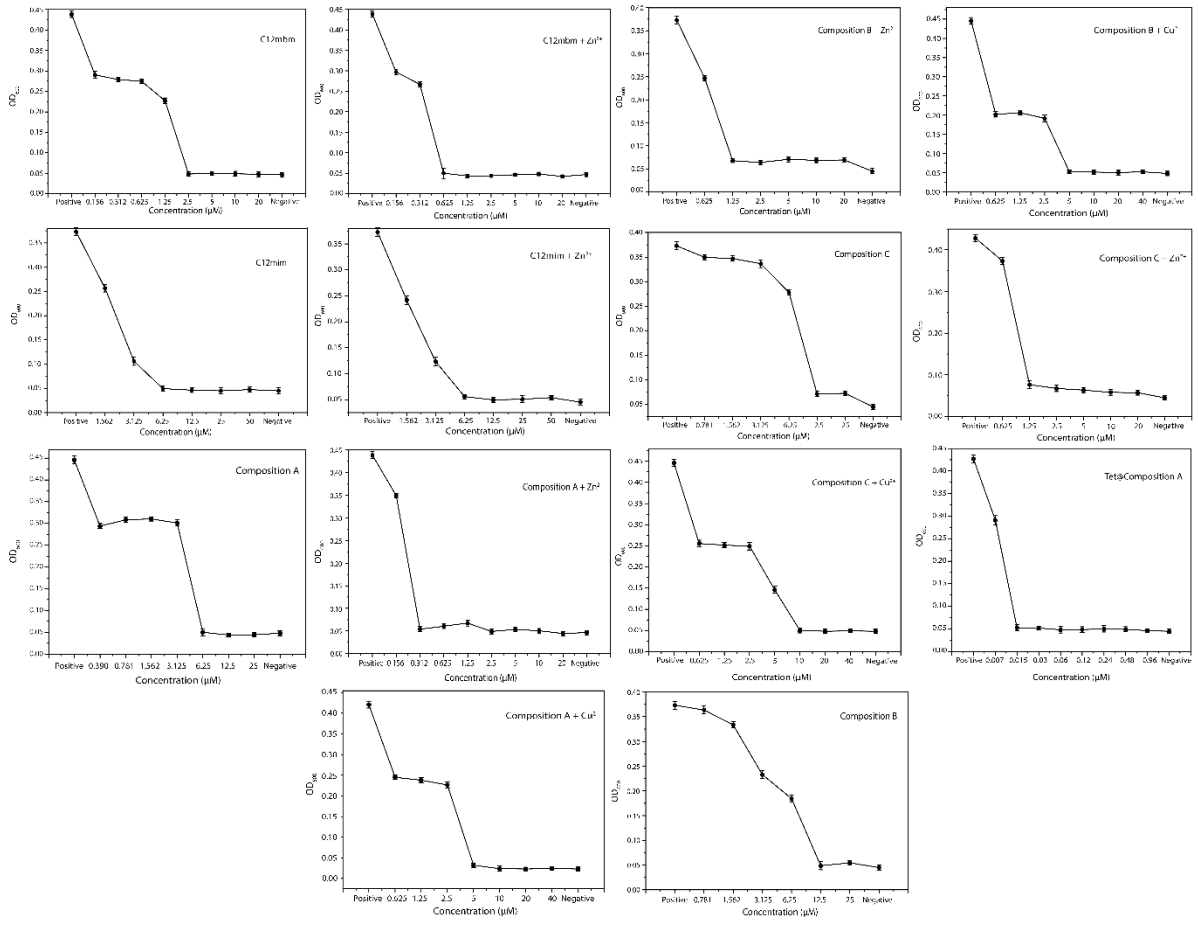


**Figure 2.20** $OD_{600}$ vs concentration plot of different additives for *S. aureus* bacterial cells.

*Staphylococcus aureus* (*S. aureus*; MTCC-96). The Glycerol stock of the bacterial culture was streaked onto an agar plate containing Luria-Bertani (LB) medium. A single colony was inoculated into broth medium and allowed to grow until the mid-logarithmic phase at 37 ºC, 180 rpm in a shaker incubator. In a 96-well plate, additives were sequentially diluted in PBS supplemented with 4 % DMSO.

Using the microbroth dilution method, the antibacterial efficacy of the compounds was evaluated against Gram-positive (*S. aureus* and MRSA) and Gram-negative (E. coli) strains. A compound's MIC was calculated as its lowest concentration at which visible growth of the microorganism was inhibited. At 37 °C and 180 rpm, the bacteria were grown in LB medium (Luria-Bertani broth). As soon as the desired optical density was attained, the bacteria were centrifuged and washed with distilled water before being diluted to $10^6$ CFU/mL in LB medium. Serial dilution of the compound was performed in a 96-well plate using a micropipette.

**Table 2.4** Calculated MIC values of the additives against different bacterial strains.

| Composition | MIC (μM) | | |
|---|---|---|---|
| | S. aureus | MRSA | *E. coli* |
| C12Mbm | 2.50 ± 0.5 | 10 ± 1.0 | 20 |
| C12Mbm + $Zn^{2+}$ (250 μM) | 0.62 ± 0.1 | 2.5 ± 1.5 | |
| Composition A | 6.25 ± 1.0 | 5.0 ± 0.5 | 20 |
| Composition A + $Zn^{2+}$ (250 μM) | 0.31 ± 0.1 | 2.5 ± 1.5 | |

### 2.4.13 Mechanistic Origin of Tunable Antibacterial Activity

Further analysis revealed that the antibacterial activity of suprasomes in the absence and presence of $Zn^{2+}$ could be due to the abundance of free C12Mbm under experimental conditions. To quantify the free C12Mbm, either in its micellar state or entrapped within suprasomes, we performed UV-Vis spectral analysis across three distinct conditions: firstly, in its original micellar form; secondly, following the addition of beta-cyclodextrin (β-CD), facilitating suprasome formation; and lastly, when $Zn^{2+}$ was introduced for the disruption of suprasomes. This experimental investigation revealed a compelling relationship between suprasome formation induced by β-CD and the sequestration of C12Mbm within the suprasomes, where the encapsulation of the alkyl long chain of C12Mbm occurs by β-CD

molecules. Simultaneously, during suprasome formation, the charge of the free benzimidazolium will be masked by excess free oleate, as shown, leading to the overall

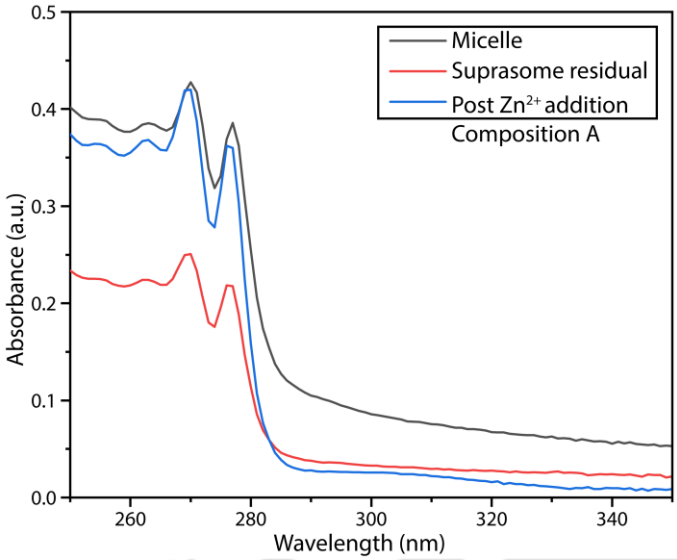


**Figure 2.21** Absorbance spectra of free C12Mbm before and after treatments.

masking property. The $Zn^{2+}$ triggered disruption of the suprasomes, resulting in the liberation of C12Mbm. Remarkably, the observed behaviour was intimately connected to the antibacterial efficacy exhibited by the micellar system, the suprasomes, and the system after $Zn^{2+}$-triggered disruption.

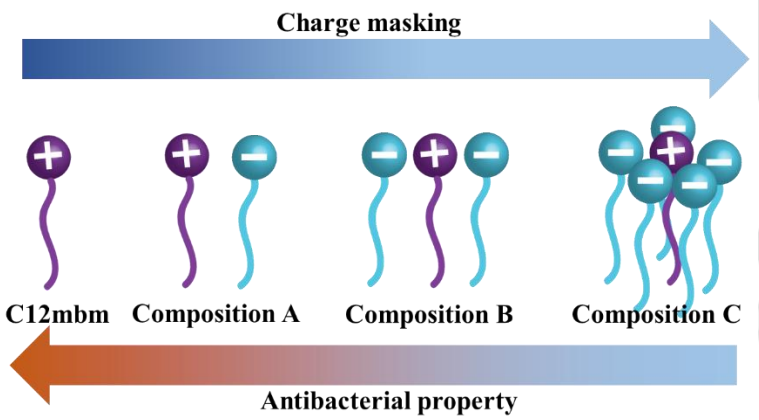


**Figure 2.22** Charge masking of free C12Mbm by free NaOle.

### 2.4.13.1 Bacterial Cell Morphology Analysis by FESEM

For morphological analysis of the additive-treated bacterial cells, *S. aureus* cells were treated as in the aforementioned sections until the mid-logarithmic phase. Cells were harvested and treated with the compound at its MIC value. After incubation at 37 ℃ and 180 rpm, the cells

were centrifuged, and the pellet was resuspended in buffer and treated with 3% glutaraldehyde for 30 min to fix the cells. Bacterial cells were again centrifuged to wash them and then incubated in Milli-Q water. For the analysis, 10 µL of the sample was mounted onto a glass grid and allowed to dry under laminar airflow. Before the analysis, the sample containing glass was stacked onto the FESEM grid and coated with gold.

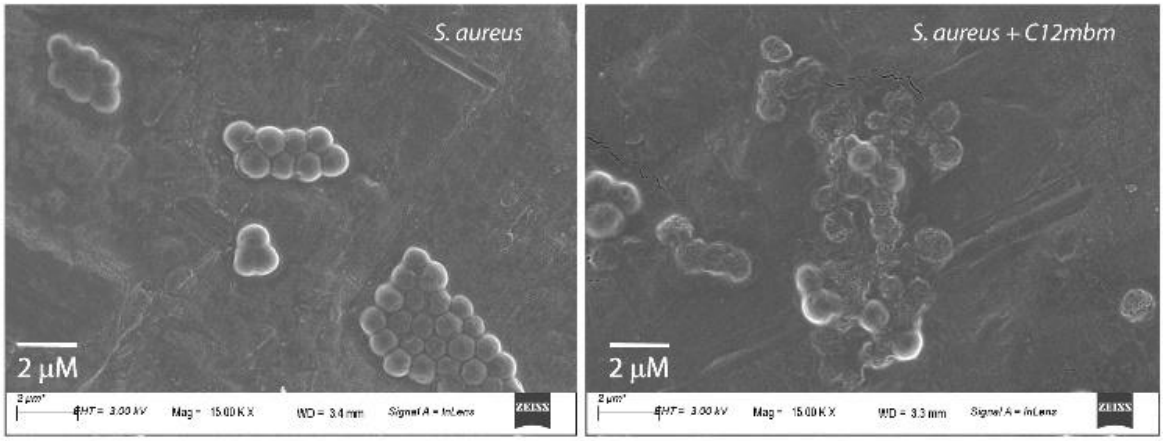


**Figure 2.23** Representative FESEM images of untreated and **C12Mbm** treated *S. aureus* cells.

### 2.4.13.2 Blood Cells Cytocompatibility Test

Biocompatibility of the benzimidazolium containing β-CD compositions was performed against fresh erythrocytes human blood as per our earlier reported protocol and as per the guidelines of the Institutional Human Ethics Committee (IHEC). Before assay, blood was

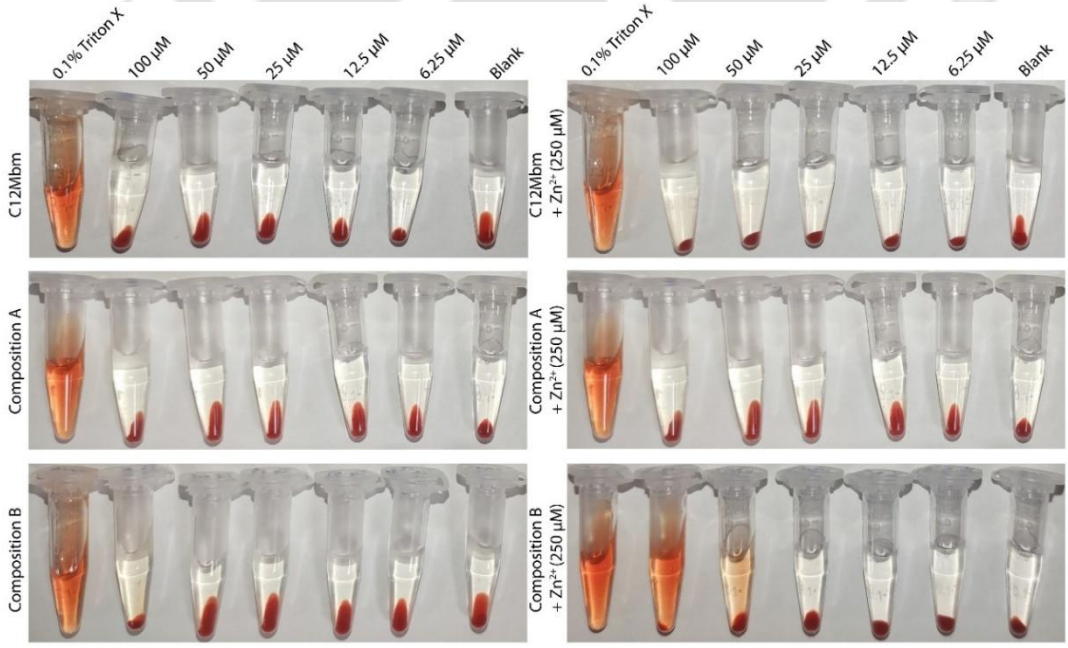


**Figure 2.24** Extent of hemolysis of C12Mbm, Composition A, and Composition B.

centrifuged to separate the plasma from erythrocytes at 1500 rpm for 5 min and washed twice with buffer at 7.4 pH (20 mM HEPES, 100 mM NaCl). 5% hematocrit was prepared. Serially diluted different compounds were prepared in the same buffer, and for the negative control, only buffer was taken, while for positive control, detergent (0.1 % Triton-X) was taken for complete cell lysis.

To the serially diluted samples, hematocrit was added and incubated at room temperature for 1 hr. After incubation, the sample vial was centrifuged, and 200 µL of the supernatant from the sample vials was aliquoted into 96-well plates, and its absorbance was measured at 410 nm by using a plate reader (Biotech).[16] The hemolytic assessment was made by comparing the absorbance of the samples with negative and positive control.

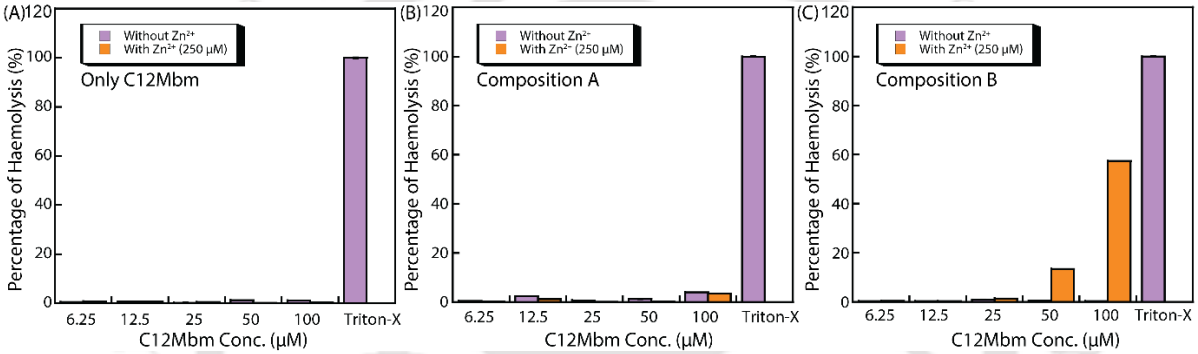


**Figure 2.25** Percentage of hemolysis of C12Mbm (A), Composition A (B), Composition B (C).

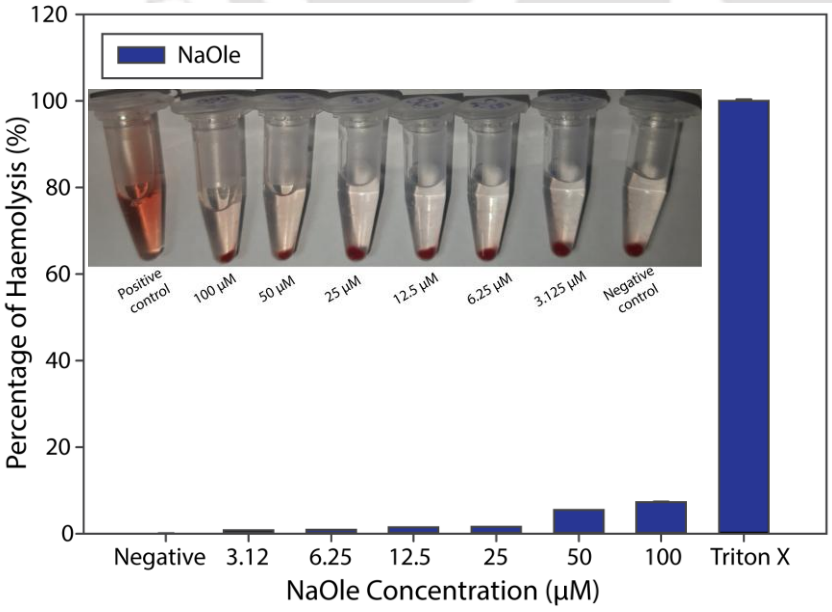


**Figure 2.26** Extent of hemolysis of NaOle.

### 2.4.14 Cell Viability Assay

The cellular cytotoxicity of the compounds was assessed by the standard 3-[4,5-dimethylthiazol-2-yl]-2,5-diphenyl tetrazolium bromide (MTT) assay on the HEK293 cell line. Approximately $10^5$ cells/well (per 100 µL) were seeded in 96-well flat-bottom tissue culture plates and grown in media containing 10% fetal bovine serum (FBS) in Dulbecco's Modified Eagle Medium (DMEM), and incubated at 37 °C in 5% $CO_2$. After 12-16 hours, the media was discarded, and each well was washed with phosphate-buffered saline (PBS). Then, the serially diluted compounds in plain DMEM media without FBS were added to each well, and the wells were incubated for 24 hours at 37 °C in 5% CO2. Next, 100 µL of fresh plain DMEM medium with MTT (5 mg/mL) was added to the wells and incubated for an additional 2 h at 37 °C. The MTT-containing medium was removed from each well, and the formazan crystal formed was solubilized in 100 µL, and absorbance was recorded on a microplate reader (Multiskan™ GO) at the wavelength of 570 nm. All experiments were performed in triplicate, and the relative cell viability (%) was expressed as a percentage relative to the untreated cells.

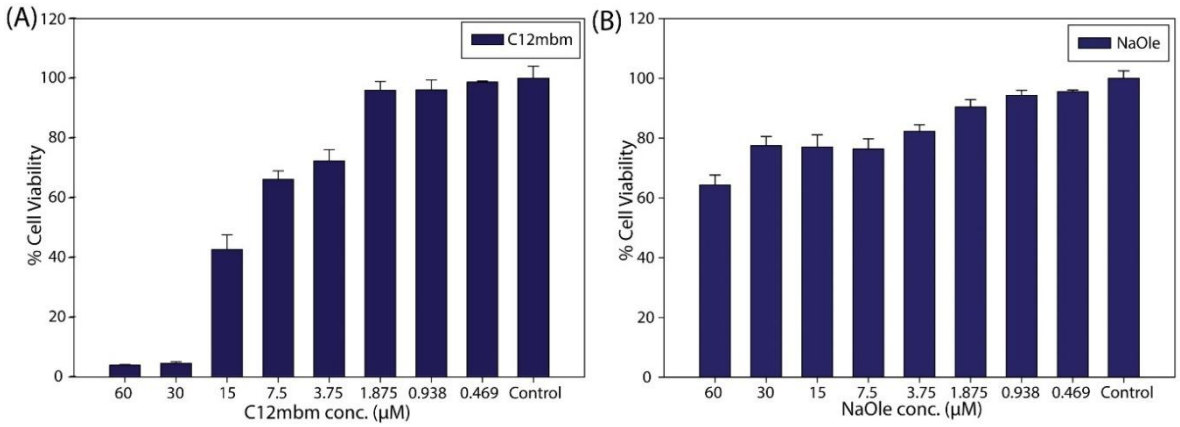


**Figure 2.27** Percentage of cell viability in the presence of different concentrations of C12Mbm (A) and NaOle (B) after 24 h of treatment.

**Note:** The $IC_{50}$ value of C12Mbm was found to be 12.57 µM. The results indicated that C12Mbm exhibits biocompatibility at concentrations 20-30 times higher than the MIC value of tetracycline composition A. Although C12Mbm showed cytotoxicity against normal cell lines, its antibacterial effect was achieved at very low concentrations, which could be due to the synergistic effect of C12Mbm, $Zn^{2+}$, and tetracycline. The combined action of these components enhances the antimicrobial efficacy of the system, allowing for effective antibacterial activity at significantly reduced concentrations of C12Mbm. These findings highlight the potential of our developed system for targeted antibacterial applications, where

low concentrations can achieve the desired therapeutic effects while maintaining biocompatibility.

### 2.4.15 Membrane Depolarization Assay

The membrane depolarization assay was performed against *S. aureus* cells, which were grown in LB broth at 37 °C, 180 rpm, till the mid-logarithmic phase. The cells were collected by centrifugation at 5000 rpm for 3 mins. After resuspending the bacterial pellet in HEPES buffer (10 mM HEPES in 50 mM glucose), $DiSC_3(5)$ dye (membrane depolarization sensing dye) at 0.4 µM final concentration was added, and cells were incubated at 37 °C for 1 hour. Thereupon, 100 mM KCl was added, followed by 15 mins of incubation. Afterward, varied compound concentrations (0, 5, and 10 µM) were added to the cell suspension along with 10 µM valinomycin as a positive control. The fluorescence spectra of cell suspensions were recorded ($\lambda_{ex}$ = 620 nm, $\lambda_{em}$ = 650 nm).

### 2.4.16. Propidium Iodide Uptake Assay

The propidium iodide (PI) uptake assay was performed to assess the membrane integrity of bacteria in the presence of compounds. The previously outlined methodology was used to culture and harvest *S. aureus* cells.[17] After resuspending the bacterial pellet in PBS buffer, the compound was added to the cell suspension at a concentration equivalent to its MIC value. The cells were also resuspended in the buffer for the control. Furthermore, the cells were incubated

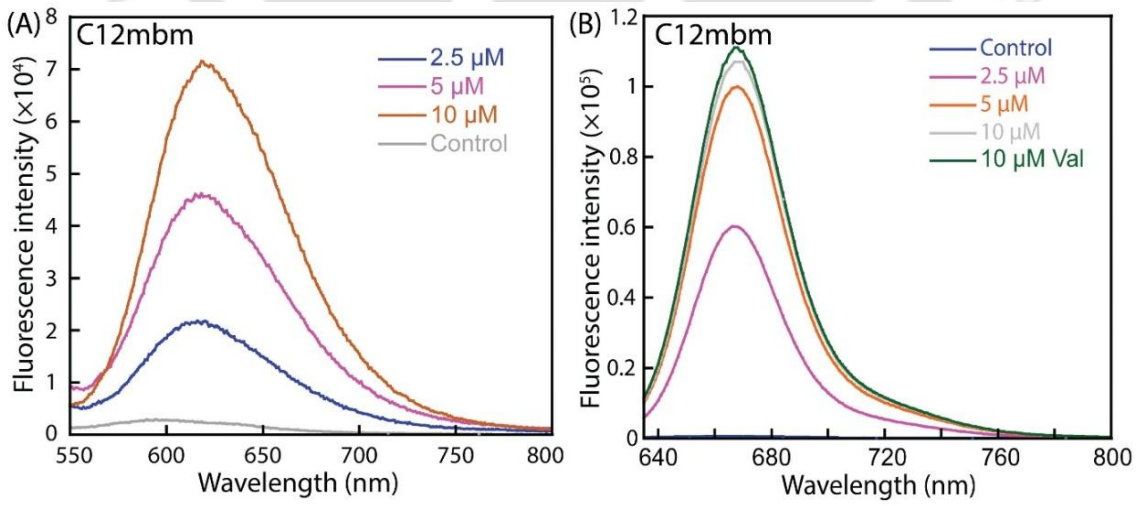


**Figure 2.28** Fluorescence-based PI uptake (A) and membrane depolarization (B) studies of C12Mbm treated *S. aureus* cells. Val = Valinomycin.

at 37 °C and 180 rpm. After sampling at different time intervals (0.5, 1, and 2 hrs), samples were centrifuged and resuspended in the buffer. After that, it was treated with PI (30 µM) for

30 minutes. The unbound dye was removed through centrifugation, and the bacterial cells were then resuspended in the buffer. The fluorescence spectrum of the samples was recorded after a certain period of time ($\lambda_{ex}$ = 535 nm, $\lambda_{em}$ = 610 nm).

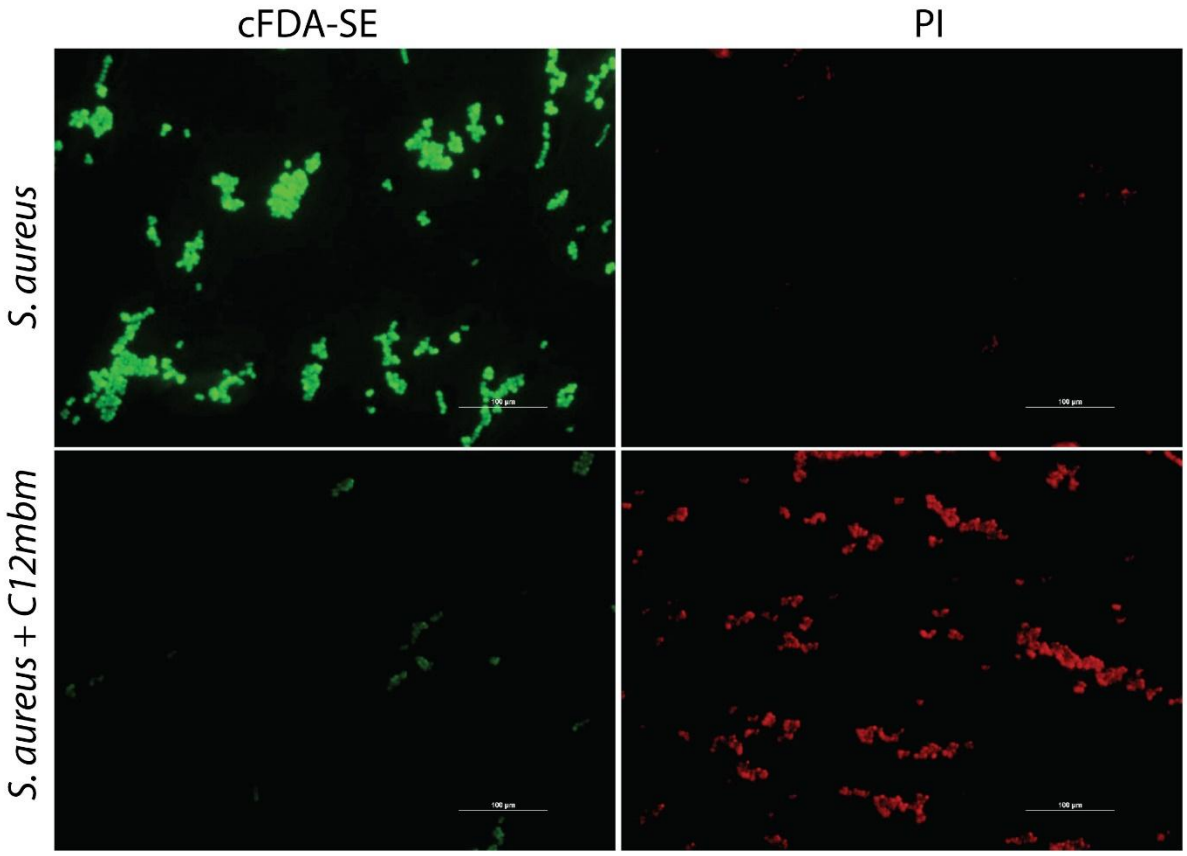


**Figure 2.29** Microscopic images of PI uptake and membrane depolarization studies of C12Mbm treated *S. aureus* cells.

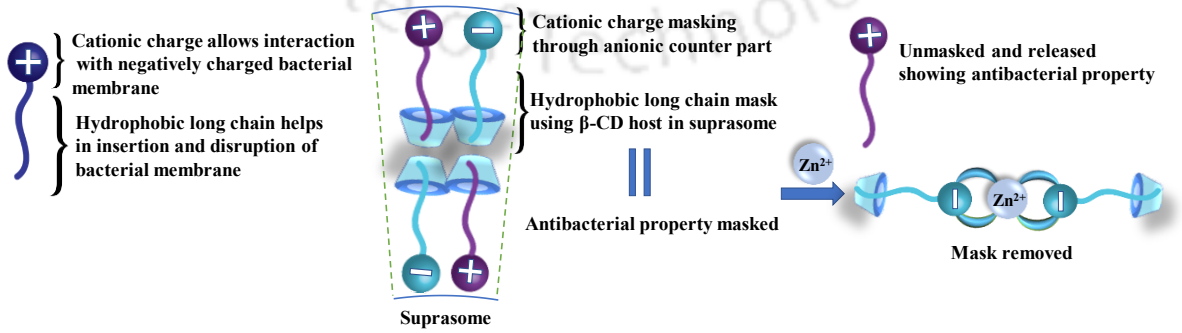


**Figure 2.30** Plausible explanation for the masking and unmasking of cationic charge.

**Note: Metal-Responsive Behaviour of the Suprasome**

We also conducted a DLS-based size increment experiment upon metal ion addition to provide a clear picture of which metal can destabilise the suprasome-based DDSs. The change in $D_H$ values suggested that monovalent metal ions are ineffective in causing any disruption to the suprasome, even at very high concentrations. So, we tried to investigate the role of biologically available divalent metal ions, which can cause suprasome disruption. We scanned the concentration range of metal ions, including $Zn^{2+}$, $Cu^{2+}$, $Ca^{2+}$, $Ni^{2+}$, $Mg^{2+}$, and $Fe^{3+}$, by adding them to the suprasome solution of composition A.

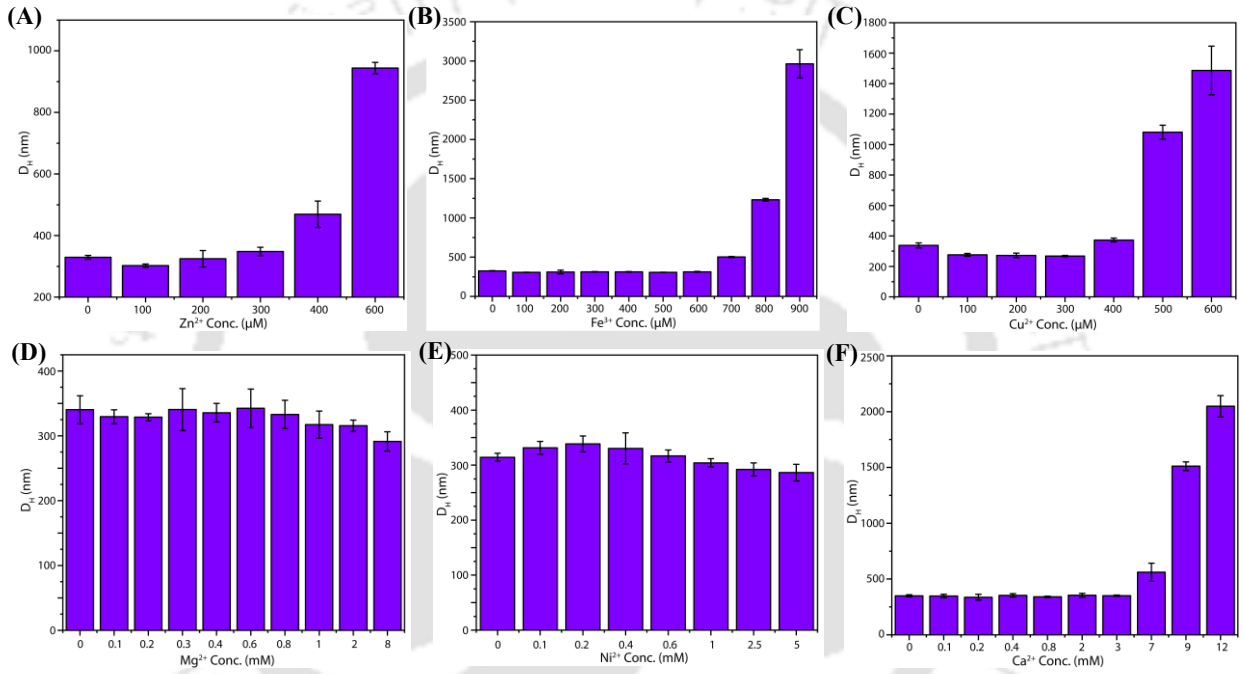


**Figure 2.31** Metal-responsive behaviour of suprasome, hydrodynamic diameter at different metal ion concentration, $Zn^{2+}$ (A). $Fe^{3+}$ (B), $Cu^{2+}$ (C), $Mg^{2+}$ (D), $Ni^{2+}$ (E), $Ca^{2+}$ (F).

The change in $D_H$ values upon these metal ion additions at different concentrations indicates that the $Zn^{2+}$ causes a significant change in hydrodynamic diameter at 400 µM, whereas $Cu^{2+}$ and $Fe^{3+}$ at 500 µM and 700 µM, respectively. Other metal ions, such as $Ca^{2+}$, $Ni^{2+}$, and $Mg^{2+}$, showed no significant change in $D_H$ at very high concentrations of 5-12 mM. We further investigated the literature reports for the abundance of free metal ion concentration in the body (Blood serum), which were in the range of 10-50 µM. The concentrations of these metal ions in body fluid (blood serum) were found to be well below the disruptive levels, indicating likely stability in the presence of these metal ions in body fluid. It is essential to note that only the free metal ion concentration is relevant, as most metal ions are bound to specific proteins.

Hence, the suprasomal system should remain stable in body fluid. Additionally, we provided a table to clarify the change in size with respect to different metals, and we hope this will add clarity and enhance comprehension for our readers.

**Table 2.5** Metal ion concentrations are required for significant destabilisation of suprasome.

| Metal ions | Concentration required for suprasome disruption (μM) | Concentration of metal ion in blood serum (μM) |
|---|---|---|
| $Zn^{2+}$ | 400 | 0.1-2[22] |
| $Cu^{2+}$ | 500 | 11-24[23] |
| $Fe^{3+}$ | 700 | 30-40[24] |
| $Ca^{2+}$ | 7000 | 2500[25] |
| $Mg^{2+}$ | > 8000 | 750-1050[26] |
| $Ni^{2+}$ | > 5000 | 0.002[27] |

Though this study suggested the suprasomes had higher responsiveness to a few metal ions, such as $Zn^{2+}$, $Cu^{2+}$, and $Fe^{3+}$, we believe that this can be utilised as an opportunity to get wider applications. We presume that this could be treated as an opportunity to deliver drugs to tissues or pathological conditions where these metal ions ($Zn^{2+}$, $Cu^{2+}$, $Fe^{3+}$) have a high concentration level. We provided a table with the tissues and pathological conditions in the body with high concentrations of these metal ions.

**Table 2.6** Tissues and pathological conditions with very high metal ion concentrations.

| Metal ions | Tissues with higher concentration | Pathological conditions with higher concentration |
|---|---|---|
| $Zn^{2+}$ | hippocampus, amygdala, cortex, pancreas, and prostate | Prostrate related pathological conditions[28] |
| $Cu^{2+}$ | Liver, kidney | Wilson's disease[29] |
| $Fe^{3+}$ | Spleen | Hemochromatosis[30] |

**2.5 Reference:**

1. Davies, T. S.; Ketner, A. M.; Raghavan, S. R., Self-assembly of surfactant vesicles that transform into viscoelastic wormlike micelles upon heating. J. Am. Chem. Soc. **2006**, 128 (20), 6669-6675.

2. Dutta, R.; Ghosh, S.; Banerjee, P.; Kundu, S.; Sarkar, N., Micelle-vesicle-micelle transition in aqueous solution of anionic surfactant and cationic imidazolium surfactants: Alteration of the location of different fluorophores. J. Colloid Interface Sci. **2017**, 490, 762-773.

3. Yang, K.; Hua, B.; Qi, S. L.; Bai, B.; Yu, C. Y.; Huang, F. H.; Yu, G. C., Suprasomes Based on Host-Guest Molecular Recognition: An Excellent Alternative to Liposomes in Cancer Theranostics. Angew. Chem., Int. Ed. **2022**, 61 (12), e202213572.

4. Hu, X. Y.; Gao, L.; Mosel, S.; Ehlers, M.; Zellermann, E.; Jiang, H.; Knauer, S. K.; Wang, L. Y.; Schmuck, C., From Supramolecular Vesicles to Micelles: Controllable Construction of Tumor-Targeting Nanocarriers Based on Host-Guest Interaction between a Pillararene-Based Prodrug and a RGD-Sulfonate Guest. Small **2018**, 14 (52), 1803952.

5. Wang, S. N.; Yu, S. H.; Lin, Y. W.; Zou, P. Z.; Chai, G. H.; Yu, H.; Wickremasinghe, H.; Shetty, N.; Ling, J. H.; Li, J.; Zhou, Q., Co-Delivery of Ciprofloxacin and Colistin in Liposomal Formulations with Enhanced In Vitro Antimicrobial Activities against Multidrug Resistant Pseudomonas aeruginosa. Pharm. Res. **2018**, 35 (10), 187.

6. Dey, S.; Patel, A.; Raina, K.; Pradhan, N.; Biswas, O.; Thummer, R.; Manna, D., A stimuli-responsive anticancer drug delivery system with inherent antibacterial activities. Chem. Commun. **2020**, 56 (11), 1661-1664.

7. Dai, C. L.; Yang, Z.; Yang, H. L.; Liu, Y. F.; Fang, J. C.; Chen, W. X.; Li, W. T.; Zhao, M. W., Micelle-to-vesicle transition induced by beta-cyclodextrin in mixed catanionic surfactant solutions. Colloids Surf., A **2016**, 498, 1-6.

8. Ghosh, A.; Seth, S. K.; Purkayastha, P., Surfactant and Cyclodextrin Induced Vesicle to Micelle to Vesicle Transformation in Aqueous Medium. Langmuir **2018**, 34 (38), 11503-11509.

9. Fa, K.; Liu, H. Y.; Gong, H. N.; Zhang, L.; Liao, M. R.; Hu, X. Z.; Ciumac, D.; Li, P. X.; Webster, J.; Petkov, J.; Thomas, R. K.; Lu, J. R., In-Membrane Nanostructuring of Cationic Amphiphiles Affects Their Antimicrobial Efficacy and Cytotoxicity: A Comparison Study between a De Novo Antimicrobial Lipopeptide and Traditional Biocides. Langmuir **2022**, 38, 6623-6637.

10. Furi, L.; Ciusa, M. L.; Knight, D.; Di Lorenzo, V.; Tocci, N.; Cirasola, D.; Aragones, L.; Coelho, J. R.; Freitas, A. T.; Marchi, E.; Moce, L.; Visa, P.; Northwood, J. B.; Viti, C.; Borghi, E.; Orefici, G.; Morrissey, I.; Oggioni, M. R.; Consortium, B., Evaluation of Reduced Susceptibility to Quaternary Ammonium Compounds and Bisbiguanides in Clinical Isolates and Laboratory-Generated Mutants of Staphylococcus aureus. Antimicrob. Agents Chemother. **2013**, 57 (8), 3488-3497.

11. Singh, A.; Sharma, S.; Kaur, N.; Singh, N., Self-assembly of imidazolium/benzimidazolium cationic receptors: their environmental and biological applications. New J. Chem. **2020**, 44 (44), 19360-19375.

12. Kaurd, N.; Fischerb, M.; Kumard, S.; Gahlaya, G. K.; Scheidtb, H. A.; Mithuc, V. S., Interaction of POPG membranes with ionic liquids containing 1-Dodecyl-3-

methylbenzimidazolium and 1-Dodecyl-1-methylmorpholinium Cations: Structural details from 31P and 2H-based solid-state NMR spectroscopy. J. Magn. Reson. Open **2022**, 10-11, 100036.

13. Jiang, L. X.; Deng, M. L.; Wang, Y. L.; Liang, D. H.; Yan, Y.; Huang, J. B., Special Effect of beta-Cyclodextrin on the Aggregation Behaviour of Mixed Cationic/Anionic Surfactant Systems. J. Phys. Chem. B **2009**, 113 (21), 7498-7504.

14. Chen, L.; Meng, H.; Jiang, L.; Wang, S. T., Fatty-Acid-Metal-Ion Complexes as Multicolor Superhydrophobic Coating Materials. Chem. Asian J. **2011**, 6 (12), 1757-1760.

15. Cui, S. L.; Qiao, J.; Xiong, M. P., Antibacterial and Biofilm-Eradicating Activities of pH-Responsive Vesicles against Pseudomonas aeruginosa. Mol. Pharmaceutics **2022**, 19, 2406-2417.

16. Patel, A.; Dey, S.; Shokeen, K.; Karpinski, T. M.; Sivaprakasam, S.; Kumar, S.; Manna, D., Sulfonium-based liposome-encapsulated antibiotics deliver a synergistic antibacterial activity. RSC Med. Chem. **2021**, 12 (6), 1005-1015.

17. Patel, A.; Paul, S.; Akhtar, N.; Das, S.; Kar, S.; Bhattacharjee, S.; Manna, D., Onium- and Alkyl Amine-Decorated Protein Nanoparticles as Antimicrobial Agents and Carriers of Antibiotics to Promote Synergistic Antibacterial and Antibiofilm Activities. ACS Appl. Nano Mater. **2022**, 5 (11), 16602-16611.

18. Rusch, P.; Hirner, A. V.; Schmitz, O.; Kimmig, R.; Hoffmann, O.; Diel, M., Zinc distribution within breast cancer tissue of different intrinsic subtypes. Arch. Gynecol. Obstet. **2021**, 303 (1), 195-205.

19. Zaichick, V.; Sviridova, T. V.; Zaichick, S. V., Zinc in the human prostate gland: normal, hyperplastic and cancerous. Int. Urol. Nephrol. **1997**, 29 (5), 565-74.

20. Yang, J. E.; Huang, H. J.; Zhu, L.; Xie, H.; Gao, F., Effect of beta-cyclodextrin, alcohol and temperature on the aggregation transitions of cationic/cationic surfactant systems. Colloids Surf., A **2019**, 582, 123878.

21. Lou, J. C.; Schuster, J. A.; Barrera, F. N.; Best, M. D., ATP-Responsive Liposomes via Screening of Lipid Switches Designed to Undergo Conformational Changes upon Binding Phosphorylated Metabolites. J. Am. Chem. Soc. **2022**, 144 (8), 3746-3756.

22. Gotru, S. K.; van Geffen, J. P.; Nagy, M.; Mammadova-Bach, E.; Eilenberger, J.; Volz, J.; Manukjan, G.; Schulze, H.; Wagner, L.; Eber, S.; Schambeck, C.; Deppermann, C.; Brouns, S.; Nurden, P.; Greinacher, A.; Sachs, U.; Nieswandt, B.; Hermanns, H. M.; Heemskerk, J. W. M.; Braun, A., Defective $Zn^{2+}$ homeostasis in mouse and human platelets with alpha- and delta-storage pool diseases. Sci. Rep. **2019**, 9, 19866.

23. Blicharska, B.; Witek, M.; Fornal, M.; Mackay, A. L., Estimation of free copper ion concentrations in blood serum using $T_1$ relaxation rates. J. Magn. Reson. **2008**, 194 (1), 41-45.

24. Kim, Y. O.; Chung, H. J.; Kong, H. S.; Choi, D. W.; Cho, D. H., The application of ion chromatographic method for bioavailability and stability test of iron preparations. Arch. Pharmacal Res. **1999**, 22 (3), 288-293.

25. Bilezikian, J. P.; Raisz, L. G.; Martin, T. J., Eds. Principles of Bone Biology, 3rd ed.; Elsevier: San Diego, CA, **2008**.

26. Bilezikian, J. P.; Raisz, L. G.; Martin, T. J., Eds. Principles of Bone Biology, 4th ed.; Elsevier: San Diego, CA, **2020**.

27. Nordberg, G. F.; Fowler, B. A.; Nordberg, M., Eds. Handbook on the Toxicology of Metals, 4th ed.; Elsevier: Amsterdam, **2015**.

28. Zastrow, M. L.; Radford, R. J.; Chyan, W.; Anderson, C. T.; Zhang, D. Y.; Loas, A.; Tzounopoulos, T.; Lippard, S. J., Reaction-Based Probes for Imaging Mobile Zinc in Live Cells and Tissues. ACS Sens. **2016**, 1 (1), 32-39.

29. Linder, M. C.; Wooten, L.; Cerveza, P.; Cotton, S.; Shulze, R.; Lomeli, N., Copper transport. Am. J. Clin. Nutr. **1998**, 67 (5), 965s-971s.

30. Luck, A. N.; Mason, A. B. Transferrin-Mediated Cellular Iron Delivery. In Metal Transporters; Harris, J. R.; Marone, P., Eds.; Academic Press: Waltham, MA, **2012**; Vol. 69, pp 3-35.

# Chapter 3

# Supramolecular Nanochannels: Suprasome-Mediated Delivery of Ionophore to Regulate Transmembrane $Zn^{2+}$ Ion Transport

### 3.1 Background and Objective of the Present Work

The integration of supramolecular drug delivery systems with synthetic ion channels holds significant potential for advancements in ion transport-related studies. Suprasomes are innovative delivery vehicles that use dynamic host-guest interactions for controlled, stimulus-responsive release, enabling targeted delivery of therapeutics and minimising off-target effects.[1] On the other hand, synthetic ionophores that form supramolecular nanochannels within lipid bilayers show promise for the efficient transport of ions.[2-6] However, they encounter substantial challenges in deliverability due to their inherent hydrophobicity. The low water solubility of these ion transporters hinders their clinical application. At the same time, their high lipophilicity can lead to off-target interactions and aggregation, limiting effective delivery to the targeted site.[7, 8] Artificial transmembrane ion channels mimic the function of biological ion channels by facilitating selective ion transport across lipid bilayers. These synthetic systems offer powerful tools for studying ion transport mechanisms and hold potential for therapeutic applications, particularly in disrupting ionic homeostasis in cancer and bacterial cells. However, a majority of research on synthetic ion transporter-based therapeutics has focused on the transmembrane transport of monovalent ions such as $K^+$, $Na^+$, and $Cl^-$.[2-6, 9] The development of synthetic nanochannels that selectively transport biologically important divalent metal ions, such as $Zn^{2+}$, remains largely unexplored.[10]

The $Zn^{2+}$ ion offers unique therapeutic potential due to its ability to disrupt metal-dependent catalysis, compromising protein structural integrity and interfering with metabolic functions; the $Zn^{2+}$ ion proves particularly effective in inhibiting bacterial growth through protein dysfunction.[11] $Zn^{2+}$ also plays pivotal roles in cellular metabolism, enzymatic regulation, and immune responses, making its dysregulation a powerful strategy for combating pathogenic bacteria. However, the design of synthetic ion channels that can selectively transport $Zn^{2+}$ across lipid bilayers poses considerable challenges due to its coordination chemistry and the need for precise supramolecular channel architecture.

The integration of ionophores into supramolecular drug delivery platforms has been hardly investigated. To the best of our knowledge, no prior work has demonstrated the use of an ionophore as both the cargo and the functional agent within a stimuli-responsive suprasome. Addressing this dual challenge requires not only innovative ionophore design capable of integrating into membranes to form rare $Zn^{2+}$-selective nanochannels but also optimal host-

guest complexation that can be disassembled upon stimuli treatment, thereby releasing the channel forming ionophores to the lipid membrane when triggered. This approach demands a sophisticated balance between structural stability in the delivery phase and dynamic responsiveness when triggered by stimuli.

Inspired by natural ion channel-based antibacterial agents, such as colicin, we aimed to develop a synthetic $Zn^{2+}$ ion channel that disrupts metal ion homeostasis in bacteria, leading to their eradication. Additionally, we sought to address the long-standing challenge of delivering hydrophobic synthetic ionophores by developing suprasomes (Figure 3.1). We hypothesise that the conformationally restricted bis(vinylbenzimidazole)phenol scaffold can interact with the $Zn^{2+}$ ion and self-assemble within the hydrophobic bilayer to form supramolecular nanochannels.[12] In addition, the benzimidazole moiety may undergo dynamic host-guest

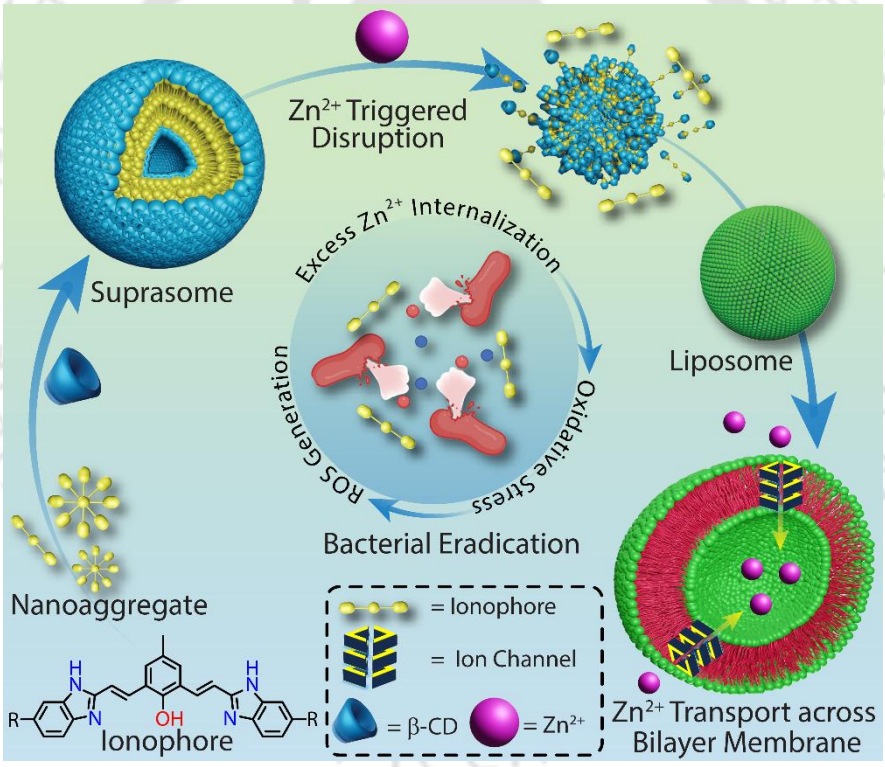


**Figure 3.1** Schematic representation of suprasomal assembly of the potent ion transporter with β-cyclodextrin (β-CD) through dynamic host-guest interactions and $Zn^{2+}$ ions mediated disassembly of suprasomes to release the ion transporter. Additionally, the diagram illustrates the ability of the released ion transporter to penetrate lipid bilayers, where it self-assembles into a supramolecular nanochannel, facilitating the selective and efficient transport of $Zn^{2+}$ ions across the lipid bilayers via an electrogenic pathway that leads to ROS-mediated bacterial cell death.

complexation with β-cyclodextrin (β-CD), facilitating suprasome formation.[13, 14] Therefore, we synthesised bis(benzimidazole)phenol and bis(vinylbenzimidazole)phenol derivatives to meet such a multidimensional goal. Systematic ion transport studies revealed compounds **3.4** and **3.6** as the most potent $Zn^{2+}$ ionophores, which create supramolecular channels within lipid bilayers to transport $Zn^{2+}$ ions. The real-time electrophysiological measurements confirmed the formation of supramolecular nanochannels of the potent compound within the lipid bilayers. Furthermore, suprasomes were formulated from compound **3.6** and β-CD, with $Zn^{2+}$ ions acting as the stimuli for disassembly. To the best of our knowledge, this could be the first attempt of a two-bird-with-one-stone approach to deliver a synthetic ionophore through suprasome, which, upon release, assembles into supramolecular nanochannels within the lipid bilayers. The delivered ionophore also exhibited excellent antibacterial activity against both Gram-negative and drug-resistant Gram-positive bacteria, resulting from the enhanced internalization of $Zn^{2+}$ ions and the subsequent generation of reactive oxygen species (ROS). This strategy of employing suprasome to deliver novel therapeutics, specifically ionophores, demonstrates the integration of multiple disciplines, leading to improved outcomes and the exploration of new research avenues.

## 3.2 Results and Discussion

### 3.2.1 Synthesis of Compounds

To develop potent transmembrane $Zn^{2+}$ ion transporters, we synthesised a series of bis(benzimidazole)phenols and bis(vinylbenzimidazole)phenols. First, 2-hydroxy-5-methylisophthalaldehyde was synthesised from p-cresol using the Duff reaction process. Then, oxidation of 2-hydroxy-5-methylisophthalaldehyde with silver oxide ($Ag_2O$) resulted in the formation of 2-hydroxy-5-methylisophthalic acid. The condensation of 2-hydroxy-5-methylisophthalic acid with substituted o-phenylenediamines provided the targeted derivatives (3.1 and 3.2) (Scheme 3.1). On the other hand, 2-hydroxy-5-methylisophthalaldehyde was

methylated with methyl iodide to produce 2-methoxy-5-methylisophthalaldehyde, and its phenylene)diacrylic acid. Further condensation reactions with various substituted o-phenylenediamines yielded the compounds 3.3 and **3.4**. Finally, the dealkylation of the methoxy group using boron tribromide ($BBr_3$) produced compounds 3.5 and **3.6** (Scheme 3.1). The field-emission scanning electron microscopic (FESEM) analysis of compound 3.6 (200 μM) in an organic solvent mixture (EtOAc/MeOH) after slow evaporation was performed to explore its self-assembly pattern in a hydrophobic environment, simulating a bilayer

membrane. The FESEM images revealed a nanorod-like arrangement, indicating the characteristic self-assembly pattern of compound **3.6** in the hydrophobic environment (Figure 3.5). However, the FESEM images of compound **3.6** (200 µM) prepared in an aqueous medium revealed the agglomerated structural arrangement (Figure 3.6).

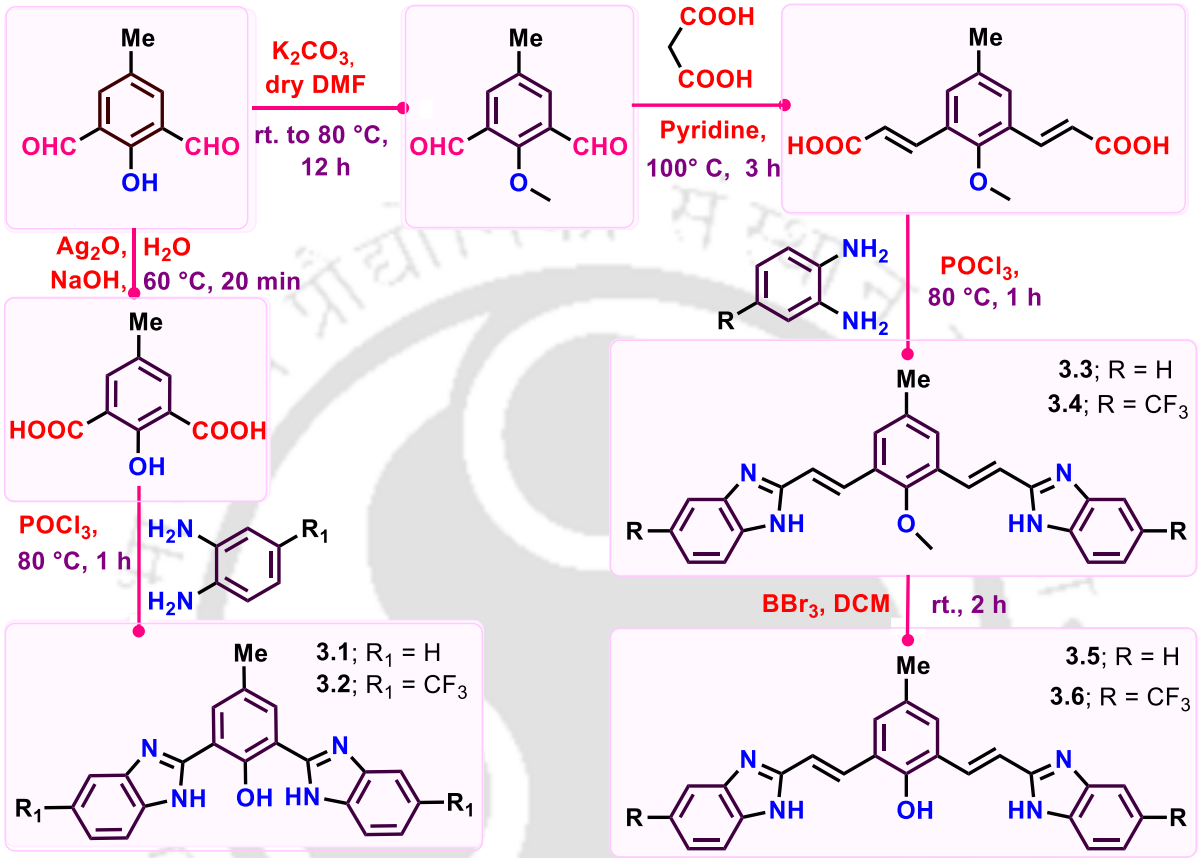


**Scheme 3.1** Synthetic routes for preparing bis(benzimidazole)phenols and bis(vinylbenzimidazole)phenols.

### 3.2.2 Ion Transport Studies

The impact of the synthesised compounds on transmembrane ion transport was initially examined by monitoring the fluorescence signal modulation of penta-potassium salt of magnesium green (MgG) in large unilamellar vesicles (LUVs) serving as model membranes.[15] The LUVs were prepared from egg-yolk phosphatidylcholine (EYPC) and cholesterol (CHOL) (8:2 molar ratios) by encapsulating MgG in 10 mM HEPES buffer containing 100 mM KCl and 100 µM EDTA at pH 7.0. The LUVs were dispersed in 10 mM HEPES buffer containing 100 mM potassium gluconate (KGlc) and 100 µM EDTA at pH 7.0 (Figure 3.2A). EDTA was used at a low concentration to minimise interference from transition metal ions. The vesicles were equilibrated with valinomycin and $Zn^{2+}$ ions; at 50 s, the compounds were introduced to

the stirring solution. Valinomycin (a transporter of K+ ions) was introduced to obtain electroneutrality. The presence of both valinomycin and the compound in the membrane resulted in enhanced fluorescence of MgG, indicating that the influx of $Zn^{2+}$ ions occurs only when there is a concurrent efflux of $K^+$ ions.

However, when valinomycin was not included, the $Zn^{2+}$ ion transport efficacy of the compounds was not observed, indicating the compound-mediated $Zn^{2+}$ ion transport follows an electrogenic mechanism.[16] To rule out other possible reasons for MgG fluorescence enhancement, control experiments were performed using combinations like valinomycin alone with a $Zn^{2+}$ ion pulse, which demonstrated no enhancement of MgG fluorescence (Figure 3.2B). The MgG assay indicated the transmembrane $Zn^{2+}$ ion transport ability of the synthesised compounds via the electrogenic pathway.

This MgG assay was used to screen all the synthesised compounds for their potential to transport $Zn^{2+}$ ions. The extent of enhancement of MgG fluorescence intensity indicated that compounds **3.4** and **3.6** have a higher ability to transport $Zn^{2+}$ ions than the other derivatives (Figure 3.2C and 3.7). The higher transport efficacy of these two potent compounds could be due to the interaction of lone pairs present in benzimidazole ($N\cdots Zn^{2+}$) and phenoxy ($O\cdots Zn^{2+}$) moieties and higher lipophilicity (log P 7.21 and 7.47 for compounds **3.4** and **3.6** respectively).[17] The MgG-based concentration-dependent transport studies revealed that the half-maximal activity ($EC_{50}$) values for compounds **3.4** and **3.6** were 347 ± 35 nM and 270 ± 18 nM, respectively (Figure 3.2D, 3.8A, and 3.9A). The calculated Hill coefficient (n) values for **3.4** and **3.6** were found to be 1.8 and 2.2, respectively, suggesting that more than one molecule (positive cooperativity) might facilitate the formation of supramolecular ion channels for the transport of $Zn^{2+}$ ions (Figures 3.8B and 3.9B). Due to the lower $EC_{50}$ value, further transmembrane transport studies were conducted using compound **3.6**. We also measured the critical aggregation constant (CAC) value of compound **3.6** from the concentration-dependent transport study. A distinct inflection point was observed at approximately 60 nM concentration of compound **3.6** (Figure 3.10). This result suggests the initiation of supramolecular nanochannels of compound **3.6** (> 60 nM) under liposomal conditions. The cation and anion selectivity transport of potent ionophores were also investigated. The variation of $M_nX_m$ salts (M = $Mn^{2+}$, $Fe^{3+}$, $Co^{2+}$, $Ni^{2+}$, $Cu^{2+}$, $Zn^{2+}$) in the extravesicular solution exhibited the highest transport activity for $Zn^{2+}$ ions compared to other metal ions (Figure 3.2E and 3.11). Due to the higher $Zn^{2+}$ ions transport activities of the compounds, further studies were carried out with

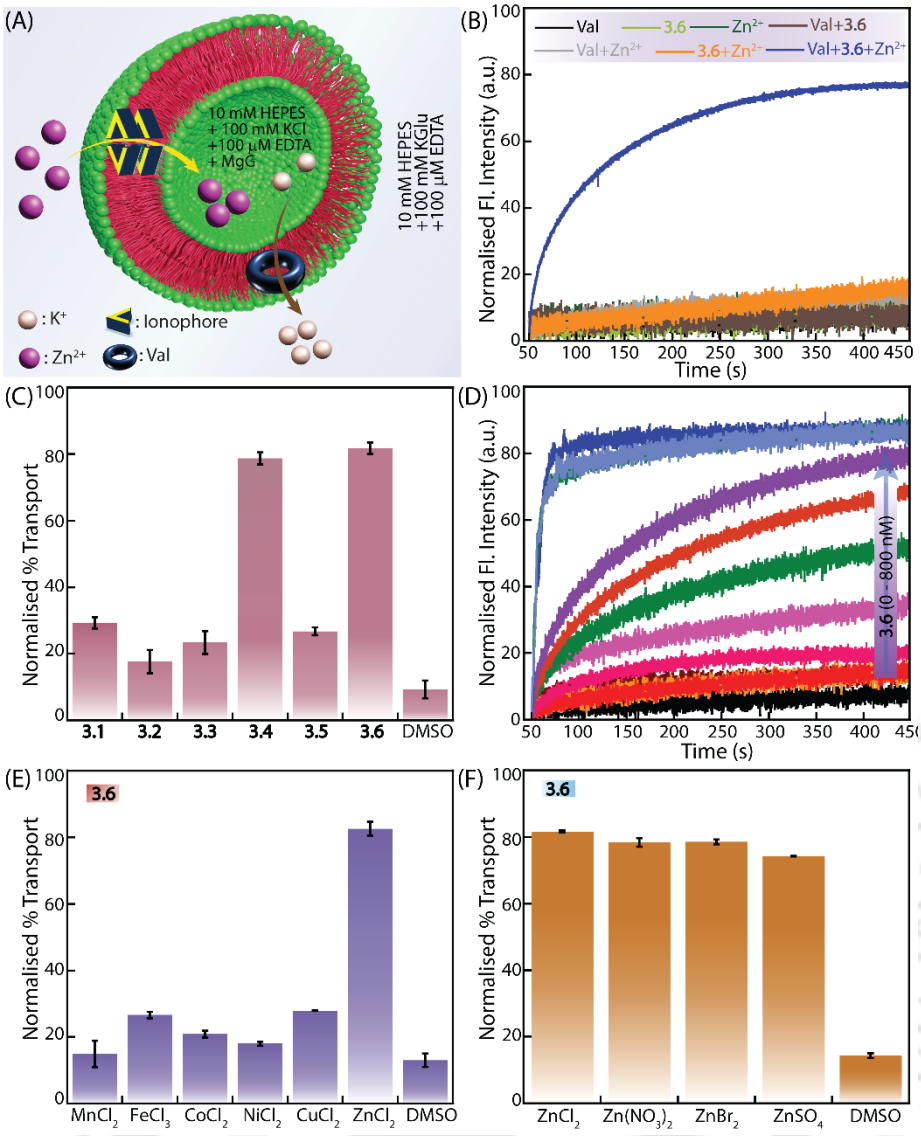


**Figure 3.2** (A) Schematic representation of ion transport studies of the compounds via an electrogenic pathway across EYPC/CHOL-LUV⊃MgG in the presence of valinomycin (Val; 12 pM). The intravesicular solution was 10 mM HEPES buffer containing 100 mM KCl and 100 μM EDTA at pH 7.0, and the extravesicular solution was 10 mM HEPES buffer containing 100 mM KGlc and 100 μM EDTA at pH 7.0. The LUVs were equilibrated with 1 mM $ZnCl_2$, and a pulse of compound **3.6** (500 nM) was added externally to initiate the transport studies. (B) Ion transport properties of compound **3.6** (500 nM) via electrogenic pathway across EYPC/CHOL-LUV⊃MgG. (C) Assessment of the $Zn^{2+}$ ion transport activity of the synthesised compounds (500 nM) across EYPC/CHOL-LUVs⊃MgG in the presence of valinomycin (Val; 12 pM). (D) Concentration-dependent transmembrane $Zn^{2+}$ ions transport

efficacy of compound **3.6** across EYPC/CHOL-LUVs⊃MgG. Comparison of (E) cation and (F) anion transport activity of compound **3.6** (500 nM) across the bilayers of EYPC/CHOL-LUV⊃MgG.

various $Zn^{2+}$ salts. The variation of $Z_nX_m$ salts (X = $Cl^-$, $Br^-$, $NO_3^-$, $SO_4^{2-}$) in the extravesicular solution resulted in similar transport efficiency, ruling out the possibility of the anion affecting the transport (Figure 3.2F and 3.12). These experiments confirmed the $Zn^{2+}$ ion transport ability of compound **3.6**. The carboxyfluorescein assay revealed no membrane leakage under the experimental conditions after treatment with potent compounds at concentrations up to 30 μM (Figure 3.14). Meanwhile, UV-Vis-based titration of compound **3.6** (10 μM) with $Zn^{2+}$ ions (10-700 μM) in an aqueous solution revealed its binding affinity of $6.5 \times 10^4\ M^{-1}$ (Figure 3.15). The spectral analysis showed that the interaction of compound **3.6** with the $Zn^{2+}$ ions preferably follows 1:1 binding stoichiometry. The phenolic oxygen and nitrogen atoms of the benzimidazole moieties of compound **3.6** could be involved in binding with the $Zn^{2+}$ ion. Furthermore, we performed $Zn^{2+}$ ion transport-mediated ester hydrolysis of nonfluorescent reporter, acyl-8-hydroxy-1,3,6-pyrenetrisulfonic acid (AHPTS), to fluorescent HPTS within the vesicles in the presence of (1E,1'E)-6-((E)-(hydroxyimino)methyl)picolinaldehyde oxime (HMPO) (Figure 3.16).[18] The EYPC/CHOL-LUV⊃AHPTS/HMPO were prepared in 20 mM HEPES buffer containing 100 mM KCl at pH 7.0 and dispersed in 20 mM HEPES buffer containing 100 mM KGlc at pH 7.0. With the addition of compound **3.6** and $Zn^{2+}$ ions into the extravesicular solution, rapid generation of HPTS was observed. This could be due to the transmembrane transport of $Zn^{2+}$ ions into the lumen of vesicles and the in-situ generation of HMPO-$Zn^{2+}$ complex, leading to the hydrolysis of nonfluorescent AHPTS into fluorescent HPTS inside the vesicles. Therefore, this HMPO-$Zn^{2+}$ complex-mediated catalysis confirmed the influx of $Zn^{2+}$ ions in the presence of compound **3.6**.

### 3.2.3 Determination of Transporter Pathway

A temperature-dependent ion transport assay was performed using LUVs composed of dipalmitoylphosphatidylcholine (DPPC) lipids to investigate the nature of the ion transport pathway, whether carrier or channel. As the temperature increases, membrane fluidity is enhanced, improving the efficacy of ion transport through carrier pathways, while the efficacy of supramolecular ion channels remains relatively unchanged.[19] The temperature-dependent ion transport assay in the presence of compound **3.6** showed no significant difference in $Zn^{2+}$ ion transport efficacy at 30 °C compared to 45 °C (Figure 3.17), indicating a potential formation

of ion channels. The classical U-tube-based ion transport measurements of compound **3.6** showed no significant increase in $Zn^{2+}$ concentration in the receiver arm, indicating compound **3.6** could not act as a carrier through an apolar phase ($CHCl_3$). Meanwhile, the control U-tube-based transport study with clioquinol (CQ, a $Zn^{2+}$ ion carrier) showed an increase in $Zn^{2+}$ ion concentration over time in the receiver arm (Figure 3.18). Therefore, DPPC-based and U-tube-based ion transport studies indicate that compound **3.6** forms channels in the hydrophobic environment.

Real-time measurements of current across a bilayer lipid membrane (BLM) composed of diphytanoyl phosphatidylcholine (diPhyPC) can be performed to gain a deeper understanding of the channel-forming capabilities of compound **3.6**. The planer lipid bilayer was prepared over the orifice in the Teflon foil connecting two electrolyte chambers containing $ZnCl_2$ (0.5 M) solution. Upon adding compound **3.6** (4 μM), we observed rapid flickering events at different holding potentials, confirming the formation of an ion channel within the planar lipid bilayer by compound **3.6** (Figure 3.3A, 3.19). In a symmetrical solution of 0.5 M $ZnCl_2$, we measured a single-channel conductance (G) of 51 ± 9 pS, corresponding to a simple pore model with a pore diameter (d) of 1.4 Å. The change in current with voltage (I–V plot) was further monitored with a symmetrical 0.5 M $ZnCl_2$ solution. When examining the variation of current with voltage (I–V plot) in the presence of a symmetric A solution of $ZnCl_2$ (0.5 M in both chambers) was used, and we observed a linear variation, indicating ohmic behaviour and confirming the non-dipole nature of the channel (Figure 3.20).

### 3.2.4 MD Simulation Study for Transporter

We first optimized the structure using density functional theory-level quantum mechanical calculations to understand the mechanistic details of $Zn^{2+}$ ion permeation through the supramolecular channel formed by compound **3.6**. Then, we built a proposed model of the channel, embedded in a membrane, with two molecules in each layer where the hydroxyl groups of each molecule face the channel pore (Figure 3.3B). We then performed steered molecular dynamics simulation to investigate the permeation mechanism of zinc ion. We observed that $Zn^{2+}$ ions can permeate the lipid bilayer by partially losing their water interaction in the bulk environment and forming interaction with the channel atoms, especially with the oxygen atoms (Figure 3.3C).

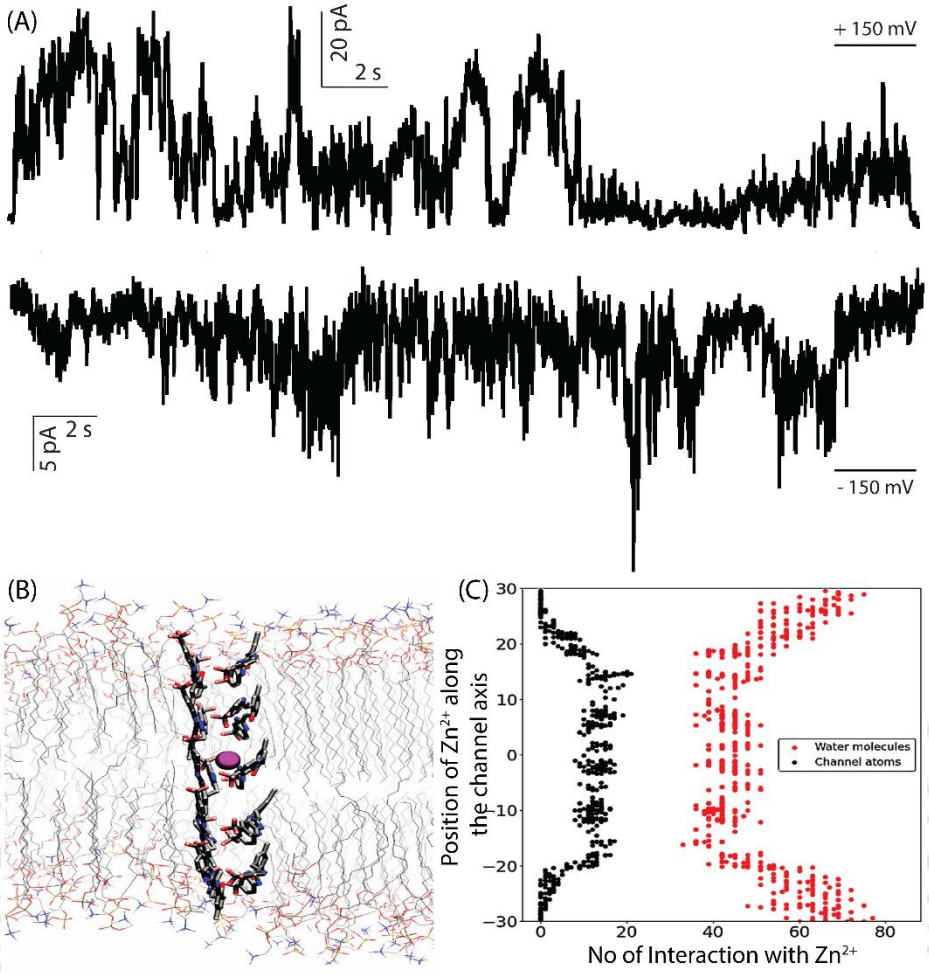


**Figure 3.3** (A) Ion conductance of compound **3.6** (4 μM) at +150 mV and −150 mV in symmetrical $ZnCl_2$ solution (0.5 M). Note the upward spikes at +150 mV and the downward spikes at -150 mV are of ms-long openings of one or several channels. (B) The permeation mechanism of $Zn^{2+}$ ions is through a model channel formed by the assembly of our molecule. Membrane view of the channel. (C) Zoomed view of a $Zn^{2+}$ ion interacting with the channel atoms. Number of interactions of a $Zn^{2+}$ ion with water molecules and channel atoms during permeation. Interactions are calculated with a 5 Å distance cut-off.

### 3.2.5 Formation and Disruption of Suprasome

The inherent hydrophobicity of ionophores often leads to poor pharmacokinetics and bioavailability. Therefore, to improve the biological applicability of these synthetic ionophores, we developed a suprasome-based delivery system for ionophores. The benzimidazoles are known to be involved in host-guest interactions with β-CD.20,21 Therefore, the benzimidazole moiety of compound 3.6 may be involved in host-guest interactions with β-CD. The isothermal titration calorimetry (ITC) measurements showed a

significant binding of compound **3.6** with β-CD, with a dissociation constant ($K_{d1}$) of 2.35 μM (Figure 3.4A). UV-Vis spectroscopic studies revealed a substantial increase in the absorbance peak of compound 3.6 at 260 nm upon addition of β-CD, indicating the encapsulation of benzimidazole within the β-CD cavity (Figure 3.21). Therefore, ITC and UV-Vis measurements confirmed the interaction of compound **3.6** with β-CD. Dynamic Light Scattering (DLS) measurements revealed that increasing the β-CD concentration resulted in an increase in hydrodynamic diameters (Dh), which could be attributed to host-guest interactions between the benzimidazole moiety of the ionophore and β-CD (Figures 3.4B, 3.22, and 3.33). The FESEM images revealed smaller nanoaggregates (Dh ~95 nm) with compound 3.6 alone (Figure 3.22), whereas larger spherical suprasomes formed after β-CD addition (Figure 3.4C), consistent with the DLS data. Additional DLS measurements revealed the stability of the suprasome over a longer period of 7 days (Figures 3.24 and 3.25). Hence, these biophysical studies indicate the formation of suprasomes of compound **3.6** in the presence of β-CD, which can be applied to deliver compound **3.6** to cellular systems.

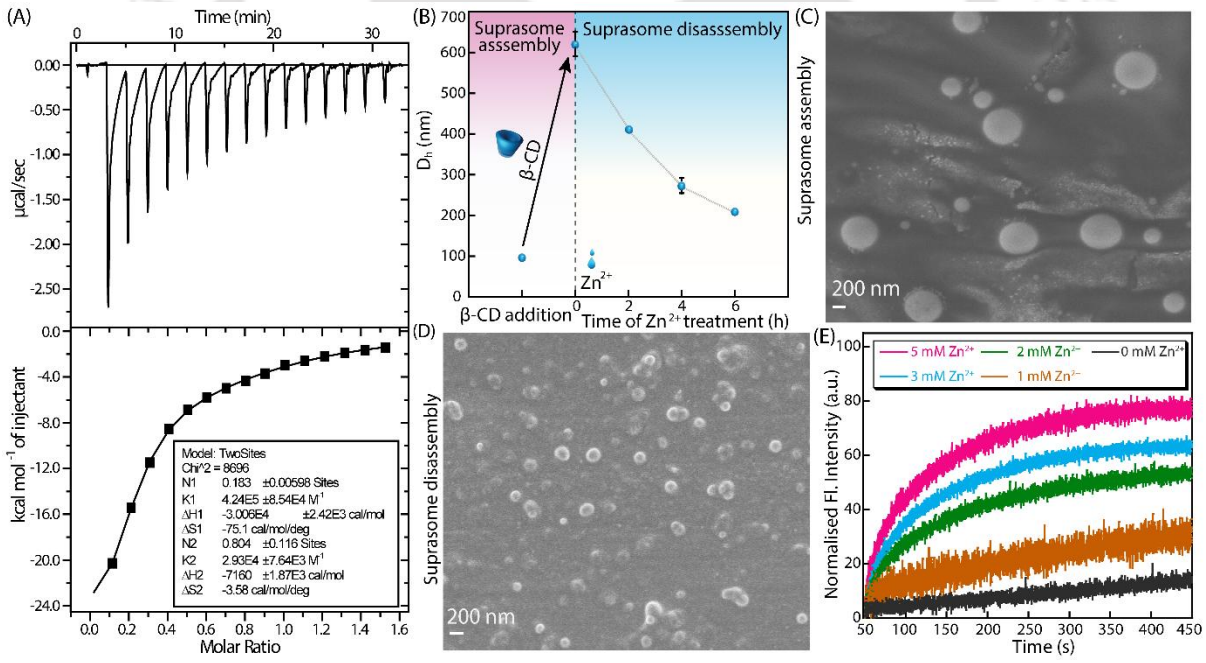


**Figure 3.4** (A) ITC measurement of compound **3.6** (150 μM) with different concentrations of β-CD. Representative ITC thermograph and analysis of the ITC titration curve with the appropriate binding model. The inset shows the thermodynamic parameter obtained from the ITC measurement. (B) Variation of hydrodynamic diameter ($D_H$) of compound **3.6** (200 μM) after the addition of β-CD (7 mM) and that of suprasomes in the presence of $Zn^{2+}$ ions (400 μM) at different time intervals. (C) Representative FESEM images of suprasomes of compound

**3.6** (200 μM) and β-CD (7 mM). (D) Representative FESEM images of aggregates after 6 h treatment of suprasomes with $Zn^{2+}$ ions (400 μM). (E) Transmembrane ion transport activity of disrupted suprasome at different $Zn^{2+}$ ion concentrations across EYPC/CHOL-LUV⊃MgG.

For the suprasome disruption study, $Zn^{2+}$ ion was selected as the stimulus, as its binding ability can induce slow decomplexation of the ionophore-β-CD complex, leading to the disassembly of the suprasome. The $Zn^{2+}$-mediated disassembly of the suprasome was investigated using a polarity-sensitive fluorescent dye, Nile Red (NR). Upon treatment with $Zn^{2+}$ ion, the fluorescence of NR dye was quenched, indicating the release of NR dye into the aqueous environment and disassembly of suprasomes (Figure 3.26).[22, 23] The effect of $Zn^{2+}$ ion on suprasomes was also monitored using DLS measurement. Upon $Zn^{2+}$ ion treatment, the size of the suprasomes initially decreased from ~620 nm to ~207 nm, which could be due to suprasome disruption, releasing the guest molecule and resulting in the rearrangement of the remaining host-guest complexes into smaller structures (Figure 3.4B). The FESEM-based morphological analysis of the suprasomes of compound **3.6** in the presence of $Zn^{2+}$ revealed the formation of rectangular morphology (Figure 3.4D). To validate the hypothesis that these rectangular structures originated from the interaction between compound **3.6** and $Zn^{2+}$ ion, a separate self-assembly study was conducted using compound **3.6** in the presence of $Zn^{2+}$ ion in aqueous media. Similar rectangular structures were observed, further substantiating the hypothesis (Figure 3.26). Therefore, the $Zn^{2+}$ ions serve as a stimulus to disrupt the suprasomes, leading to the release of compound 3.6 into the aqueous medium. To examine the relationship between $Zn^{2+}$ concentration and suprasome disassembly, suprasomes were treated with 100 μM and 400 μM $Zn^{2+}$ ions while stirred continuously, and fluorescence measurements were recorded over 6 hours. The results showed that 400 μM $Zn^{2+}$ enabled about 64% cargo release, compared to 20% with 100 μM $Zn^{2+}$ (Figure 3.27). This indicates that 400 μM $Zn^{2+}$ effectively disrupt suprasomes and releases cargo, whereas 100 μM $Zn^{2+}$ can induce disassembly but takes a longer time, which is beneficial for the controlled delivery of compound **3.6** using suprasomes. To investigate whether the $Zn^{2+}$ ion-mediated disruption of suprasome results in the partitioning of the ionophore into the lipid bilayers of the vesicles, we conducted MgG-based $Zn^{2+}$ ion transport studies. Various concentrations of $Zn^{2+}$ ions were added to a solution of suprasome (composed of compound **3.6** and β-CD) and EYPC/CHOL-LUV⊃MgG. The enhancement of time-dependent MgG fluorescence intensity with increased $Zn^{2+}$ ion concentration in the extravesicular solution indicates ion transport activity. This observation

suggests that the $Zn^{2+}$ ion-mediated release of compound **3.6** from suprasomes and its subsequent partitioning into the lipid bilayer of the vesicles (Figure 3.4E). Additionally, the stability of suprasomes in the presence of various cations was evaluated using DLS measurements. Only $Zn^{2+}$ and $Cu^{2+}$ ions caused a significant decrease in particle size after 6 hours of treatment, suggesting that these cations induce suprasome disruption and slow release of ionophore to aqueous solution (Figure 3.28).

### 3.2.6 Antibacterial Studies

Metal ions, such as $Fe^{3+}$, $Cu^{2+}$, and $Zn^{2+}$, are essential for bacterial survival and play a crucial role in maintaining cellular processes. However, an imbalance in these metal ions could be detrimental to bacteria, presenting a unique opportunity to target this vulnerability of ionic imbalance across the membranes for therapeutic purposes.[19, 24] We hypothesised that the potent synthetic zinc transporters could disrupt bacterial ion homeostasis by inducing cytosolic $Zn^{2+}$ ion concentration, leading to oxidative stress and subsequent bacterial death. Therefore, the antibacterial activities of the potent ionophores were investigated across various bacterial strains, including Gram-positive bacteria (*Staphylococcus aureus* (*S. aureus*) and *methicillin-resistant S. aureus* (MRSA)) and Gram-negative bacterial strains (*Escherichia coli* (*E. coli*) and *Pseudomonas aeruginosa* (*P. aeruginosa*)), in the presence and absence of 400 μM $Zn^{2+}$ ion. The selected $Zn^{2+}$ ion concentration was based on physiological levels found in specific tissues.[19] However, it remains well below the minimum inhibitory concentration (MIC) of $Zn^{2+}$ ion for *S. aureus* (~1.56 mM), reflecting conditions under pathological states.[19] The compounds **3.4** and **3.6** showed a strong antibacterial activity against *S. aureus*, with MIC values of 20 nM and 50 nM, respectively, in the presence of $Zn^{2+}$ ion. Their efficacy against the drug-resistant strain MRSA was also notable, with MIC values of 80 nM and 150 nM. In contrast, the compounds exhibited poor antibacterial activity against E. coli and P. aeruginosa (Table 3.1), which may be attributed to the two-layer cell envelope structure of Gram-negative bacteria. The MIC values of the suprasomes of compound **3.6** in the presence of $Zn^{2+}$ ions against *S. aureus* and MRSA were around 300 nM and 600 nM, respectively, which is slightly higher than that of only compound **3.6** in the presence of $Zn^{2+}$ ions. This difference in MIC values could be due to partial disassembly of the suprasome under experimental conditions. Interestingly, there was a significant improvement in the antibacterial activity of suprasomes containing compound **3.6** compared to just compound **3.6** when tested against Gram-negative bacteria. This indicates that the presence of β-CD in suprasomes could facilitate the penetration

of compound **3.6** through the outer membrane barrier and improve the transport of $Zn^{2+}$ ion across the membranes of Gram-negative bacteria.[24]

To confirm compound **3.6**-mediated $Zn^{2+}$ ion transport across the bacterial membrane, we conducted the AQZ dye-based internalization assay.[19] Bacteria were first treated with AQZ dye and then with compounds **3.4** and **3.6**, both in the presence and absence of $Zn^{2+}$ ion, alongside controls of untreated bacteria and those treated with only $Zn^{2+}$ ion. The AQZ dye-treated bacteria showed a significant fluorescence enhancement in the presence of compound **3.6** and

**Table 3.1** MIC values of compounds against various bacterial strains.

| MIC values (μM) | | | | |
|---|---|---|---|---|
| Additives | *S. aureus* | MRSA | *E. coli* | *P. aeruginosa* |
| Compound **3.4** | >100 | >100 | >100 | >100 |
| Compound **3.4** + $Zn^{2+}$ (400 μM) | 0.02 ± 0.01 | 0.08 ± 0.01 | >100 | >100 |
| Compound **3.6** | >100 | >100 | >100 | >100 |
| Compound **3.6** + $Zn^{2+}$ (400 μM) | 0.05 ± 0.01 | 0.15 ± 0.02 | 25 ± 5 | 25 ± 5 |
| Compound **3.6** + $Zn^{2+}$ (100 μM) | 0.15 ± 0.01 | - | - | - |
| Suprasome (compound **3.6**) | >100 | >100 | >100 | >100 |
| Suprasome (compound **3.6**) + $Zn^{2+}$ (400 μM) | 0.31 ± 0.12 | 0.63 ± 0.12 | 3.12 ± 1.2 | 6.25 ± 1.2 |
| $Zn^{2+}$ | 1560 ± 390 | 1560 ± 140 | 2000 ± 250 | - |
| Tetracycline | 3.41 ± 0.80 | - | 3.77 ± 0.9 | - |

$Zn^{2+}$ ion. In contrast, untreated bacteria and those treated with either the $Zn^{2+}$ ion or the compounds alone exhibited no significant fluorescence (Figure 3.29A). However, a slight increase in AQZ fluorescence was noted in the presence of compound **3.4**, which could be due

to its inherent fluorescence emission spectral overlapping with the excitation wavelength of AQZ dye. These results demonstrate the effective transport of $Zn^{2+}$ ion across the bacterial membrane by compounds **3.4** and **3.6**. Fluorescence microscopic imaging of the bacterial cells further corroborated these findings, demonstrating fluorescence signals from the bacterial cells treated with the compounds and $Zn^{2+}$ ion, whereas control samples showed no fluorescence (Figure 3.30).

To investigate whether excess $Zn^{2+}$ ion transport generates reactive oxygen species (ROS) in bacteria, we conducted the DCF-DA dye-based assay. ROS production was observed only when bacteria were treated with the compounds in combination with $Zn^{2+}$ ion (Figure 3.29B). The fluorescence microscopic images also indicated the ROS production in the presence of compound and $Zn^{2+}$ ions (Figure 3.31). Notably, the compounds do not inherently generate ROS, indicating that the observed ROS generation results from oxidative stress due to excess $Zn^{2+}$ ions inside the bacterial cells. The propidium iodide (PI) uptake assay suggests that membrane disruption is not the primary mechanism of action of the compounds, as the treated samples showed minimal PI uptake, comparable to that of the control buffer (Figure 3.32A). Membrane depolarization assays also indicated negligible effects on membrane polarization (Figure 3.32B). These results suggest that the antibacterial activities of compounds **3.4** and **3.6** in combination with $Zn^{2+}$ ion could be driven by intracellular ROS generation pathways rather than direct membrane disruption. Furthermore, the hemolytic activity of the compounds was assessed using human erythrocytes, revealing negligible toxicity even at concentrations as high as 100 μM (Figure 3.33). This indicates that the compounds are well-tolerated by human blood cells, suggesting their potential for therapeutic applications. To assess the effects of compounds **3.4** and **3.6** combined with $Zn^{2+}$ ion on *S. aureus* morphology, we treated bacterial cells and analyzed morphological changes using FESEM. Control samples displayed intact, smooth cell surfaces, while treated *S. aureus* cells exhibited significant structural alterations indicative of cellular collapse, including a crumpled and deformed appearance (Figure 3.34). This visual evidence highlights the bactericidal action of compounds **3.4** and **3.6** when used in conjunction with the $Zn^{2+}$ ion.

Our findings highlight the development of small molecule-based supramolecular nanochannels that could selectively transport $Zn^{2+}$ ions via the electrogenic pathway. By facilitating $Zn^{2+}$ ion internalization, these transporters create a cytosolic metal ion imbalance and induce oxidative stress, supported by increased fluorescence in AQZ dye assays and ROS generation in DCF-DA assays. The remarkable antibacterial activity of compounds **3.4** and **3.6**, observed at

nanomolar concentrations with $Zn^{2+}$ ion, underscores their effectiveness. These results validate the functionality of these transporters and pave the way for further research on metal ion transporters as therapeutic agents against bacterial infections.

### 3.3 Summary

This study demonstrates the potential of ionophores that self-assemble within lipid bilayers to form supramolecular nanochannels. Their ability to generate suprasomes allows for effective delivery to target sites, highlighting new opportunities for targeted drug delivery and medical applications. A series of bis(benzimidazole)phenols and bis(vinylbenzimidazole)phenols were synthesised from *p*-cresol via a multi-step synthesis process. Comprehensive fluorescence-based ion transport studies identified a $K^+$-dependent $Zn^{2+}$ ion transport mechanism as the primary mode of action for the potent bis(vinylbenzimidazole)phenol derivative **3.6**. The real-time electrophysiological measurements across bilayer lipid membrane confirmed the formation of supramolecular nanochannels by the potent ionophore with single channel conductance of 51 pS, corresponding to a simple pore model with a pore diameter of 1.4 Å across a symmetrical $ZnCl_2$ solution. The ITC and UV-Vis-based titration studies demonstrated that the dynamic host-guest complexation of the potent ionophore with β-CD leads to the formation of a suprasome-based ionophore delivery system, which disassembles in response to the $Zn^{2+}$ ion. This stimuli-responsive release of ionophore **3.6** from the suprasomes in an aqueous medium allows it to penetrate the lipid bilayers of vesicles, where it self-assembles to form supramolecular nanochannels that facilitate selective $Zn^{2+}$ ion transport into the cell. This approach also demonstrated excellent antibacterial activity of the potent ionophore against different bacterial strains in the presence of $Zn^{2+}$ ions. The antibacterial mechanistic studies revealed that disrupting $Zn^{2+}$ ion homeostasis within the bacterial cells leads to oxidative stress and subsequent ROS-mediated bacterial cell death. The suprasome provides a controlled assembly-disassembly mechanism, ensuring precise release of the ionophore at the target site, thereby enhancing therapeutic efficacy. This unique strategy not only exploited the vulnerability of bacteria to $Zn^{2+}$ ion overload but also resolved the longstanding challenge of delivering synthetic ionophores effectively. Overall, this study presents a multidisciplinary approach to developing an ionophore-based supramolecular ion channel, delivering the ionophore through the assembly and stimuli-responsive disassembly of suprasomes, and eradicating bacteria through transmembrane $Zn^{2+}$ transport. Furthermore, this strategy can potentially be expanded for the treatment of other metal ion-related diseases or disorders by tailoring the selectivity of the ion channel.

### 3.4 Experimental Section

#### 3.4.1 General Information

As mentioned in the previous chapter.

#### 3.4.2 Synthesis and Characterisation of Compounds

##### 3.4.2.1 Synthesis of 2-hydroxy-5-methylisophthalaldehyde

To the stirring solutions of *p*-cresol (1 gm, 9.25 mmol, 1.0 equiv.) in 2.5 mL Trifluoroacetic Acid (TFA), Hexamethylenetetramine (HMTA) (2.60 gm, 18.57 mmol, 2.0 equiv.)

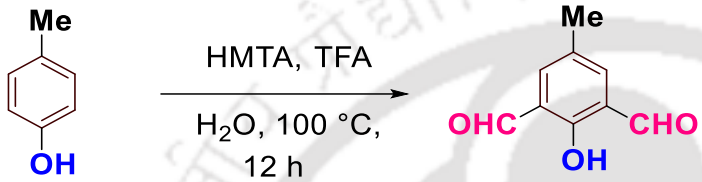


**Scheme 3.2** Synthesis of 2-hydroxy-5-methylisophthalaldehyde.

was added. The reaction mixture was refluxed at 100 °C for 12 hours. Then water (3 mL) was added and heated at 100 °C for 15 min. The reaction mixture was brought to room temperature and added to ice-cold water, yielding a yellow precipitate. The yellow precipitate was filtered through a Buchner funnel and then dried, yielding 95%.[25] The compound was characterized by $^{1}$H NMR, $^{13}$C NMR, and HRMS (ESI) analysis. **$^{1}$H NMR** (600 MHz, Chloroform-d) $\delta$: 11.48 (s, 1H), 10.23 (s, 2H), 7.79 (s, 2H), 2.41 (s, 3H). **$^{13}$C NMR** (151 MHz, Chloroform-*d*) $\delta$: 192.42, 161.80, 138.05, 129.55, 122.90, 20.13. **HRMS** (ESI) m/z: calculated for $C_9H_8O_3$ $[M+H]^+$ : 165.0546, found 165.0542.

##### 3.4.2.2 Synthesis of 2-methoxy-5-methylisophthalaldehyde

To the stirring solutions of 2-hydroxy-5-methylisophthalaldehyde (100 mg**,** 0.61 mmol, 1.0 equiv.) and potassium carbonate (400 mg, 2.9 mmol, 1.0 equiv.) in dry DMF (5 mL), methyl iodide (300 µl) was added dropwise. The reaction mixture was allowed to stir at room temperature for 20 min and then

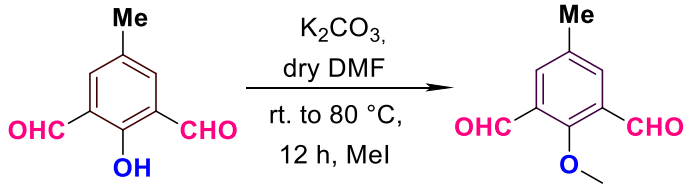


**Scheme 3.3** Synthesis of 2-methoxy-5-methylisophthalaldehyde.

heated at 60 °C overnight. The progress of the reaction was monitored through TLC. After cooling down the reaction mixture, the product was extracted with EtOAc (25 × 3 mL) and dried over $MgSO_4$. Thereafter, the organic solvent was evaporated under reduced pressure, followed by purification with column chromatography using EtOAc: Hexane (1: 5), resulting in a yield of 95%.[26] The compound was characterized by $^1$H NMR, $^{13}$C NMR, and HRMS (ESI) analysis. **$^1$H NMR** (600 MHz, Chloroform-*d*) *δ*: 10.42 (s, 2H), 7.94 (s, 2H), 4.07 (s, 3H), 2.44 (s, 3H). **$^{13}$C NMR** (151 MHz, Chloroform-*d*) *δ*: 188.69, 16**3.6**7, 135.4, 135.04, 129.68, 66.84, 20.60. **HRMS** (ESI) m/z: calculated for $C_{10}H_{10}O_3$ $[M+H]^+$ : 179.0703, found 179.0702.

### 3.4.2.3 Synthesis of 2-hydroxy-5-methylisophthalic acid

To the stirring solutions of 2-hydroxy-5-methylisophthalaldehyde (100 mg, 0.66 mmol, 1 equiv.) and NaOH (267 mg, 6.67 mmol, 10 equiv.) in 2.5 mL of water, $Ag_2O$ (309 mg, 1.32 mmol, 2 equiv.) was added. The reaction mixture was allowed to stir at 60 °C for 20 min. The progress of the reaction was monitored by TLC. After the completion reaction, it was cooled down. The pH of the reaction mixture was adjusted to 1.0 using HCl (1M). The products were extracted using EtOAc (10 × 2 mL). The organic layer was dried over $MgSO_4$ and evaporated under reduced pressure. The crude product was purified with column chromatography using EtOAc: Hexane (1:10), resulting in a yield of 80%.[27] The compound was characterized by $^1$H NMR, $^{13}$C NMR, and HRMS (ESI) analysis. **$^1$H NMR** (600 MHz, DMSO-*d*$_6$) *δ*: 7.75 (s, 2H), 2.24 (s, 3H).**$^{13}$C NMR** (151 MHz, DMSO-*d*$_6$) *δ*: 169.62, 136.27, 126.78, 126.73 117.32, 20.12. **HRMS** (ESI) m/z: calculated for $C_9H_8O_5$ $(M - H)^-$: 195.0299, found: 195.0310.

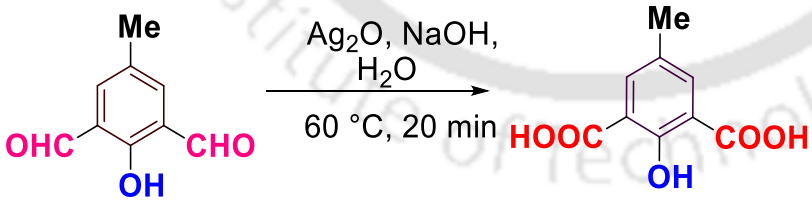


**Scheme 3.4** Synthesis of 2-hydroxy-5-methylisophthalic acid.

### 3.4.2.4 Synthesis of 3,3'-(2-methoxy-5-methyl-1,3-phenylene) diacrylic acid

To the stirring solutions of 2-methoxy-5-methylisophthalaldehyde (100 mg, 0.56 mmol, 1 equiv.) in pyridine (1 mL), malonic acid (116 mg, 1.12 mmol, 2 equiv.) was added. The reaction mixture was allowed to stir at 50 °C for 3 hours, and then the temperature was increased to

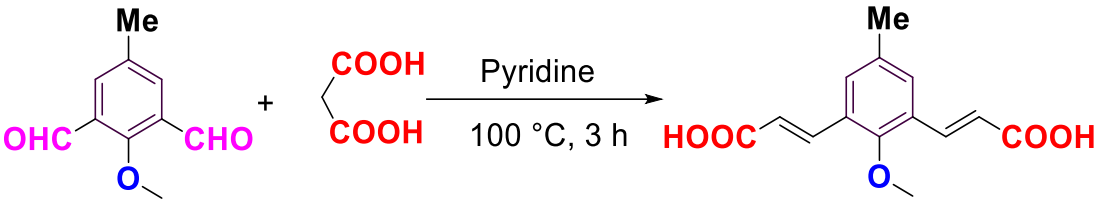


**Scheme 3.5** Synthesis of 3,3'-(2-methoxy-5-methyl-1,3-phenylene)diacrylic acid.

100 °C for 3 hours. The progress of the reaction was monitored through TLC. After the reaction mixture was cooled down, pH was adjusted to 1.0 by adding $H_2SO_4$ (1M), resulting in a white precipitate. Thereafter, a white precipitate was filtered using a Buchner funnel and dried, yielding 70%.[28] The compound was characterized by $^1$H NMR, $^{13}$C NMR, and HRMS (ESI) analysis. **$^1$H NMR** (600 MHz, DMSO-$d_6$) $\delta$: 12.53 (s, 2H), 7.73 (d, $J$ = 16.1 Hz, 2H), 7.70 (s, 2H), 6.58 (d, $J$ = 16.1 Hz, 2H), **3.6**8 (s, 3H), 2.31 (s, 3H). **$^{13}$C NMR** (151 MHz, DMSO-$d_6$) $\delta$: 168.06, 155.95, 137.83, 134.73, 130.68, 128.16, 121.36, 63.56, 20.72. **HRMS** (ESI) m/z: calculated for $C_{14}H_{14}O_5$ $(M + H)^+$ : 263.0914, found: 263.0914.

### 3.4.2.5 General Procedure for the Synthesis of Benzimidazole Derivatives

To the stirring solutions of substituted o-phenylenediamine (1 equiv.) in 1 mL of $POCl_3$, 2-hydroxy-5-methylisophthalic acid or (2E,2'E)-3,3'-(2-methoxy-5-methyl-1,3-phenylene) diacrylic was added. The reaction mixture was allowed to stir at 80 $^0$C for 1 hour. The progress of the reaction was monitored by TLC. After completion of the reaction, it was cooled down and added to ice water. Further, the pH was adjusted to 7 by adding NaOH (1M). The products were extracted using EtOAc (10 × 3 mL), and the organic layer was dried over $MgSO_4$. After that, the organic solvent was evaporated under reduced pressure, followed by purification of the crude product with column chromatography using EtOAc: Hexane, resulting in a 70-75% yield.[29]

#### 3.4.2.5.1 Synthesis of 2,6-bis(1*H*-benzo[d]imidazol-2-yl)-4-methylphenol

The 2,6-bis(1*H*-benzo[d]imidazol-2-yl)-4-methylphenol **(3.1)** was synthesised according to the procedure as mentioned previously in the general procedure section (3.4.2.5), using o-phenylenediamine (100 mg, 0.92 mmol, 2 equiv.) and 2-hydroxy-5-methylisophthalic acid

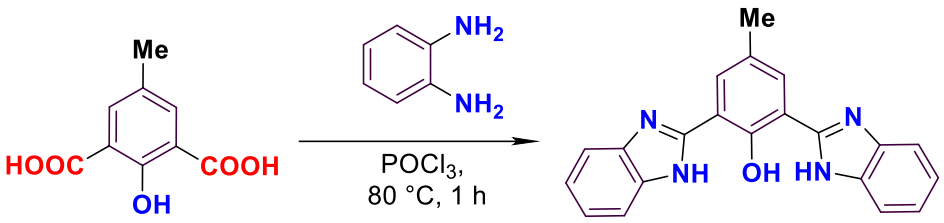


**Scheme 3.6** Synthesis of 2,6-bis(1*H*-benzo[d]imidazol-2-yl)-4-methylphenol (**3.1**).

(362 mg, 1 equiv.). The resulting compound **3.1** was obtained with a 74% yield. The compound was characterized by $^{1}$H NMR, $^{13}$C NMR, and HRMS (ESI) analysis. **$^{1}$H NMR** (400 MHz, DMSO-$d_6$) δ: 14.75 (s, 1H), 13.08 (s, 2H), 8.11 (s, 2H), 7.63 (dd, $J$ = 6.0, 3.2 Hz, 4H), 7.22 (dd, $J$ = 6.0, 3.1 Hz, 4H), 2.39 (s, 3H). **$^{13}$C NMR** (151 MHz, DMSO-$d_6$) δ: 151.86, 151.52, 130.36, 130.07, 127.95, 126.17, 122.48, 117.93, 20.80. **HRMS** (ESI) m/z: calculated for $C_{21}H_{16}N_4O$ $(M + H)^+$ : 341.1397, found: 341.1395.

### 3.4.2.5.2 Synthesis of 4-methyl-2,6-bis(6-(trifluoromethyl)-1*H*-benzo[d]imidazol-2-yl)phenol

The 4-methyl-2,6-bis(6-(trifluoromethyl)-1*H*-benzo[d]imidazol-2-yl)phenol **(3.2)** was synthesised according to the procedure as mentioned in the earlier section (3.4.2.5), using

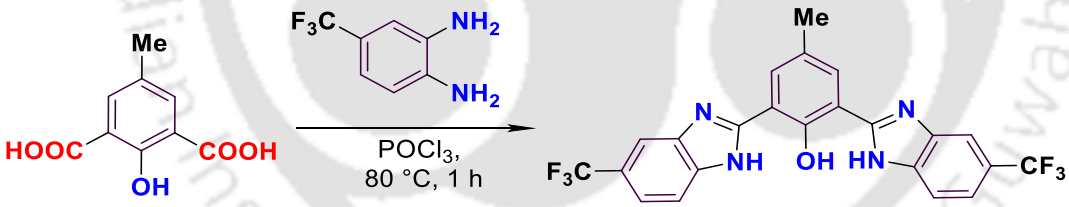


**Scheme 3.7** Synthesis of 4-methyl-2,6-bis(6-(trifluoromethyl)-1*H*-benzo[d]imidazol-2-yl) phenol (**3.2**).

4-(trifluoromethyl)benzene-1,2-diamine (164 mg, 1 mmol, 2 equiv.) and 2-hydroxy-5-methylisophthalic acid (352 mg, 1 equiv.). The resulting compound **3.2** was obtained with a yield of 82%. The compound was characterized by $^{1}$H NMR, $^{13}$C NMR and HRMS (ESI) analysis. **$^{1}$H NMR** (600 MHz, DMSO-$d_6$) δ: 14.49 (s, 1H), 1**3.49** (s, 2H), 8.23 (s, 2H), 8.05 (s, 2H), 7.88 (d, $J$ = 8.4 Hz, 2H), 7.61 (d, $J$ = 8.4 Hz, 2H), 2.46 (s, 3H) (Figure 17). **$^{13}$C NMR** (151 MHz, DMSO-$d_6$) δ: 155.60, 128.93, 126.58, 125.62, 124.78, 122.98, 122.61, 122.40, 118.76, 118.73, 118.70, 20.77. **$^{19}$F NMR** (565 MHz, DMSO-d6) δ: -58.91. **HRMS** (ESI) m/z: calculated for $C_{23}H_{14}F_6N_4O$ $(M + H)^+$ : 477.1145, found: 477.1137.

### 3.4.2.5.3 Synthesis of 2,2'-((1E,1'E)-(2-methoxy-5-methyl-1,3-phenylene)bis(ethene-2,1-diyl))bis(1*H*-benzo[d]imidazole)

The 2,2'-((1E,1'E)-(2-methoxy-5-methyl-1,3-phenylene)bis(ethene-2,1-diyl))bis(1*H*-benzo[d]imidazole) **(3.3)** was synthesised according to the procedure as mentioned in the earlier section (3.4.2.5), using o-Phenylenediamine (58 mg, 0.54 mmol, 2 equiv.) and (2E,2'E)-3,3'-(2-methoxy-5-methyl-1,3-phenylene)diacrylic (70 mg, 0.27 mmol, 1 equiv.). The resulting

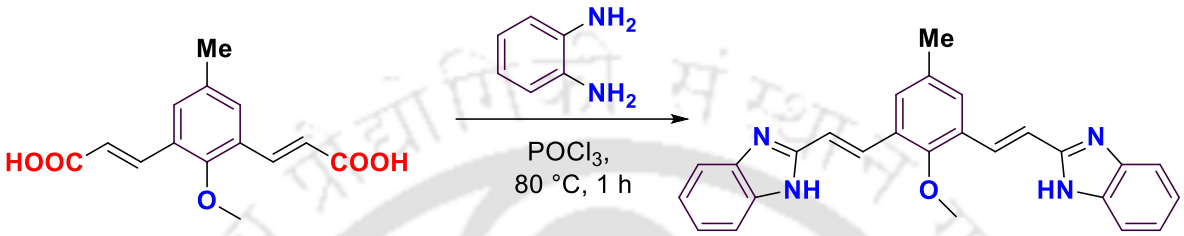


**Scheme 3.8** Synthesis of 2,2'-((1E,1'E)-(2-methoxy-5-methyl-1,3-phenylene)bis(ethene-2,1-diyl))bis(1*H*-benzo[d]imidazole) (**3.3**).

compound **3.3** was obtained with a 73% yield. The compound was characterized by $^{1}$H NMR, $^{13}$C NMR and HRMS (ESI) analysis. **$^{1}$H NMR** (600 MHz, DMSO-$d_6$) δ: 12.77 (s, 2H), 7.90 (s, 1H), 7.88 (s, 1H), 7.67 (s, 2H), 7.57 (d, $J$ = 39.8 Hz, 4H), 7.31 (s, 1H), 7.28 (s, 1H), 7.20 (d, $J$ = 6.5 Hz, 4H), 3.83 (s, 3H), 2.40 (s, 3H). **$^{13}$C NMR** (151 MHz, DMSO-$d_6$) δ: 154.81, 151.51, 134.54, 129.76, 128.60, 128.05, 119.59, 111.58, 63.35, 21.03. **HRMS** (ESI) m/z: calculated for $C_{26}H_{22}N_4O$ $(M + H)^+$: 407.1866, found: 407.1858.

### 3.4.2.5.4 Synthesis of 2,2'-((1E,1'E)-(2-methoxy-5-methyl-1,3-phenylene)bis(ethene-2,1-diyl))bis(6-(trifluoromethyl)-1*H*-benzo[d]imidazole)

The 2,2'-((1E,1'E)-(2-methoxy-5-methyl-1,3-phenylene)bis(ethene-2,1-diyl))bis(1*H*-benzo[d]imidazole) **(3.4)** was synthesised according to the procedure as mentioned in the earlier section (2.5), using 4-(trifluoromethyl)benzene-1,2-diamine (188 mg, 1.07 mmol, 2 equiv.) and (2E,2'E)-3,3'-(2- methoxy-5-methyl-1,3-phenylene)diacrylic (140 mg, 0.53 mmol, 1 equiv.).

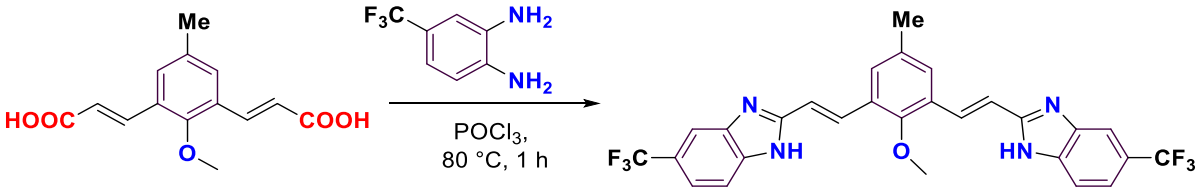

**Scheme 3.9** Synthesis of 2,2'-((1E,1'E)-(2-methoxy-5-methyl-1,3-phenylene)bis(ethene-2,1-diyl))bis(6-(trifluoromethyl)-1*H*-benzo[d]imidazole) (**3.4**).

The resulting compound **3.4** was obtained with a yield of 71%. The compound was characterized by $^{1}$H NMR, $^{13}$C NMR and HRMS (ESI) analysis. **$^{1}$H NMR** (600 MHz, DMSO-$d_6$) δ: 13.19 (d, J = 21.8 Hz, 2H), 7.99 (d, J = 7.8 Hz, 2H), 7.95 (s, 1H), 7.86 – 7.81 (m, 2H), 7.74 (s, 1H), 7.72 (d, J = 9.1 Hz, 2H), 7.54 (d, J = 8.3 Hz, 1H), 7.51 (d, J = 8.2 Hz, 1H), 7.38 (d, J = 4.8 Hz, 1H), 7.35 (d, J = 4.8 Hz, 1H), 3.84 (s, 3H), 2.41 (s, 3H). **$^{13}$C NMR** (151 MHz, DMSO-$d_6$) δ: 156.28, 155.46, 143.18, 136.09, 134.74, 131.97, 129.37, 125.61, 124.84, 123.80, 118.71, 115.95, 113.51, 63.77, 20.97. **HRMS** (ESI) m/z: calculated for $C_{28}H_{20}F_6N_4O$ $(M + H)^+$: 543.1614, found: 543.1616.

### 2.5.5. Synthesis of 2,6-bis((E)-2-(1*H*-benzo[d]imidazol-2-yl)vinyl)-4-methylphenol and 4-methyl-2,6-bis((E)-2-(6-(trifluoromethyl)-1*H*-benzo[d]imidazol-2-yl)vinyl)phenol

To the stirring solutions of 50 mg compound **3.3** (or **3.4**) in dry DCM (2 mL) under $N_2$ atmosphere, $BBr_3$ (100 µL) was added dropwise at 0 °C. After 10 min, the reaction mixture was brought to room temperature and stirred for 2 hours. The progress of the reaction was monitored by TLC. After completion of the reaction, it was cooled down to room temperature, and then ice water was added. After that, the product was extracted with EtOAc (2 × 10 mL). The organic layer was dried with $MgSO_4$, and the solvent was removed under reduced pressure. The crude product was purified with column chromatography using EtOAc: Hexane (2:3), yielding 70-75%. The compounds **3.5** and **3.6** were characterized by $^{1}$H NMR, $^{13}$C NMR, and HRMS (ESI) analysis.[30] Compound**3.5: $^{1}$H NMR** (600 MHz, DMSO-$d_6$) δ: 13.16 (s, 2H), 9.57 (s, 1H), 8.08 (s, 1H), 8.06 (s, 1H), 7.59 (dd, J = 5.5, 3.1 Hz, 4H), 7.55 (s, 2H), 7.24 (dd, J = 5.7, 3.0 Hz, 4H), 7.22 (s, 1H), 7.19 (s, 1H), 2.36 (s, 3H). **$^{13}$C NMR** (126 MHz, DMSO-d6) δ: 151.67, 151.62, 131.04, 130.21, 130.19, 128.28, 126.03, 122.89, 117.29, 20.74. **HRMS** (ESI) m/z: calculated for $C_{25}H_{20}N_4O$ $(M + K)^+$ : 431.1269, found: 431.1269. Compound**3.6: $^{1}$H NMR** (600 MHz, DMSO-$d_6$) δ: 13.08 (s, 1H), 13.04 (s, 1H), 9.59 (s, 1H), 8.11 (t, J = 15.4 Hz, 2H), 7.95 (s, 1H), 7.81 (d, J = 14.6 Hz, 2H), 7.69 (d, J = 8.2 Hz, 1H), 7.58 (s, 2H), 7.52 (d, J = 9.7 Hz, 2H), 7.24 (d, J = 16.2 Hz, 2H), 2.36 (s, 3H). **$^{13}$C NMR** (126 MHz, DMSO-d6) δ: 154.85, 153.01, 131.25, 128.94, 126.53, 124.37, 123.97, 123.72, 12**3.4**7, 123.22, 115.32, 20.64. **$^{19}$F NMR** (565 MHz, DMSO-d6) δ: -58.59. **HRMS** (ESI) m/z: calculated for $C_{27}H_{18}F_6N_4O$ (M +

H)$^+$ : 529.1458, found:529.1459. In $^{13}$C NMR, a few other peaks were observed due to trapped EtOAc. For confirmation, $^{19}$F NMR was also been provided.

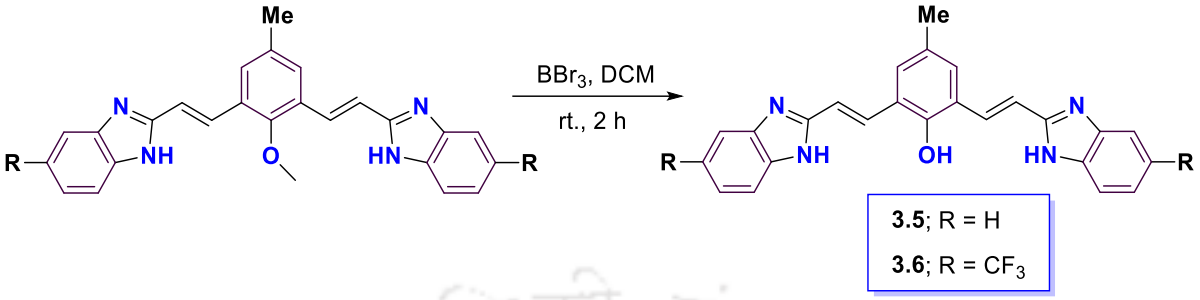


**Scheme 3.10** Synthesis of 2,6-bis((E)-2-(1*H*-benzo[d]imidazol-2-yl)vinyl)-4-methylphenol (**3.5**) and 4-methyl-2,6-bis((E)-2-(6-(trifluoromethyl)-1*H*-benzo[d]imidazol-2-yl)vinyl)phenol (**3.6**).

### 3.4.3 Morphology Studies

To investigate the self-assembly properties of compound **3.6**, we recorded FESEM images in both ethyl acetate/methanol and aqueous mediums. We drop-casted a solution of compound **3.6** in ethyl acetate/methanol and analyzed its morphology using FESEM. We also added compound **3.6** to an aqueous solution, which was then vortexed and sonicated briefly. The resulting sample was also examined using FESEM. Additionally, we analyzed the morphology of compound **3.6** using the dynamic light scattering (DLS) method in the aqueous medium. When compound **3.6** was introduced to the aqueous solution, nanostructures formed with a hydrodynamic diameter ($D_h$) of approximately 95 nm. The spherical nature of the aggregation could be attributed to the hydrophobic nature of the compound. The spherical configuration minimises interaction with water due to a reduced surface area relative to its volume.

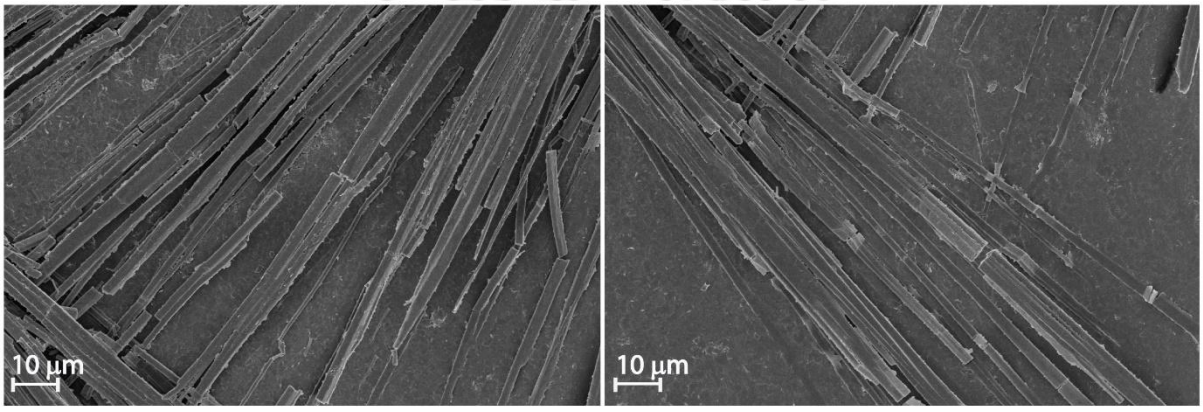


**Figure 3.5** Representative FESEM images of compound **3.6** in EtOAc/MeOH.

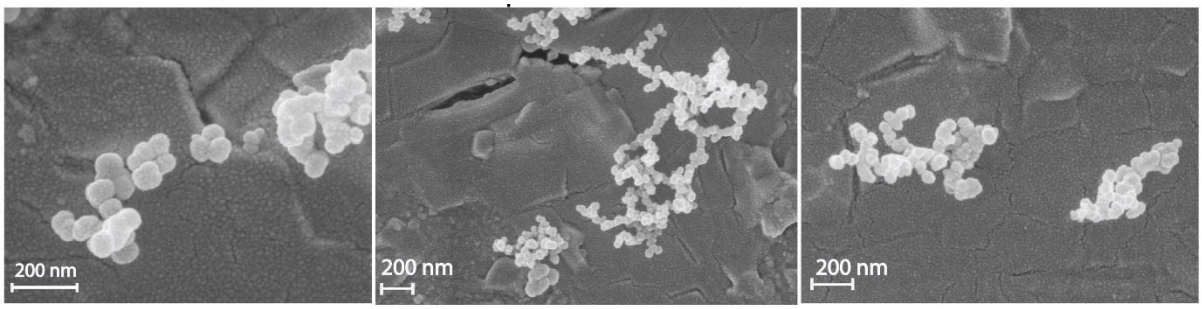


**Figure 3.6** Representative FESEM images of compound **3.6** in aqueous media.

### 3.4.4 Ion Transport Methodology

#### 3.4.4.1 Preparation of EYPC/CHOL-LUV⊃MgG Vesicles

To conduct the MgG fluorescence-based ion-transport studies, we took EYPC (50 mg/mL in deacidified $CHCl_3$) and cholesterol (CHOL; 25 mg/mL in deacidified $CHCl_3$) in a clean, dry glass vial in a molar ratio of 8:2. The solution was evaporated for 6 hours under reduced pressure to form a thin lipid film. After that, we rehydrated the film with 10 mM HEPES buffer containing 100 mM KCl, 100 µM EDTA and 50 µM MgG dye at pH 7.0.[15] The resulting suspension was vortexed six to seven times over 1 hour. Next, we performed 6-7 freeze-thaw cycles followed by 10 minutes of constant vortexing. We then extruded the lipid suspension 19–21 times using a mini extruder with a 200 nm pore size to achieve a uniform liposome size of 200 nm. Finally, we removed the unencapsulated MgG dye using the gel filtration technique (Sephadex G-50) and 10 mM HEPES buffer containing 100 mM potassium gluconate (KGlc) and 100 µM EDTA at pH 7.0 as the eluting solution. This process yielded a final lipid concentration of 25 mM (assuming 100% lipid regeneration).

#### 3.4.4.2 Ion Transport Study via an Electrogenic Pathway across EYPC/CHOL-LUV⊃MgG

The transmembrane ion transport properties of the compounds were investigated by a fluorescence-based assay using a Fluoromax-4 spectrofluorometer (Horiba Scientific, Singapore).[16] For the fluorescence-based electrogenic assay, 10 mM HEPES buffer containing 100 mM KGlc and 100 µM EDTA at pH 7.0 (1920 µL) and EYPC/CHOL-LUV⊃MgG (40 µL) was taken in a clean, dry fluorescence cuvette (3 mL). The cuvette was placed under slow stirring conditions in a fluorescence spectrophotometer for about 3 minutes to equilibrate with

added valinomycin (final concentration of 12 pM added in the solution and assuming that all the molecules penetrate the membrane) and $Zn^{2+}$ (final concentration 1 mM) with the LUVs. The MgG fluorescence was monitored as a function of time ($\lambda_{em}$ = 531 nm, $\lambda_{ex}$ = 506 nm). At 50 s, 10 µL of compound (From DMSO stock, final concentration 500 nM) was added to the cuvette solution to initiate the $Zn^{2+}$ influx.

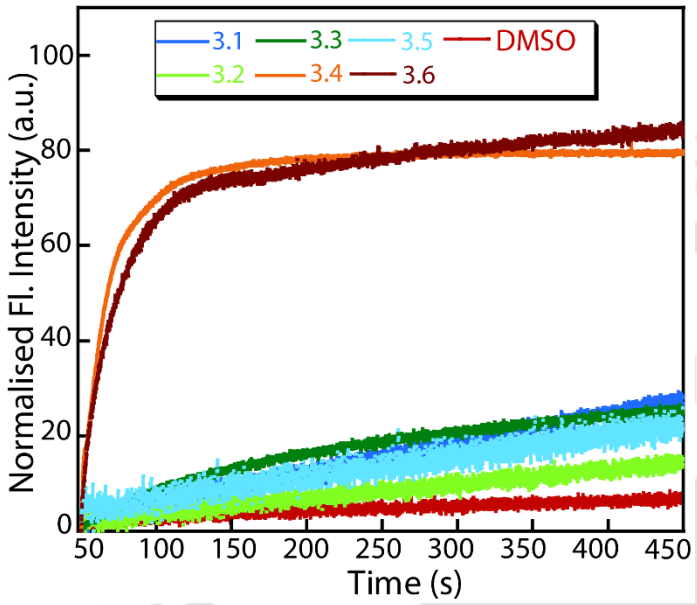


**Figure 3.7** Assessment of the $Zn^{2+}$ ion transport activity of the synthesised compounds (500 nM) across EYPC/CHOL-LUVs⊃MgG in the presence of valinomycin (Val; final concentration 12 pM). The intravesicular solution was 10 mM HEPES buffer containing 100 mM KCl and 100 µM EDTA at pH 7.0, and the extravesicular solution was 10 mM HEPES buffer containing 100 mM KGlc and 100 µM EDTA at pH 7.0. The LUVs were equilibrated with 1 mM $ZnCl_2$, and a pulse of the compound was added to initiate the transport studies.

Finally, the vesicles were completely lysed at 450 s by adding 20 µL of 20% Triton X-100. The fluorescence intensity measurement was continued for a further 50 s. The normalized % transport efficiency (%EE) at t = 450 s was considered for the particular ion-transport efficiency of the compounds. This assay system was followed to screen all compounds to assess their $Zn^{2+}$ transport efficacy. The transmembrane transport studies for the compounds were performed in repetition.

Transport activity, $T_{HPTS} = \frac{F_t - F_0}{F_\infty - F_0} \times 100\%$

### 3.4.4.3 Concentration-Dependent Transport Assays with EYPC/CHOL-LUV⊃MgG Vesicles

For the MgG-based ion transport assay, in a clean and dry fluorescence cuvette (3 mL), 10 mM HEPES buffer containing 100 mM KGlc and 100 µM EDTA, pH 7.0 (1930 µL), EYPC/CHOL-LUV⊃MgG (40 µL), valinomycin (final concentration 12 pM) and $ZnCl_2$ (final concentration 1 mM) were added. The cuvette was placed under slow stirring conditions in a fluorescence spectrophotometer for about 3 min to equilibrate. The fluorescence was evaluated as a function of time ($\lambda_{em}$ = 531 nm, $\lambda_{ex}$ = 506 nm). At 50 s, 10 µL of compound was added to the cuvette solution to initiate the transport studies.

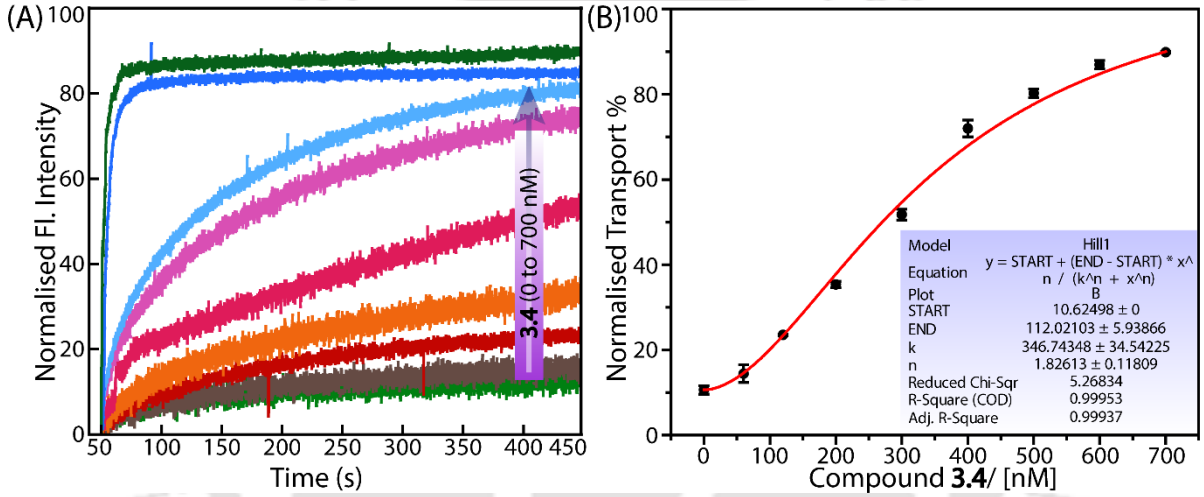


**Figure 3.8** (A) Concentration-dependent transmembrane $Zn^{2+}$ ions transport efficacy of compound **3.4** across EYPC/CHOL-LUVs⊃MgG. (B) The $EC_{50}$ value was calculated using the Hill equation.

Finally, the vesicles were completely lysed at 450 s by adding 20 µL of 20% Triton X-100. Transport studies for the compounds were performed in triplicate at various concentrations of compound **3.4** (20 nM to 700 nM) and compound **3.6** (20 nM to 800 nM). The fluorescence intensity measurement was continued for a further 50 s. The normalized % transport efficiency (%EE) at t = 450 s was considered for the particular transport efficiency of the compounds.

Transport activity, $T_{MgG} = (\frac{F_t - F_0}{F_\infty - F_0} \times 100)$ %

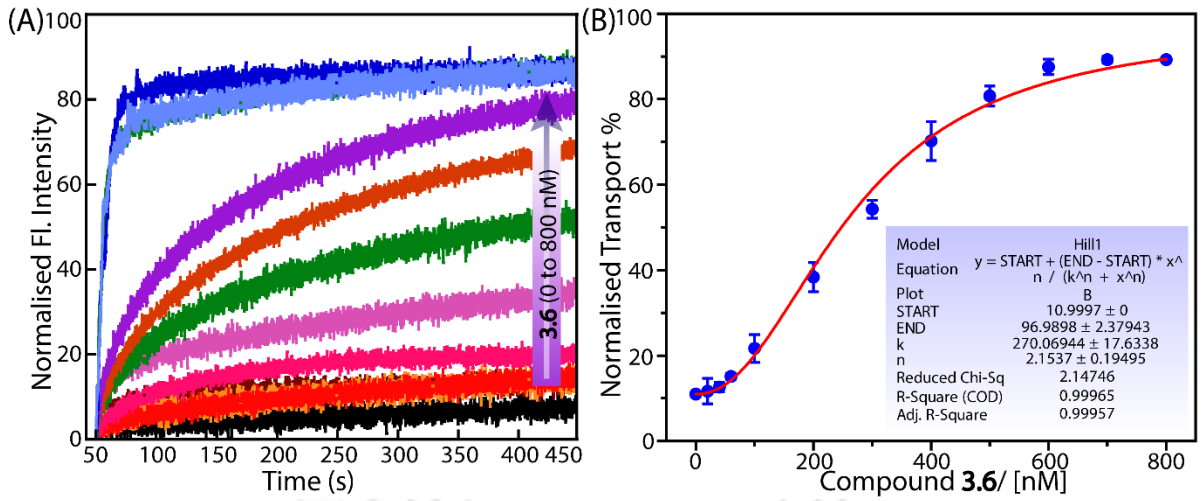


**Figure 3.9** (A) Concentration-dependent transmembrane $Zn^{2+}$ ions transport efficacy of compound **3.6** across EYPC/CHOL-LUVs⊃MgG. (B) The $EC_{50}$ value was calculated using the Hill equation.

### 3.4.4.4 Critical Aggregation Concentration Determination

The critical aggregation concentration (CAC) of compound **3.6** was determined using its concentration-dependent transport curve. A distinct inflecion point was observed through the linear fitting after analysing the transported percentage in the lower concentration range. Below

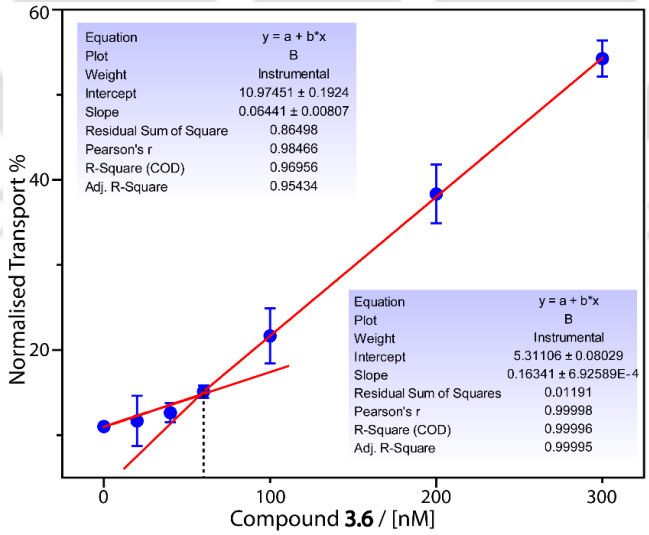


**Figure 3.10** Measurement of critical aggregation concentration (CAC) of compound **3.6** calculated from the concentration-dependent $Zn^{2+}$ ions transport properties across EYPC/CHOL-LUVs⊃MgG.

60 nM, the slope of the linear fit was 0.06 ± 0.008, while above 60 nM, the slope increased to 0.16 ± 0.0007. The change in slope at the inflection point suggests the initiation of supramolecular nanochannels under liposomal conditions.

### 3.4.4.5 Cation Selectivity Studies across EYPC/CHOL-LUV⊃MgG Vesicles

For the cation-selectivity studies, a similar procedure was followed for liposome preparation and ionophore activity studies, as mentioned in the previous section.

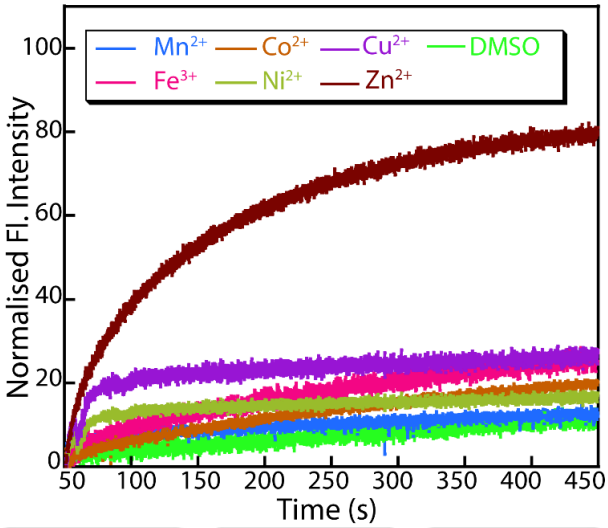


**Figure 3.11** Comparison of cation transport activity of compound **3.6** (500 nM) across the bilayers of EYPC/CHOL-LUV⊃MgG. The intravesicular solution was 10 mM HEPES buffer containing 100 mM KCl and 100 µM EDTA at pH 7.0, and the extravesicular solution was 10 mM HEPES buffer containing 100 mM KGlc and 100 µM EDTA at pH 7.0 and 1 mM $M_xCl_y$ (where M = $Mn^{2+}$, $Fe^{3+}$, $Co^{2+}$, $Ni^{2+}$, $Cu^{2+}$ and $Zn^{2+}$). DMSO (10 µL) was used as a control.

For the fluorescence assay, 10 mM HEPES buffer containing 100 mM KGlc and 100 µM EDTA, pH 7.0 (1930 µL), EYPC/CHOL-LUV⊃MgG (40 µL), valinomycin (final concentration 12 pM) and $M_xCl_y$ salt (1 mM final conc.) ($MnCl_2$, $FeCl_3$, $CoCl_2$, $NiCl_2$, $CuCl_2$, $ZnCl_2$) were taken in a clean fluorescence cuvette (3 mL). The cuvette was placed in the spectrofluorometer under a slow stirring condition for ~3 min. The MgG fluorescence intensity was recorded as a function of time ($\lambda_{em}$ = 531 nm, $\lambda_{ex}$ = 506 nm). At 50 s, 10 µL of compound **3.6** was added to the cuvette solution (final concentration 500 nM) to initiate the transport studies. Finally, the vesicles were lysed entirely by adding 20 µL of 20% Triton X-100 at 450

s, and the fluorescence intensity measurement was continued for a further 50 s. The studies on cation selectivity were conducted multiple times.

### 3.4.4.6 Anion Selectivity Studies across EYPC/CHOL-LUV⊃MgG Vesicles

For the MgG-based anion selectivity studies, liposomes were prepared in a manner similar to that described in the earlier section. For the fluorescence assay, 10 mM HEPES buffer containing 100 mM KGlc, and 100 μM EDTA pH 7.0 (1930 μL), EYPC/CHOL-LUV⊃MgG (40 μL), valinomycin (final concentration 12 pM), and $Zn_xB_y$ (1 mM final concentration, $ZnCl_2$, $ZnBr_2$, $ZnSO_4$, and $Zn(NO_3)_2$ ) were taken in a clean fluorescence cuvette (3 mL).

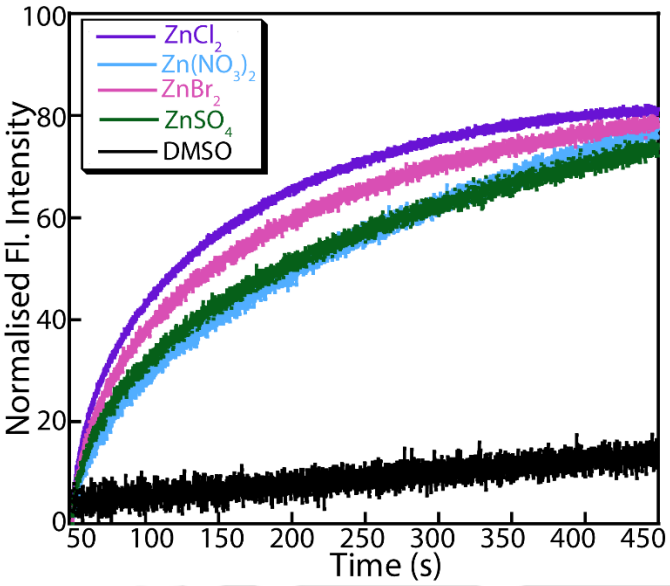


**Figure 3.12** Comparison of anion transport activity of compound **3.6** (500 nM) across the bilayers of EYPC/CHOL-LUV⊃MgG in the presence of different zinc salts. The intravesicular solution was 10 mM HEPES buffer containing 100 mM KCl and 100 μM EDTA at pH 7.0, and the extravesicular solution was 10 mM HEPES buffer containing 100 mM KGlc and 100 μM EDTA at pH 7.0 and 1 mM $Zn_xB_y$ ($ZnCl_2$, $ZnBr_2$, $ZnSO_4$, and $Zn(NO_3)_2$ ). DMSO (10 μL) was used as a control.

The cuvette was placed in a spectrofluorometer under a slow stirring condition for ~3 min. The MgG fluorescence intensity was monitored as a function of time ($\lambda_{em}$ = 531 nm, $\lambda_{ex}$ = 506 nm). At 50 s, 10 μL of compound **3.6** (final conc. 500 nM) was added to the cuvette solution to initiate the transport studies. Finally, the vesicles were lysed by adding 20 μL of 20% Triton

X-100 at 450 s, and the fluorescence intensity measurement was continued for a further 50 s. The studies on anion selectivity were conducted multiple times.

### 3.4.4.7 Investigation of $Cl^-$ Ion Transport Ability of the Compound across the EYPC/CHOL-LUVs⊃Lucigenin

To study ion transport using lucigenin fluorescence, large unilamellar vesicles (LUVs) composed of egg yolk phosphatidylcholine (EYPC) and cholesterol (CHOL) were prepared. EYPC (50 mg/mL in deacidified $CHCl_3$) and CHOL (25 mg/mL in deacidified $CHCl_3$) were mixed in a clean glass vial in an 8:2 molar ratio. The organic solvent was evaporated under reduced pressure for 6 hours, forming a uniform thin lipid film. The lipid film was hydrated by adding 800 µL of 20 mM HEPES buffer containing 1 mM lucigenin and 100 mM $NaNO_3$ (pH 7.0). The resulting suspension was subjected to six to seven vortex cycles over one hour to ensure homogeneity, followed by 17–19 freeze-thaw cycles. Subsequently, the suspension underwent constant vortexing for 10 minutes to encapsulate lucigenin within the lipid bilayer. Using a mini extruder, the lipid suspension was extruded through a 200 nm polycarbonate membrane (Avanti Polar Lipids). This extrusion process was repeated 19–21 times (ensuring an odd number of passes) to obtain uniformly sized LUVs. Unencapsulated lucigenin dye was removed by size-exclusion chromatography using a Sephadex G-50 column equilibrated with 20 mM HEPES buffer containing 100 mM NaCl (pH 7.0) to get the final lipid concentration of 25 mM (assuming 100% lipid regeneration). For the fluorescence-based transport assay, 1940 µL of 20 mM HEPES buffer containing 100 mM NaCl (pH 7.0) and 50 µL of the EYPC/CHOL-LUVs⊃lucigenin suspension was transferred to a quartz fluorescence cuvette. The sample was maintained at room temperature under slow stirring. Fluorescence emission was monitored using a spectrophotometer at an excitation wavelength of 455 nm and an emission wavelength of 505 nm. After recording the baseline fluorescence for 50 seconds, 10 µL of compound **3.4** or **3.6** (from a DMSO stock solution) was added to initiate ion transport. At 450 seconds, the vesicles were lysed by adding 20 µL of 20% Triton X-100 solution, and fluorescence was recorded until 500 seconds to determine the endpoint.

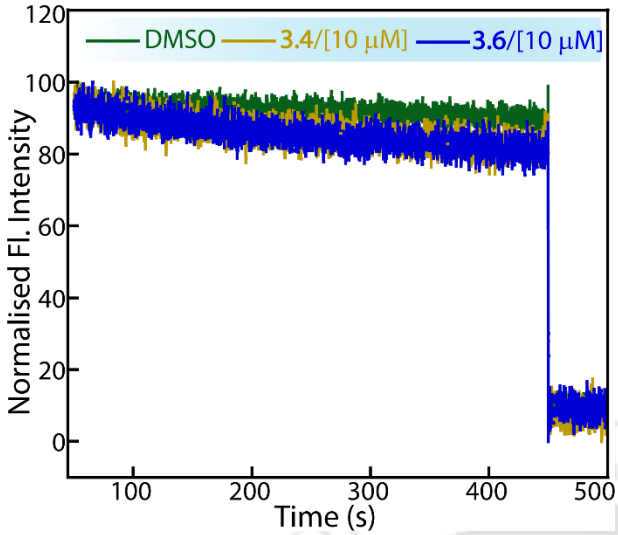


**Figure 3.13** Chloride ion transport activity of compounds **3.4** and **3.6** (10 μM) across EYPC/CHOL-LUVs⊃lucigenin, with DMSO (10 μL) as the control.

**Note:** The lucigenin-based ion transport studies across the bilayers of EYPC/CHOL-LUVs⊃lucigenin in the absence and presence of compound **3.4** or **3.6** clearly suggest the inability of $Cl^-$ transport by both the compounds under the experimental conditions.

### 3.4.4.8 Vesicle Leakage Assay

#### 3.4.4.8.1 Preparation of EYPC/CHOL−LUV⊃Carboxyfluorescein

A thin lipid film was prepared by evaporating a solution of 154 μL of EYPC (50 mg/mL stock in chloroform), and 39 μL cholesterol (25 mg/mL stock in chloroform) under vacuum for 6 h.[31] After that, lipid film was hydrated with 500 mL buffer (10 mM HEPES, 10 mM KCl, 50 mM carboxyfluorescein (CF), pH 7.0) for 1 h with occasional vortexing of 4−5 times and then subjected to freeze-thaw cycle (≥ 15 times). The vesicle solution was extruded through a polycarbonate membrane with 200 nm pores 19 times to give vesicles with a mean diameter of ~ 200 nm. The unencapsulated CF dye was removed with size exclusion chromatography (Sephadex G-50) column using 10 mM HEPES buffer (100 mM KGlc, pH 7.0.) as elution buffer. The final concentration of EYPC-CHOL liposome: ~25 mM; intravesicular solution: 10 mM HEPES, 100 mM KCl, 50 mM CF, pH 7.0; extravesicular solution: 10 mM HEPES, 100 mM KGlc, pH 7.0.

### 3.4.4.8.2 Carboxyfluorescein (CF) Leakage Assay

In a clean and dry fluorescence cuvette, 50 µL of the above liposome solution and 2940 µL of 10 mM HEPES buffer containing 100 mM KGlc at pH 7.0 were taken and kept in slowly stirring condition by a magnetic stirrer equipped with the fluorescence instrument (at t = 0 s). The temporal profile of CF fluorescence emission intensity, $F_t$, was monitored at an emission wavelength of 517 nm ($\lambda_{ex}$ = 492 nm). Compound **3.6** was added at t = 50 s, and at t = 450 s, 20 µL of 20% Triton X-100 was added to lyse the vesicles for 100% release of CF into solution. This study confirmed that the integrity of the bilayer membranes is intact in the presence of compound **3.6,** as no leakage of CF was observed at different compound concentrations.

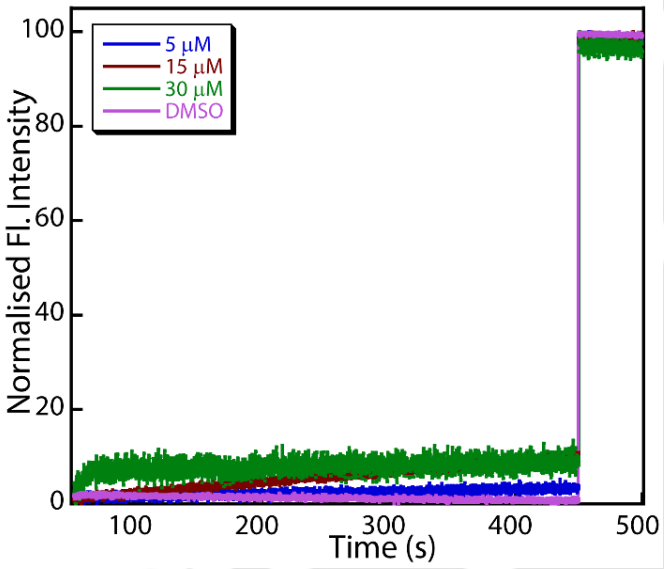


**Figure 3.14** Carboxyfluorescein (CF) leakage assay of compound **3.6** at different concentrations**.**

### 3.4.4.9 UV-Vis-based $Zn^{2+}$ Ion Binding Affinity of compound 3.6

To investigate the binding affinity of compound **3.6** with $Zn^{2+}$ ions, the UV-Vis-based titration of compound **3.6** (10 µM) was performed with $ZnCl_2$ in aqueous media. A decrease in absorbance was observed with each subsequent addition of $Zn^{2+}$ ions. The association constant ($K_a$) for the interaction between compound **3.6** and $Zn^{2+}$ ion was determined by fitting the absorbance data using a 1:1 binding model in the Bindfit v0.5 program. The calculated $K_a$ = 6500 $M^{-1}$ under the experimental conditions.

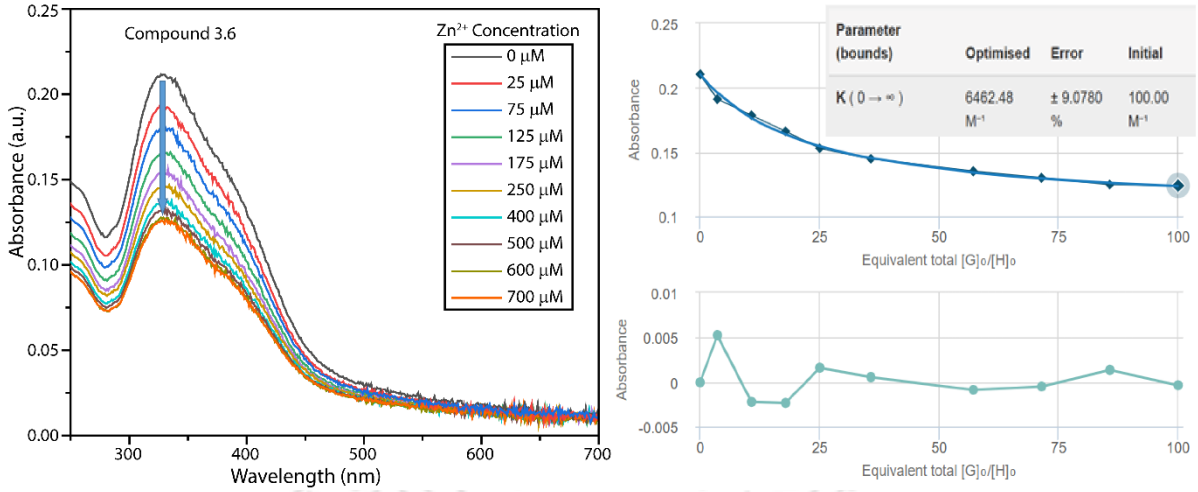


**Figure 3.15** (A) UV-Vis absorbance titration of compound **3.6** (10 µM) with $ZnCl_2$. (B) Calculation of binding constant using Bindfit v0.5 program.

### 3.4.4.10 $Zn^{2+}$ Ion-Mediated Catalysis

#### 3.4.4.10.1 Preparation of EYPC/CHOL-LUVs⊃AHPTS/HMPO Vesicles

To perform AHPTS ester hydrolysis-based transmembrane $Zn^{2+}$ ion transport studies, we prepared large unilamellar vesicles (LUVs) of EYPC (50 mg/mL in deacidified $CHCl_3$) and cholesterol (CHOL; 25 mg/mL in deacidified $CHCl_3$) in a clean, dry sample vial with a molar ratio of 8:2. The solution was evaporated under reduced pressure for 6 hours, resulting in the formation of a thin lipid film. Following that, the lipid film was rehydrated using 20 mM HEPES buffer containing 100 mM KCl, 2 mM AHPTS and 1 mM HMPO at pH 7.0.[32] The resulting suspension was vortexed six to seven times over the course of an hour. This was followed by 17–19 freeze-thaw cycles and 15 minutes of continuous vortexing. The lipid suspension was then extruded 19–21 times using a mini extruder with a 200 nm pore size to obtain uniformly sized liposomes of approximately 200 nm. Finally, the unencapsulated AHPTS dye and HMPO was removed using size exclusion chromatography (Sephadex G-50) with 20 mM HEPES buffer containing 100 mM KGlc at pH 7.0 as the elution buffer. This process resulted in a final lipid concentration of 25 mM (assuming 100% lipid regeneration).

### 3.4.4.10.2 Ester Hydrolysis-based Ion Transport Study across EYPC/CHOL-LUVs⊃AHPTS/HMPO

The transmembrane ion transport properties of the compounds were investigated by a fluorescence-based assay using a Fluoromax-4 spectrofluorometer (Horiba Scientific, Singapore). For the fluorescence-based assay, 20 mM HEPES buffer containing 100 mM KGlc at pH 7.0 (2920 μL) and EYPC/CHOL-LUV⊃AHPTS/HMPO (50 μL) was taken in a clean, dry fluorescence cuvette (3 mL). The cuvette was placed under slow stirring conditions in a fluorescence spectrophotometer for about 3 minutes to equilibrate the added valinomycin (final

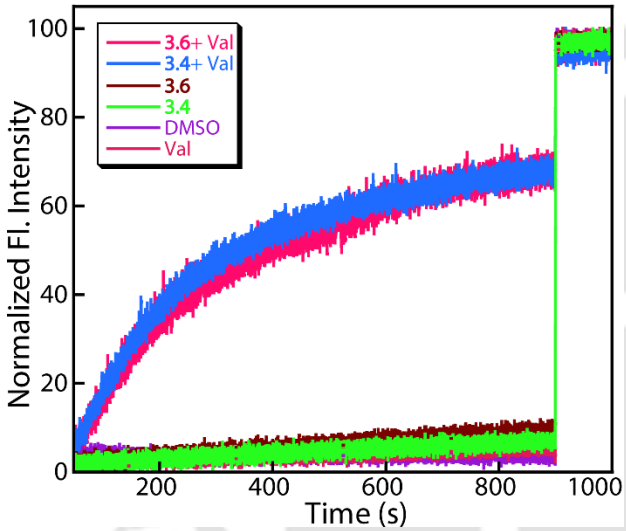


**Figure 3.16** AHPTS to HPTS ester hydrolysis based $Zn^{2+}$ ion transport properties of compounds **3.4** and **3.6** (10 μM) across EYPC/CHOL-LUVs⊃AHPTS/HMPO.

concentration 12 pM), and $Zn^{2+}$ ions (final concentration 15 mM) with the LUVs. The HPTS fluorescence was monitored as a function of time ($\lambda_{em}$ = 510 nm, $\lambda_{ex}$ = 450 nm). At 50 s, 10 μM of compound (From DMSO stock) was added to the cuvette solution to initiate the $Zn^{2+}$ ion influx. Finally, the vesicles were completely lysed at 450 s by adding 20 μL of 20% Triton X-100. The fluorescence intensity measurement was continued for a further 50 s. The normalized % transport efficiency (%EE) at t = 450 s was considered for the particular ion-transport efficiency of the compounds. The transmembrane transport studies for the compounds were performed in repetition.

### 3.4.4.11 Temperature-Dependent Ion Transport Studies across DPPC-LUV⊃HPTS

#### 3.4.4.11.1 Preparation of DPPC-LUV⊃MgG Vesicles

The MgG assay using 1,2-dipalmitoylphosphatidylcholine (DPPC) was employed to determine the transport mechanism of the compounds. DPPC-LUV⊃MgG vesicles were prepared in 10 mM HEPES buffer pH 7.0, containing 100 mM KCl and 100 µM EDTA. For the preparation, 50 µL of DPPC (100 mg/mL stock in de-acidified $CHCl_3$) was taken in a clean and dry glass vial, and the organic solvent was removed under reduced pressure (for 5-6 h) at room temperature. The dry, thin film was then hydrated with 500 µL of 10 mM HEPES buffer, pH 7.0, containing 100 mM KCl and 100 µM EDTA with 50 mM MgG dye. The solution was then sonicated for 20 min at 50 °C and was vortexed occasionally for 15-20 minutes. After that, the solution was subjected to a freeze-thaw cycle 12-13 times and again was sonicated 10 times (40 s sonication followed by 20 s incubations in ice water). The LUVs were prepared by extrusion at 45 °C using Avanti Mini-Extruder (Avanti Polar Lipids, Alabaster, AL) through 200 nm pore-size polycarbonate membranes according to the manufacturer's protocol. The unencapsulated dye was removed using a size exclusion column (Sephadex G-50) with 10 mM HEPES buffer, pH 7.0, containing 100 mM KGlc and 100 µM EDTA. The final volume of the collected vesicle solution was adjusted to 500 µL with 10 mM HEPES buffer pH 7.0 containing 100 mM KGlc and 100 µM EDTA. The final lipid concentration was 14 mM (assuming 100 % lipid regeneration).

#### 3.4.4.11.2 Temperature-Dependent Ion Transport Studies across DPPC-LUV⊃MgG

The DPPC assay was performed using a Fluoromax-4 spectrofluorometer (Horiba Scientific, Singapore) connected with a temperature controller. In this assay, 1930 µL of 10 mM HEPES buffer, pH 7.0 containing 100 mM KGlc and 100 µM EDTA, and 40 µL of the DPPC-LUV⊃MgG, valinomycin (final concentration 12 pM), $Zn^{2+}$ (1 mM final concentration) were taken in a 3 mL fluorescence cuvette. The kinetic experiment was started (at t = 0 s), and MgG fluorescence emission was monitored, as mentioned in an earlier section.

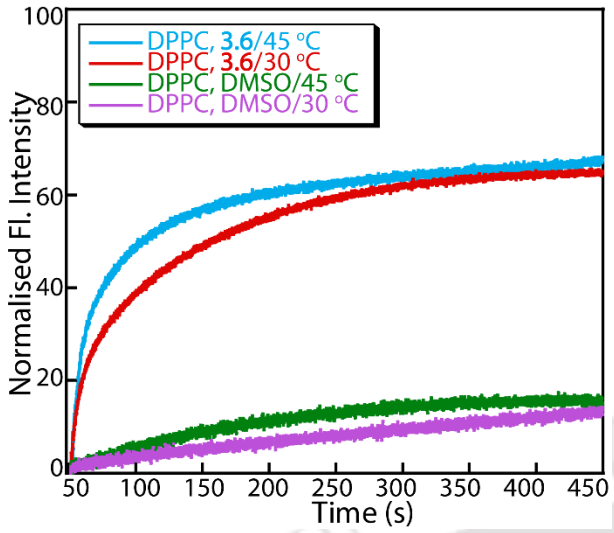


**Figure 3.17** Temperature-dependent transmembrane $Zn^{2+}$ ion transport activities of compound **3.6** across DPPC-LUV⊃MgG.

The cuvette was then kept under stirring conditions, and the chamber temperature was set to 30 ºC. After 50 s, compound **3.6** (final concentration 500 nM) was added to initiate the transport studies. Finally, to terminate the kinetic experiment, the vesicles were lysed by adding 20% Triton X-100 (20 µL) in the cuvette at t = 450 sec, and fluorescent measurements were continued for another 50 s (i.e., up to t = 500 s). Following the same procedure, kinetics in DPPC-LUV⊃MgG was measured at 45 ºC.

### 3.4.4.11.3 U-Tube Assay for Compound 3.6

The classical U-tube experiment was performed according to the reported procedure to confirm the mechanistic pathway for the $Zn^{2+}$ ion transport by compound **3.6**. The lipid bilayer was mimicked using chloroform (12 mL) as the organic layer. The compound **3.6** (2 mM) in chloroform was placed at the bottom of the U-tube with mild stirring conditions. The left arm of the tube was filled with 20 mM HEPES and $ZnCl_2$ solution (12 mL, 0.1 M), and the right

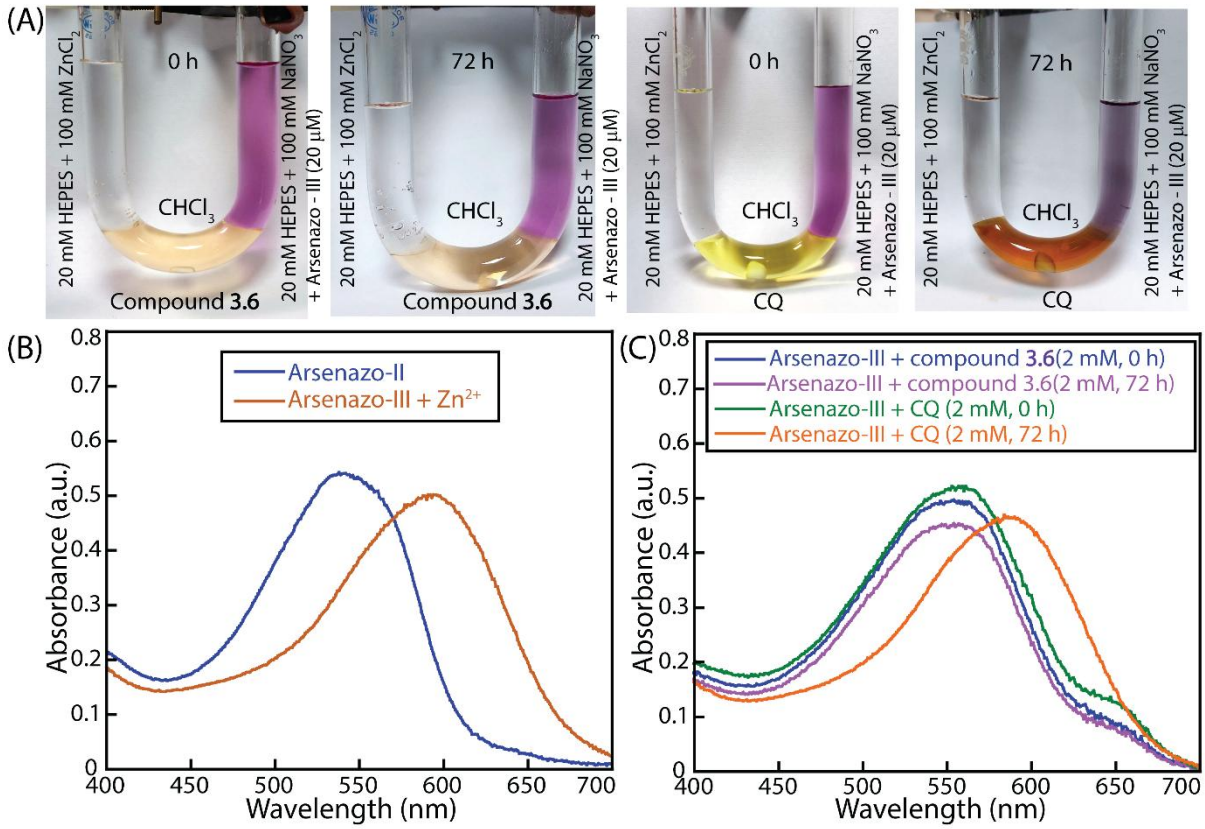


**Figure 3.18** (A) U-tube assay of compound **3.6** and clioquinol (CQ; control). (B) UV-Vis absorbance spectra of arsenazo-III dye (20 µM) in the absence and presence of $Zn^{2+}$ ion. (C) UV-Vis absorbance spectra of arsenazo-III dye-containing solution from the receiver end of the U-tube in the presence of compound **3.6** and clioquinol (CQ) at 0 and 72 h.

one was filled with 20 mM HEPES and 0.1 M aqueous $NaNO_3$ solution (12 mL). Arsenazo-III, a metal ion-sensing dye (20 µM), was added to the receiver arm for sensing $Zn^{2+}$ ions. The $Zn^{2+}$ ion binding to arsenazo-III dye (20 uM; $\lambda_{max}$ = 545 nm) showed a significant shift in UV-Vis spectra ($\lambda_{max}$ = 600 nm). The $Zn^{2+}$ concentration at the receiver end was monitored using a UV-Vis spectrophotometer after 72 hours. The obtained spectra suggested that after 72 hours, no significant amount of $Zn^{2+}$ ions was carried to the receiver end of the U-tube. Hence, compound **3.6** could not act as a carrier through an apolar phase ($CHCl_3$). A similar study was performed in the presence of clioquinol (CQ, 2 mM), a $Zn^{2+}$ ion carrier.

### 3.4.5 Black Lipid Membrane Conductance Measurements

A solvent-free black lipid membrane (BLM) was formed, as mentioned previously.[33, 34] Briefly, a 20 µm thick Teflon foil (Goodfellow) containing a 50-100 µm orifice was sandwiched between two homemade Delrine half-cells. The orifice in the Teflon foil was carefully pre-painted with 3 µL of hexane/hexadecane on both sides, dried for 20 min, and filled with 2.5 mL buffer on each side. Before forming the lipid bilayer, about 10 µL (size of the surface around 1×1 $cm^2$) of a 1 v% 1,2-diphytanoyl-sn-glycero-3-phosphocholine (diPhyPC) in pentane was introduced on the buffer surface. After 5-10 min drying, the bilayer was formed by lowering and raising the buffer level. Measurements were performed with Ag-AgCl reference electrodes with a diaphragm (Metrohm, Filderstadt, Germany). One electrode (GND) was connected to the ground, and the other electrode (Active) was connected to the head-stage of an axo-patch 200B amplifier that was used for the conductance measurements in the voltage clamp mode. Signals were filtered by an onboard low-pass Bessel filter at 1 kHz and recorded onto a computer hard drive with a sampling frequency of 2 kHz. The conductance was obtained from the averaged ion current for a series of voltage steps. All measurements were taken from at least three independent measurements. Compound **3.6** (1 mM) was prepared in DMSO and diluted to the desired concentration. To accelerate equilibrium, we added compound **3.6** (4 µM) on both sides of the membrane with equimolar concentrations (equilibrated for 1 h). For single-channel conductance (G) measurements, both chambers (GND and Active) were filled with a symmetrical solution containing 0.5 M $ZnCl_2$. Channel formation in the presence of compound **3.6** was confirmed by the distinctive channel opening and closing events after applying voltages. All data were analyzed by the ClampFit 9 software (Molecular Devices). The complete data traces were recorded over a long period, and from a large trace, a small portion is presented in the manuscript and SI.

**Calculation of Ion Channel Diameter**

The pore size is estimated from the measured single-channel pore conductance G and is proportional in first order to the bulk conductivity kappa to the pore area $S = \frac{\pi d^2}{4}$ and inversely proportional to the pore length L.[33, 34]

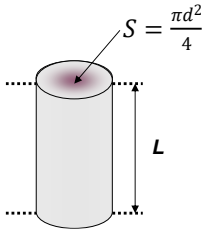


$$G = \kappa \frac{\pi d^2}{4L}; \qquad \kappa = \sum_{i=1}^{N} c_i \rho_i$$

Where our experimentally measured (from I-V plot, Figure S10A) conductance G = 51 pS, d = diameter of the pore, L = length of the channel

= 40 Å, $c_i$ = concentration of the ion *i,* [mol/m$^3$], and $\rho_i$ = specific conductance of the ion *i*, [S·m$^2$/mol]. Using published values for $\rho_{zn(II)}$ = specific conductance of the $Zn^{2+}$ ion = 52.8 × $10^{-4}$ [S·m$^2$/mol] and $\rho_{Cl(I)}$ = specific conductance of the $Cl^-$ ion = 76.31 ×$10^{-4}$ [S·m$^2$/mol].[35] We obtained the κ = bulk conductivity = 12.9 S/m for a concentration of $ZnCl_2$ = 0.5 M. Inverting the equation yields for the pore diameter (d) = 1.4 Å.

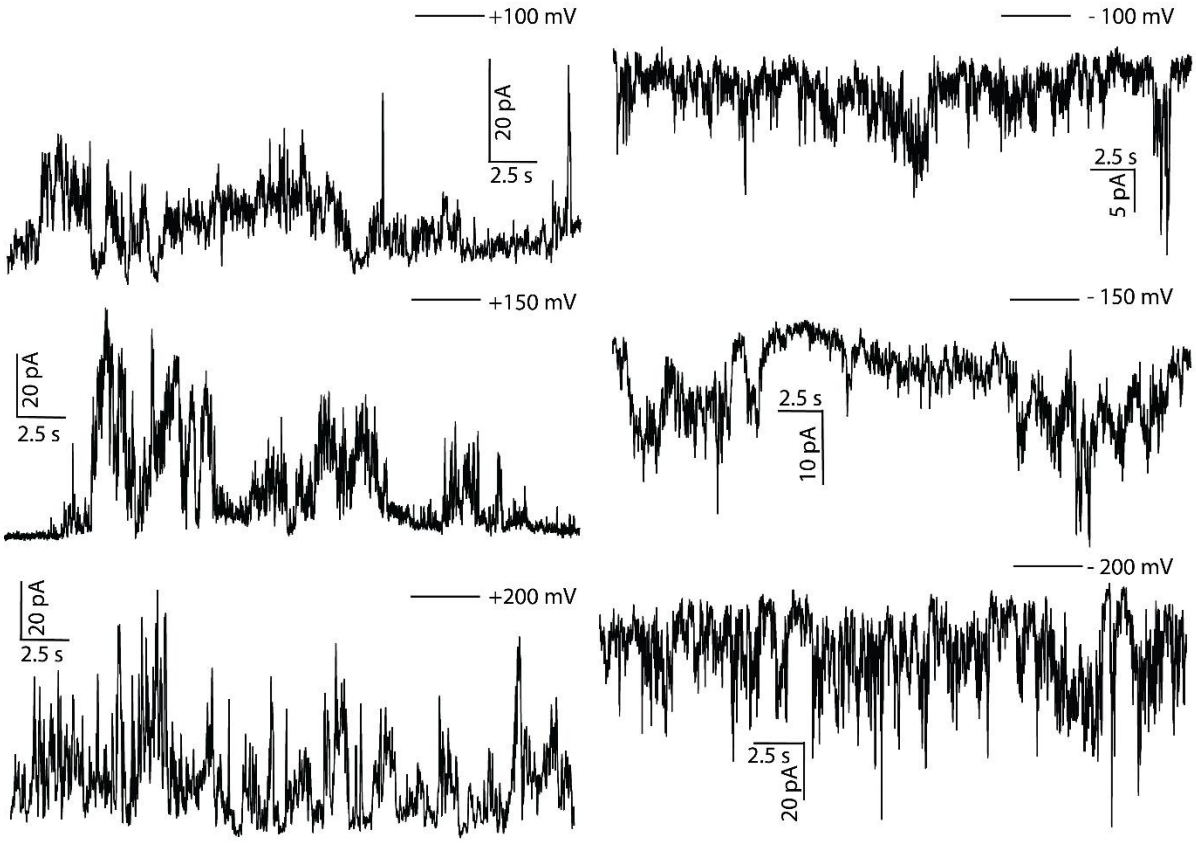


**Figure 3.19** Ion conductance measurements of compound **3.6** (4 μM) were recorded at +100, +150 mV, +200 mV, -100 mV, −150 mV, and -200 mV under symmetrical $ZnCl_2$ solutions (0.5 M).

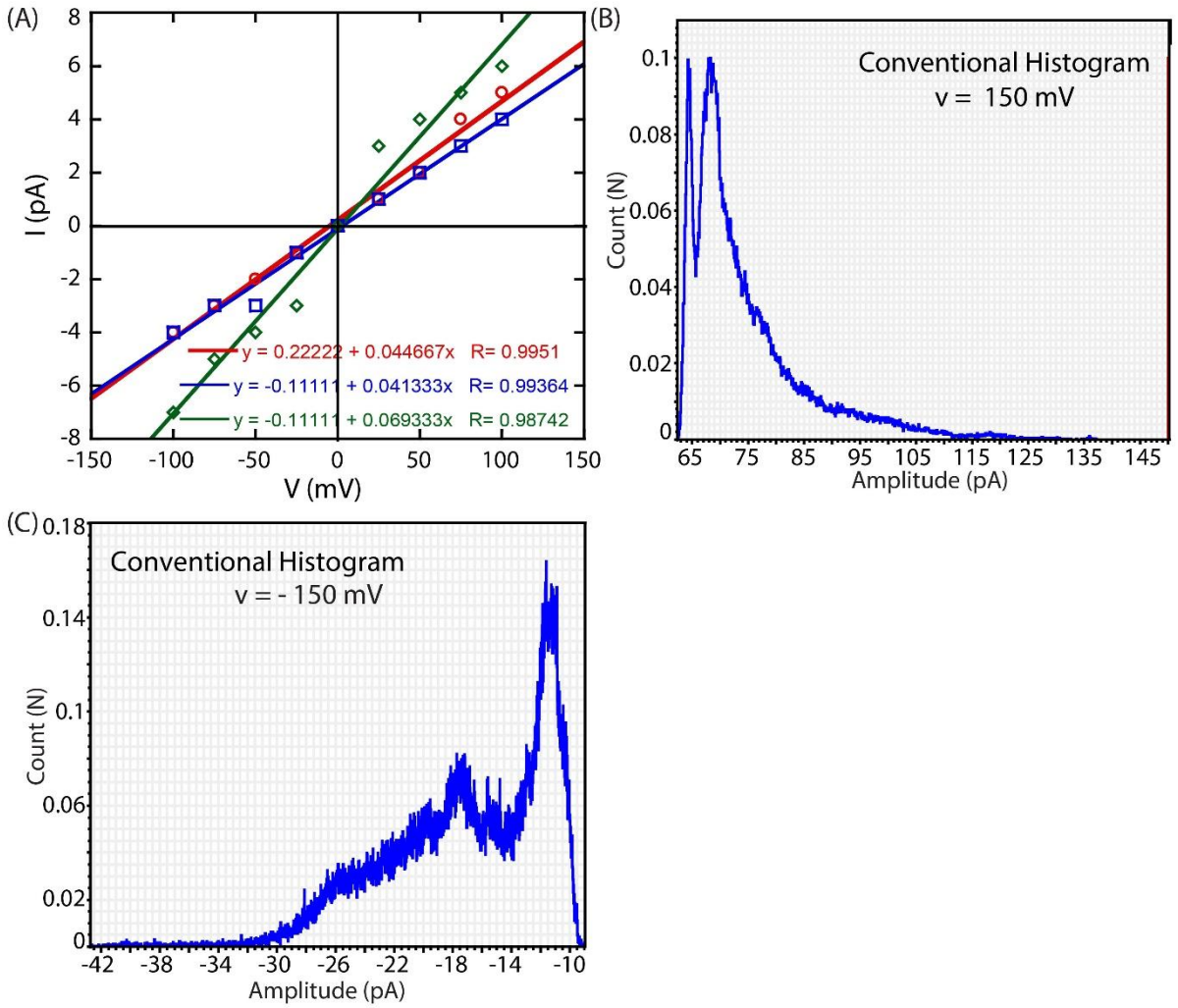


**Figure 3.20** (A) I–V plots of compound **3.6** in symmetrical $ZnCl_2$ solution (0.5 M). This curve presents the average of a highly fluctuating ion current. Histograms of the fluctuating ion current for (B) +150 mV and (C) -150 mV in a symmetrical $ZnCl_2$ solution (0.5 M). The pronounced peak was observed at around 68 pA and 18 pA at +150 mV and -150 mV, respectively. This peak we identified as a stable single channel. Less pronounced are multiple of them.

### 3.4.6 MD Simulation Studies

#### 3.4.6.1. Simulation Setup

We built a proposed model for an ion channel formed by the molecule. To build the model, we first geometry-optimized two molecules with one zinc and two chloride atoms using the B3LYP density functional theory (DFT) method in the Gaussian 09 program package.[37-39] We used the optimized 2-molecule + zinc complex and formed an ion channel spanning the

membrane, with six layers, each containing two molecules. The membrane contains 1,2-dipalmitoyl-sn-phosphocholine (DPPC) lipid molecules. The system was then solvated with TIP3P water[40] and neutralized with 150 mM of $ZnCl_2$. Each step of the system-building process was carried out using the Membrane Builder module of CHARMM.[41] The final system contained ~100,000 atoms with dimensions of 100×100×100 $Å^3$. The prepared systems were minimised using the steepest descent algorithm for 5,000 steps, followed by 10 ns of molecular dynamics (MD) equilibration. During equilibration, following the recommendation from CHARMM-GUI, multiple steps with gradual release of restraints were carried out both to the channel and lipid atoms. Then, steered MD simulations were performed to pull a zinc ion through the channel at a speed of 1 Å/ns. During simulations, mild restraints with a force constant of 500 kJ $mol^{-1}$ $nm^{-2}$ were applied to the zinc atom of the channel.

#### 3.4.6.2 MD Simulation Protocol

MD simulations in this study were performed using GROMACS-2024utilising CHARMM36m force field parameters.[42, 43] The force field parameters for the ligands were generated using the CHARMM General Force Field (CGenFF).[37, 38, 44] Forcefield parameters for zinc ions were taken from elsewhere.[45] Bonded and short-range non-bonded interactions were calculated every 2 fs, and periodic boundary conditions were employed in all three dimensions. The particle mesh Ewald (PME) method[46] was used to calculate long-range electrostatic interactions with a grid density of 0.1 nm−3. A force-based smoothing function was employed for pairwise nonbonded interactions at 1 nm with a cutoff of 1.2 nm. Pairs of atoms whose interactions were evaluated were searched and updated every 20 steps. A cutoff (1.2 nm) slightly longer than the non-bonded cutoff was applied to search for the interacting atom pairs. A constant pressure of 1 bar was maintained using the c-rescale algorithm.[47] Temperature coupling was kept at 310K with the v-rescale algorithm.[48]

### 3.4.7 Investigation of Host-Guest Interactions: ITC and UV-Vis Spectroscopy

The host-guest interaction of β-CD with compound **3.6** was investigated by isothermal titration calorimetry (ITC) measurements. The heat change induced by the interaction was measured at 28 °C (301 K) and a stirring speed of 350 rpm using a Microcal PEAQ-ITC. A 0.15 mM solution

of compound **3.6** was titrated against a β-CD (2 mM) solution. The titration method involved 16 injections (2 μL of each) of titrant (β-CD) into the sample cell containing compound 3.6 (300 μL), performed at 2-minute intervals with continuous stirring. The ΔH and ΔS values were obtained using a nonlinear least-squares fit of the data. Gibbs free energy (ΔG) was calculated by using the Gibbs equation: $\Delta G = \Delta H - T\Delta S$. The ΔH and ΔS values suggested that this process is enthalpy-driven.

UV-Vis absorbance of compound **3.6** (5 μM) was monitored in the absence and presence of β-CD (5 mM) in aqueous media. A significant change in the absorbance spectra of compound **3.6** was observed in the presence of β-CD, suggesting their host-guest interaction.

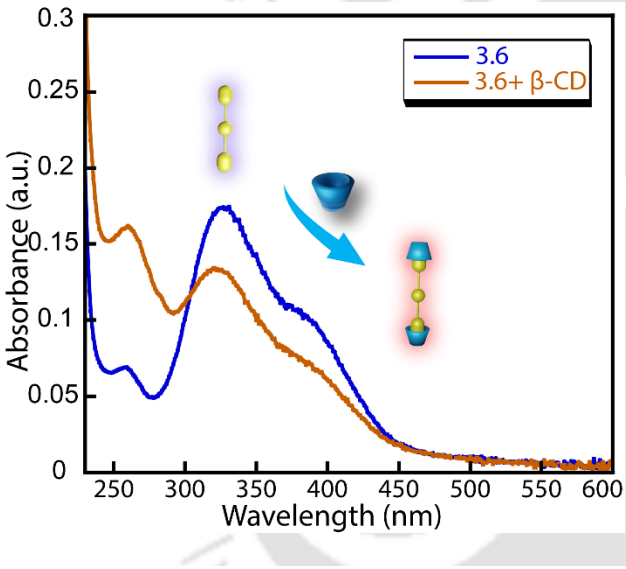


**Figure 3.21** UV-Vis-based interaction study of compound **3.6** with β-CD and a Schematic representation of dynamic host-guest complexation between compound **3.6** and β-CD.

### 3.4.8 Formulation and Characterisation of Suprasomes

Compound **3.6** was added to an aqueous solution containing β-CD in a clean vial, sonicated and vortexed for 15 minutes, and then kept in a shaker at 180 rpm for 1 hour to form the suprasome. This gave a slightly cloudy solution, indicating the formation of larger particles, i.e. suprasomes.[22] Upon adding different concentrations of β-CD in the sample vial containing compound **3.6**, suprasomes of different hydrodynamic diameters ($D_h$) were formed.

### 3.4.8.1 Measurements of Hydrodynamic Diameter by Dynamic Light Scattering (DLS) Measurements

Suprasomes were prepared using different β-CD concentrations according to the aforementioned method. The $D_h$ values were recorded using a DLS instrument (Zetasizer Nano ZS90, Malvern, Westborough, MA) at 25 °C. These measurements were performed for all the compositions mentioned in this study in multiple times.

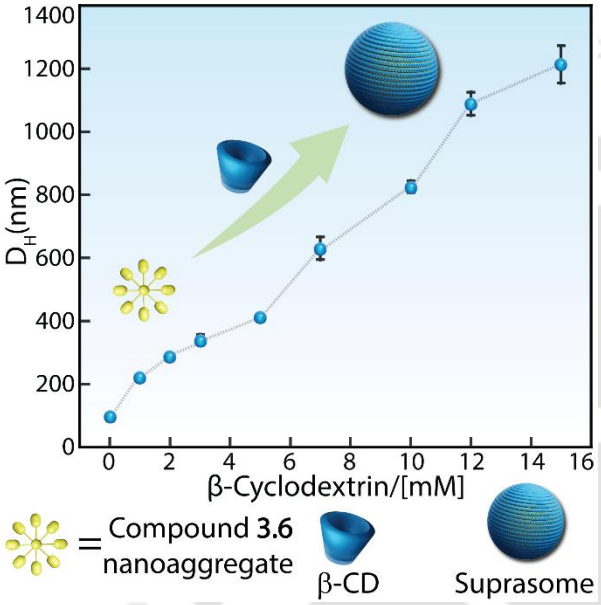


**Figure 3.22** Variation of hydrodynamic diameter ($D_h$) during suprasome formation with compound **3.6** and increasing β-CD concentration.

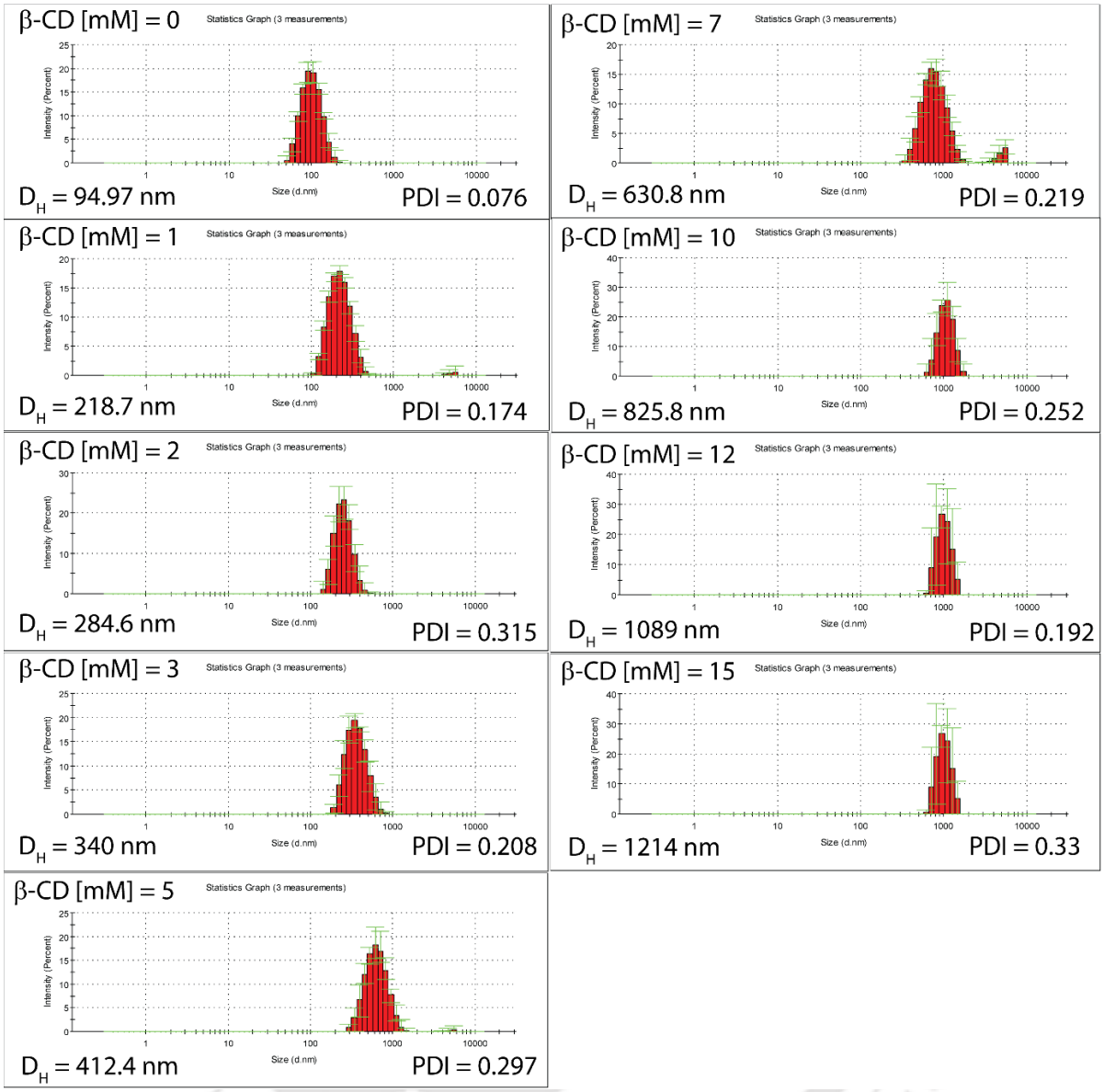


**Figure 3.23** Variation of hydrodynamic diameter ($D_h$) distribution of suprasomes of compound **3.6** at different concentrations of β-CD.

### 3.4.8.3 Stability of Suprasomes

As previously mentioned, the suprasomes were prepared with compound **3.6** and β-CD in aqueous solution and diluted to lower concentrations. After each day, the hydrodynamic diameter was tested to determine if there had been any change in the $D_h$ values, which would indicate aggregation. Thus, a stable hydrodynamic diameter over several days indicated the stability of the suprasome.

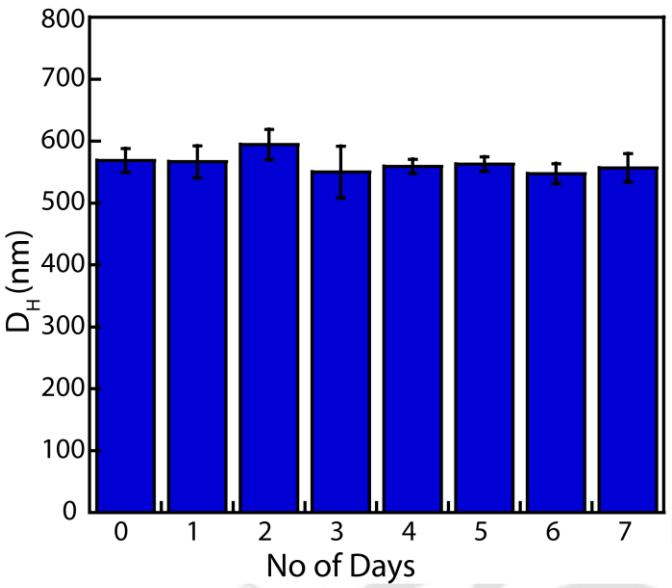


**Figure 3.24** Variation of hydrodynamic diameter ($D_h$) of suprasomes at different times (days).

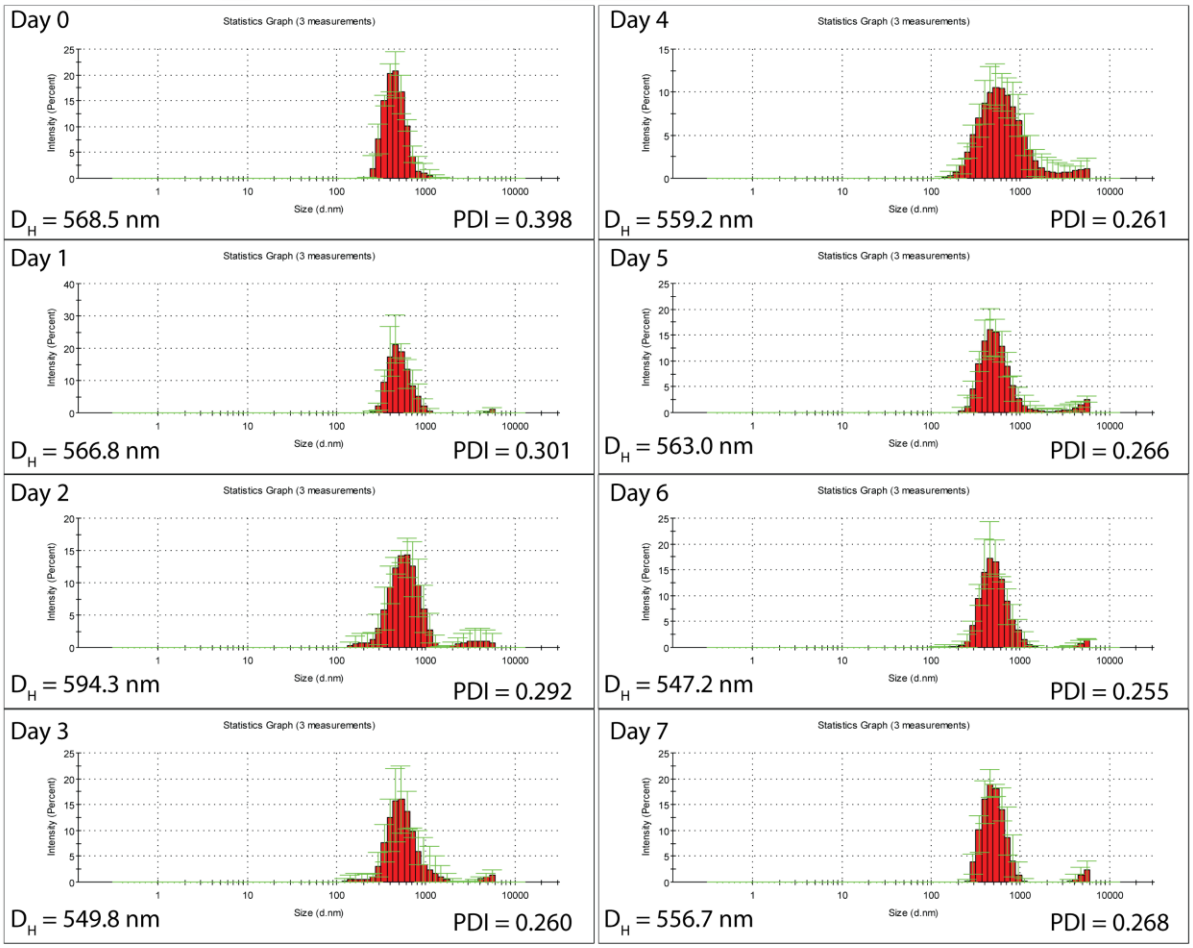


**Figure 3.25** Size distribution plots of suprasomes containing solutions at different times (days).

### 3.4.9 Investigation of Suprasome Disassembly

#### 3.4.9.1 Investigating Suprasome Disassembly using Nile Red Dye

To incorporate the Nile red dye within the suprasomes, the suprasomes of compound **3.6** in the presence of β-CD were prepared in an aqueous solution containing Nile red dye (100 μM). Further, these Nile red-containing suprasomes were subsequently utilised to study the disassembly of suprasomes. For this experiment, a 2 mL solution of the suprasomes containing Nile red was exposed to $Zn^{2+}$ ions at a final concentration of 4 mM, resulting in the swift disassembly of the suprasomes. It is important to note that the higher concentration of $Zn^{2+}$ ion treatment is designed to demonstrate an immediate disassembly effect within a time-frame of 1000 seconds. The addition of $Zn^{2+}$ ion caused a decrease in the fluorescence intensity of Nile red ($\lambda_{ex}$ = 550 nm, $\lambda_{em}$ = 645 nm), as evidenced by a decrease in the fluorescence signal at 645 nm, suggesting the release of Nile red from the hydrophobic bilayer to the aqueous solution.

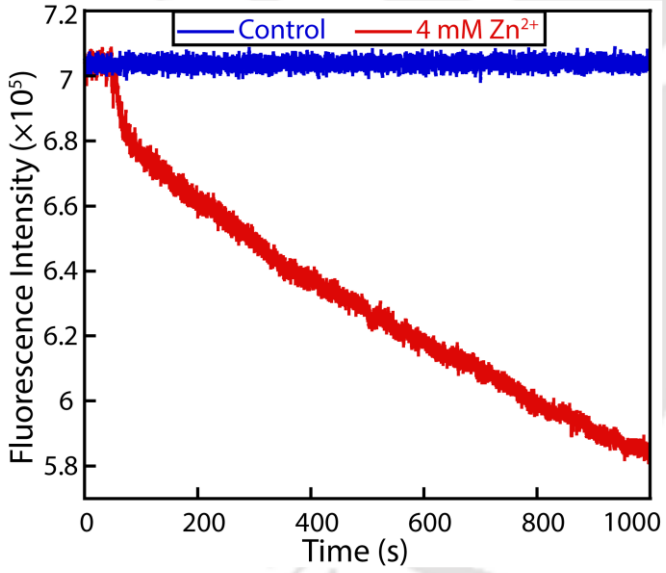


**Figure 3.26** Spectral representation of the kinetics-based Nile red assay for suprasome disruption in the presence of $Zn^{2+}$ (4 mM).

**Note:** Nile Red (NR) dye, known for its strong fluorescence within hydrophobic environments, can serve as a marker for vesicle integrity. When vesicles disintegrate, NR is released into the aqueous phase, resulting in quenched fluorescence due to the solvatochromic effect as well as precipitation. However, as the NR dye is hydrophobic, a certain extent of the molecules would stay within the nanoaggregates of compound **3.6** and $Zn^{2+}$ ions.[21, 22] In Figure 3.26, we demonstrated the disruption of suprasomes and the release of cargo in the presence of 4 mM

$Zn^{2+}$ ions using a Nile Red-based kinetic assay. The higher concentration of $Zn^{2+}$ was used to accelerate the release process within a kinetic timescale of 1000 seconds.

**3.4.9.2 Degree of Suprasome Disruption Assessed via Nile Red Fluorescence Assay.** Suprasomes were prepared using β-cyclodextrin (β-CD) and compound 3.6, following the previously described protocol in Section 3.4.8. During suprasome formation, Nile Red (100 μM) was incorporated into the solution and stirred for 1 hour to ensure suprasome assembly. To evaluate suprasome stability, the structures were subsequently treated with $Zn^{2+}$ at final concentrations of 100 μM and 400 μM and maintained under continuous stirring. The fluorescence emission of Nile Red ($\lambda_{ex}$ =545 nm, $\lambda_{em}$ = 650 nm) was recorded at 0 hours and 6 hours to assess the extent of suprasome disruption, as the release of encapsulated Nile Red is expected to result in a decrease in fluorescence intensity. A control sample consisting of Nile Red in water was used to quantify the degree of suprasome disruption.

$$Degree\ of\ disruption\ (\%) = \left(\frac{F_S - F_{Zn}}{F_S - F_C}\right) \times 100$$

Where, $F_S$ = Nile Red fluorescence of untreated suprasome at 0 h, $F_{Zn}$ = Nile Red fluorescence of $Zn^{2+}$ treated suprasome for 6 h, $F_C$ = Nile Red fluorescence in only water as control.

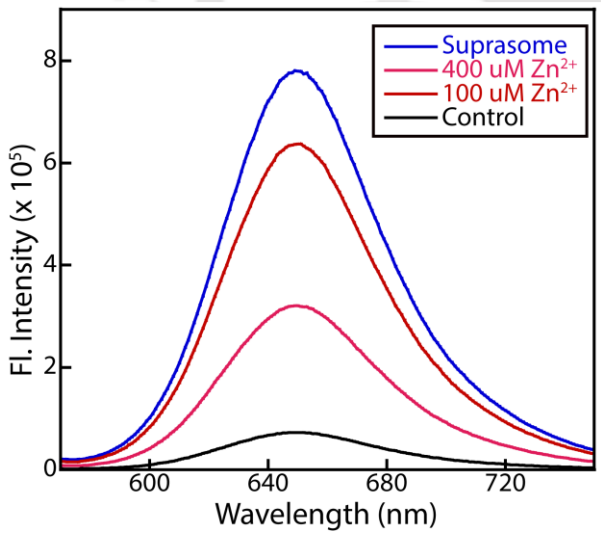


**Figure 3.27** Nile Red-based fluorescence assay to assess suprasome disruption upon $Zn^{2+}$ treatment.

**Note:** To clarify the relationship between $Zn^{2+}$ concentration and the degree of suprasome disassembly, suprasomes were treated with 100 μM and 400 μM $Zn^{2+}$ ion while being continuously stirred. Fluorescence measurements were then recorded over an extended period of 6 hours. The results showed that a concentration of 400 μM $Zn^{2+}$ facilitated approximately

64% cargo release within this timeframe, whereas 100 μM $Zn^{2+}$ resulted in about 20% release. These findings confirm that 400 μM $Zn^{2+}$ is effective for disrupting suprasomes and releasing cargo, while 100 μM $Zn^{2+}$ can induce disassembly but requires a longer time to achieve a significant effect.

#### 3.4.9.3 Physiological Relevance of $Zn^{2+}$-Triggered Suprasome Disruption

To better understand our findings in the context of physiological conditions, we reviewed the literature on $Zn^{2+}$ ion concentrations in the human body. Our study shows that significant disruption of suprasomes occurred at a high concentration of $Zn^{2+}$ ions (400 μM). The concentration of $Zn^{2+}$ ions in serum typically ranges from 10 to 20 μM in healthy individuals. However, free $Zn^{2+}$ ion levels are generally within 1-3 nM in serum.[49, 50] Interestingly, the concentrations of $Zn^{2+}$ ions vary among different tissues and under various pathological conditions. Various organs, such as the hippocampus, amygdala, cortex, pancreas, and prostate, naturally have elevated levels of $Zn^{2+}$ ions. Dysregulation of $Zn^{2+}$ is associated with prostate-related diseases. The concentration of $Zn^{2+}$ ions in prostate epithelial cells has been identified to range from 800 to 1500 μM.[51] The $Zn^{2+}$ ions concentration in breast cancer cells has been reported to be 19 times higher than those found in healthy cells.[52] Given this physiological variability, our $Zn^{2+}$-responsive suprasome system represents a promising strategy for targeted ionophore delivery, particularly in tissues and pathological states characterized by elevated $Zn^{2+}$ concentrations. However, further experimental validation at physiological $Zn^{2+}$ concentrations would be beneficial for future studies.

#### 3.4.9.4 Suprasome Disruption-based Ion Transport Activity across EYPC/CHOL-LUV⊃MgG

A $Zn^{2+}$ concentration-dependent study was conducted to assess suprasome disruption, revealing that higher $Zn^{2+}$ levels facilitate improved ion transport through the progressive release of encapsulated molecules. The suprasome was treated with varying concentrations of $Zn^{2+}$ (1 mM, 2 mM, 3 mM, 5 mM) for 10 minutes and in a clean, dry fluorescence cuvette (3 mL) containing 10 mM HEPES buffer with 100 mM KGlc and 100 μM EDTA (pH 7.0, 1920 μL). Following treatment, EYPC/CHOL-LUV⊃MgG (50 μL) liposomes were added to the solution under slow stirring conditions to allow equilibration and the diffusion of released molecules

into the lipid bilayer membrane. MgG fluorescence was monitored over time ($\lambda_{em}$ = 531 nm, $\lambda_{ex}$ = 506 nm) using a fluorescence spectrophotometer. At 50 seconds, valinomycin was added (final concentration 12 pM) to the cuvette, and the kinetics were measured up to 450 s. At this point, vesicles were fully lysed by adding 20 µL of 20% Triton X-100, and fluorescence measurements continued for an additional 50 s. The normalized percent transport efficiency at 450 s was taken as the ion transport efficiency of $Zn^{2+}$-treated suprasome at each $Zn^{2+}$ concentration.

### 3.4.9.5 Effect of Metal Ions on the Hydrodynamic Diameter of Suprasome

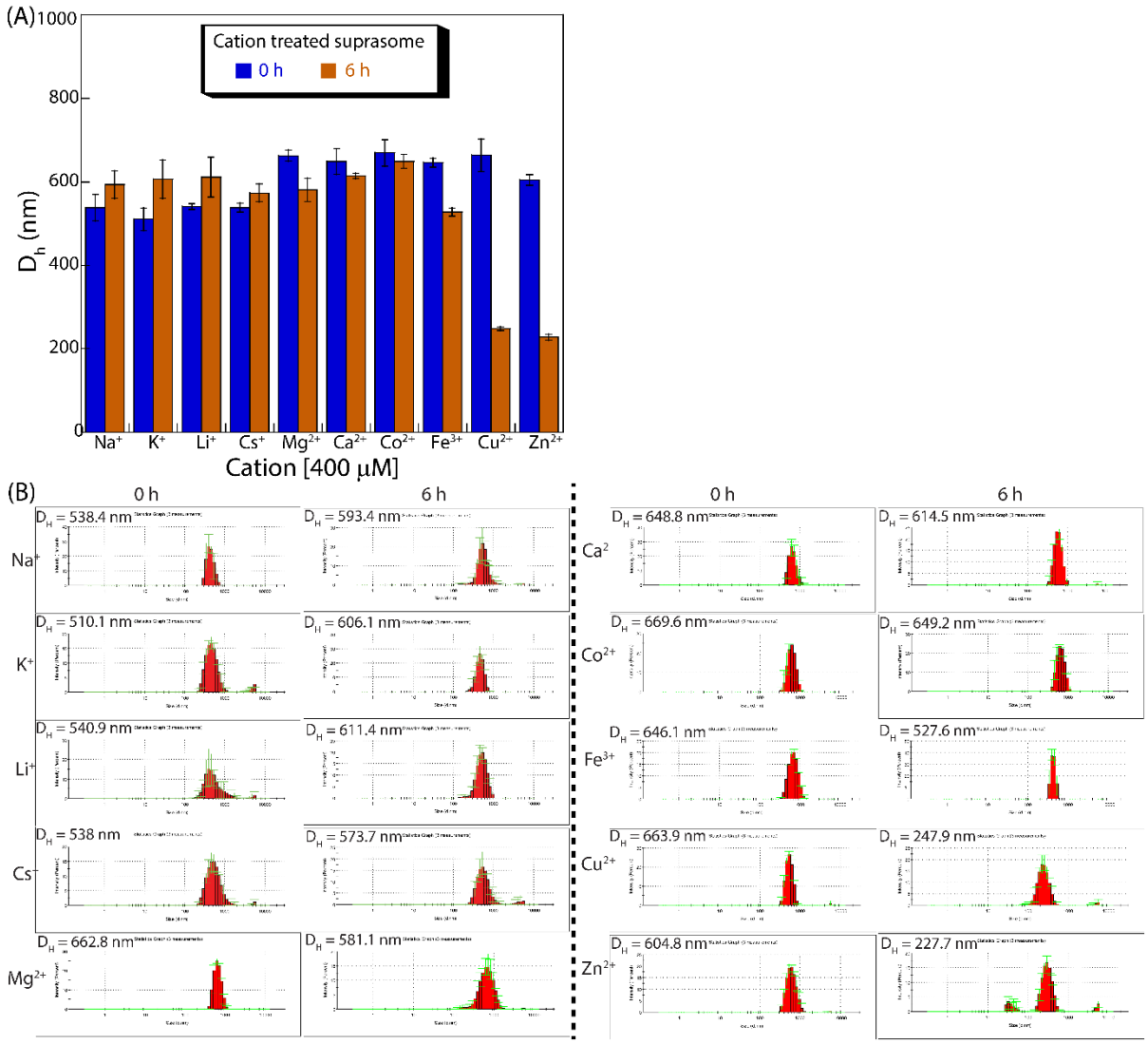


**Figure 3.28** The effect of different metal ions on the stability of suprasomes was measured by (A) hydrodynamic diameter and (B) corresponding size distribution plots.

Suprasomes were prepared using the aforementioned methods and then treated with 400 μM of different cations ($Na^+$, $K^+$, $Li^+$, $Cs^+$, $Mg^{2+}$, $Ca^{2+}$, $Co^{2+}$, $Fe^{3+}$, $Cu^{2+}$, $Zn^{2+}$) for 6 h to understand the effect of different metal ions on the stability of suprasome. Among the treated metals, $Zn^{2+}$ and $Cu^{2+}$ showed maximum effect on the size ($D_h$ values) of suprasomes. The observed decrease in size suggested a slow release of compound **3.6** from the suprasome and subsequent rearrangement to form smaller structures.

### 3.4.10 Antimicrobial Activity Assessment

The antimicrobial activities of the potent compounds, along with suprasomes, were assessed by the micro-broth dilution method in the absence and presence of $Zn^{2+}$ ions. The minimum inhibitory concentration (MIC) was assessed against various gram-positive bacteria (*S. aureus* and MRSA) and gram-negative bacteria (*E. coli* and *P. aeruginosa*). The glycerol stock of the bacterial culture was streaked onto the agar plate containing the Luria Bertani (LB) media. A single colony was inoculated into broth media and incubated at 37 ºC with shaking at 180 rpm until the mid-logarithmic phase was reached. The compounds were serially diluted in PBS buffer containing 4% DMSO in a 96-well plate. Subsequently, a bacterial suspension adjusted to an optical density (OD) of 0.02 at 600 nm was added to the serially diluted compounds. The plate was then incubated at 37 ºC for 14-16 hours. After incubation, the MIC was determined by visually assessing wells with growth inhibition. Additionally, the OD was measured using a BioTek microplate reader at 600 nm to quantify bacterial growth.

### 3.4.11 Evidence of $Zn^{2+}$ Ion Internalisation in *S. aureus* through the AQZ Assay

To validate the internalization of $Zn^{2+}$ ions inside the bacterial cells, an AQZ dye-based assay was performed. The *S. aureus* bacterial cells were grown till mid logarithmic phase and further

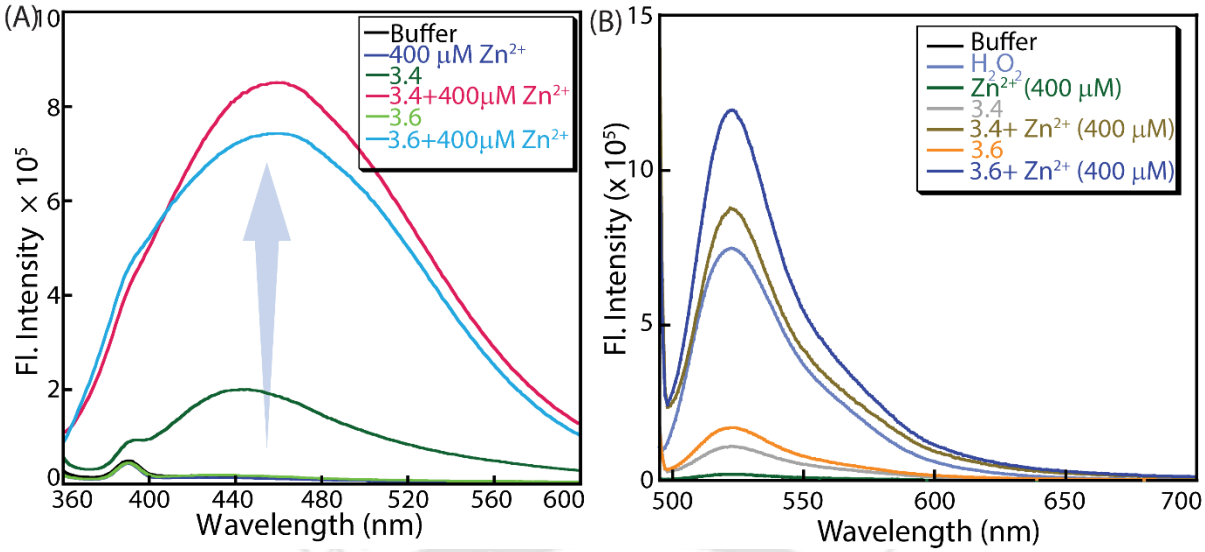


**Figure 3.29** (A) AQZ fluorescence-based $Zn^{2+}$ ion internalization to the S. aureus cells in the presence of compounds **3.4** and **3.6**. (B) DCF-DA fluorescence-based assay to investigate $Zn^{2+}$ ion transport mediated ROS generation efficacy within *S. aureus* cells.

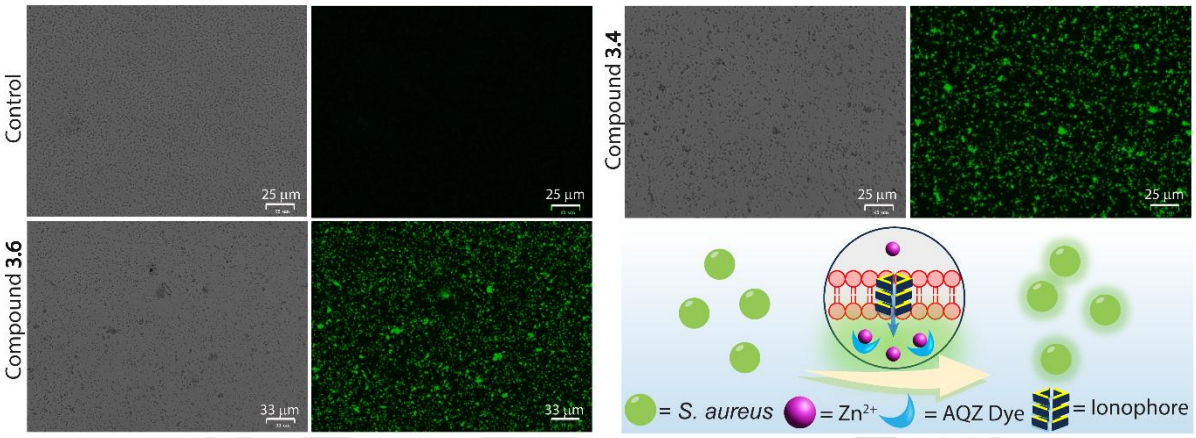


**Figure 3.30** Representative fluorescence microscopic images of $Zn^{2+}$ ion delivery through AQZ assay in *S. aureus* in the absence and presence of compounds **3.4** and **3.6**.

treated with compounds **3.4** and **3.6** in the presence and absence of $Zn^{2+}$ ions for 1 h in an incubator-shaker at 37 °C, 180 rpm. The bacterial cells treated with only $Zn^{2+}$ ions were used as controls. After the incubation period, the cells were centrifuged at 5000 rpm for 3 minutes to remove excess compounds. Further, cells were resuspended in Milli-Q water. Fluorescence spectra were taken just after the addition of AQZ dye (50 µM) at 360 nm ($\lambda_{ex}$ = 344 nm). Fluorescent images of bacterial samples were captured using a ZOE fluorescent cell imager with a blue excitation channel (355/40 nm) and a green emission channel (517/23 nm).

### 3.4.12 DCF-DA (2',7'-Dichlorodihydrofluorescein diacetate) Assay for ROS Generation

The generation of reactive oxygen species (ROS) in *S. aureus* treated with compounds **3.4** and **3.6**, with and without $Zn^{2+}$, was assessed using the 2′,7′-dichlorofluorescein diacetate ($H_2$-DCF-DA) oxidation assay. Cells in the mid-logarithmic phase were used for the measurements. Bacterial cells were cultured, harvested, and treated with the compounds at their MIC value, both in the presence and absence of $Zn^{2+}$ ions and kept for 1 h in a shaker incubator at 37 °C, 180 rpm. Controls included cells treated with 3% DMSO (negative control) and 2% $H_2O_2$ (positive control) in buffer (HEPES 10 mM, glucose 20 mM). After treatment, the cells were centrifuged, resuspended in buffer, and incubated with 100 µM $H_2$-DCF-DA dye in the dark for 30 minutes. ROS levels were measured by detecting DCF fluorescence at 515 nm (emission) ($\lambda_{ex}$ = 485 nm).

Additionally, ROS production was confirmed via fluorescence microscopy. The treated cells were washed, stained with DCF-DA, and incubated at 37 °C for 30 minutes. Excess dye was removed by washing, and the cells were fixed with 2% formaldehyde. Fluorescent images of bacterial samples were captured using a ZOE fluorescent cell imager with a blue excitation channel (355/40 nm) and a green emission channel (517/23 nm).

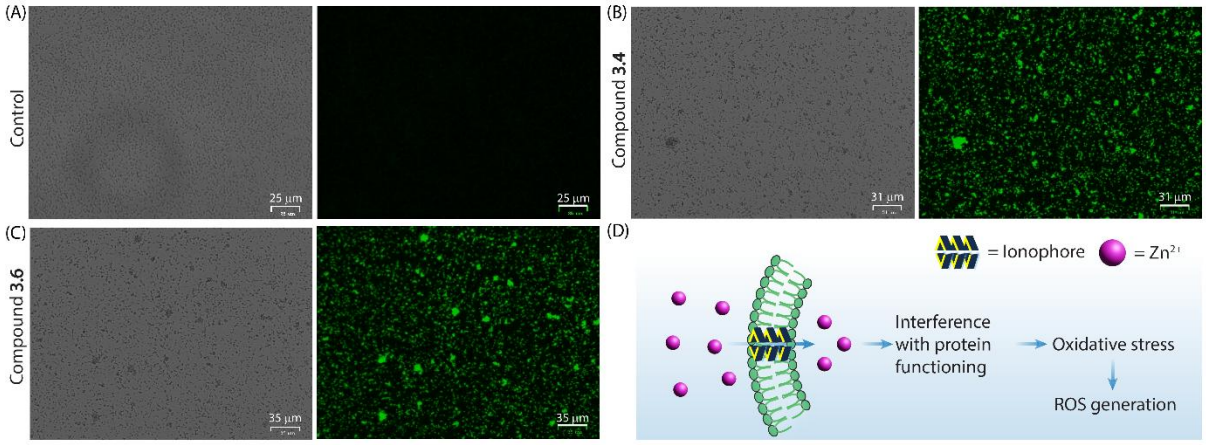


**Figure 3.31** Fluorescence microscopy-based DCF-DA assay for confirmation of ROS generation in *S. aureus*; (A) control, (B) compound **3.4,** and (C) compound **3.6** along with $Zn^{2+}$ ion treatment. (D) Schematic representation of ROS generation activity within the bacterial cells.

### 3.4.13 Propidium Iodide Uptake Assay and Membrane Depolarization Assay

The propidium iodide (PI) uptake assay was performed to assess the membrane integrity of bacteria in the presence of compounds. The previously outlined methodology was used to

culture and harvest *S. aureus* cells. After resuspending the bacterial pellet in PBS buffer, the compounds were added at their MIC value, with and without $Zn^{2+}$ (400 µM) to the cell suspension. The cells were also resuspended in the buffer for the control. Furthermore, the cells were incubated at 37 °C, 180 rpm for 1 h. After incubation, samples were centrifuged and resuspended in the buffer. Further, it was treated with PI (30 µM) for 30 minutes. Unbound dye was removed through centrifugation, and the bacterial cells were resuspended in the buffer. The fluorescence spectrum of the samples was recorded ($\lambda_{ex}$ = 535 nm, $\lambda_{em}$ = 610 nm).

Membrane depolarization assay was performed against *S. aureus* cells, which were grown in LB broth at 37 °C, 180 rpm, till the mid-logarithmic phase. The cells were collected by centrifugation at 5000 rpm for 3 mins. After re-suspending the bacterial pellet in HEPES buffer (10 mM HEPES in 50 mM glucose), $DiSC_3(5)$ dye (membrane depolarization sensing dye) at 0.4 µM final concentration was added, and cells were incubated at 37 °C, 180 rpm for 1 hour. Thereupon, 100 mM KCl was added, followed by 15 mins of incubation. Afterwards, compounds were added at varied concentrations (0.5, 1, 10 µM) with $Zn^{2+}$ (400 µM) to the cell suspension along with 10 µM valinomycin as a positive control. The fluorescence spectra of suspended cells were recorded at 650 nm ($\lambda_{ex}$ = 620 nm).

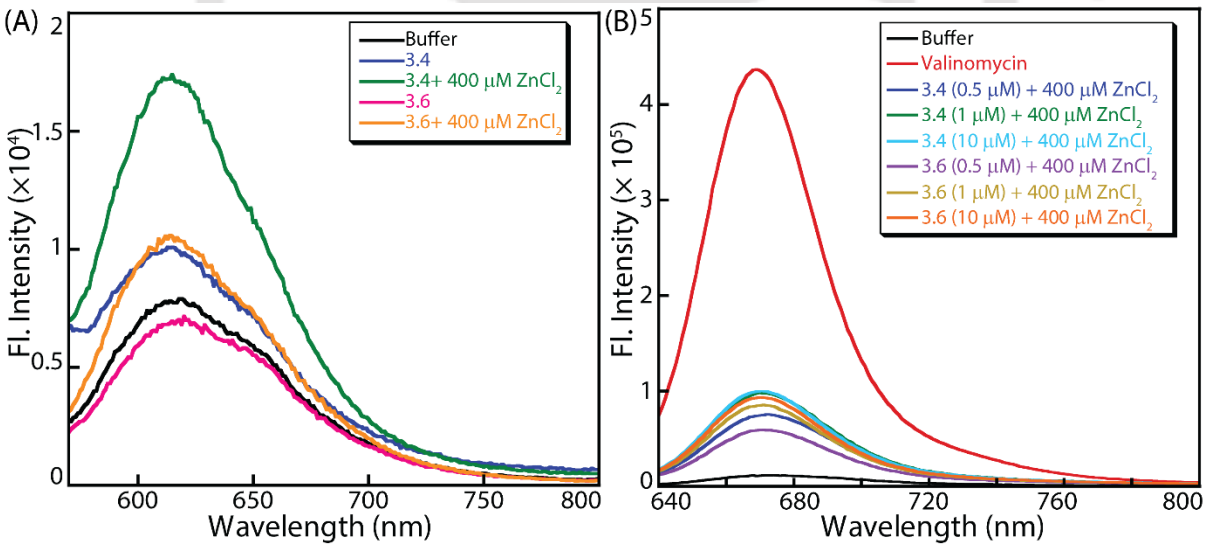


**Figure 3.32** (A) PI uptake and (B) membrane depolarization assay for compounds **3.4** and **3.6** in *S. aureus* cells.

### 3.4.14 Evaluation of Cytotoxicity in Red Blood Cells

Biocompatibility of the potent compounds **3.4** and **3.6** was performed against fresh erythrocytes as per our earlier reported protocol and as per the guidelines of the Institutional Human Ethics Committee (IHEC).

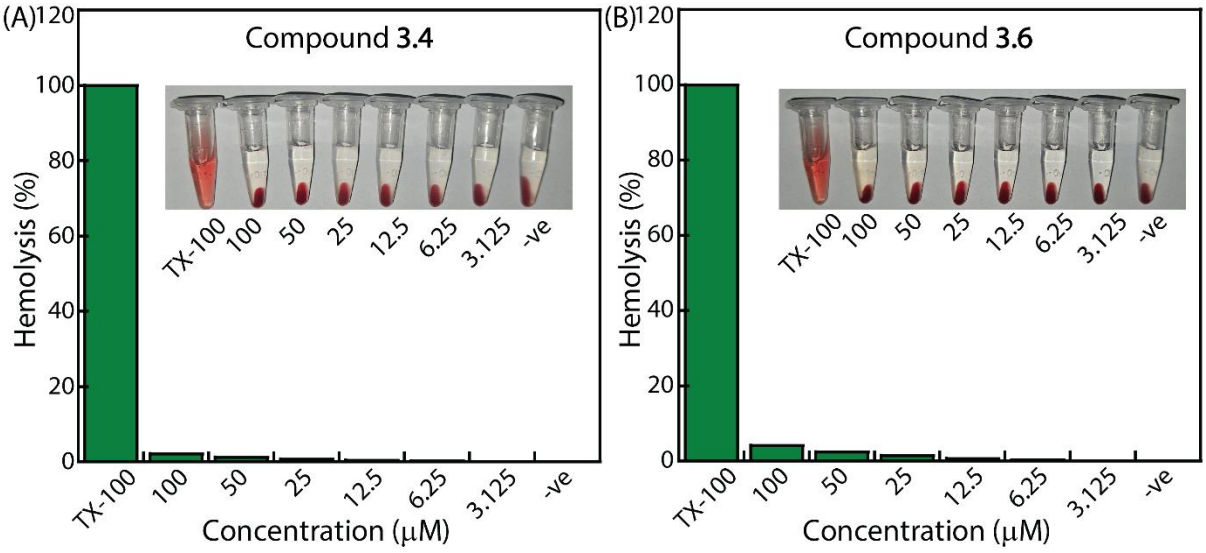


**Figure 3.33** Hemolytic assay of (A) compound **3.4** and (B) compound **3.6**.

Before assay, blood was centrifuged to separate the plasma from erythrocytes at 1500 rpm for 5 min and washed twice with PBS buffer (7.4 pH). 5% hematocrit was prepared by resuspending erythrocytes in the buffer. Compounds **3.4** and **3.6** were serially diluted in the same buffer, and for the negative control, only buffer was taken, while for the positive control, detergent (0.1 % Triton-X) was taken for complete cell lysis. To the serially diluted compounds, hematocrit was added and incubated at room temperature for 1 h. After incubation, the sample vials were centrifuged, and 200 μL of the supernatant from the sample vials was aliquoted into 96-well plates, and its absorbance was measured at 410 nm by using a plate reader (BioTek).[53] The hemolytic assessment was done by comparing the absorbance of the samples with negative and positive control.

### 3.4.15 Bacterial Cell Morphology Analysis

For morphological analysis, *S. aureus* cells were treated with compounds until the mid-logarithmic phase. Cells were harvested and treated with the potent compounds (**3.4** and **3.6**) in the presence of $Zn^{2+}$ (400 μM) at their MIC values. Bacterial cells present only in the buffer were used as a control. After incubation at 37 °C and 180 rpm, the cells were centrifuged, and the bacterial pellet was resuspended in PBS buffer and treated with 2% formaldehyde for 30

minutes to fix the cellular morphology. Bacterial cells were again centrifuged and resuspended in Milli-Q water. For the analysis, 10 µL of the sample was mounted onto a glass grid and allowed to dry under laminar airflow. Before the analysis, the sample glass grid was coated with gold and FESEM images were taken in the Sigma 300 FESEM instrument.

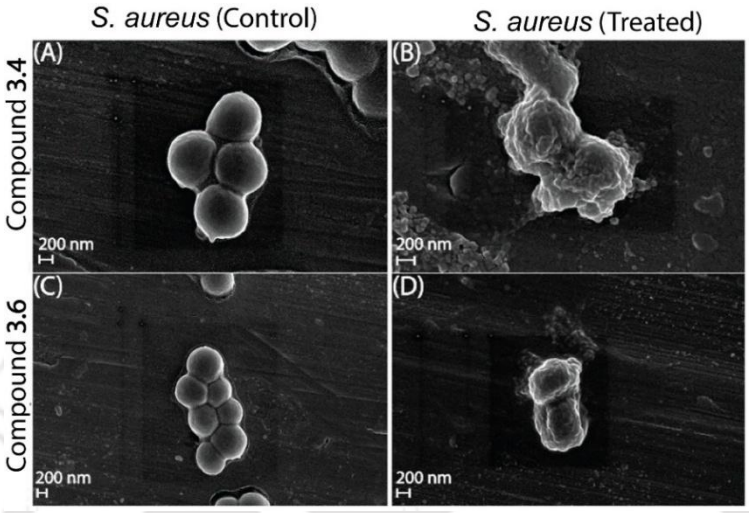


**Figure 3.34** Morphological analysis of *S. aureus* through FESEM. Control images of bacteria before (A, C) and after (B, D) treatment by compound **3.4** and **3.6**, respectively (at MIC value) along with $Zn^{2+}$ (400 µM), respectively.

### 3.4.16 Absorption and Emission Spectral Analysis of Compound 3.6

The UV-Vis absorbance and fluorescence ($\lambda_{ex}$ = 400 nm) properties of compound **3.6** (10 µM) in 40% DMSO/water were studied to investigate the absorbance and emission spectra.

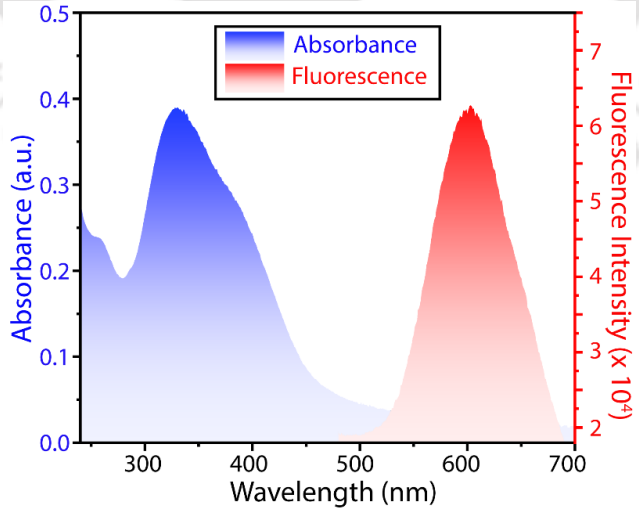


**Figure 3.35** UV-Vis absorbance and fluorescence spectra of compound **3.6** (10 µM) in 40% DMSO/water.

### 3.4.17 NMR and HRMS Spectra of the Synthesised Compounds

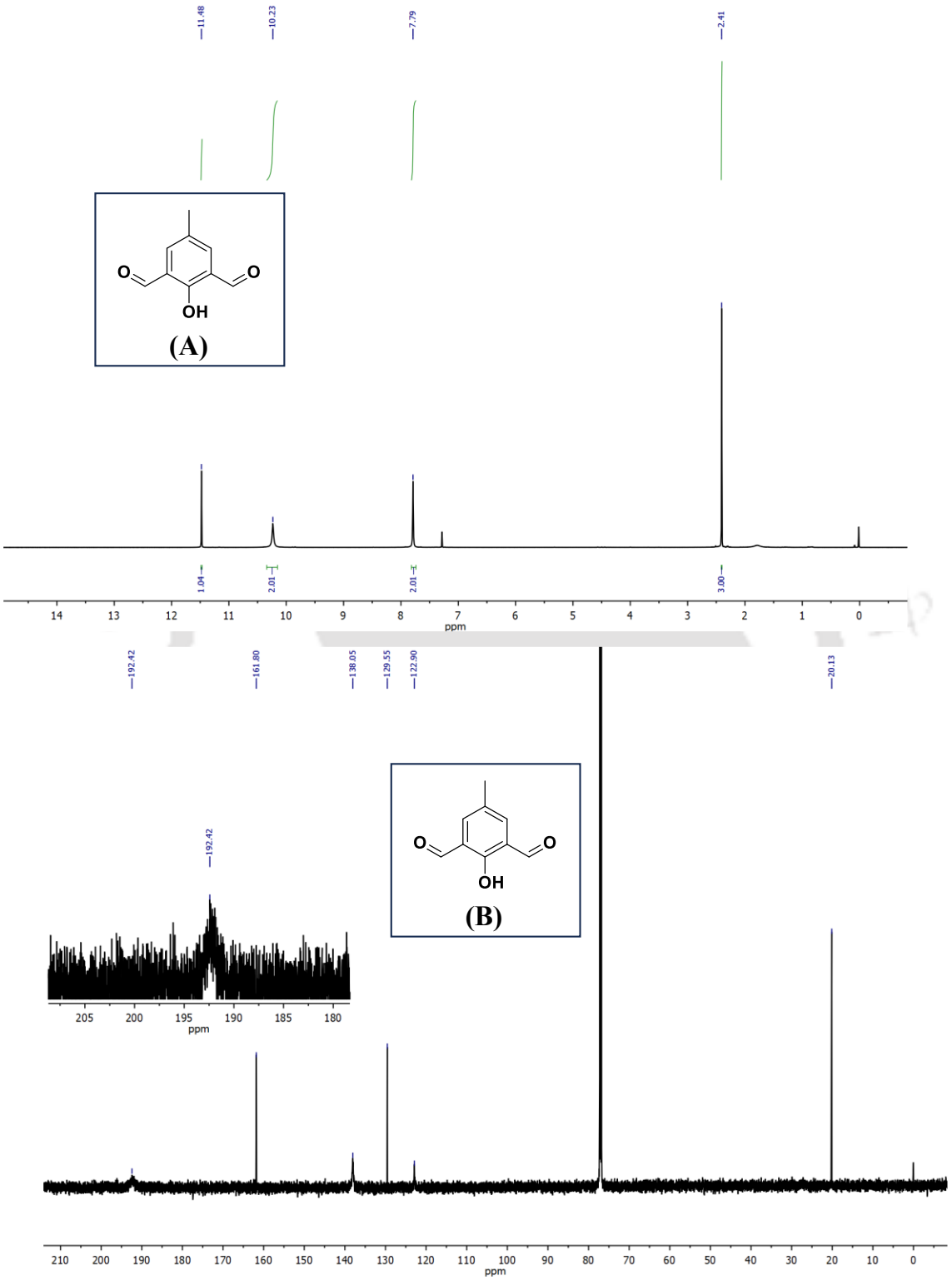


**Figure 3.36** $^{1}$H NMR (A) and $^{13}$C NMR (B) spectra of 2-hydroxy-5-methylisophthalaldehyde in the Chloroform-*d* solvent


**Figure 3.37** $^{1}$H NMR (A) and $^{13}$C NMR (B) spectra of 2-methoxy-5-methylisophthalaldehyde in the Chloroform-*d* solvent**.**

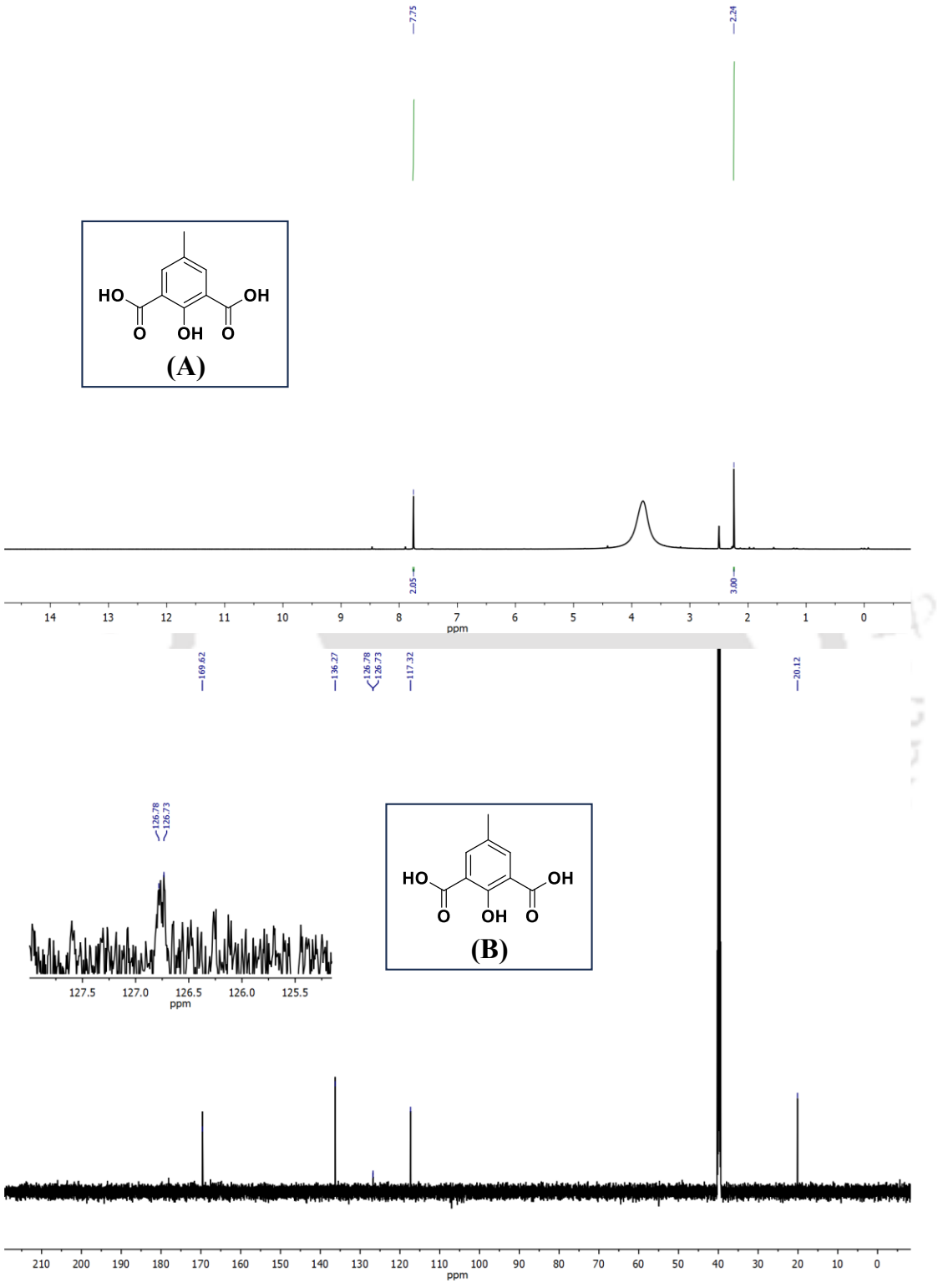


**Figure 3.38** $^{1}$H NMR (A) and $^{13}$C NMR (B) spectra of 2-hydroxy-5-methylisophthalic acid in DMSO-$d_6$

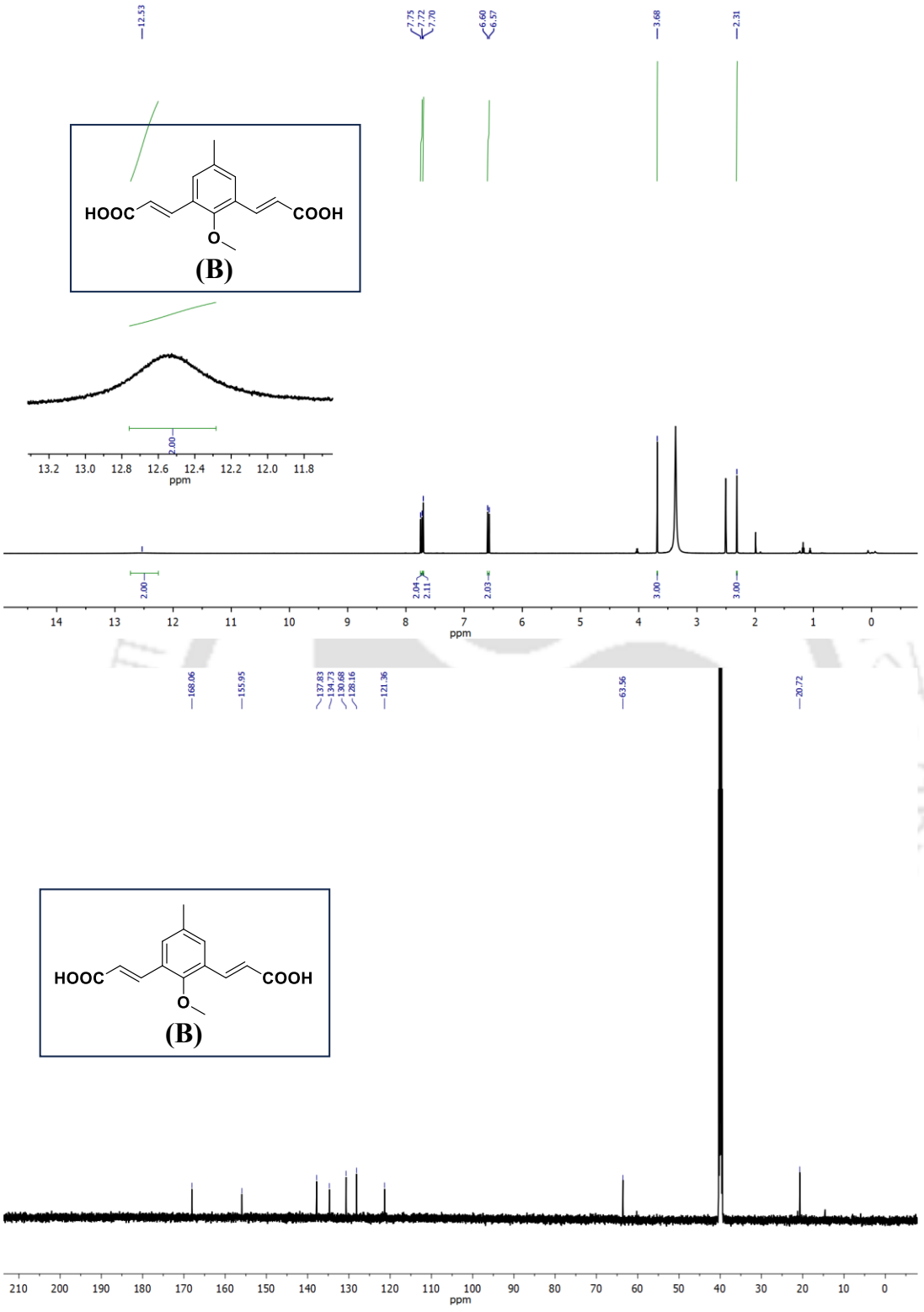


**Figure 3.39** $^{1}$H NMR (A) and $^{13}$C NMR (B) spectra of 3,3'-(2-methoxy-5-methyl-1,3-phenylene)diacrylic acid in the DMSO-$d_6$ solvent**.**

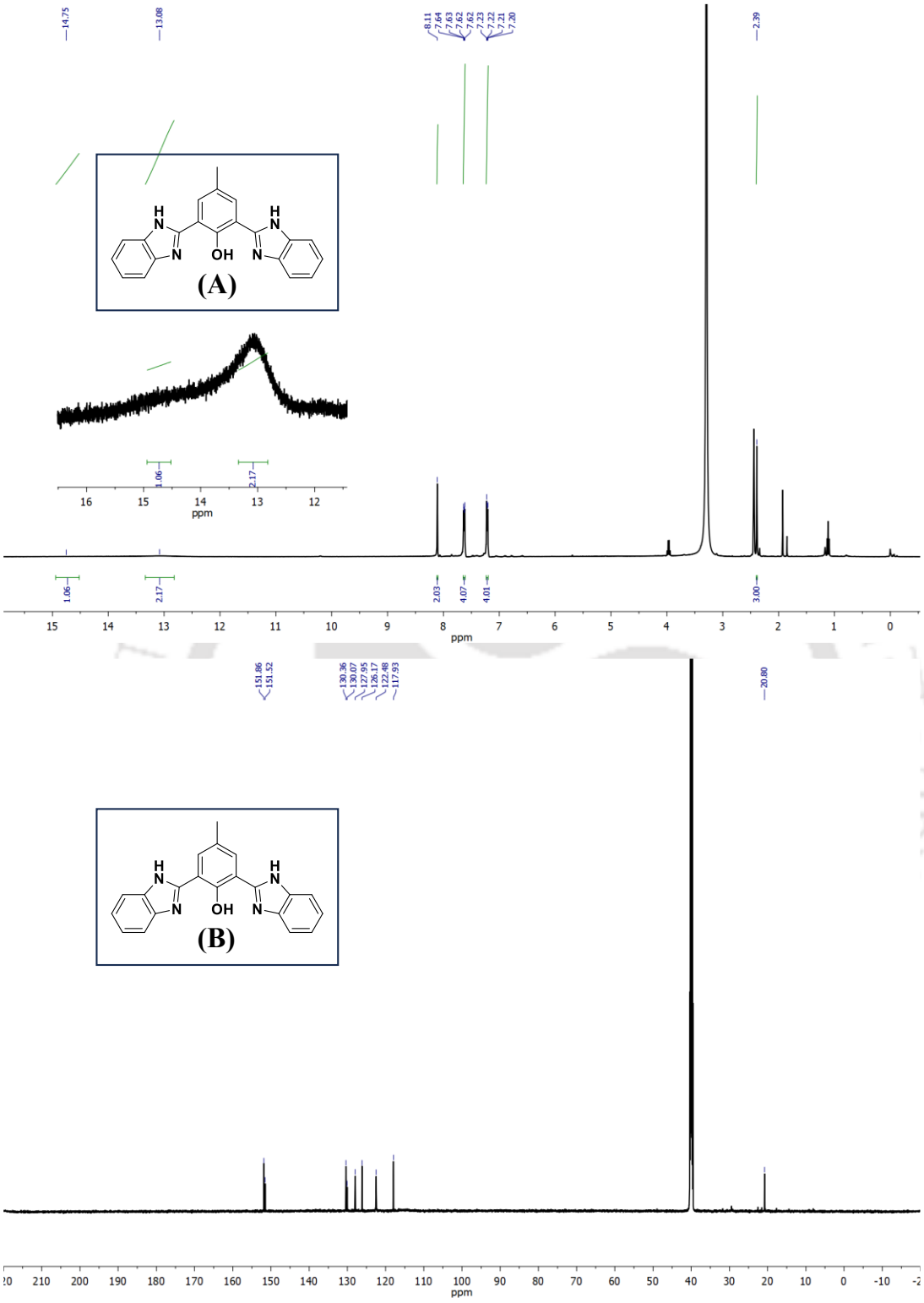


**Figure 3.40** $^{1}$H NMR (A) and $^{13}$C NMR (B) spectra of compound **3.1** in the DMSO-$d_6$ solvent.

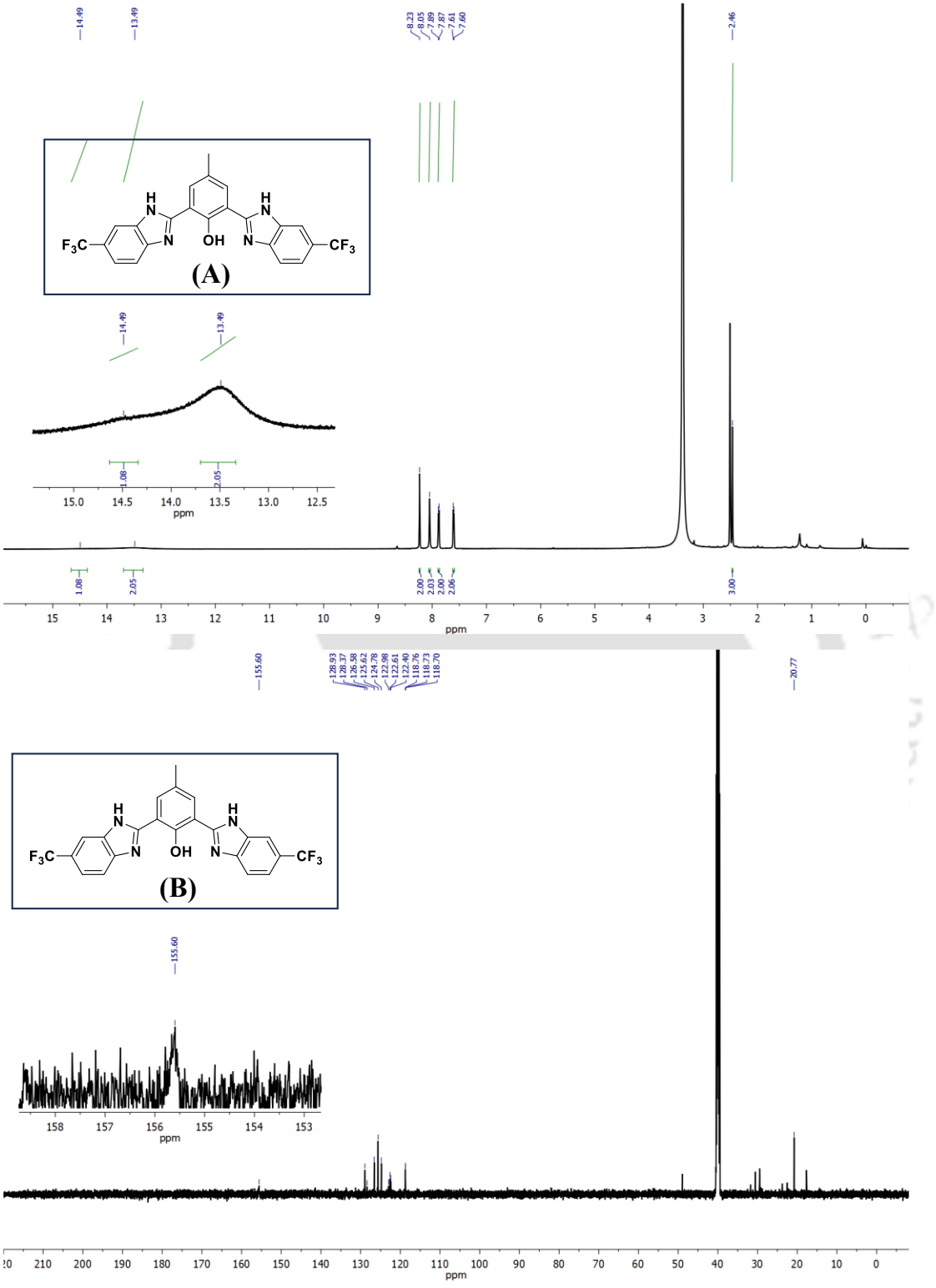


**Figure 3.41** $^{1}$H NMR (A) and $^{13}$C NMR (B) spectra of compound **3.2** in the DMSO-$d_6$ solvent**.**

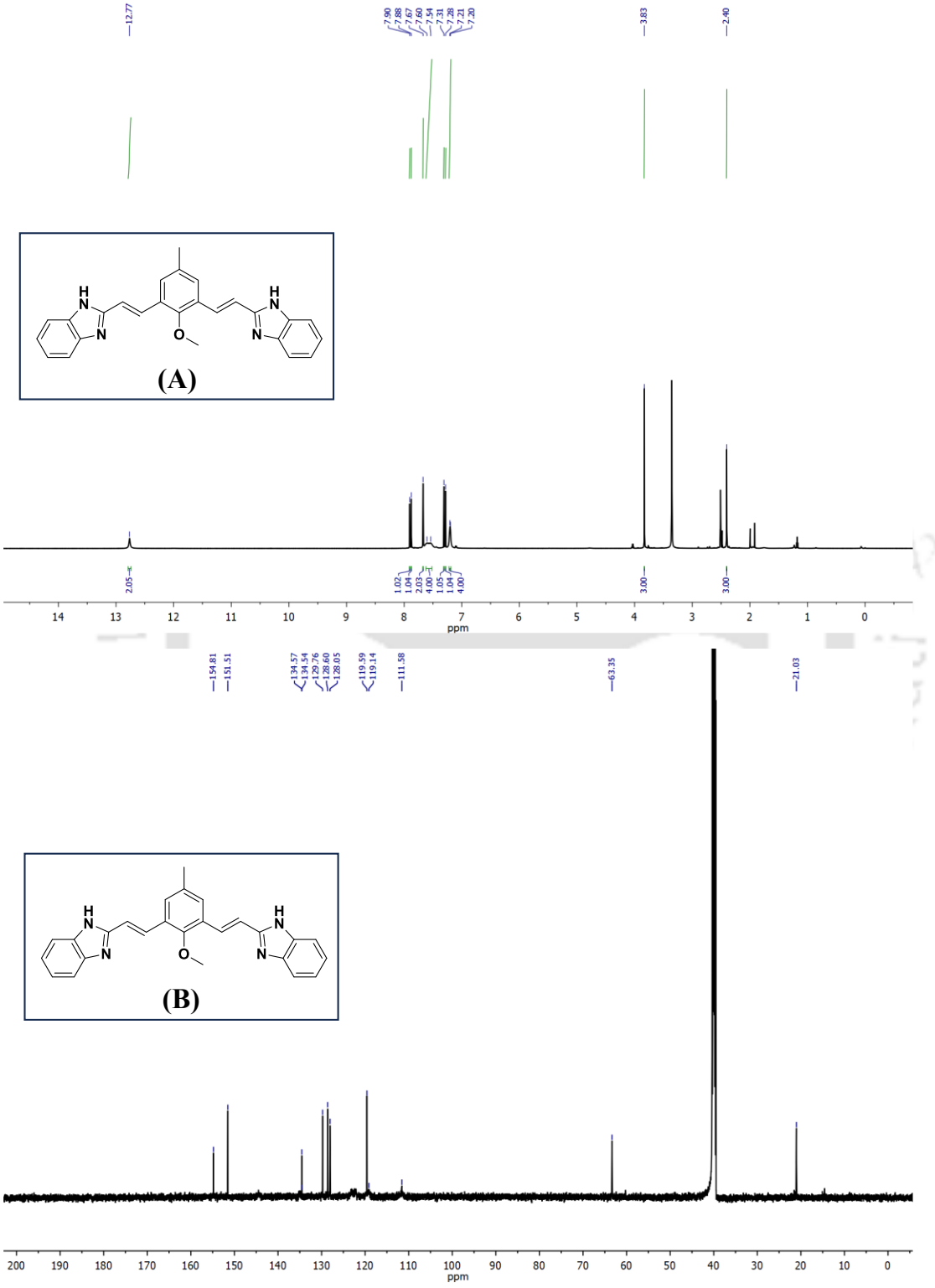


**Figure 3.42** $^{1}$H NMR (A) and $^{13}$C NMR (B) spectra of compound **3.3** in the DMSO-$d_6$ solvent**.**

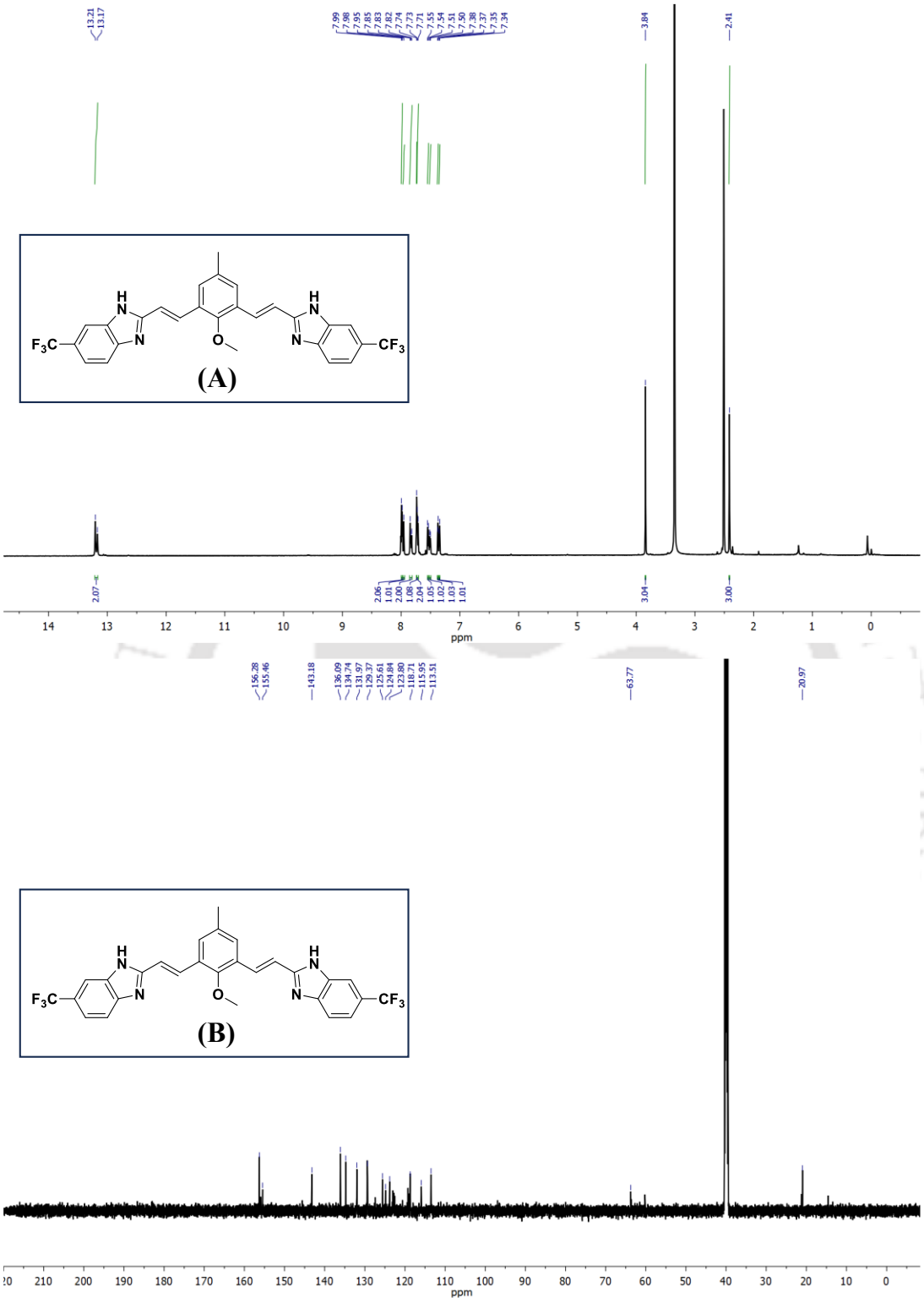


**Figure 3.43** $^{1}$H NMR (A) and $^{13}$C NMR (B) spectra of compound **3.4** in the DMSO-$d_6$ solvent**.**

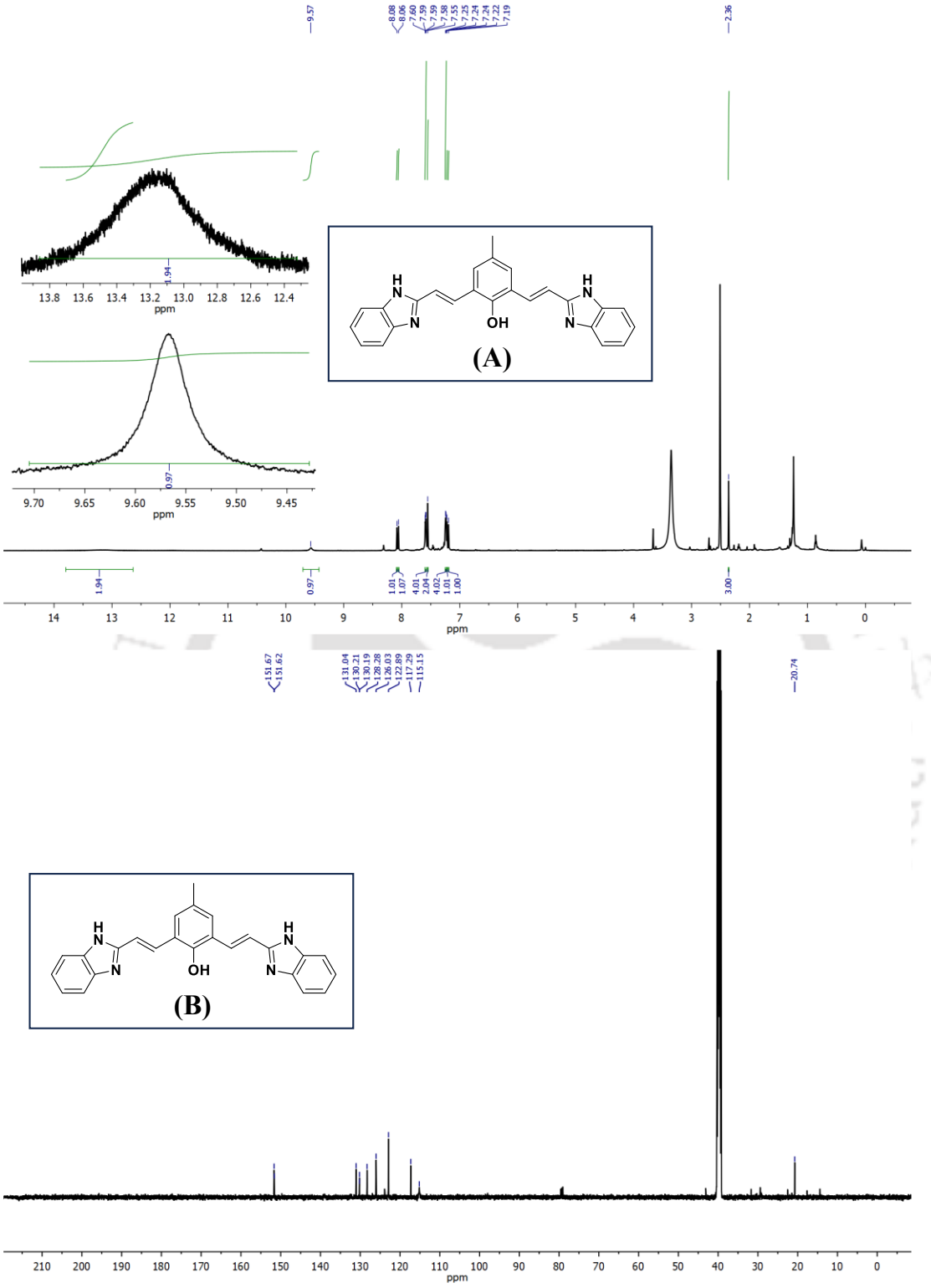


**Figure 3.44** $^{1}$H NMR (A) and $^{13}$C NMR (B) spectra of compound **3.5** in the DMSO-$d_6$ solvent**.**

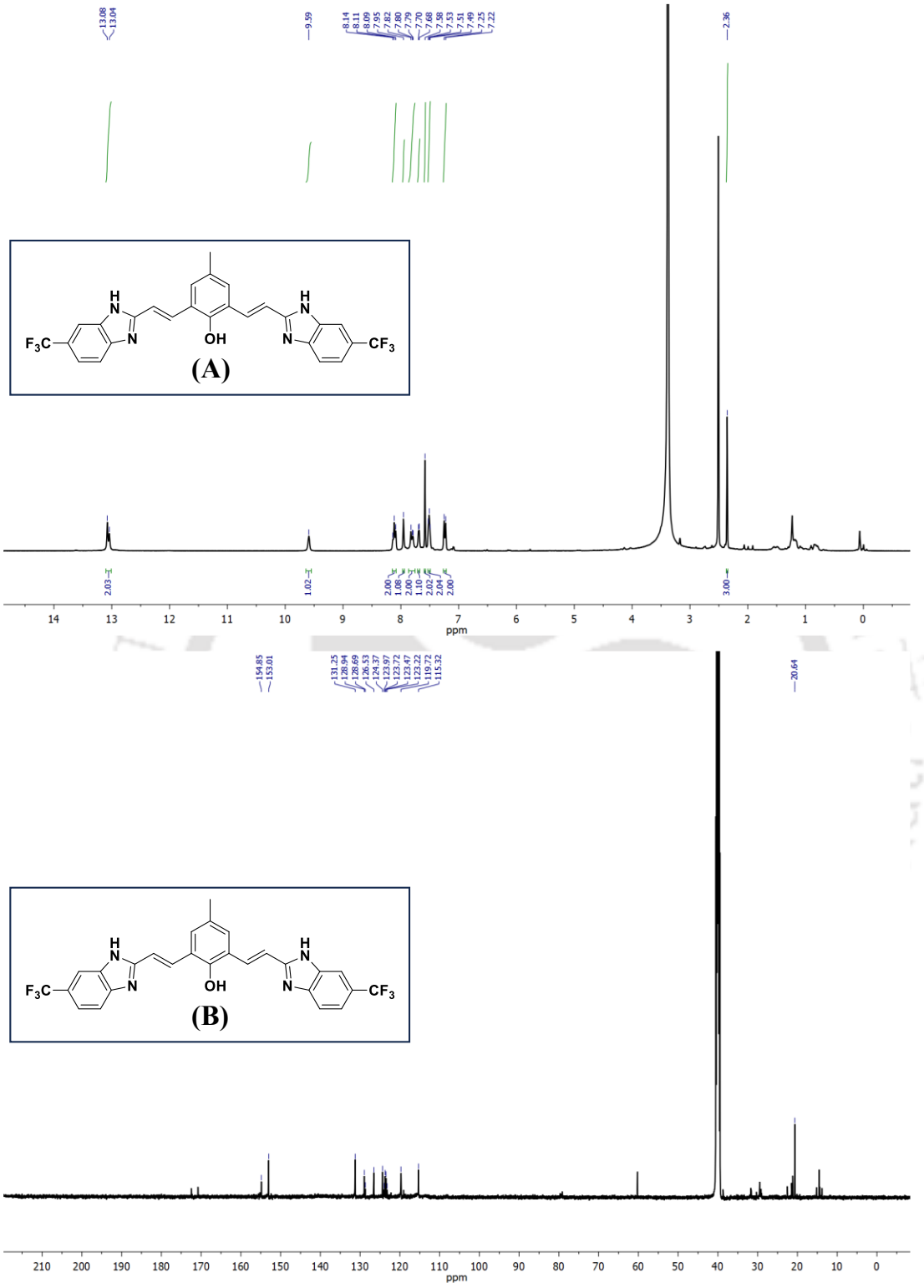


**Figure 3.45** $^{1}$H NMR (A) and 13C NMR (B) spectra of compound **3.6** in DMSO-$d_6$ solvent.

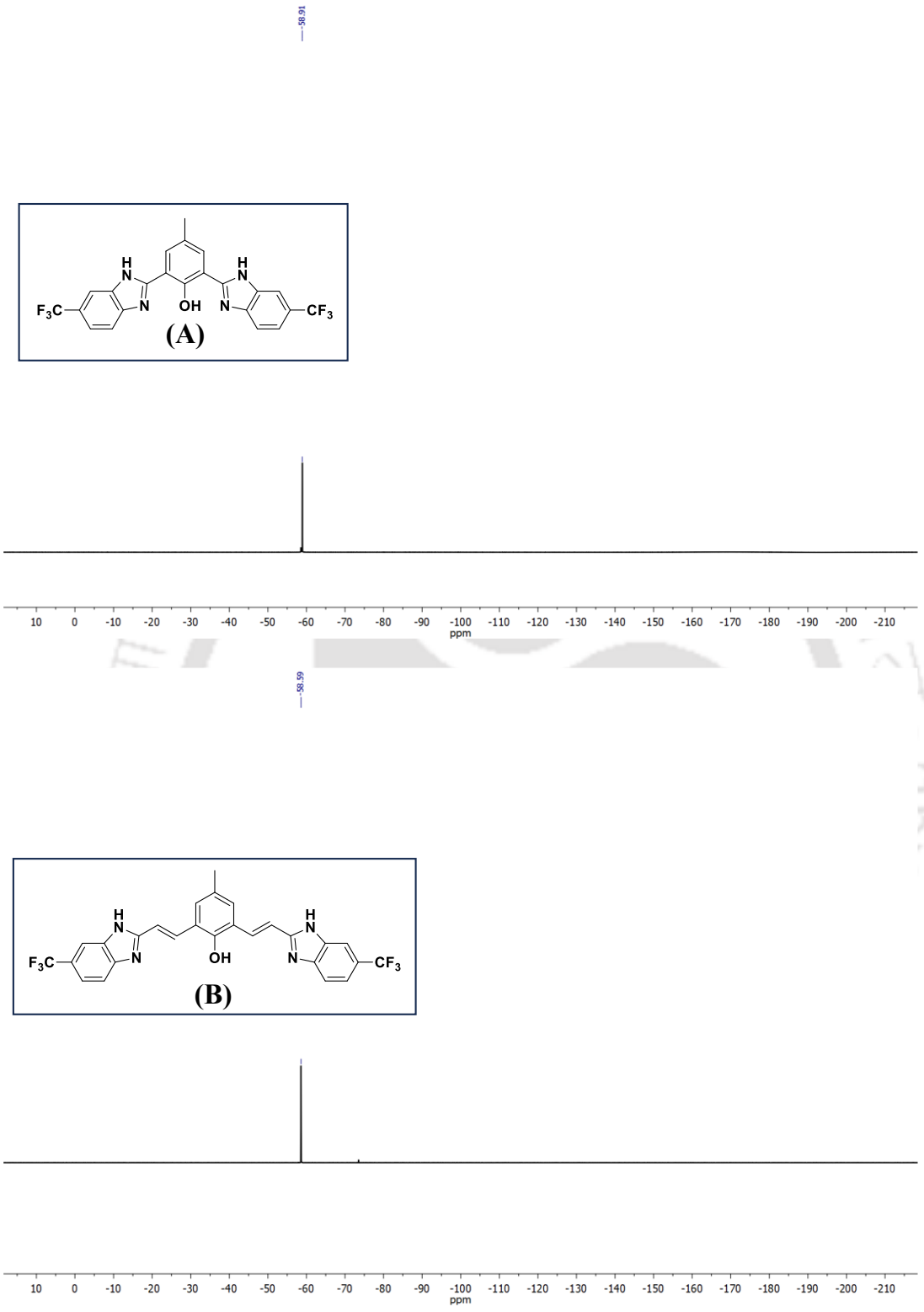


**Figure 3.46** $^{19}$F NMR of compound **3.2** (A) and **3.6** (B) in DMSO-$d_6$ solvent.

**HRMS Analysis of the Synthesised Compounds**

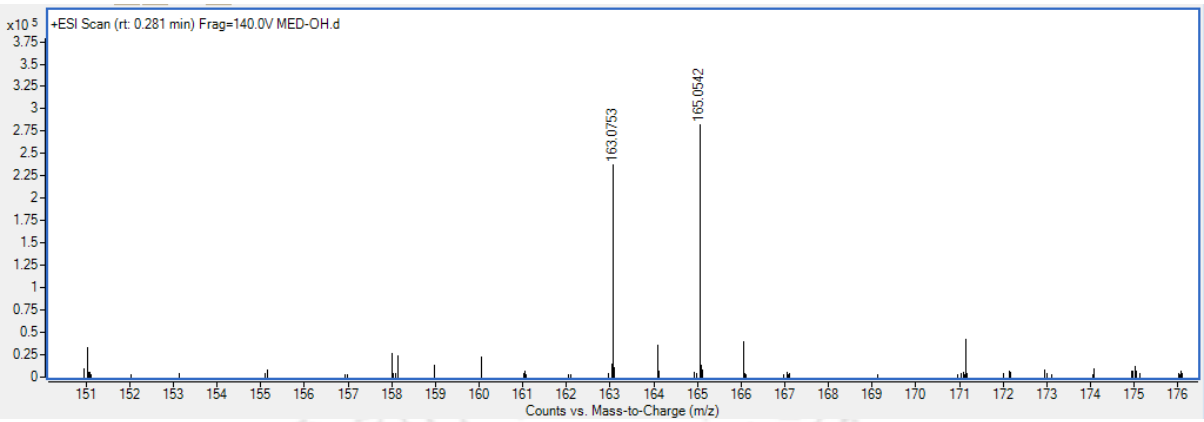


**Figure 3.47** HRMS spectra of 2-hydroxy-5-methylisophthalaldehyde.

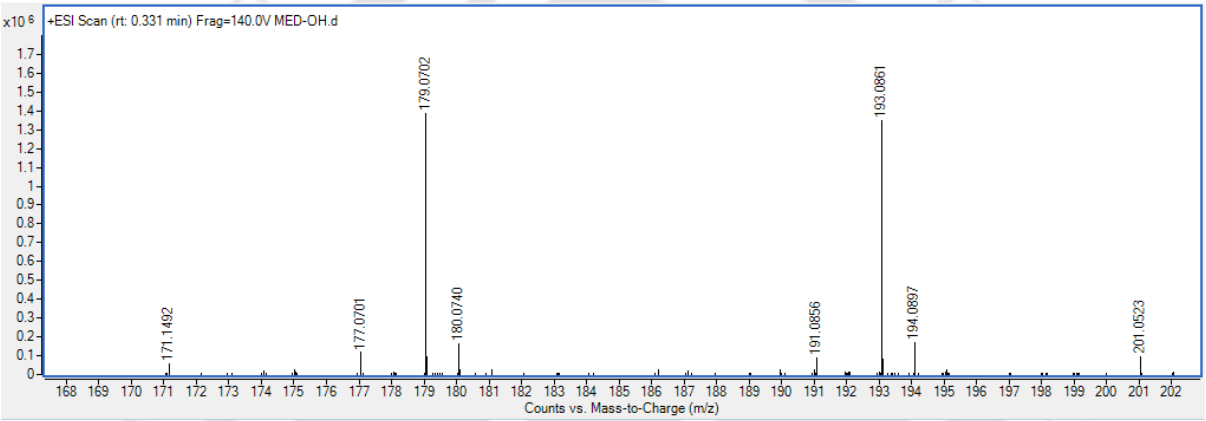


**Figure 3.48** HRMS spectra of 2-methoxy-5-methylisophthalaldehyde.

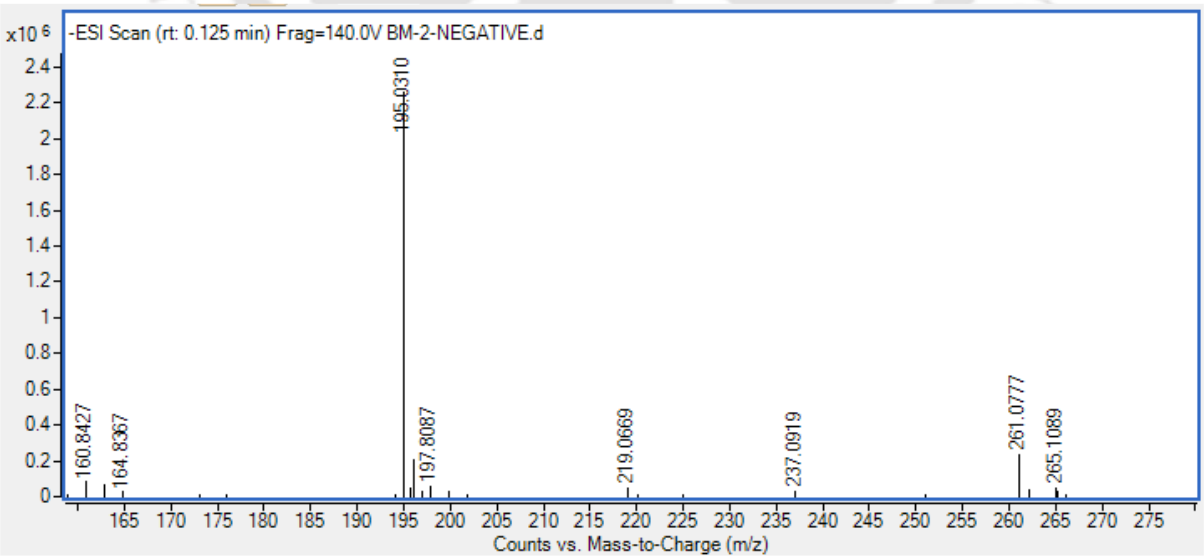


**Figure 3.49** HRMS spectra of 2-hydroxy-5-methylisophthalic acid.

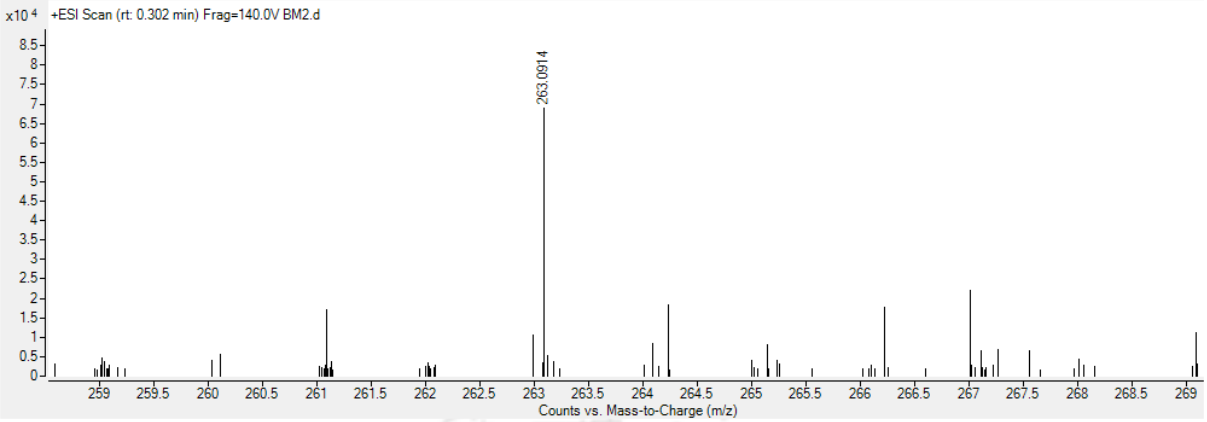


**Figure 3.50** HRMS spectra of 3,3'-(2-methoxy-5-methyl-1,3-phenylene)diacrylic acid.

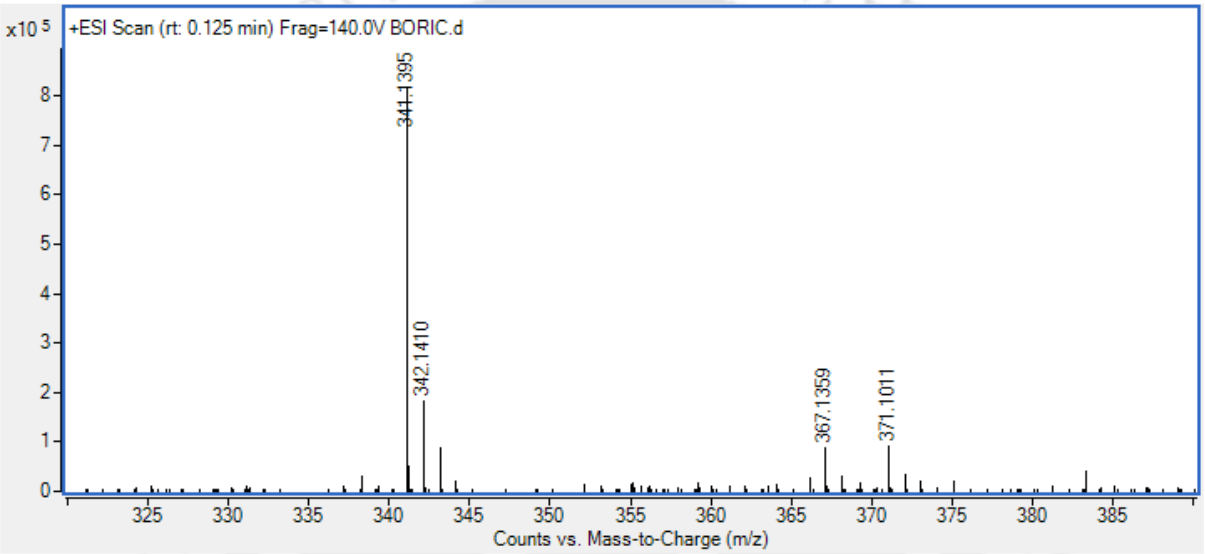


**Figure 3.51** HRMS spectra of compound **3.1**.

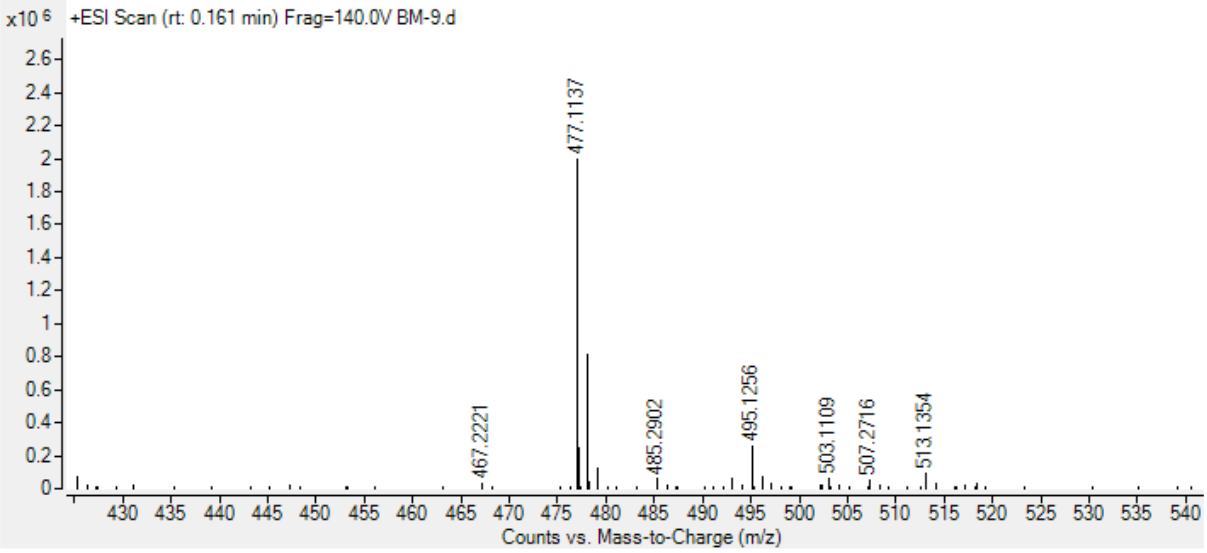


**Figure 3.52** HRMS spectra of compound **3.2**.

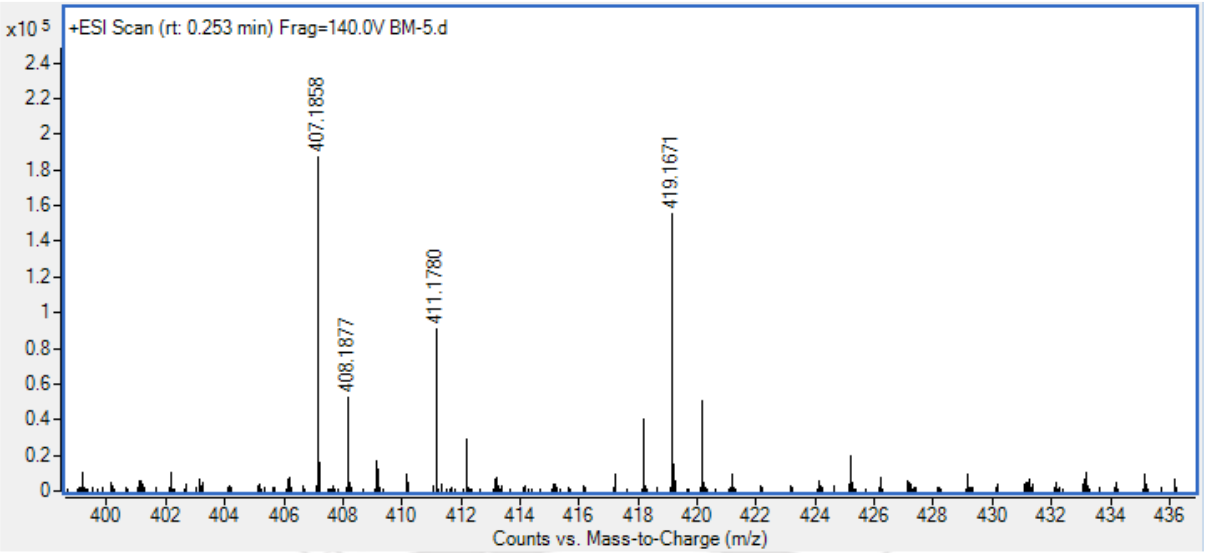


**Figure 3.53** HRMS spectra of compound **3.3**.

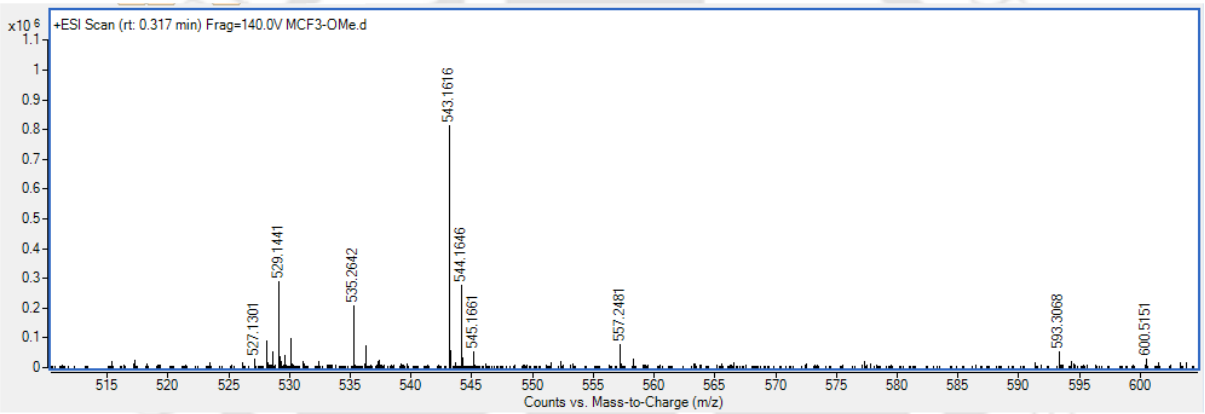


**Figure 3.54** HRMS spectra of compound **3.4**.

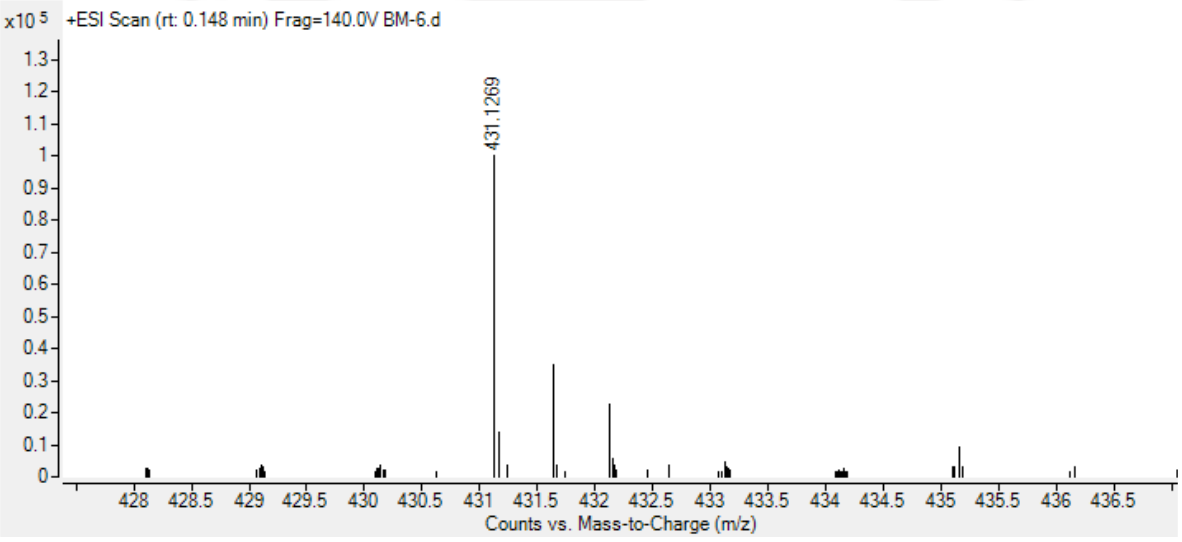


**Figure 3.55** HRMS spectra of compound **3.5**.

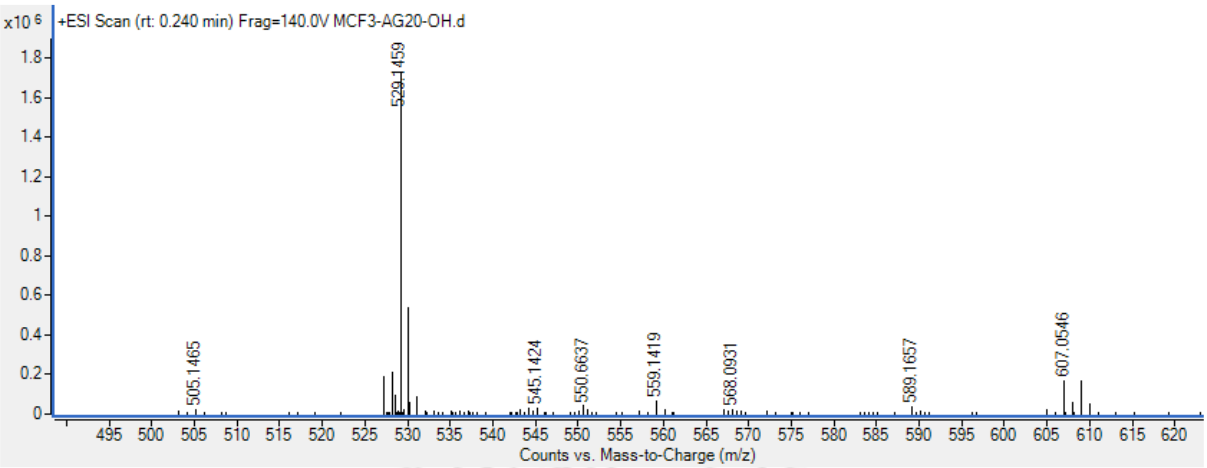


**Figure 3.56** HRMS spectra of compound **3.6**.

## 3.5 References

1. Yang, K.; Hua, B.; Qi, S.; Bai, B.; Yu, C.; Huang, F.; Yu, G., Suprasomes based on host–guest molecular recognition: an excellent alternative to liposomes in cancer theranostics. *Angew. Chem.* **2022,** *134* (52), e202213572.

2. Mondal, A.; Save, S. N.; Sarkar, S.; Mondal, D.; Mondal, J.; Sharma, S.; Talukdar, P., A Benzohydrazide-Based Artificial Ion Channel that Modulates Chloride Ion Concentration in Cancer Cells and Induces Apoptosis by Disruption of Autophagy. *J. Am. Chem. Soc.* **2023,** *145* (17), 9737-9745.

3. August, D. P.; Borsley, S.; Cockroft, S. L.; Della Sala, F.; Leigh, D. A.; Webb, S. J., Transmembrane ion channels formed by a Star of David [2] catenane and a molecular pentafoil knot. *J. Am. Chem. Soc.* **2020,** *142* (44), 18859-18865.

4. Sato, K.; Muraoka, T.; Kinbara, K., Supramolecular transmembrane ion channels formed by multiblock amphiphiles. *Acc. Chem. Res.* **2021,** *54* (19), 3700-3709.

5. Yang, J.; Yu, G.; Sessler, J. L.; Shin, I.; Gale, P. A.; Huang, F., Artificial transmembrane ion transporters as potential therapeutics. *Chem.* **2021,** *7* (12), 3256-3291.

6. Zhang, L.; Tian, J.; Lin, Z.; Dong, Z., Efficient sodium transmembrane permeation through helically folded nanopores with natural channel-like ion selectivity. *J. Am. Chem. Soc.* **2024,** *146* (12), 8500-8507.

7. Dewhirst, M. W.; Secomb, T. W., Transport of drugs from blood vessels to tumour tissue. *Nat. Rev. Cancer.* **2017,** *17* (12), 738-750.

8. Ermondi, G.; Lorenti, M.; Caron, G., Contribution of ionization and lipophilicity to drug binding to albumin: a preliminary step toward biodistribution prediction. *J. Med. Chem.* **2004,** *47* (16), 3949-3961.

9. Yan, T.; Liu, J., Transmembrane ion channels: from natural to artificial systems. *Angew. Chem. Int. Ed.* **2025,** *64* (1), e202416200.

10. McDevitt, C. A.; Ogunniyi, A. D.; Valkov, E.; Lawrence, M. C.; Kobe, B.; McEwan, A. G.; Paton, J. C., A molecular mechanism for bacterial susceptibility to zinc. *PLoS Pathog.* **2011,** *7* (11), e1002357.

11. McCall, K. A.; Huang, C. C.; Fierke, C. A., Function and mechanism of zinc metalloenzymes. *J. Nutr.* **2000,** *130* (5), 1437s-1446s.

12. Keri, R. S.; Hiremathad, A.; Budagumpi, S.; Nagaraja, B. M.; design, d., Comprehensive review in current developments of benzimidazole-based medicinal chemistry. *Chem. Biol. Drug Des.* **2015,** *86* (1), 19-65.

13. Hu, Q.-D.; Tang, G.-P.; Chu, P. K., Cyclodextrin-based host–guest supramolecular nanoparticles for delivery: from design to applications. *Acc. Chem. Res.* **2014,** *47* (7), 2017-2025.

14. Schmidt, B. V.; Barner-Kowollik, C., Dynamic macromolecular material design—The versatility of cyclodextrin-based host–guest chemistry. *Angew. Chem. Int. Ed.* **2017,** *56* (29), 8350-8369.

15. Gartland, S. A.; Johnson, T. G.; Walkley, E.; Langton, M. J., Inter-Vesicle Signal Transduction Using a Photo-Responsive Zinc Ionophore. *Angew. Chem. Int. Ed.* **2023,** *62* (38), e202309080.

16. Jowett, L. A.; Howe, E. N. W.; Wu, X.; Busschaert, N.; Gale, P. A., New Insights into the Anion Transport Selectivity and Mechanism of Tren-based Tris-(thio)ureas. *Chem. Eur. J.* **2018,** *24* (41), 10475-10487.

17. Dey, S.; Patel, A.; Haloi, N.; Srimayee, S.; Paul, S.; Barik, G. K.; Akhtar, N.; Shaw, D.; Hazarika, G.; Prusty, B. M., Quinoline thiourea-based zinc ionophores with antibacterial activity. *J. Med. Chem.* **2023,** *66* (16), 11078-11093.

18. Langton, M. J.; Williams, N. H.; Hunter, C. A., Recognition-Controlled Membrane Translocation for Signal Transduction across Lipid Bilayers. *J. Am. Chem. Soc.* **2017,** *139* (18), 6461-6466.

19. Sarkar, B.; Das, K.; Saha, T.; Prasad, E.; Gardas, R. L., Insights into the formations of host–guest complexes based on the Benzimidazolium based ionic liquids− β-Cyclodextrin systems. *ACS Phys. Chem. Au.* **2021,** *2* (1), 3-15.

20. Gao, Y. R.; Li, G. Y.; Zhou, Z. S.; Guo, L.; Liu, X. Y., Supramolecular assembly of poly(β-cyclodextrin) block copolymer and benzimidazole-poly(ε-caprolactone) based on host-guest recognition for drug delivery. *Colloid. Surface. B* **2017,** *160*, 364-371.

21. Lou, J. C.; Schuster, J. A.; Barrera, F. N.; Best, M. D., ATP-Responsive Liposomes via Screening of Lipid Switches Designed to Undergo Conformational Changes upon Binding Phosphorylated Metabolites. *J. Am. Chem. Soc.* **2022,** *144* (8), 3746-3756.

22. Prusty, B. M.; Karn, R.; Patel, A.; Mazumder, P.; Kumar, S.; Manna, D., Stimuli-responsive assembly and disassembly of anionic suprasomes with tunable antibacterial activity. *Chem. Commun.* **2023,** *59*, 10624-10627.

23. Carter, K. P.; Young, A. M.; Palmer, A. E., Fluorescent Sensors for Measuring Metal Ions in Living Systems. *Chem. Rev.* **2014,** *114* (8), 4564-4601.

24. Allen-Vercoe, E.; Waddell, B.; Livingstone, S.; Deans, J.; DeVinney, R., Enteropathogenic Escherichia coli Tir translocation and pedestal formation requires membrane cholesterol in the absence of bundle-forming pili *Cell Microbiol.* **2006,** *8* (4), 613-624.

25. Larrow, J. F.; Jacobsen, E. N.; Gao, Y.; Hong, Y.; Nie, X.; Zepp, C. M., A practical method for the large-scale preparation of [N, N'-Bis (3, 5-di-tertbutylsalicylidene)-1, 2-cyclohexanediaminato (2-)] manganese (III) chloride, a highly enantioselective epoxidation catalyst. *J. Org. Chem.* **1994,** *59* (7), 1939-1942.

26. Okada, Y.; Sugai, M.; Chiba, K., Hydrogen-bonding-induced fluorescence: water-soluble and polarity-independent solvatochromic fluorophores. *J. Org. Chem.* **2016,** *81* (22), 10922-10929.

27. Kurouchi, H., Enhancement of the carbamate activation rate enabled syntheses of tetracyclic benzolactams: 8-oxoberbines and their 5-and 7-membered C-ring homologues. *Org. Biomol. Chem.* **2021,** *19* (3), 653-658.

28. Wang, J.; Zhang, X.; Yan, J.; Li, W.; Jiang, Q.; Wang, X.; Zhao, D.; Cheng, M., Design, synthesis and biological evaluation of curcumin analogues as novel LSD1 inhibitors. *Bioorg. Med. Chem. Lett.* **2019,** *29* (23), 126683.

29. Kalalbandi, V. K. A.; Seetharamappa, J. J. S. C., POCl3-mediated synthesis of 2-substituted benzimidazolyl-coumarin, benzimidazolyl-indole, and styrylbenzimidazole derivatives. *Synth. Commun.* **2016,** *46* (7), 626-635.

30. Van Epp Jr, J. E.; Boyd, D. R.; Berchtold, G. A. J. T. J. o. O. C., Aromatization of arene 1, 2-oxides. 1-(trimethylsilyl) benzene 1, 2-oxide. *J. Org. Chem.* **1981,** *46* (9), 1817-1820.

31. Malla, J. A.; Upadhyay, A.; Ghosh, P.; Mondal, D.; Mondal, A.; Sharma, S.; Talukdar, P., Chloride Transport across Liposomes and Cells by Nontoxic 3-(1 H-1, 2, 3-Triazol-1-yl) benzamides. *Org. Lett.* **2022,** *24* (23), 4124-4128.

32. Goyard, D.; Telligmann, S. M.; Goux-Henry, C.; Boysen, M. M. K.; Framery, E.; Gueyrard, D.; Vidal, S., Carbohydrate-based spiro bis(isoxazolines): synthesis and evaluation in asymmetric catalysis. *Tetrahedron Lett.* **2010,** *51* (2), 374-377.

33. Gutsmann, T.; Heimburg, T.; Keyser, U.; Mahendran, K. R.; Winterhalter, M., Protein reconstitution into freestanding planar lipid membranes for electrophysiological characterization. *Nat. Protoc.* **2015,** *10* (1), 188-198.

34. Montal, M.; Mueller, P., Formation of Bimolecular Membranes from Lipid Monolayers and a Study of Their Electrical Properties. *Proc. Natl. Acad. Sci.* **1972,** *69* (12), 3561-3566.

35. Lide, D. R., Ed., CRC Handbook of Chemistry and Physics, 87th ed. *Taylor and Francis: Boca Raton, FL* **2007**.

36. Becke, A. D., Density-Functional Thermochemistry .III. The Role of Exact Exchange. *J. Chem. Phys.* **1993,** *98* (7), 5648-5652.

37. Vanommeslaeghe, K.; Hatcher, E.; Acharya, C.; Kundu, S.; Zhong, S.; Shim, J.; Darian, E.; Guvench, O.; Lopes, P.; Vorobyov, I.; MacKerell, A. D., CHARMM General Force Field: A Force Field for Drug-Like Molecules Compatible with the CHARMM All-Atom Additive Biological Force Fields. *Journal of Computational Chemistry* **2010,** *31* (4), 671-690.

38. Vanommeslaeghe, K.; MacKerell, A. D., Automation of the CHARMM General Force Field (CGenFF) I: Bond Perception and Atom Typing. *Journal of Chemical Information and Modeling* **2012,** *52* (12), 3144-3154.

39. Vanommeslaeghe, K.; Raman, E. P.; MacKerell, A. D., Automation of the CHARMM General Force Field (CGenFF) II: Assignment of Bonded Parameters and Partial Atomic Charges. *Journal of Chemical Information and Modeling* **2012,** *52* (12), 3155-3168.

40. Jorgensen, W. L.; Chandrasekhar, J.; Madura, J. D.; Impey, R. W.; Klein, M. L., Comparison of Simple Potential Functions for Simulating Liquid Water. *Journal of Chemical Physics* **1983,** *79* (2), 926-935.

41. Jo, S.; Kim, T.; Iyer, V. G.; Im, W., CHARMM-GUI: A web-based graphical user interface for CHARMM. *J. Comput. Chem.* **2008,** *29* (11), 1859-1865.

42. Páll, S.; Zhmurov, A.; Bauer, P.; Abraham, M.; Lundborg, M.; Gray, A.; Hess, B.; Lindahl, E., Heterogeneous parallelization and acceleration of molecular dynamics simulations in GROMACS. *J. Chem. Phys.* **2020,** *153* (13), 134110.

43. Klauda, J. B.; Venable, R. M.; Freites, J. A.; O'Connor, J. W.; Tobias, D. J.; Mondragon-Ramirez, C.; Vorobyov, I.; MacKerell, A. D.; Pastor, R. W., Update of the CHARMM All-Atom Additive Force Field for Lipids: Validation on Six Lipid Types. *J. Phys. Chem. B* **2010,** *114* (23), 7830-7843.

44. Vanommeslaeghe, K.; Raman, E. P.; MacKerell, A., Automation of the CHARMM General Force Field (CGenFF) II: Assignment of Bonded Parameters and Partial Atomic Charges. *J. Chem. Inf. Model* **2012,** *52* (12), 3155-3168.

45. Li, P. F.; Roberts, B. P.; Chakravorty, D. K.; Merz, K. M., Rational Design of Particle Mesh Ewald Compatible Lennard-Jones Parameters for +2 Metal Cations in Explicit Solvent. *J. Chem. Theory Comput.* **2013,** *9* (6), 2733-2748.

46. Darden, T.; York, D.; Pedersen, L., Particle Mesh Ewald - an N.Log(N) Method for Ewald Sums in Large Systems. *J. Chem. Phys.* **1993,** *98* (12), 10089-10092.

47. Bernetti, M.; Bussi, G., Pressure control using stochastic cell rescaling. *J. Chem. Phys.* **2020,** *153* (11), 114107.

48. Bussi, G.; Donadio, D.; Parrinello, M., Canonical sampling through velocity rescaling. *J. Chem. Phys.* **2007,** *126* (1), 014101.

49. Michielsen, C. M. S.; van Aalen, E. A.; Merkx, M., Ratiometric Bioluminescent Zinc Sensor Proteins to Quantify Serum and Intracellular Free Zn. *Acs Chem Biol* **2022,** *17* (6), 1567-1576.

50. Meng, H. Y.; Ruan, J. J.; Chen, Y. Q.; Yan, Z. H.; Meng, X.; Li, X. D.; Liu, J. S.; Mao, C. Y.; Yang, P., Serum Zinc Ion Concentration Associated with Coronary Heart Disease: A Systematic Review and Meta-Analysis. *Cardiol Res Pract* **2022,** *2022*.

51. Zaichick, V.; Sviridova, T. V.; Zaichick, S. V., Zinc in the human prostate gland: normal, hyperplastic and cancerous. *Int Urol Nephrol* **1997,** *29* (5), 565-74.

52. Rusch, P.; Hirner, A. V.; Schmitz, O.; Kimmig, R.; Hoffmann, O.; Diel, M., Zinc distribution within breast cancer tissue of different intrinsic subtypes. *Arch Gynecol Obstet* **2021,** *303* (1), 195-205.

53. Patel, A.; Dey, S.; Shokeen, K.; Karpinski, T. M.; Sivaprakasam, S.; Kumar, S.; Manna, D., Sulfonium-based liposome-encapsulated antibiotics deliver a synergistic antibacterial activity. *Rsc Med Chem* **2021,** *12* (6), 1005-1015.

# Chapter 4

# Temporally Controlled Interconversion Between Suprasome and Supracube Structures to Regulate Catalytic Activities

### 4.1 Background and Objective of Current Work

The development of catalytically active compartmentalised structures that can be maintained in a metastable state is crucial for the development of protocell-based applications aimed at understanding cellular architecture and its functions.[1-3] Prior to the emergence of modern cells, compartmentalised structures likely acted as reaction hubs, driving early chemical processes without enzymes.[4, 5] This underscores the significance of compart-mentalization in understanding the origin of life and developing synthetic biomimetic systems.[1] Compartmentalised structures with prolonged stability can diminish the dynamic features essential for growth, division, and chemical communication, their dynamic nature enables adaptation and evolution.[6] Integrating time-gated activation and deactivation of chemical reactions with compartmentalised structures could create temporal localization and concentration gradients within these structures.[7] This integration facilitates the generation of a metastable compartment while remaining in a far-from-equilibrium state, which is essential in understanding the cellular processes necessary for the intricate balance of life.[5, 8]

Synthetic systems provide exciting platforms to explore how compartmentalisation influences chemical reactivity under non-equilibrium (transient) conditions by altering their energy landscape furthering efforts toward protocell development.[8-11] Recent studies demonstrate progress in creating synthetic compartments that can adjust their lifetimes through thermodynamically activated molecule in non-equilibrium environments.[9, 10, 12] However, practical demonstrations of compartment growth and division are still necessary. A recent study revealed that redox- responsive amphiphilic foldamers undergo conformational changes from 2D sheet-like structures to 3D vesicular morphologies through both enzymatic and non-enzymatic decay. The concentrations of fuel and enzyme regulate its temporal characteristics of transient assembly. However, the functions of the metastable state were not explored.[13] The binding of the amphiphilic triazacyclononane-$Zn^{2+}$ complex with phosphate substrates demonstrated dissipative self-assembly processes, forming transient vesicles that degraded autonomously. This degradation increased hydrolysis rates and showcased the synergy of catalysis and compartmentalisation in chemical systems.[14] Other studies also reported the development of self-assembled compartments, catalytic assemblies, and active droplets to gain insights into cellular architectures and their functions.[1, 9, 12, 15, 16] However, developing well-defined assembly of compartmentalised structures under non-equilibrium conditions to temporally regulate catalytic activity and subsequent restoration to their original compartmentalised structure has not been adequately demonstrated.[15, 16] In non-equilibrium

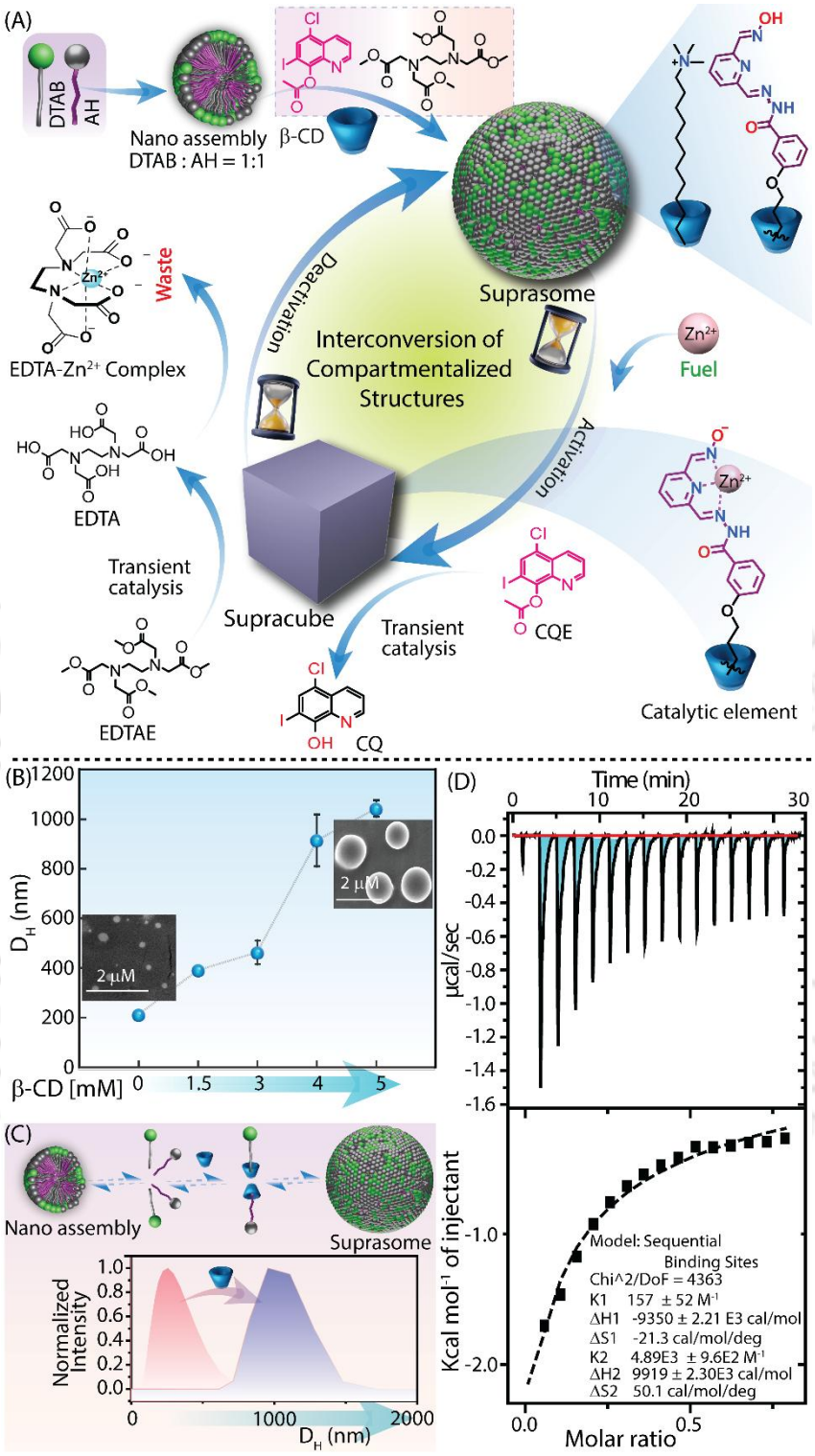


**Figure 4.1** (A) Schematic representation of $Zn^{2+}$ and EDTAE-fueled interconversion of compartmentalised structures with catalytic activity. (B) Variation of hydrodynamic diameter (DH) during nanoassembly to suprasome transition upon increasing β-CD concentration; inset:

representative FESEM images of nanoassemblies and suprasomes. (C) Plausible suprasome growth mechanism; inset: DH distribution of nanoassemblies and suprasomes. (D) ITC profile of DTAB–AHPO (1:1) with β-CD.

environments, the growth, differentiation, and decay of compartmentalised structures are essential for enhancing the complexity of reaction cycles and supporting diverse functionalities.[6] We hypothesise that host-guest supramolecular interactions can facilitate compartment formation, while $Zn^{2+}$ serves as a stimulus to regulate controlled growth, differentiation, and transient catalytic activation.

Herein, we demonstrated the development of a stimuli-regulated system for the interconversion of compart-mentalized structures. Host-guest supramolecular interactions facilitated the self-assembly of spherical supramolecular compartments (suprasomes) from amphiphilic nanoassembly (Figure 4.1A).[17, 18] Chemical stimulus ($Zn^{2+}$) dependent modulation induced a supramolecular differentiation event, transforming suprasomes into metastable and catalytically active supracubes with esterase-like activity, that hydrolyzed the ester derivatives of clioquinol (CQE) and ethylenediaminetetraacetic acid (EDTAE) to CQ and EDTA, respectively.[19, 20] The introduction of EDTAE induced temporal $Zn^{2+}$ depletion via slow EDTA release, triggering the reversal of supracubes to suprasomes and imparting dynamic transience. This reversible 3D-compartment interconversion enabled controlled ionophore release from a proionophore, activating ion transport in a separate liposomal compartment. These events demonstrate how such differentiation can mediate chemical communication between compartments, resembling life-like processes and paving the way for innovative applications in synthetic biology.

## 4.2 Results and Discussion

### 4.2.1 Suprasomal Assembly, Disassembly and Supracube Formation

To develop advanced compartmentalised structures capable of undergoing chemical stimulus regulated dynamic interconversion and controlled chemical reactivity, we harnessed the potential of nano assembled structures using the alkylated derivative of AHPO and DTAB. The AHPO was selected to integrate the properties of amphiphiles in binding with small molecular cofactors that could demonstrate dynamic catalytic activities within the compartmentalised structures. The dynamic light scattering (DLS) measurements showed that DTAB promoted

the solubility of AHPO via nanoassembly (hydrodynamic diameter, $D_H$ = 200 nm) in the aqueous medium. Interestingly, the addition of β-cyclodextrin (β-CD) leads to the formation of suprasomes ($D_H$ = 1000 nm) (Figure 4.1B and 4.5). The observed morphological transition measured by field emission scanning electron microscopy (FESEM) corroborates the role of β-CD in modulating the nanoassembly (Figure 4.1C and 4.6).[18] The isothermal titration calorimetry (ITC) measurements of a 1:1 mixture of DTAB and AHPO with β-CD revealed that the entropy-driven host-guest interactions lead to the formation of suprasomes in the aqueous medium (Figure 4.1D and 4.7).

To investigate the interconversion of compartmentalised structures, the DLS measurements of suprasomes were performed. The addition of $Zn^{2+}$ to the suprasomes ($D_H$ = 1000 nm) resulted in the formation of larger self-assembled structures ($D_H$ ~2500 nm) (Figure 4.8). The FESEM images revealed the formation of well-defined, cube-like morphology of comparable dimensions after $Zn^{2+}$ treatment (Figure 4.9A). Therefore, $Zn^{2+}$ acts as a stimulus that transforms suprasomes into supracubes, highlighting a regulated differentiation process in supra-molecular assembly. The morphological analysis of AHPO + $Zn^{2+}$ and AHPO + β-CD + $Zn^{2+}$ and other control measurements revealed that the $Zn^{2+}$ treatment of suprasome was required to generate cube-like architectures, respectively (Figure 4.9 and 4.10). The FESEM-EDX mapping and elemental analysis showed the elemental composition of the supracube structure (Figure 4.11-4.12). TEM-SAED pattern analysis of the supracube showed diffuse concentric rings, indicating a polycrystalline or partially crystalline nature (Figure 4.13). Powder XRD analysis of the supracube confirmed its polycrystalline nature, ruling out the possibility of it being only $Zn^{2+}$ or β-CD, since its pattern was different from the reported p-XRD patterns of these controls (Figure 4.14). The TEM-EDX analysis also showed the elemental composition of the supracube structure (Figure 4.13). Hence, both FESEM and TEM analyses suggest that the formation of AHPO-$Zn^{2+}$ complex and host-guest interactions of the alkyl chain of the AHPO-$Zn^{2+}$ complex with the hydrophobic cavity of β-CD are the driving force for the 3D arrangements of the supracube. We also investigated the transformation from suprasomes to supracubes arrangements in the presence of $Zn^{2+}$, using Nile Red as a hydrophobic fluorescence probe. Time-dependent fluorescence microscopy images showed a gradual disappearance of suprasomal structures, which coincided with the appearance of distinct supracube assemblies, indicating the morphological transition was driven by $Zn^{2+}$ (Figure 4.2A, 4.15).

### 4.2.2 Catalytic Activity Study

Inspired by the role of $Zn^{2+}$ in driving the suprasomes to supracubes arrangements and the decoration of $Zn^{2+}$-bound AHPO headgroup along the surface of the supracube, the catalytic activity of the supracube was investigated by using CQE (Figure 4.2B). The CQ and CQE were selected for their ionophore and proionophore like behaviour, respectively, emphasising the potential use of our transient system in ion transport modulation. A continuous decrease in CQE fluorescence was observed with supracube, indicating the cleavage of the ester bond and

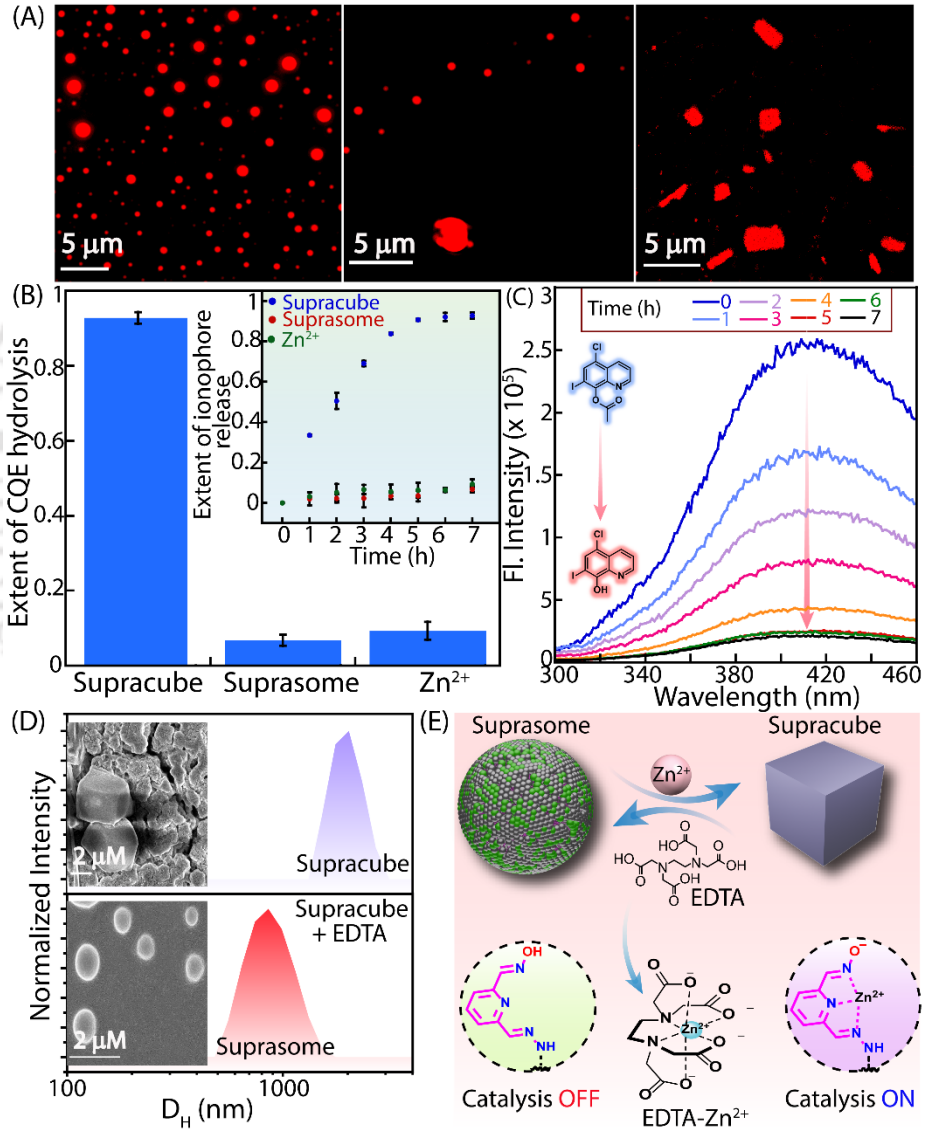


**Figure 4.2** (A) Representative fluorescence microscopic images for the suprasome to supracube transformation. (B) Comparison of CQE hydrolysis efficacy of the compartmentalised structures and only $Zn^{2+}$; inset: shows the time-dependent CQE hydrolysis efficacy. (C) Time-dependent reduction in fluorescence intensity of CQE by the supracube

structures. (D) EDTA-induced supracube-to-suprasome transition analyzed by FESEM and DLS. (E) Schematic representation for the interconversion between suprasome and supracube structures and catalytic ON/OFF cycles.

the subsequent release of CQ (Figure 4.2C, 4.16). Notably, CQE hydrolysis activity was observed only after the addition of $Zn^{2+}$. This suggests that the $Zn^{2+}$ mediated conversion of suprasome to supracube is a result of the complexation of $Zn^{2+}$ with β-CD-bound AHPO, which is essential for catalytic activity. The catalytic efficacy was also investigated through HPLC analysis, which confirmed the hydrolysis of CQE to CQ only in the presence of supracube (suprasome + $Zn^{2+}$). The rate of reaction was found to be $2.78\times10^{-8}$ M/s (Figure 4.17). The $Zn^{2+}$ complexation with the pre-catalyst (pyridine-oxime moiety) lowers the pKa of oxime from 11 to <6, promoting deprotonation and oximate formation, which acts as a catalyst.[21] However, this increased catalytic activity could also be attributed to the presence of nucleophilic water that is complexed with $Zn^{2+}$. This also suggests that the hydrophilic head group of AHPO-$Zn^{2+}$ complexes localize at the surface of the supramolecular cubic architecture, facilitating ester hydrolysis.

To explore the dynamic interconversion of these compartmentalised structures, we investigated the morphological transition using EDTA, a known chelator of $Zn^{2+}$ (Figure 4.2D).[20] The UV-Vis measurements of AHPO in aqueous solution indicated a decrease in the absorbance peak at 315 nm, while a new peak emerged at 390 nm after the addition of $Zn^{2+}$, signifying the complexation of AHPO with $Zn^{2+}$ (Figure 4.18A). The variation of absorbance against different concentrations of $Zn^{2+}$ suggests moderate binding affinity (Figure 4.18B and 4.18C). However, the addition of EDTA restored the initial absorbance profile of AHPO (Figure 4.18D). We also examined the conversion from supracube to suprasome architectures using DLS and FESEM analyses in the presence of EDTA (Figure 4.2E, 4.19). The variation of $D_H$ values and morphology suggests that the sequestration of $Zn^{2+}$ by EDTA drives the rearrangement of the supracube back to suprasomes. Meanwhile, the addition of EDTA also switched off the CQE hydrolysis activity (Figure 4.20). This transition from supracube to supra-some morphology, along with the inhibition of ester hydrolysis activity, was further utilised to develop a stimuli-responsive transient compartmentalised structure via a negative feedback mechanism.

To investigate the interconversion of these, compartmentalised structures, we used $Zn^{2+}$ and EDTAE in tandem. We hypothesised that the use of EDTAE would facilitate the reversal of the supracube to suprasome structure within a defined time frame, allowing for temporal

regulation of catalytic activity and effective control of ion transport activity. The DLS measurements showed that initially, the $D_H$ values increased from ~1000 nm to ~2500 nm, and after ~6 hours, the size reverted to ~1000 nm, confirming the transient nature of the supracube architecture, which exists only for a limited time period (Figure 4.23). This dynamic interconversion cycle was repeated multiple times, where each iteration re-quired the introduction of $Zn^{2+}$ as the fuel and EDTAE as the feedback controller (Figure 4.3A, 4.3B and Figure 4.23-4.24). The UV-Vis studies provided additional evidence, as the characteristic 390 nm peak due to the formation of AHPO-$Zn^{2+}$ complex initially appeared and then gradually diminished, and the peak at 315 nm reappeared within ~6 hours due to the hydrolysis of EDTAE to EDTA by supracube, leading to $Zn^{2+}$ sequestration by EDTA (Figure 4.3C). The ability of the supracube to hydrolyze EDTAE to EDTA was further validated using an arsenazo-III dye assay, where only supracube-treated EDTAE sequestered free $Zn^{2+}$, leading to a blue shift of the dye absorption from 600 nm ($Zn^{2+}$-bound state) to 550 nm ($Zn^{2+}$-free state) (Figure 4.21, 4.22). The FESEM image analysis further confirmed the reversible formation of supracube structures from suprasomes and their dissociation back to suprasomes (Figure 4.3D). The dynamic interconversion of these compartmentalised structures can be attributed to the complexation of $Zn^{2+}$ with AHPO, along with ester hydrolysis catalysed by the supracube. Additionally, the simultaneous depletion of $Zn^{2+}$ from the system by EDTA and the release of AHPO play significant roles in this process. Upon closer inspection, these multicyclic events observed through hydrodynamic diameter analysis represent a pulsed behaviour with alternate half cycles presenting a catalysis ON/OFF cycle, and every single cycle displays intricate chemistry for a transient catalytic phase of active payload (ion transporter) release (Figure 4.3B).

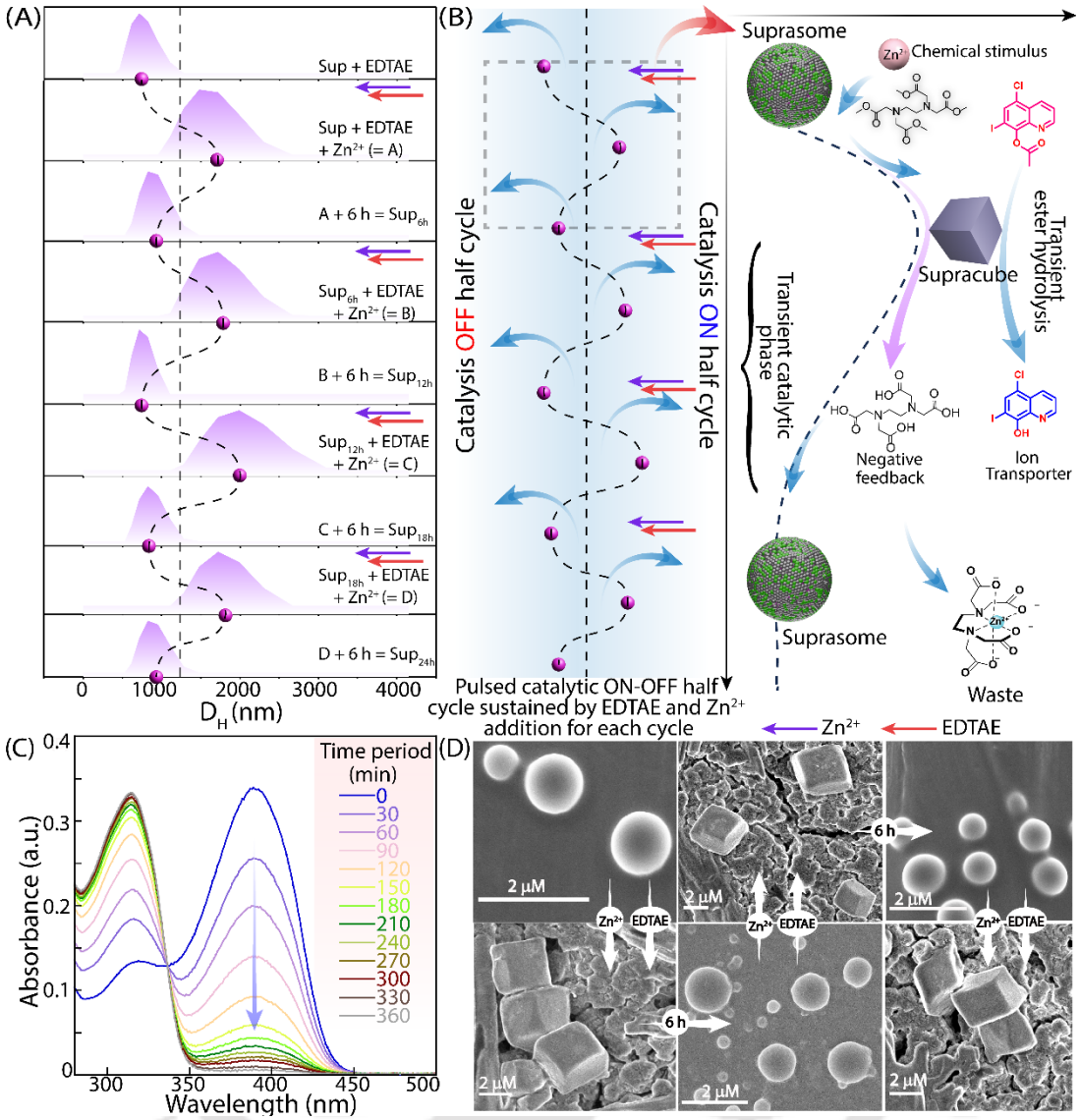


**Figure 4.3** Multicyclic interconversion between suprasome and supracube structures observed via (A) DLS measurements and (B) ON/OFF catalytic activities; each cycle involves $Zn^{2+}$ stimulated supracube formation and EDTA-mediated reversal to suprasome, (→) blue arrow indicates $Zn^{2+}$ addition, (→) red arrow indicates EDTAE addition. (C) Time-dependent UV-Vis spectral change of AHPO-$Zn^{2+}$ complex upon EDTAE treatment. (D) Representative FESEM images demonstrating morphological changes during transient interconversion cycles.

Therefore, the developed transient system demonstrated self-regulated payload release in ON/OFF cycle, controlling ion transport activity, where $Zn^{2+}$-induced transition from suprasomes to supracubes facilitated the hydrolysis of CQE for approximately six hours before stopping due to negative feedback caused by the in-situ generation of EDTA (Figure 4.4A, 4.25). The system remained inactive until refueled with $Zn^{2+}$ions, ensuring transient and cycle-dependent catalytic activity. Such a transient system is advantageous over a persistent ion

transport system, where prolonged ion transport activity could lead to potential toxicity and other side effects.

Finally, the catalytic activity of the supracube was utilised to monitor the transmembrane $Zn^{2+}$ ion transport activity of CQ in the liposomal compartment using magnesium green (MgG) dye (Figure 4.28).[19] The MgG-based transport studies revealed that CQE remained inactive (Figure 4.29), while after the addition of $Zn^{2+}$ to the solution containing suprasome and CQE, the $Zn^{2+}$ ion transport activity was observed (Figure 4.4B). This suggests that the AHPO-$Zn^{2+}$ complex of the supramolecular cubic architecture facilitates the hydrolysis of CQE to CQ. Collectively, stimuli-responsive suprasome-to-supracube transition led to structural differentiation coupled with functional activation (esterase activity), facilitating inter-compartmental communication (Figure 4.4A).

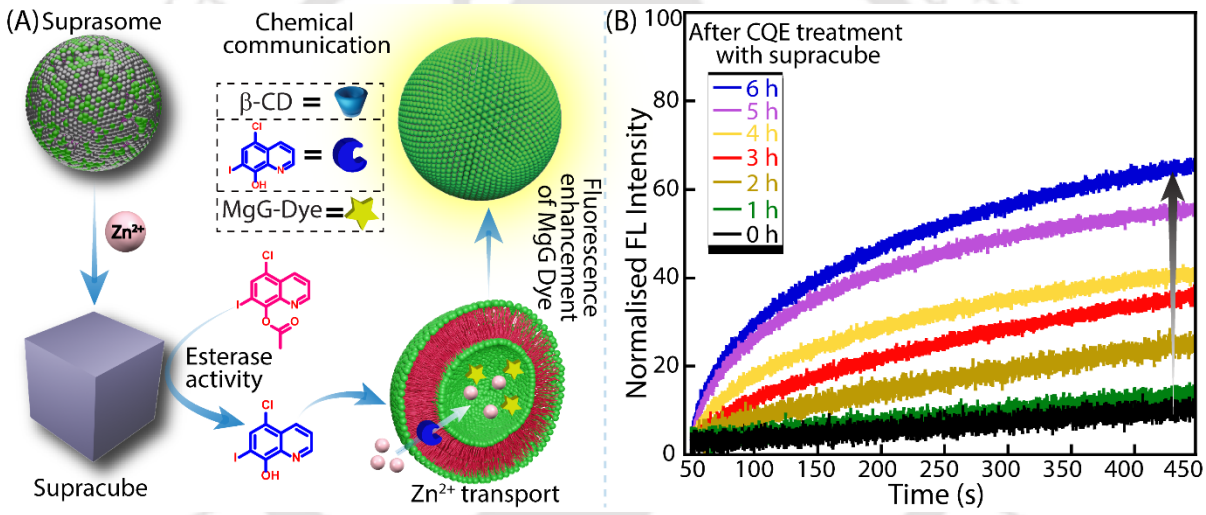


**Figure 4.4** (A) Schematic representation of supracube-mediated CQE to CQ hydrolysis and CQ-mediated transmembrane $Zn^{2+}$ transport into the secondary vesicle. (B) Time-dependent $Zn^{2+}$ transport activity of supracube-treated CQE across the bilayers of EYPC/CHOL-LUV⊃MgG.

### 4.3 Summary

In conclusion, we demonstrated the development of a supramolecular compartmentalised system that mimics essential cellular behaviours such as growth, differentiation, and catalytic activity in a transient and stimuli-responsive manner. The addition of β-CD to a 1:1 mixture of AHPO and DTAB enabled hierarchical self-assembly into suprasomes. Upon stimulation with $Zn^{2+}$ ions, these compartments transformed into catalytically active supracube structures, facilitating esterase-like activity and the con-trolled release of the ionophore (CQ) from its

esterified proionophore (CQE). The system demonstrated reversible control over its functional state, allowing EDTA to restore suprasomes and modulate esterase activity by sequestering $Zn^{2+}$ ions. By integrating EDTAE into the suprasomes, we established a programmed lifespan of 6 hours for the interconversion between suprasome and supracube structures, resulting in a transient catalytic system similar to time-regulated enzymatic cascades in metabolic pathways. This innovative system offers new possibilities for designing responsive supramolecular assemblies with controlled functions and lifespans, providing exciting opportunities for ion transporter-based therapeutics, synthetic biology, and artificial cell engineering.

## 4.4 Experimental Section

### 4.4.1 General Information

The reagents and solvents used in the experiment were purchased from commercial sources such as Sigma-Aldrich, TCI and Thermo Fisher Scientific. These were used without undergoing additional purification unless explicitly indicated. The monitoring of reactions was conducted through thin-layer chromatography (TLC) on silica gel 60 F254 (0.25 mm). Silica gel with a mesh size of 120- 200 was utilised for the execution of column chromatography. The Bruker spectrometer was used to record the $^{1}H$ NMR and $^{13}C$ NMR at 600 MHz and 151 MHz, respectively. The chemical shifts were determined using internal solvents DMSO-$d_6$ and $CDCl_3$ and were expressed in parts per million (ppm). The values of the coupling constant (J) were expressed in hertz, and the corresponding abbreviations were provided as follows: s (representing singlet), d (representing doublet), t (representing triplet), q (representing quartet), m (representing multiple), and br (representing broadened). High-resolution mass spectra (HRMS) were acquired using an Agilent Q-TOF mass spectrometer equipped with a Z-spray source. The obtained mass data were analysed using the software integrated into the instrument. The chemical compounds utilised in the study, namely cholesterol (CHOL) and egg-yolk phosphatidylcholine (EYPC), were procured from Sigma Aldrich. The reagents utilised in this study, including HEPES buffer, Triton X-100 and various inorganic salts, as well as their corresponding hydroxide bases, were procured from Sigma Aldrich. Pentapotassium salt of magnesium green (MgG) was obtained from Thermo Fisher Scientific. The buffers were prepared using ultrapure water sourced from the Milli-Q water.

### 4.4.2 Synthesis and Characterization of Acyl Hydrazone-based Compound

The synthesis of the target 6-(hydrazineylidenemethyl) picolinaldehyde oxime (AHPO) commenced with the esterification of 3-hydroxybenzoic acid via Fischer esterification in

methanol, yielding methyl 3-hydroxybenzoate. Subsequently, the free hydroxyl group underwent Williamson ether synthesis with 1-bromododecane, affording methyl 3-(dodecyloxy)benzoate. Hydrazinolysis of the ester via refluxing with hydrazine hydrate in ethanol furnished 3-(dodecyloxy)benzo hydrazide. In parallel, the head group, (E)-6-((hydroxyimino)methyl) picolinaldehyde, was synthesised through an oxime formation reaction by stirring hydroxylamine with pyridine-2,6-dicarbaldehyde in methanol at ambient temperature. Finally, the AHPO was obtained via Schiff base condensation between (E)-6-((hydroxyimino)methyl) picolinaldehyde and 3-(dodecyloxy)benzo hydrazide, yielding the desired hydrazone-linked amphiphilic lipid.

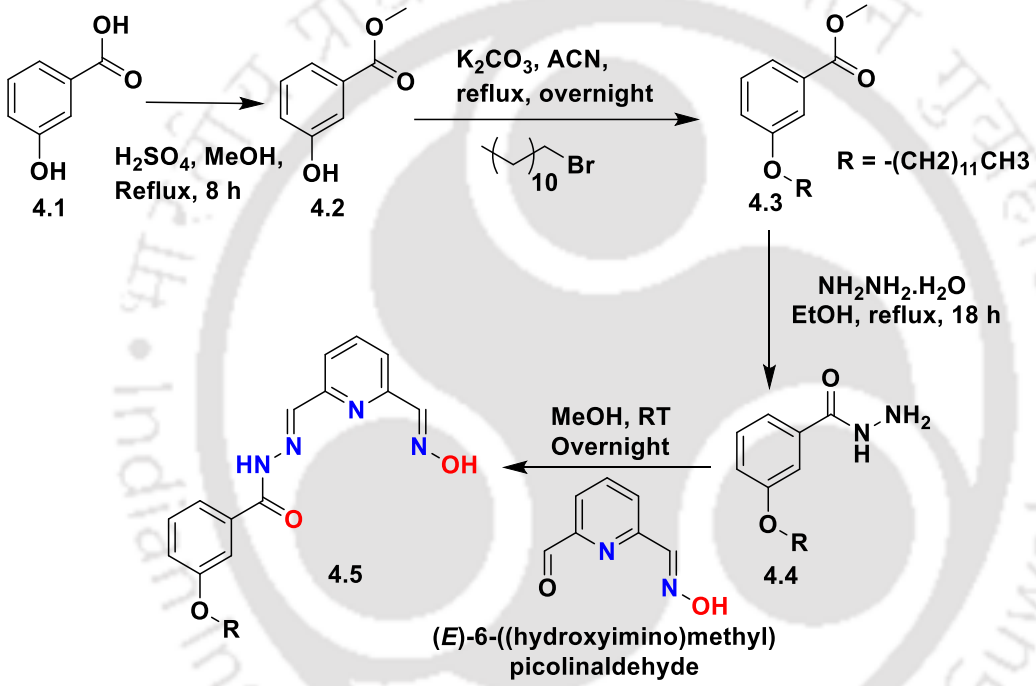


**Scheme 4.1** Synthetic routes of compound AHPO.

### 4.4.2.1 Synthesis of methyl 3-hydroxybenzoate

To the stirring solutions of 3-hydroxybenzoic acid (1.380 g, 10 mmol, 1.0 equiv.) in 5 mL MeOH, $H_2SO_4$ (500 µL) was added. The reaction mixture was refluxed at 80 °C for 8 hours. The reaction mixture was brought to room temperature, and the solvents were evaporated under reduced pressure. The compound was extracted with dichloromethane and washed with bicarbonate solution. The organic layer was dried over $MgSO_4$ and evaporated under reduced pressure, resulting in a yield of 87%. The compound was characterized by $^1$H NMR, $^{13}$C NMR, and HRMS (ESI) analysis. **$^1$H NMR** (600 MHz, Chloroform-d) δ: 7.64 (s, 1H), 7.60 (d, $J$ = 7.8

Hz, 1H), 7.31 (t, *J* = 7.8 Hz, 2H), 7.13 (d, *J* = 8.1 Hz, 1H), 3.93 (s, 2H). **$^{13}$C NMR** (151 MHz, Chloroform-*d*) *δ*: 167.94, 156.21, 131.08, 129.77, 121.76, 120.63, 116.47, 52.51. **HRMS** (ESI) m/z: calculated for $C_8H_8O_3$ $[M+H]^+$ : 152.0546, found 152.0553.

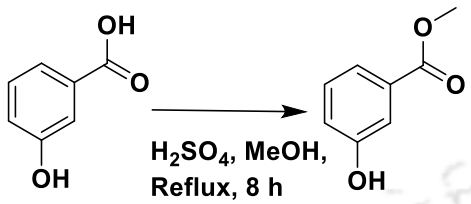


**Scheme 4.2** Synthesis of methyl 3-hydroxybenzoate.

#### 4.4.2.2 Synthesis of methyl 3-(dodecyloxy)benzoate

To the stirring solutions of methyl 3-hydroxybenzoate (1.52 g, 10 mmol, 1.0 equiv.) in 5 mL acetonitrile, $K_2CO_3$ (1.38 g, 10 mmol, 1.0 equiv.) and 1-bromododecane (2.97 g, 15 mmol, 1.5 equiv.) were added. The reaction mixture was refluxed at 80 °C for 12 hours. The progress of the reaction was monitored by TLC. After completion of the reaction, the reaction mixture was brought to room temperature. The unreacted $K_2CO_3$ was removed by filtration and the solvents were evaporated under reduced pressure. Purification of the crude product was done with column chromatography using EtOAc/Hexane, resulting in a yield of 71%. The compound was characterized by $^1$H NMR, $^{13}$C NMR, and HRMS (ESI) analysis. **$^1$H NMR** (400 MHz, Chloroform-*d*) δ: 7.61 (dt, *J* = 7.6, 1.3 Hz, 1H), 7.55 (dd, *J* = 2.7, 1.5 Hz, 1H), 7.32 (t, *J* = 8.0 Hz, 1H), 7.09 (ddd, *J* = 8.3, 2.7, 1.0 Hz, 1H), 3.99 (t, *J* = 6.6 Hz, 2H), 3.91 (s, 3H), 1.84 – 1.72 (m, 2H), 1.51 – 1.40 (m, 2H), 1.27 (m, 16H), 0.88 (t, *J* = 8, 3H). **$^{13}$C NMR** (126 MHz, Chloroform-*d*) δ: 167.05, 159.15, 131.38, 129.33, 121.77, 119.96, 114.67, 68.23, 52.13, 31.93, 29.67, 29.65, 29.61, 29.59, 29.39, 29.36, 29.21, 26.03, 22.70, 14.12. **HRMS** (ESI) m/z: calculated for $C_{20}H_{32}O_3$ $[M+H]^+$: 321.2424, found 321.2422.

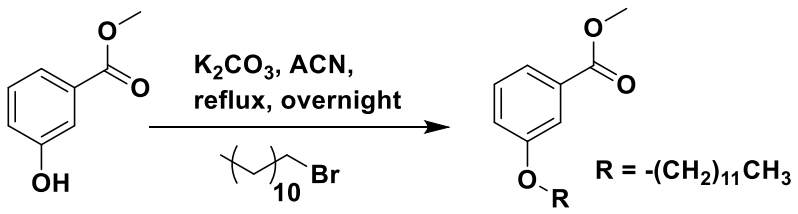


**Scheme 4.3** Synthesis of methyl 3-(dodecyloxy)benzoate.

#### 4.4.2.3 Synthesis of 3-(dodecyloxy) benzo hydrazide

To the stirring solutions of methyl 3-(dodecyloxy)benzoate (3.2 g, 10 mmol, 1.0 equiv.) in 4 mL ethanol, hydrazine monohydrate (1 g, 20 mmol, 2.0 equiv.) was added. The reaction mixture was refluxed at 80 °C for 18 hours. The progress of the reaction was monitored by TLC. After completion of the reaction, the reaction mixture was brought to room temperature. The solvents were evaporated under reduced pressure. The crude product was purified with column chromatography using EtOAc/Hexane, resulting in a yield of 65%. The compound was characterized by $^{1}$H NMR, $^{13}$C NMR, and HRMS (ESI) analysis. **$^{1}$H NMR** (600 MHz, DMSO-$d_6$) δ: 9.75 (s, 1H), 7.38-7.30 (m, 3H), 7.03 (d, $J$ = 7.2 Hz, 1H), 4.50 – 4.46 (br s, 2H), 3.97 (t, $J$ = 5.9 Hz, 3H), 1.70 (p, $J$ = 6.9 Hz, 2H), 1.40 (p, $J$ = 7.6, 7.0 Hz, 2H), 1.33 – 1.23 (m, 16H), 0.84 (t, $J$ = 6.6 Hz, 3H). **$^{13}$C NMR** (151 MHz, DMSO-$d_6$) δ: 166.06, 159.01, 135.06, 129.88, 119.53, 112.93, 67.98, 31.78, 29.54, 29.51, 29.26, 29.21, 29.10, 25.98, 22.59, 14.43. **HRMS** (ESI) m/z: calculated for $C_{19}H_{32}N_2O_2$ $[M+H]^+$: 321.2537, found 321.2525.

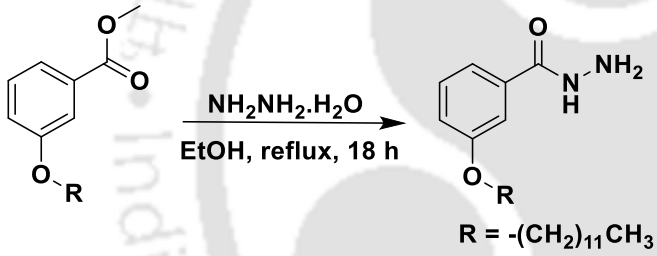


**Scheme 4.4** Synthesis of 3-(dodecyloxy)benzo hydrazide.

#### 4.4.2.4 Synthesis of (E)-6-((hydroxyimino)methyl)picolinaldehyde

To the stirring solutions of pyridine-2,6-dicarbaldehyde (1.35 g, 10 mmol, 1.0 equiv.) in 5 mL methanol, hydroxylamine (0.26 g, 8 mmol, 0.8 equiv.) was added. The reaction mixture was stirred at the room, and the progress of the reaction was monitored by TLC. The solvents were evaporated under reduced pressure. Purification of the crude product was done with column chromatography using EtOAc/Hexane, resulting in a yield of 58%. The compound was characterized by $^{1}$H NMR, $^{13}$C NMR, and HRMS (ESI) analysis. **$^{1}$H NMR** (500 MHz, DMSO-$d_6$) δ: 11.88 (s, 1H), 9.92 (s, 1H), 8.14 (s, 1H), 8.02-8.00 (m, 2H), 7.85 (dd, $J$ = 5.1, 3.6 Hz, 1H). **$^{13}$C NMR** (126 MHz, DMSO-$d_6$) δ: 193.70, 153.30, 152.61, 148.54, 138.88, 124.63, 122.25. **HRMS** (ESI) m/z: calculated for $C_7H_6N_2O_2$ $[M+H]^+$: 151.0502, found 151.0506.

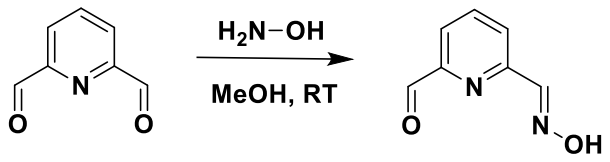


**Scheme 4.5** Synthesis of (E)-6-((hydroxyimino)methyl)picolinaldehyde.

### 4.4.2.5 Synthesis of 3-(dodecyloxy)-N'-((E)-(6-((E)-(hydroxyimino)methyl)pyridin-2-yl)methylene)benzohydrazide

To the stirring solutions of (E)-6-((hydroxyimino)methyl)picolinaldehyde (1.50 g, 10 mmol, 1.0 equiv.) in 7 mL methanol, 3-(dodecyloxy)benzo hydrazide (3.2 g, 10 mmol, 1 equiv.) was added. The reaction mixture was stirred at room temperature, and the progress of the reaction was monitored by TLC. A white precipitate appeared, which was washed with methanol, and the final pure product was collected. The compound was characterized by $^{1}$H NMR, $^{13}$C NMR, and HRMS (ESI) analysis. **$^{1}$H NMR** (600 MHz, DMSO-$d_6$) δ: 12.06 (s, 1H), 11.81 (s, 1H), 8.48 (s, 1H), 8.12 (s, 1H), 7.96 (d, $J$ = 7.8 Hz, 1H), 7.92 (t, $J$ = 7.8 Hz, 1H), 7.81 (d, $J$ = 7.6 Hz, 1H), 7.49 (d, $J$ = 7.7 Hz, 1H), 7.45 (d, $J$ = 6.6 Hz, 2H), 7.17 (d, $J$ = 8.1 Hz, 1H), 4.02 (t, $J$ = 6.5 Hz, 2H), 1.72 (p, $J$ = 6.5 Hz, 2H), 1.41 (p, $J$ = 7.7, 5.7 Hz, 3H), 1.32-1.30 (m, 2H), 1.22 (m, 14H), 0.83 (t, $J$ = 6.8 Hz, 3H). **$^{13}$C NMR** (151 MHz, DMSO-$d_6$) δ: 163.62, 159.13, 153.64, 152.56, 149.01, 147.99, 138.06, 134.88, 130.25, 120.75, 120.48, 120.29, 118.45, 114.01, 68.14, 31.78, 29.53, 29.51, 29.48, 29.24, 29.20, 29.09, 25.97, 22.58, 14.42. **HRMS** (ESI) m/z: calculated for $C_{26}H_{36}N_4O_3$ $[M+H]^+$: 453.2860, found 453.2857.

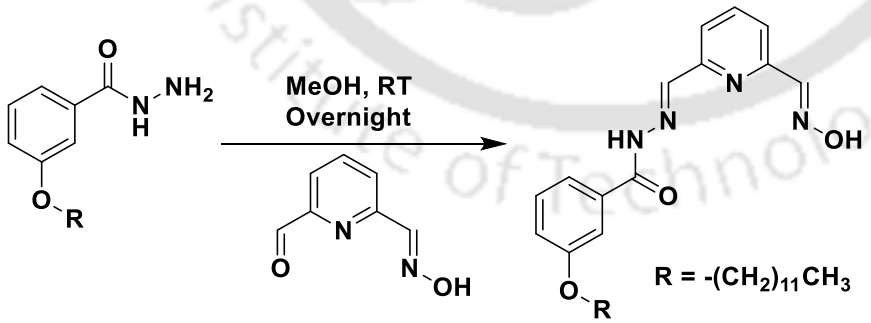


**Scheme 4.6** Synthesis of 3-(dodecyloxy)-N'-((E)-(6-((E)-(hydroxyimino)methyl)pyridin-2-yl)methylene)benzohydrazide.

#### 4.4.2.6 Synthesis of 5-chloro-7-iodoquinolin-8-yl acetate

The 5-chloro-7-iodoquinolin-8-ol (3.04 g, 10 mmol, 1.0 equiv.) was refluxed in 10 mL acetic anhydride ($Ac_2O$) for 1h. The reaction mixture was brought to room temperature. The mixture was evaporated, and the residue was dissolved in dichloromethane. Then it was washed with aqueous $NaHCO_3$ and dried over $MgSO_4$. Further, the solvent was evaporated to obtain the final compound (Yield 91%). The compound was characterized by $^1$H NMR, $^{13}$C NMR, and HRMS (ESI) analysis. **$^1$H NMR** (600 MHz, Chloroform-*d*) $\delta$: 8.96 (d, $J$ = 3.3 Hz, 1H), 8.55 (d, $J$ = 8.4 Hz, 1H), 8.02 (s, 1H), 7.59 (dd, $J$ = 8.5, 4.2 Hz, 1H), 2.58 (s, 3H). **$^{13}$C NMR** (151 MHz, Chloroform-*d*) $\delta$: 168.42, 151.58, 148.40, 141.38, 134.62, 133.41, 129.33, 127.12, 122.77, 90.48, 21.09. **HRMS** (ESI) m/z: calculated for $C_{11}H_7ClINO_2$ $[M+H]^+$: 347.9283, found 347.9299.

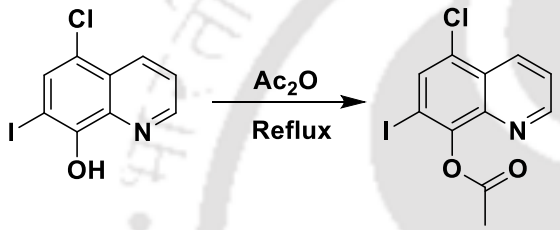


**Scheme 4.7** Synthesis of 5-chloro-7-iodoquinolin-8-yl acetate.

#### 4.4.2.7 Synthesis of tetramethyl 2,2',2'',2'''-(ethane-1,2-diylbis(azanetriyl))tetraacetate

To the stirring solutions of ethylenediaminetetraacetic acid (EDTA) (2.92 g, 10 mmol, 1.0 equiv.) in 10 mL MeOH, $H_2SO_4$ 500 µl was added. The reaction mixture was refluxed at 80 °C for 8 hours. The reaction mixture was brought to room temperature and the solvents were evaporated under reduced pressure. The compound was extracted with dichloromethane and washed with bicarbonate solution. The organic layer was dried over $MgSO_4$ and evaporated under reduced pressure, resulting in a yield of 85%. The compound was characterized by $^1$H NMR, $^{13}$C NMR, and HRMS (ESI) analysis. **$^1$H NMR** (600 MHz, Chloroform-*d*) $\delta$: 3.63 (s, 12H), 3.55 (s, 8H), 2.83 (s, 4H). **$^{13}$C NMR** (151 MHz, Chloroform-*d*) $\delta$: 171.63, 54.89, 52.05, 51.41. **HRMS** (ESI) m/z: calculated for $C_{14}H_{24}N_2O_8$ $[M+H]^+$ : 349.1605, found 349.1620.

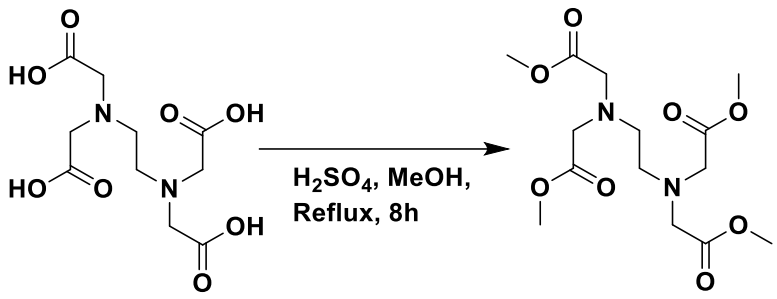


**Scheme 4.8** Synthesis of tetramethyl 2,2',2",2"'-(ethane-1,2-diylbis(azanetriyl))tetraacetate.

### 4.4.3 Suprasome Formation and Corresponding Characterisation

DTAB (200 μM) and AHPO (200 μM) were added to an aqueous solution and vortexed for 15 minutes. Different concentrations of β-cyclodextrin (β-CD) were then introduced to this solution and stirred for 1 hour. The resulting mixture became slightly cloudy, indicating the formation of larger nanostructures known as suprasomes.[22]

#### 4.4.3.1. Measurements of Hydrodynamic Diameter by DLS Measurements

Suprasomes were prepared using various concentrations of β-CD as described in the previous method. The hydrodynamic diameters ($D_H$) values were measured using a dynamic light scattering (DLS) instrument (Zetasizer Nano ZS90, Malvern, Westborough, MA) at a temperature of 25 °C. These measurements were conducted multiple times for all the compositions discussed in this study.

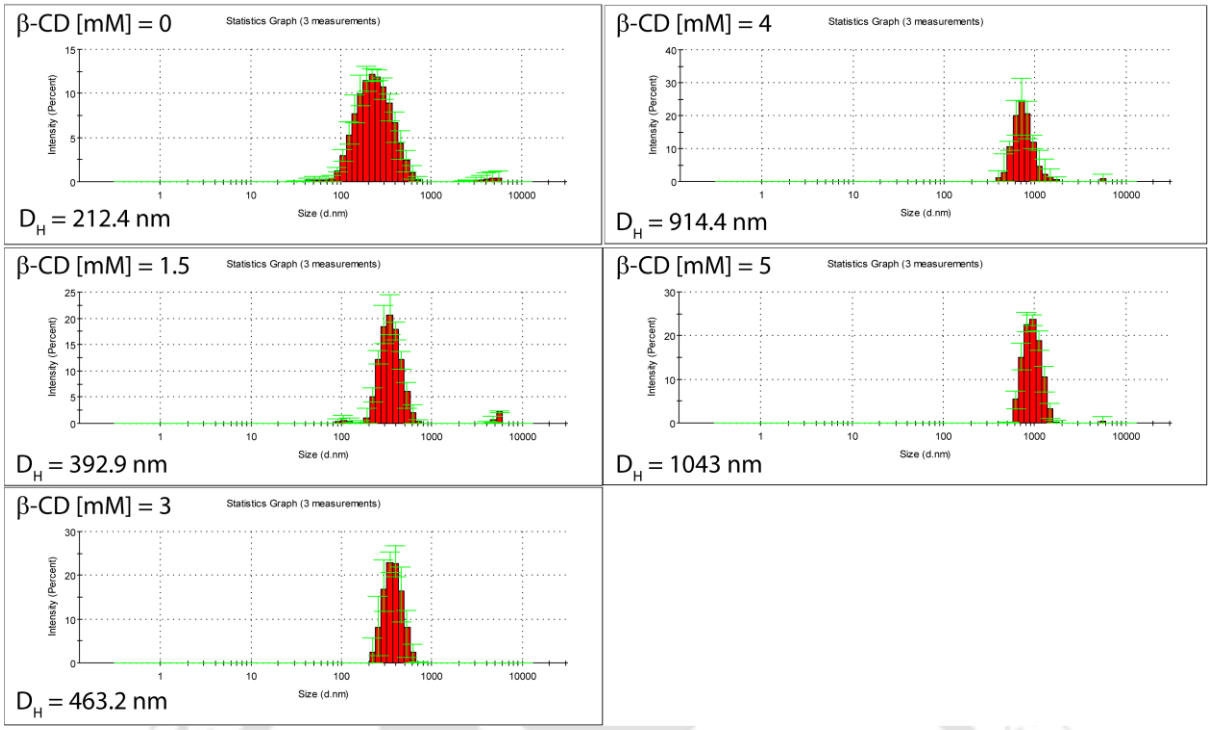


**Figure 4.5** Variation of hydrodynamic diameter ($D_H$) distribution of suprasomes of DTAB (200 μM) and AHPO (200 μM) with different concentrations of β-CD (0-5 mM).

### 4.4.3.2 Morphological Analysis through FESEM

Nanoassembly of the mixture of DTAB and AHPO (1:1) and suprasome was prepared as described in the previous method. The prepared solutions were then drop-casted onto a glass slide and dried at room temperature. Before the analysis, the glass slide containing the sample was coated with gold and loaded onto the FESEM grid for further analysis.

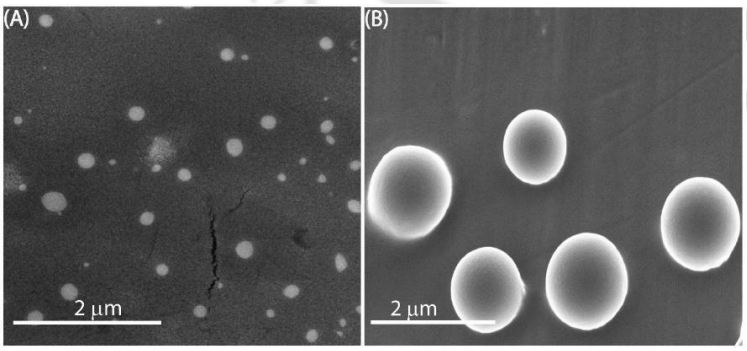


**Figure 4.6** Representative FESEM images of (A) nanoassembly (DTAB: AHPO: 1:1) and (B) suprasome.

### 4.4.3.3 ITC-based Host-Guest Interaction Study with Amphiphiles

The host-guest interaction of β-CD with DTAB and AHPO was investigated by isothermal titration calorimetry (ITC) measurements. The heat change induced due to the host-guest interactions was measured at 25 °C (301 K) and 300 rpm stirring speed using a Microcal PEAQ-ITC. A 1 mM solution of DTAB was titrated against a β-CD (10 mM) solution. The titration method followed 16 injections (2 µL of each) of titrant (β-CD) into the sample cell containing DTAB (300 µL) at 2-minute intervals with continuous stirring. The ITC thermograms were fitted with a nonlinear least-square fit analysis to calculate the enthalpy change (ΔH) and the equilibrium constant (K). From the K values, the Gibbs free energy (ΔG) was calculated. Using the Gibbs equation: $\Delta G = \Delta H - T\Delta S$, the entropy change (ΔS) value was calculated. The calculated ΔH and ΔS values suggested that the interaction of DTAB with β-CD is driven by an enthalpy-driven process. Similar measurements were performed for AHPO with β-CD and a mixture (1:1) of DTAB and AHPO with β-CD.

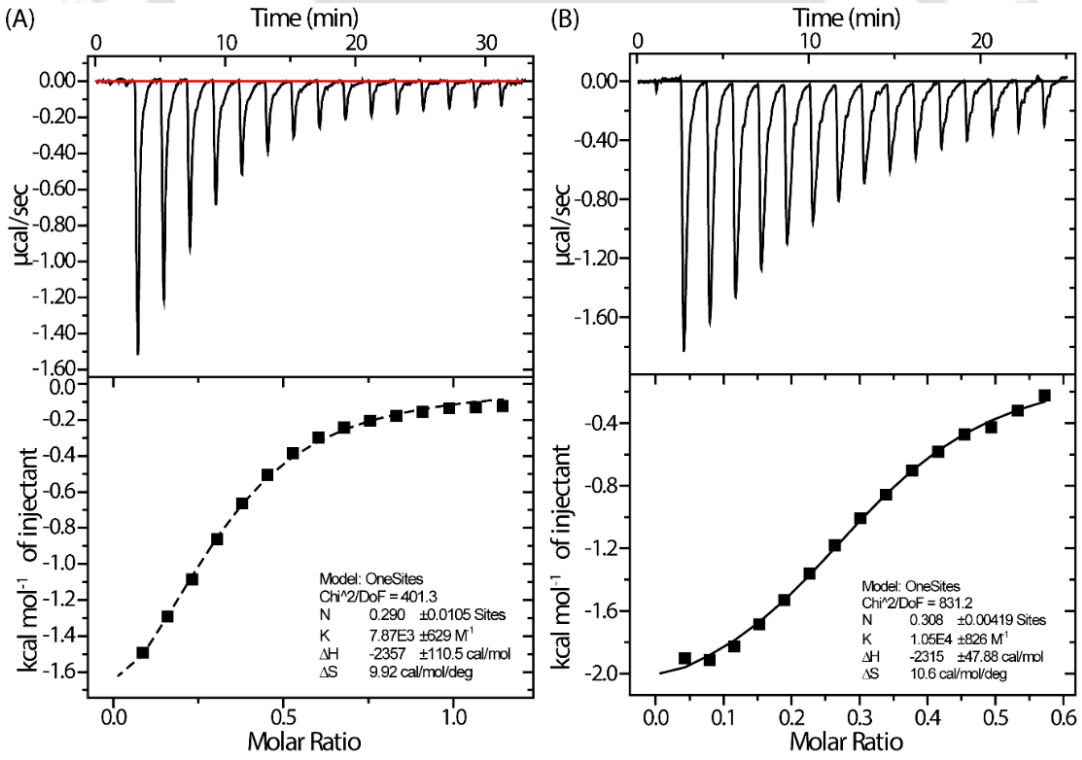


**Figure 4.7** ITC measurement of (A) DTAB (1 mM) and (B) AHPO (1 mM) with different concentrations of β-CD. Representative ITC thermograph and analysis of the ITC titration curve with the appropriate binding model.

### 4.4.3.4 Investigation of Suprasome Disassembly through DLS Measurements

Suprasomes were treated with 400 μM $Zn^{2+}$ and stirred for 15 minutes, after which their DH values were measured to explore any changes in their morphology. Upon the addition of $Zn^{2+}$, the hydrodynamic diameter exhibited a significant increase from 1066 nm to 2308 nm, indicating a distinct transformation in the supramolecular nanostructure, which could be due to the complexation of $Zn^{2+}$ with the components of the suprasomes.

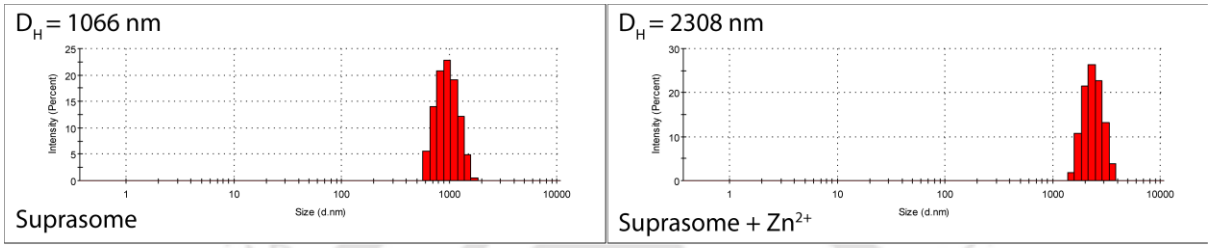


**Figure 4.8** Hydrodynamic diameters ($D_H$) of suprasomes before and after the addition of $Zn^{2+}$ (400 μM).

### 4.4.3.5 Control Morphological Analysis

The aqueous solutions of suprasome, AHPO (200 μM) and a mixture of AHPO (200 μM) and β-CD (5 mM) were treated with $Zn^{2+}$ (400 μM). The solution was kept stirring for a few minutes. The solutions were then drop-casted onto a glass slide and dried at room temperature. Before the analysis, the glass slide containing the sample was coated with a gold solution and loaded onto the FESEM grid for further analysis.

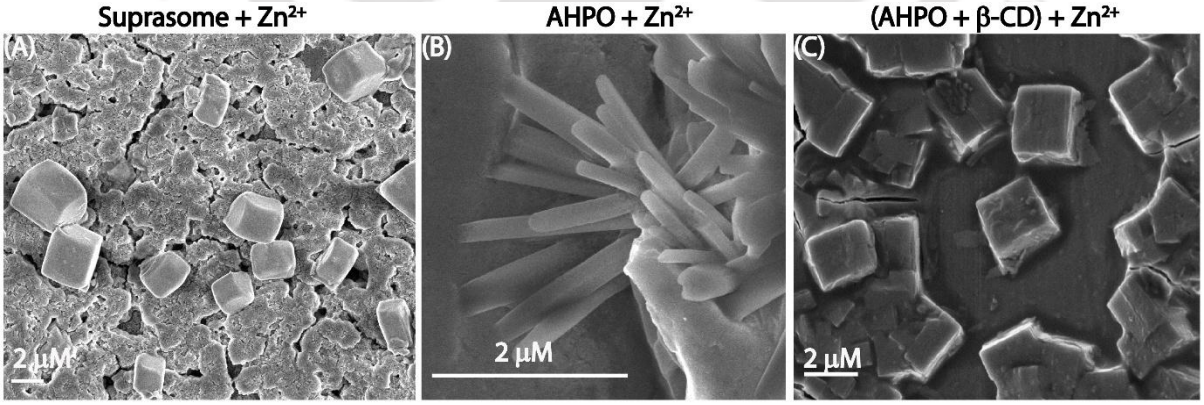


**Figure 4.9** Representative FESEM images of $Zn^{2+}$ treated (A) suprasome, (B) AHPO, and (C) a mixture of AHPO and β-CD.

The morphology of β-CD (5 mM) and $Zn^{2+}$ (400 μM) mixture was analysed through FESEM. The mixture of β-CD (5 mM) and $Zn^{2+}$ (400 μM) was kept on stirring for a few minutes and then drop-casted onto a glass slide and dried at room temperature. Similarly, other control samples were also prepared such as only AHPO (0.2 mM) and AHPO (0.2 mM) + β-CD (5 mM) and were also analysed through FESEM. Before the analysis, the glass slide containing the sample was coated with a gold solution and loaded onto the FESEM grid for further analysis.

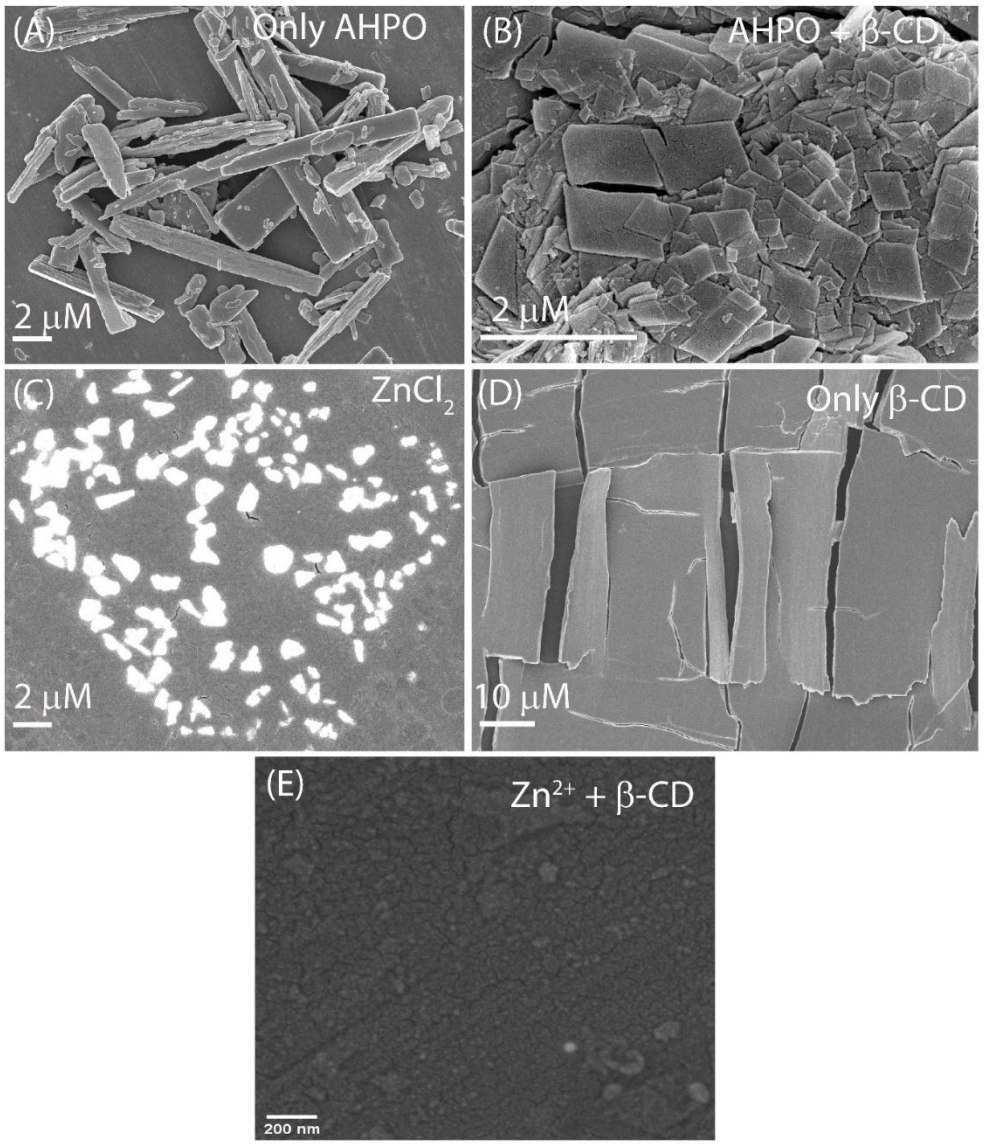


**Figure 4.10** Representative FESEM images of (A) only AHPO, (B) AHPO with β-CD, (C) only $ZnCl_2$, (D) only β-CD and (E) β-CD with $ZnCl_2$.

**Note:** The FESEM images of $ZnCl_2$ exhibit a shiny appearance and show a significantly different morphology compared to those observed for only AHPO, AHPO with β-CD, and only β-CD.

### 4.4.3.7. FESEM (EDX and Elemental Mapping Analysis)

FESEM sample of supracube was prepared following the previously mentioned method (section 4.4.3.5) for Energy Dispersive X-ray (EDX) and elemental mapping analysis.

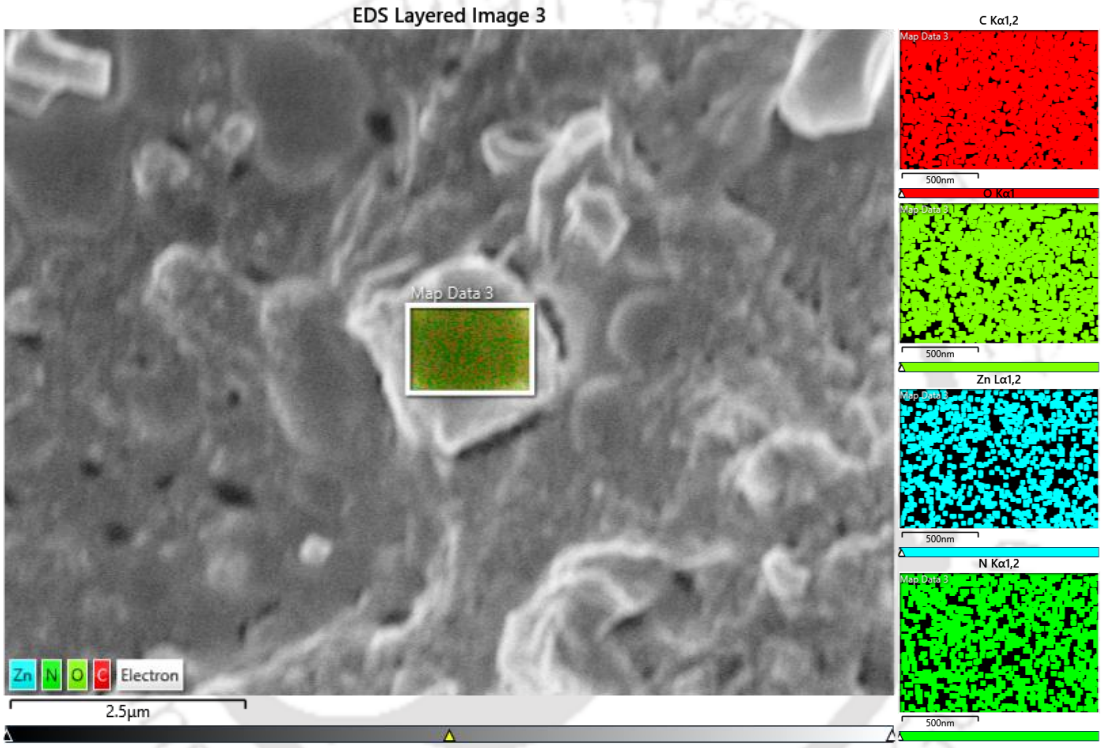


**Figure 4.11** FESEM mapping analysis for the C, O, N, and Zn. Energy Dispersive X-ray spectroscopy mapping analysis of the supracube.

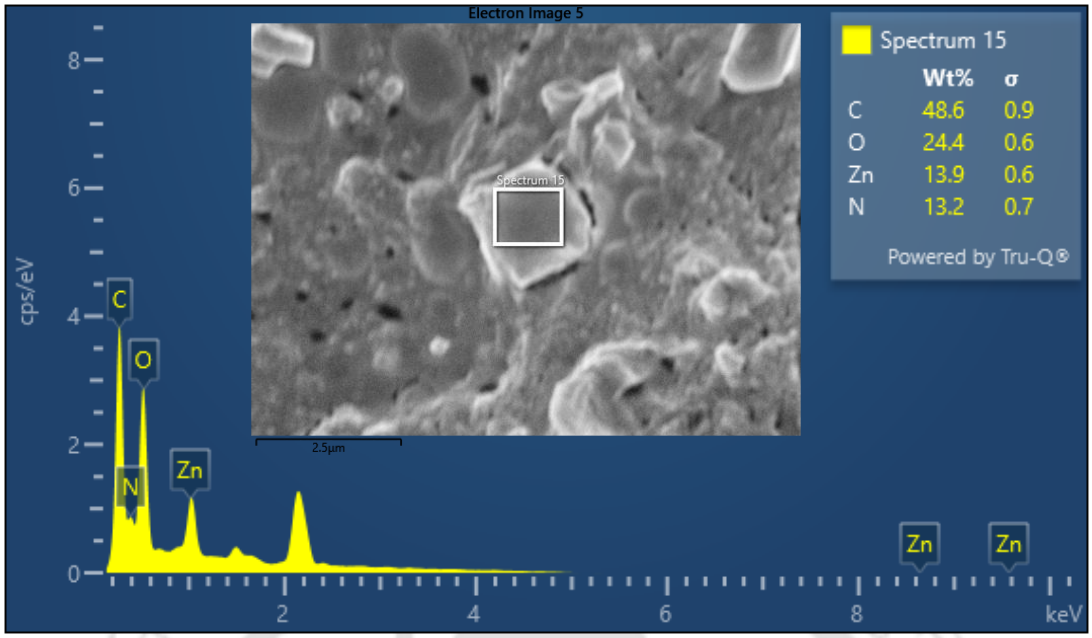


**Figure 4.12** FESEM-EDX elemental analysis of supracube in weight %.

#### 4.4.3.6 Transmission Electron Microscopy (SAED, EDX and Elemental Mapping Analysis)

The morphology of the supracubes was investigated by transmission electron microscope (TEM). First, the aqueous solution of the supracube was prepared by the addition of $Zn^{2+}$ to suprasome and stirring for a few minutes. A 10 µL of the solution was placed onto a carbon-coated copper grid and allowed to settle down for 1 minute. The grid was then carefully blotted with filter paper, and only a trace amount of the solution in the middle of the grid was kept. After that, the grid was allowed to dry for 10 minutes at 30 °C. Finally, 10 µL of 2% uranyl acetate solution (in water) was added to the grid and allowed to dry for another 1 min at room temperature. The excess uranyl acetate solution was soaked off with tissue paper, and the grid was dried overnight at 30 °C. The images were collected using a JEOL JEM 2100 transmission electron microscope (operated at a maximum accelerating voltage of 200 kV). During the analysis, Selected Area Electron Diffraction (SAED) analysis was used to get an inference about the crystallinity of the supracubes.

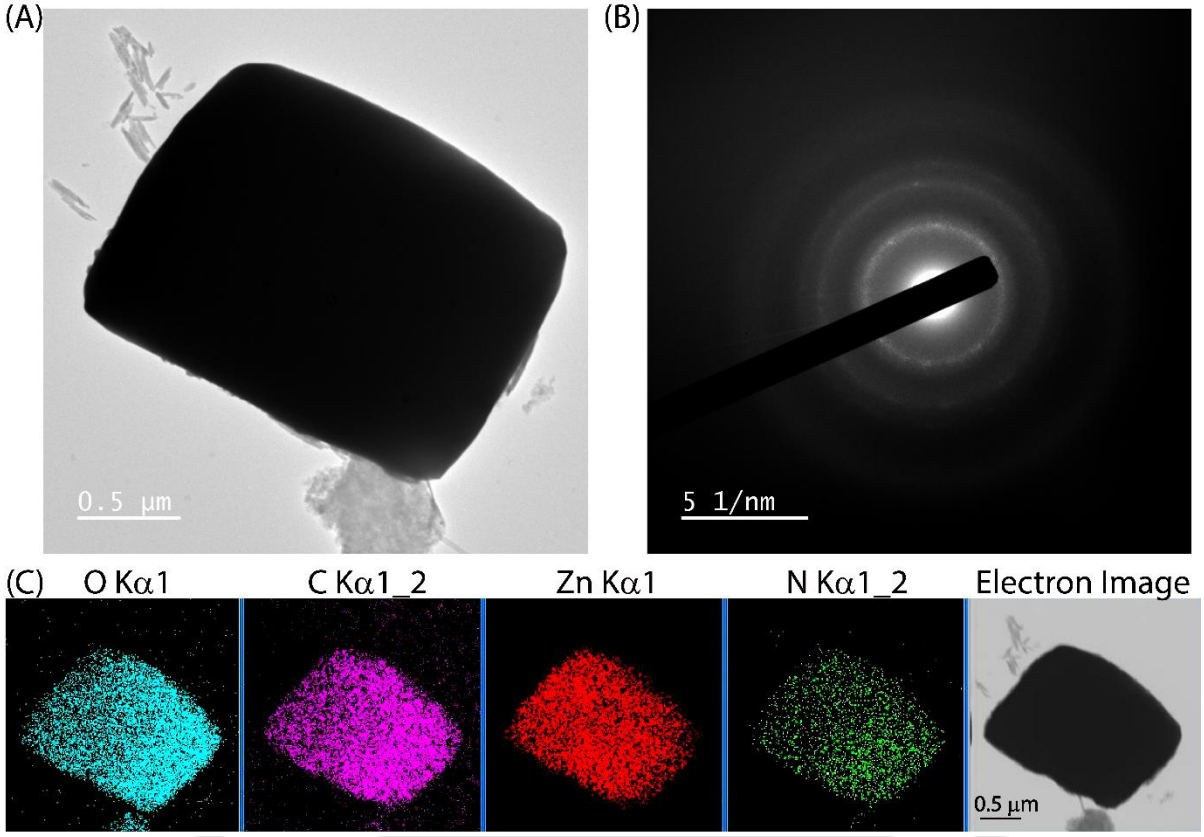


**Figure 4.13** (A) Transmission electron microscopy (TEM) and (B) selected area electron diffraction (SAED) analysis of the supracube structure. Transmission electron microscopy–energy-dispersive X-ray spectroscopy (TEM-EDS) mapping analysis of the O, C, Zn, and N of the supracube.

**Note:** The TEM-EDX analysis revealed a significant difference in $Zn^{2+}$ (C, N, O) concentration between the supracube region and the surrounding area. The concentration of $Zn^{2+}$ in the supracube region is notably higher than that in the outside region, indicating that the morphology of the supracube contains AHPO, β-CD and $Zn^{2+}$.

#### 4.4.3.7 Powder XRD Analysis

A suprasome solution was prepared as mentioned in previous sections and $Zn^{2+}$ (400 µM) was added to generate supracubes. The solution was kept on stirring for 30 minutes for complete conversion to supracubes. Then the sample were drop casted onto glass slide and dried at room temperature. This sample was used for powder XRD analysis with a speed of 10 degree/minute at room temperature. The analysis was conducted using the Phillips PAN analytical diffractometer with Cu Kα radiation (α = 1.5406 Å, 40 kV, 40 mA) and the Rigaku Micro Max

007HF diffractometer. The powder XRD analysis confirmed a polycrystalline nature of the supracube supporting the SAED analysis in TEM. Also, the powder xrd pattern does not match with reported only $Zn^{2+}$ or β-CD, further ruling out any possibility of only these controls forming these supracube like structure.[23]

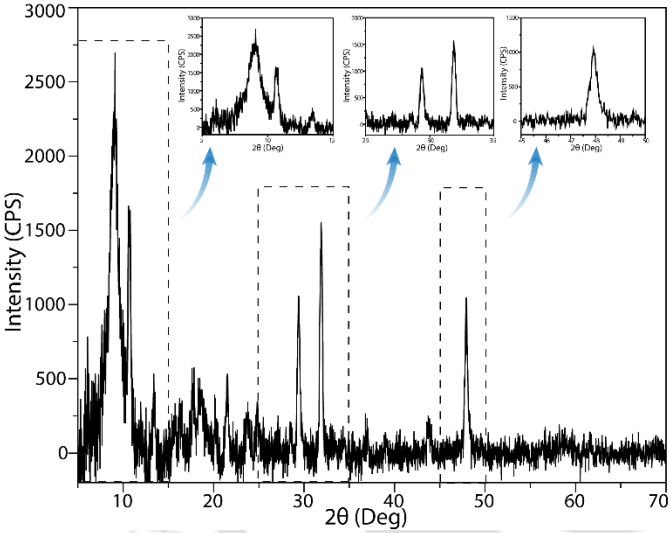


**Figure 4.14** Powder X-Ray Diffraction (PXRD) pattern of supracubes.

### 4.4.3.8 Fluorescence Microscopy-based Suprasome to Supracube Transformation

For fluorescence imaging of $Zn^{2+}$-triggered suprasome-to-supracube transformation, suprasomes were prepared following the aforementioned method. Nile Red (100 µM) was then added and incubated in the dark for 15 minutes to allow incorporation into the suprasome. An initial aliquot of the dispersion was mounted on a glass slide and imaged using a fluorescence microscope equipped with a TRITC filter ($\lambda_{ex}$ = 540–560 nm, $\lambda_{em}$ = 570–620 nm), capturing the fluorescence profile of intact suprasomes (t = 0 min). To induce supracube formation, $ZnCl_2$ (400 µM) was added to the remaining dispersion, followed by gentle mixing. Additional images were acquired after 5 minutes and 15 minutes of $Zn^{2+}$ treatment to observe the gradual disappearance of suprasome and the appearance of supracube structures.

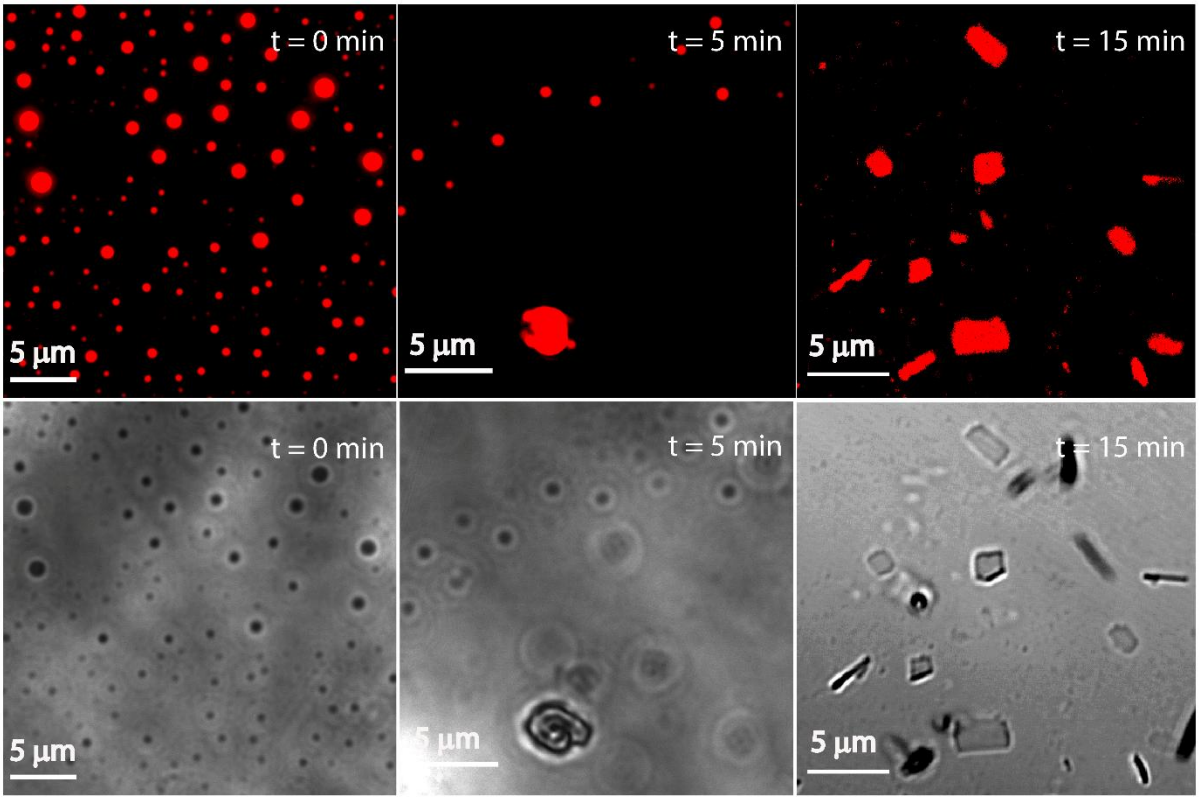


**Figure 4.15** Representative fluorescence and bright-field microscopic images for the suprasome (at t =0 min) to supracube transformation after $ZnCl_2$ addition (at t = 5 min, and t = 15 min).

### 4.4.4 Catalytic Activity

#### 4.4.4.1 Ester Hydrolysis by AHPO-$Zn^{2+}$ Complex, Suprasome and Supracube

The UV-Vis spectral analysis of clioquinol (CQ) and Clioquinol ester (CQE) was conducted in aqueous media. The CQE exhibited an absorbance peak at 240 nm, and upon excitation at this wavelength, it displayed fluorescence emission at 410 nm, serving as a spectral signature for the ester derivative. In contrast, CQ showed very weak absorbance at 240 nm indicating negligible fluorescence under identical excitation conditions. This highlights the role of esterification in modulating its photophysical properties (Figure 4.16A). In HEPES buffer (20 mM, pH 7.0), AHPO (50 µM) and $Zn^{2+}$ (100 µM) were added and stirred for a few minutes. The CQE (200 µM) was added to this buffer solution and stirred continuously. Fluorescence measurements were recorded at different time intervals to evaluate the extent of hydrolysis (Figure 4.16B).

In order to investigate the catalytic activity, suprasome and supracube were formulated as per the previous method, and the corresponding catalytic efficiency was determined through fluorometric detection of CQE (Initial working concentration 500 µM).

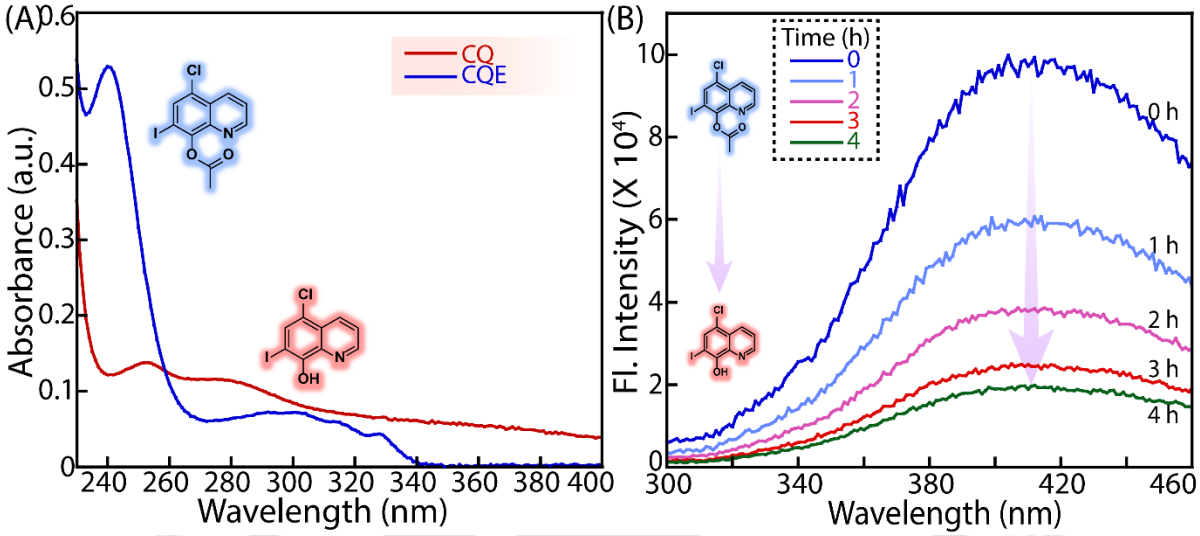


**Figure 4.16** (A) UV-Vis spectra of CQ and CQE. (B) Time-dependent CQE hydrolysis by AHPO-$Zn^{2+}$ complex.

In order to investigate the catalytic activity, supracube, suprasome were formulated as per the previous method. The catalytic efficiency of these supramolecular structures, along with only $Zn^{2+}$, was determined through fluorometric detection of CQE (Initial working concentration 500 µM). Simultaneously, these samples were also analysed through HPLC for CQE hydrolysis and CQ generation. At time intervals of 0 h, 1 h, 2 h, 3 h, 4 h, and 5 h, incubated samples were recorded. For the HPLC-based study of proionophore (CQE) to ionophore (CQ) release, various treated samples were filtered through an ultracentrifugation tube to remove the larger particles. Before injection into the HPLC port, the samples were additionally filtered using a 0.22 µm PTFE syringe filter. Column used: Ascentis® express C18, 2.7 µm HPLC column, flow rate: 0.5 mL/min, mobile phase used: gradient of acetonitrile/water.

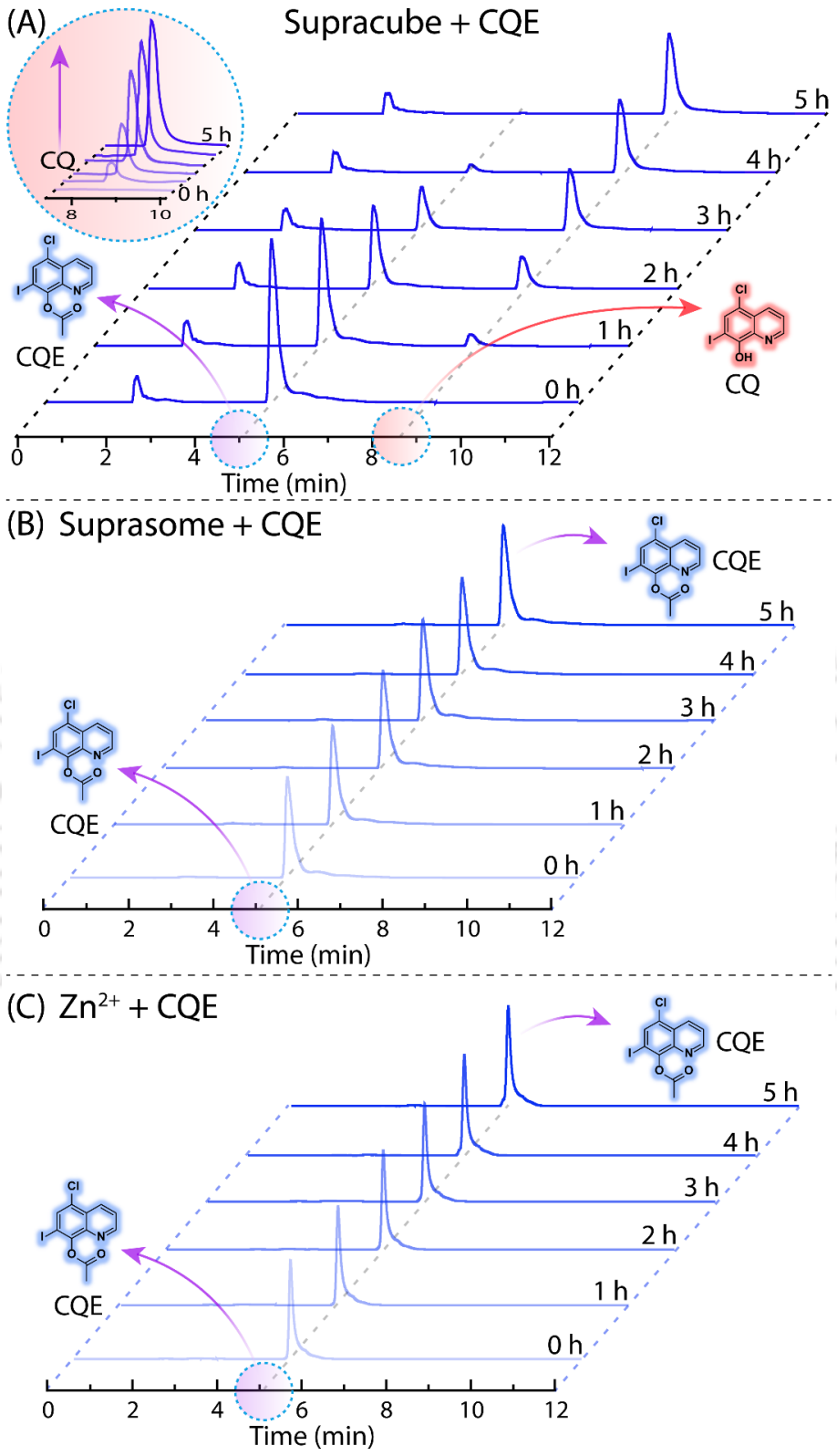


**Figure 4.17** HPLC-based measurement of CQE hydrolysis and active ionophore (CQ) release upon treatment with supracube, suprasome and $Zn^{2+}$. Chromatograms of CQE in the presence (A) supracube (B) suprasome and (C) $Zn^{2+}$.

Further rate of CQE hydrolysis was calculated from HPLC analysis.

Average rate = Change in concentration / Change in time

$$\text{Rate} = \frac{\Delta[\text{CQE}]}{\Delta t} = \frac{500\ \mu M}{18{,}000\ s} \approx 0.0278\ \mu M/s = 2.78\times10^{-8}\ M/s$$

The rate of reaction is approximately 0.0278 μM/s (or $2.78\times10^{-8}$ M/s) in the presence of the supracubes.

### 4.4.4.2 UV-Vis Absorbance-based Analysis of AHPO-$Zn^{2+}$ Complex and Effect of EDTA

The AHPO solution (10 μM) was treated with increasing amounts of $ZnCl_2$ (0-40 μM) in 50% DMSO/water, and the corresponding absorbance was measured to showcase the spectral shift of AHPO upon $Zn^{2+}$ treatment. To investigate the interaction of only AHPO with $Zn^{2+}$, we dissolved AHPO in 50% DMSO/water, due to the partial solubility of AHPO in water. A new

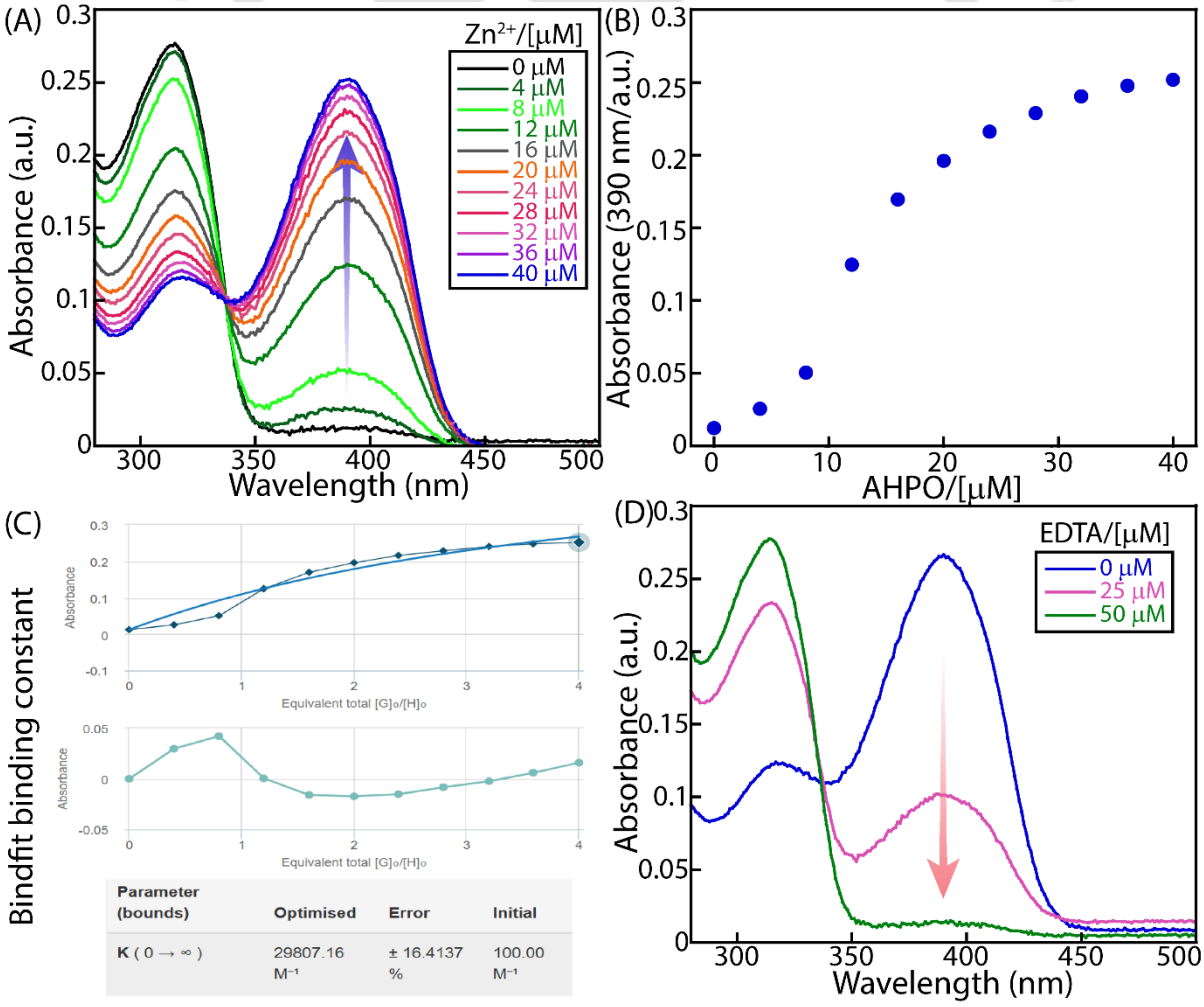

**Figure 4.18** UV-Vis spectral measurements of (A) AHPO (10 μM) with different concentrations of $Zn^{2+}$ (0-40 μM). (B) Variation of absorbance at 390 nm against different concentrations of $ZnCl_2$ (0-40 μM). (C) Binding analysis of AHPO with $Zn^{2+}$. (D) AHPO-$Zn^{2+}$ complex with different concentrations of EDTA.

absorbance peak at 390 nm was observed, which indicated the AHPO-$Zn^{2+}$ species. Meanwhile, variation of absorbance at 390 nm against different concentrations of $ZnCl_2$ (0-40 μM) was plotted to calculate the binding affinity of AHPO to $Zn^{2+}$. The Binding analysis (using BindFit v0.5 program) revealed the binding affinity of 29807 ± 16 $M^{-1}$. The AHPO-$Zn^{2+}$ complexed form was treated with EDTA (50 μM) to showcase its decomplexation ability. EDTA treatment led to decay in the 390 nm absorbance peak, showcasing $Zn^{2+}$ capture by EDTA and subsequent generation of only AHPO species.

### 4.4.4.3 Effect of EDTA on Supracube Structure

Supracube were generated as mentioned in the earlier section. Further EDTA (500 μM) was added to the solution and kept on stirring for 15 minutes. Both DLS and FESEM-based analyses were conducted to explore the effect of EDTA on the hydrodynamic diameter as well as morphology. Upon EDTA addition, the supracube ($D_H$~2500 nm) reverted to a suprasome-like state ($D_H$~1000 nm). The FESEM analyses further corroborated this morphological transition, demonstrating the reversible formation of suprasomes from supracube.

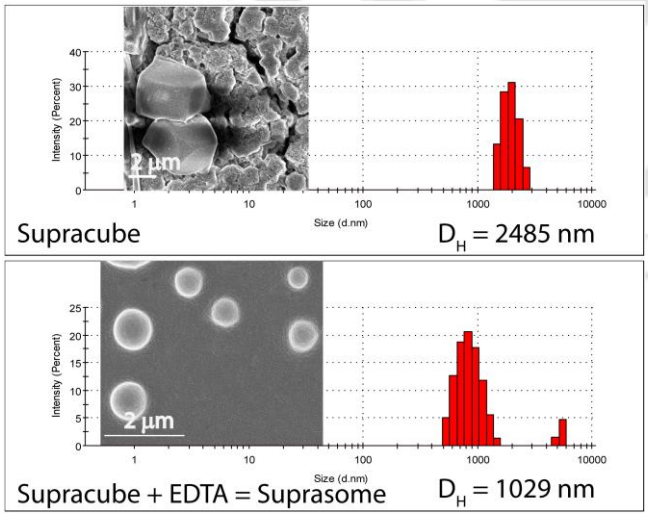


**Figure 4.19** The impact of $Zn^{2+}$ on the morphology of the supracube structure was analysed using DLS and FESEM techniques.

### 4.4.4.4. Catalytic Activity after EDTA Treatment to Supracube

Upon reversal of supracube to suprasome following the above procedure, CQE (500 μM) was added to the solution and corresponding ester hydrolysis property was observed through fluorometric detection of CQE.

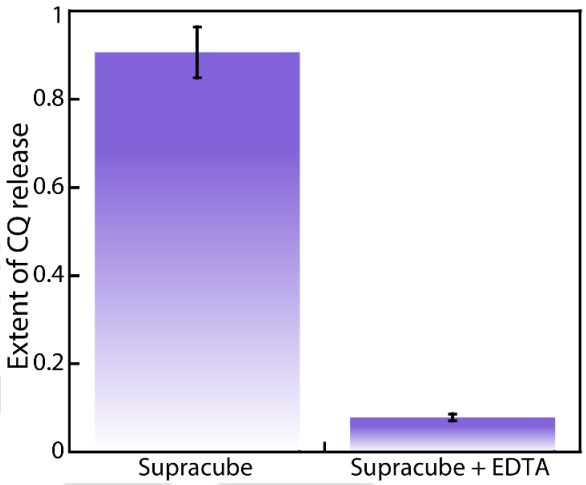


**Figure 4.20** Comparison of ester hydrolysis between supracube and EDTA-treated supracube.

### 4.4.4.5 UV-Vis Analysis of EDTAE-Mediated AHPO–$Zn^{2+}$ Complex Dissociation

To a 10 μM AHPO, 40 μM $Zn^{2+}$ was added to prepare 10 μM AHPO-$Zn^{2+}$ complex in 50% DMSO/water due to the partial solubility of AHPO in water. To this AHPO-$Zn^{2+}$ complex, EDTAE (50 μM) was added and UV-absorbance spectra were recorded after each 30 minutes. Initially a peak at 390 nm was observed due to presence of AHPO-$Zn^{2+}$ complex which eventually diminished and a peak at 315 reappeared. This confirmed the dissociation of AHPO-$Zn^{2+}$ complex and regeneration of AHPO only. Simultaneously, this experiment confirmed the hydrolysis of EDTAE by the AHPO–$Zn^{2+}$ complex and release of EDTA, which subsequently sequesters $Zn^{2+}$ ions and leads to the dissociation of the complex, restoring the system to its original AHPO state.

### 4.4.4.6 Evaluation of EDTA Release Using Arsenazo-III Dye: Supracube and AHPO–$Zn^{2+}$ Complex

Arsenazo-III dye is recognised for its capability to detect divalent metal ions like $Zn^{2+}$, exhibiting distinct spectral changes depending on whether free $Zn^{2+}$ ions are present or absent

in the solution.[24] To a solution of arsenazo-III dye (25 μM) in distilled water, $Zn^{2+}$ was added till the spectral red-shift got saturated and showed no noticeable change upon further $Zn^{2+}$ addition in absorption spectra. To the (arsenazo-III + $Zn^{2+}$) solution, equal amounts of EDTA (2 mM) and EDTAE (2 mM) were added, and the absorbance spectra were measured. The EDTA addition showcased an immediate blue shift, confirming the removal of free $Zn^{2+}$ from the solution. But EDTAE addition did not showcase any blueshift, confirming its inability to completely capture $Zn^{2+}$ and reverse the spectral shift. Nevertheless, EDTAE was able to capture only a small fraction of $Zn^{2+}$, as indicated by the slight reversal seen immediately after its addition. This demonstrated that EDTAE is unable to completely sequester $Zn^{2+}$ from the solution. This can be attributed to the absence of a strongly chelating carboxylate group and the pronounced hydrophobic character of EDTAE.

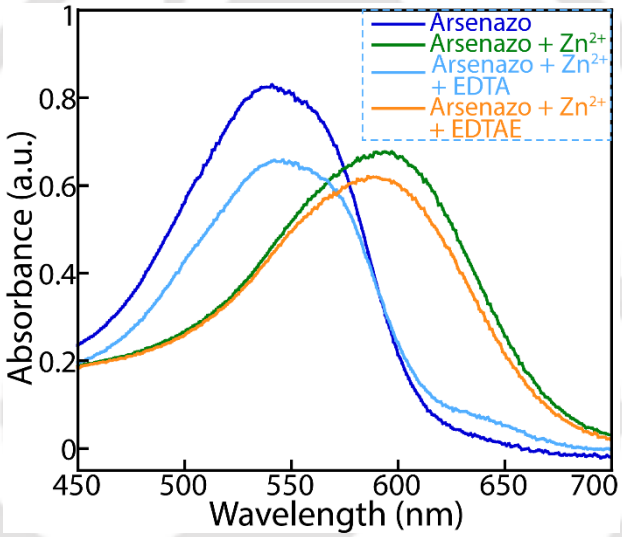


**Figure 4.21** UV-Vis absorbance spectra of arsenazo-III dye (25 μM) in the absence and presence of $Zn^{2+}$ ion (2 mM) and effect of EDTA (2 mM) and EDTAE (2 mM) on arsenazo-III + $Zn^{2+}$ complex.

In a separate time-dependent experiment, the prepared solution containing arsenazo-III (25 μM) and $Zn^{2+}$ (2 mM) was treated with either EDTAE (2 mM) alone, EDTAE (2 mM) combined with a mixture of DTAB (200 μM) and β-CD (5 mM), or only EDTAE (2 mM) combined with suprasome which converts to supracube in presence of excess $Zn^{2+}$ in the solution. The absorption spectra were recorded every 2 hours thereafter. Only the EDTAE addition and the mixture of DTAB and β-CD-treated EDTAE addition did not reverse the red shift, confirming that both cases failed to generate EDTA in the solution. This ruled out any

possibility of EDTAE ester hydrolysis to EDTA by only $Zn^{2+}$ or the mixture of DTAB and β-CD. On the contrary, the suprasome treated EDTAE successfully reversed the red shift of arsenazo-III in a period of 6 h. It is noteworthy that the suprasome converts to supracube in solution due to excess $Zn^{2+}$ presence which hydrolyses EDTAE to EDTA that preferably captures the free $Zn^{2+}$ present in solution, hence reversing the red-shift of $Zn^{2+}$ sensitive arsenazo-III dye.

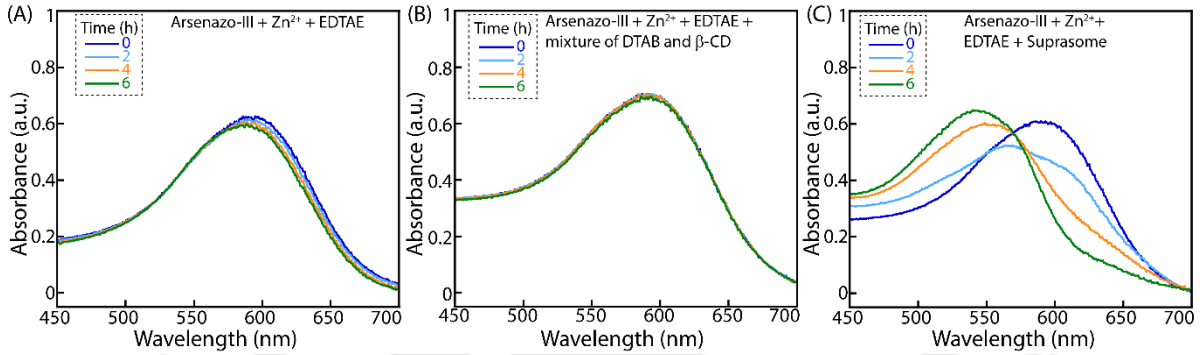


**Figure 4.22** Time dependant UV-Vis absorbance spectra of arsenazo-III dye (25 μM) with $Zn^{2+}$ in presence of (A) EDTAE, (B) suprasome treated EDTAE, (C) supracube treated EDTAE.

### 4.4.5 EDTAE-Mediated Transient Suprasome-Supracube Transformation

Suprasomes were prepared following the previous procedure. The solution of the suprasome was initially incubated with EDTAE (500 μM). To this solution, $ZnCl_2$ (400 μM) was added and kept under stirring conditions for 15 minutes. DLS measurements were performed to assess the effect of $Zn^{2+}$ addition on the variations of hydrodynamic diameters of the in situ generated compartmentalised structures. Initial DLS measurements were performed 15 min after the addition of $Zn^{2+}$. As confirmed via previous experiments that the supracube hydrolyses the EDTAE to EDTA, we further performed the DLS measurements after 360 minutes because EDTAE generates negative feedback EDTA, which makes the formation of supracubes a temporary process. After each cycle, $Zn^{2+}$ (chemical signal, 400 μM) and EDTAE (feedback controller, 500 μM) were introduced into the system for the next transient cycle to sustain.

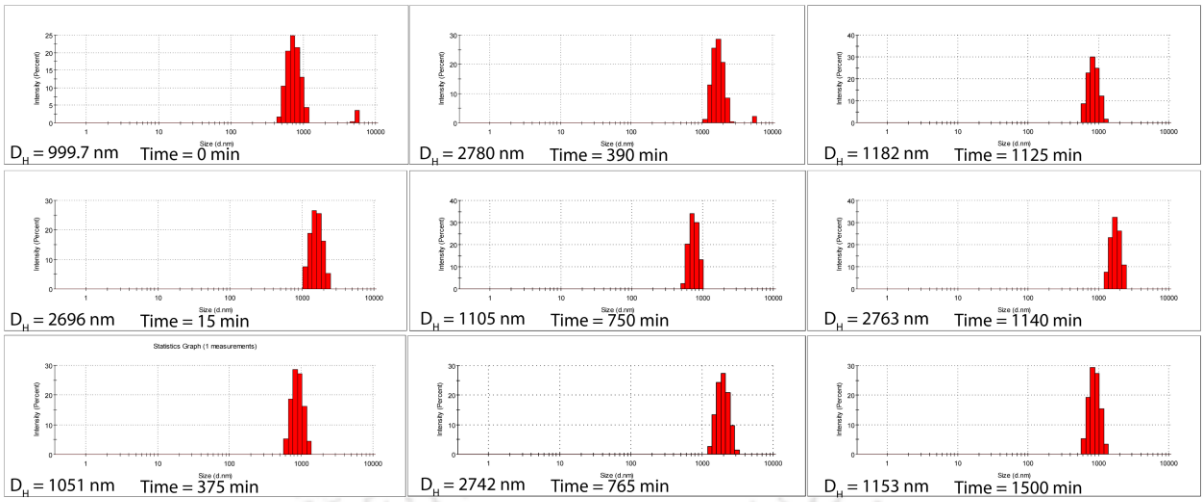


**Figure 4.23** DLS measurement-based size distribution plot of multiple transient suprasome-supracube interconversion cycles.

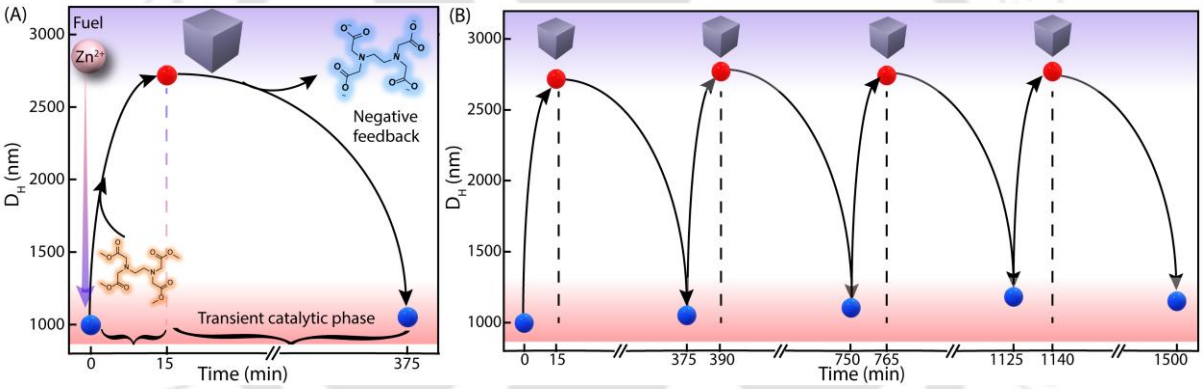


**Figure 4.24** DLS measurements of transient suprasome-supracube interconversion (Single transient catalytic cycle) (A). Multiple cycles of transient conversion through DLS measurement (B).

### 4.4.6 EDTAE-Mediated Transient Catalysis

To assess the transient catalytic behaviour of the added suprasome system, we performed a comparative study of ester hydrolysis with CQE as substrate. The first suprasome system containing only CQE (500 μM) and the second one containing both EDTAE (500 μM) and CQE (500 μM) were treated with $Zn^{2+}$ (400 μM). The corresponding ester hydrolysis was monitored at 1 h intervals through fluorescence intensity of CQE for both the system up to 6 h ($\lambda_{ex}$ = 240 nm, $\lambda_{em}$ = 410 nm). In the second cycle, CQE (500 μM) was reintroduced into both the system and stirred for 10 minutes to mix it in the solution homogeneously. Further,

fluorescence measurements were observed at 1 h intervals for 6 h. For the 3rd cycle, $Zn^{2+}$ was introduced only to the suprasomal solution of the second system to regenerate supracube. Similarly, CQE was further reintroduced only to the 1st systems. Fluorescence measurements were continued as previously to get an idea about the extent of ester hydrolysis.

The extent of CQE hydrolysis was calculated as per the equation;

$$Extent\ of\ hydrolysis = \frac{F_0 - F_t}{F_0}$$

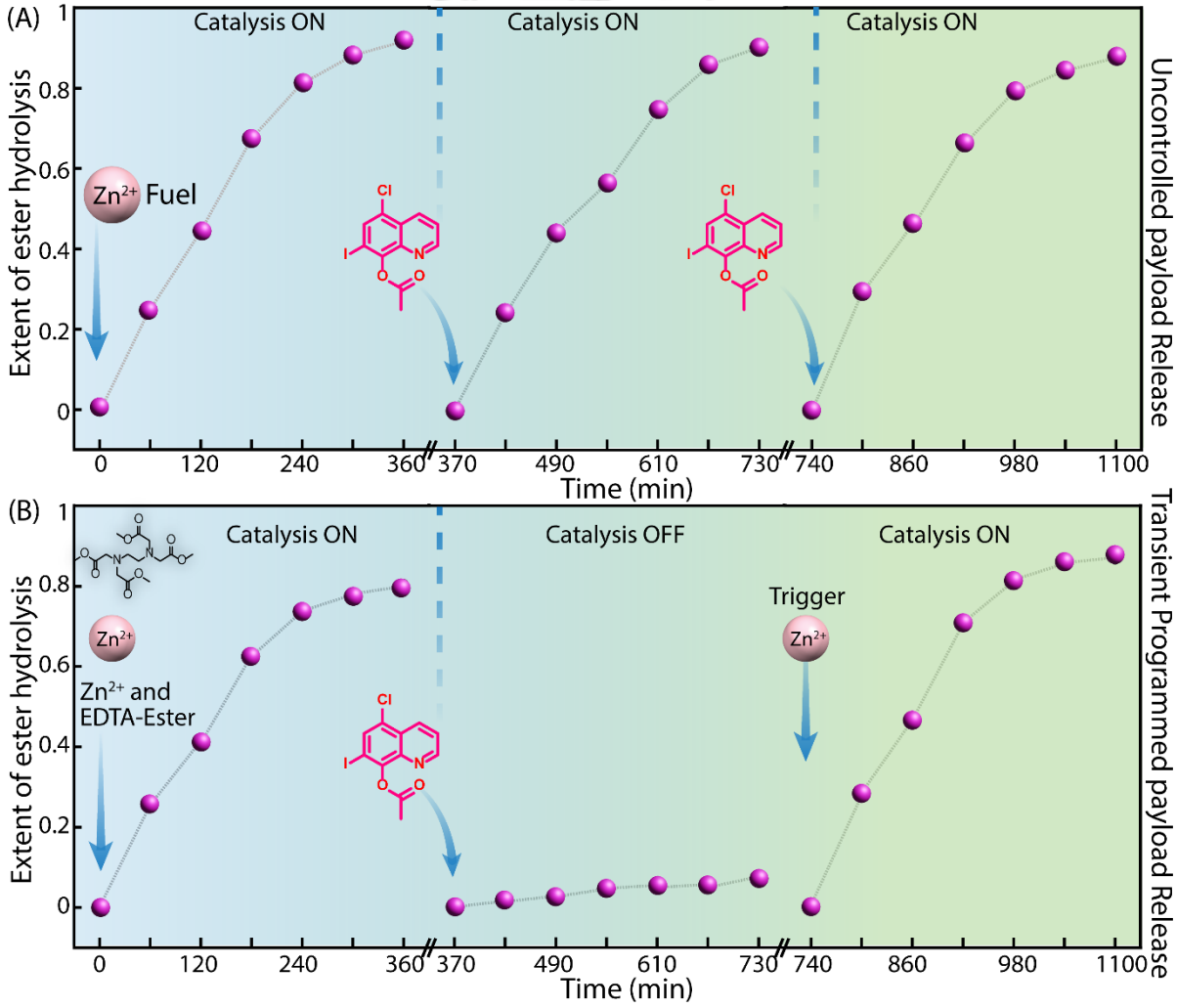


**Figure 4.25** Extent of CQE hydrolysis stimulated by $Zn^{2+}$ in multiple cycles for (A) suprasome without EDTAE and (B) suprasome with EDTAE.

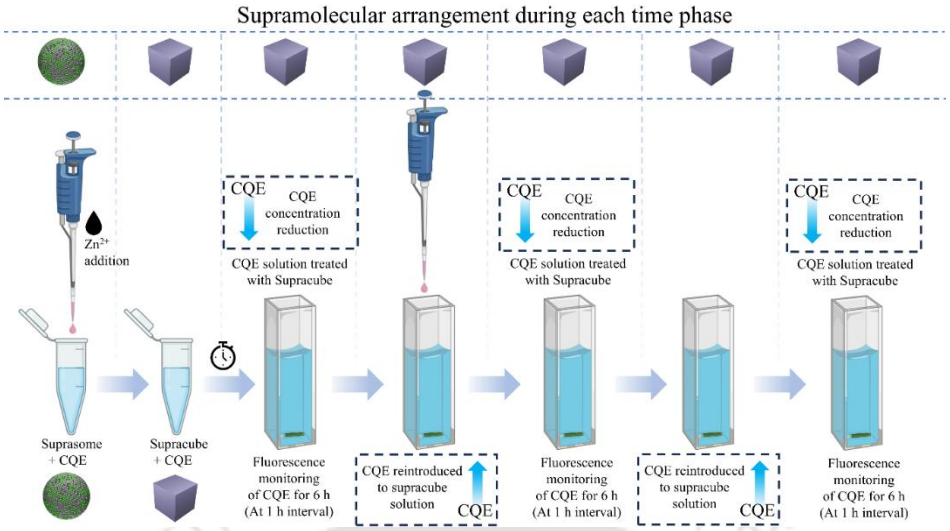


**Figure 4.26** Schematic presentation of the assay system for CQE hydrolysis stimulated by $Zn^{2+}$ in multiple cycles for suprasome without EDTAE.

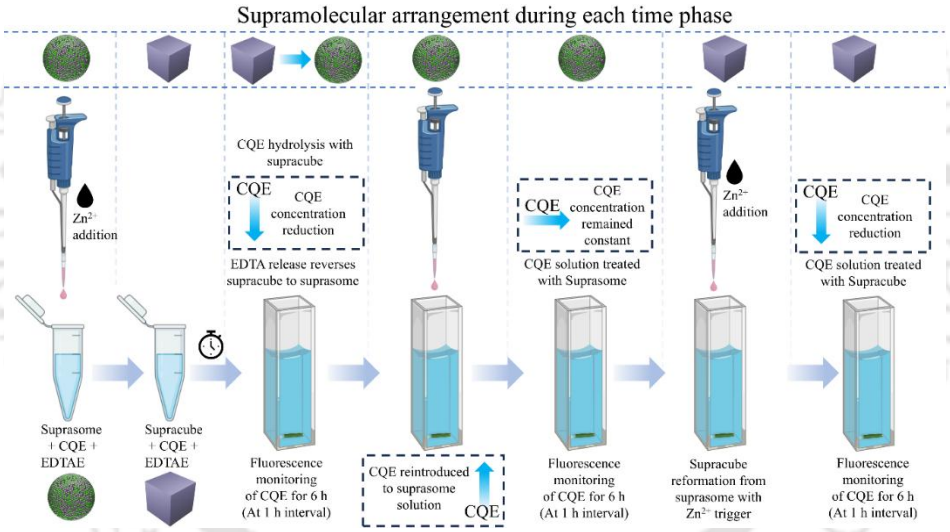


**Figure 4.27** Schematic presentation of the assay system for CQE hydrolysis stimulated by $Zn^{2+}$ in multiple cycles for suprasome with EDTAE.

### 4.4.7 Ion Transport Studies

The CQ is a known transmembrane transporter of $Zn^{2+}$. To assess the activity of the in situ-generated CQ from CQE (supracube-mediated hydrolysis), the transmembrane $Zn^{2+}$ transport activity was evaluated using fluorescence measurements.

#### 4.4.7.1 Preparation of EYPC/CHOL-LUVs⊃MgG Vesicles

Phosphatidylcholine (PC) and cholesterol (CHOL) are the two most abundant lipids in mammalian cell membranes; hence, both these lipids were used to prepare model large unilamellar vesicles (LUVs). To conduct the MgG fluorescence-based ion-transport studies, we took EYPC (50 mg/mL in deacidified $CHCl_3$) and cholesterol (CHOL; 25 mg/mL in deacidified $CHCl_3$) in a clean, dry glass vial in a molar ratio of 8:2. The solution was evaporated for 6 hours under reduced pressure to form a thin lipid film. After that, we rehydrated the film with 10 mM HEPES buffer containing 100 mM NaCl, 100 µM EDTA and 50 µM MgG dye at pH 7.0. The resulting suspension was vortexed six to seven times over 1 hour. Next, we performed 6-7 freeze-thaw cycles followed by 10 minutes of constant vortexing. We then extruded the lipid suspension 19–21 times using a mini extruder with a 200 nm pore size to achieve a uniform liposome size of 200 nm. Finally, we removed the unencapsulated MgG dye using the gel filtration technique (Sephadex G-50) and 10 mM HEPES buffer containing 100 mM NaCl at pH 7.0 as the eluting solution. This process yielded a final lipid concentration of 25 mM (assuming 100% lipid regeneration).

#### 4.4.7.2 Ion Transport Studies using EYPC/CHOL-LUVs⊃MgG Vesicles

For the MgG-based ion transport assay, in a clean and dry fluorescence cuvette (3 mL), 10 mM HEPES buffer containing 100 mM NaCl and 100 µM EDTA, pH 7.0 (1930 µL), EYPC/CHOL-LUV⊃MgG (40 µL), and $ZnCl_2$ (final concentration 1 mM) were added. The cuvette was placed under slow stirring conditions in a fluorescence spectrophotometer for about 3 minutes to equilibrate. The fluorescence was evaluated as a function of time ($\lambda_{em}$ = 531 nm, $\lambda_{ex}$ = 506

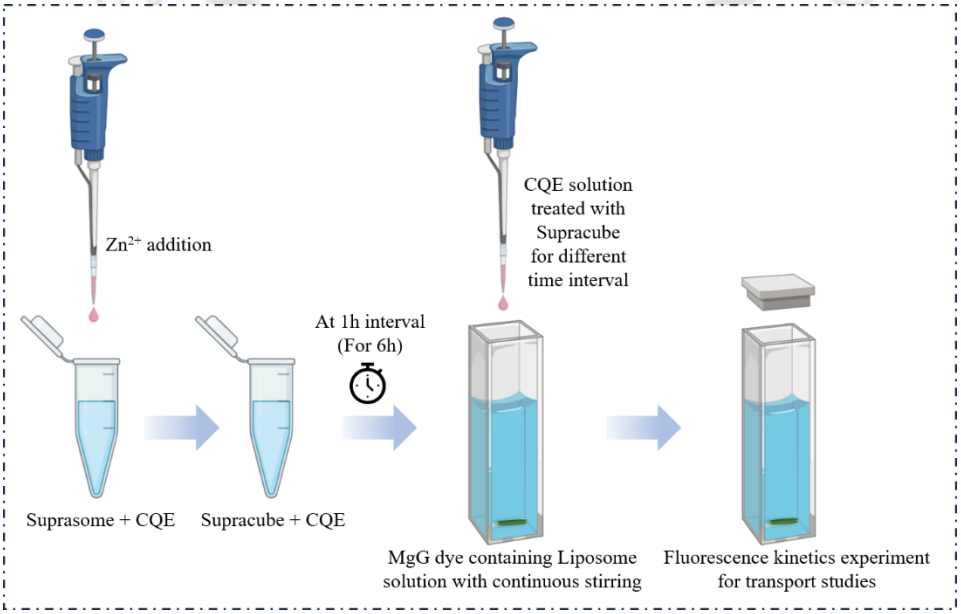

**Figure 4.28** Schematic representation of the supracube and CQE-mediated ion transport activity assay using the EYPC/CHOL-LUVs⊃MgG vesicles.

nm). At 50 s, the compound (stock solution of CQ and CQE in DMSO) was added to the cuvette solution to initiate the transport activity (Final working concentration 30 nM). Finally, the vesicles were completely lysed at 450 s by adding 20 µL of 20% Triton X-100. The fluorescence intensity measurement was continued for a further 50 s. The normalized % transport efficiency (%EE) at t = 450 s was considered for the particular transport efficiency of the compounds.

Transport activity, $T_{MgG} = (\frac{F_t - F_0}{F_\infty - F_0} \times 100)$ %

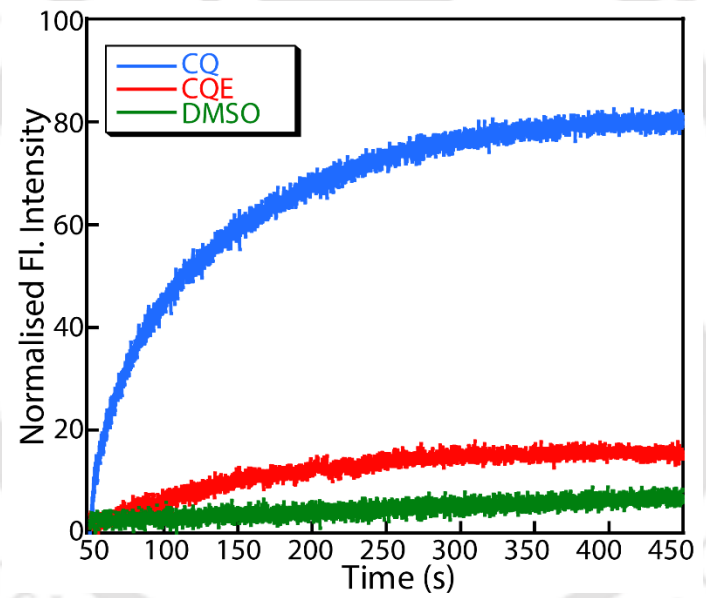


**Figure 4.29** $Zn^{2+}$ transport activity of CQ and CQE (30 nM) across the bilayers of EYPC/CHOL-LUV⊃MgG. (10 µl DMSO as a control).

### 4.4.7.3 Ion Transport Activity of CQE Exposed to $Zn^{2+}$ Treated Suprasome using EYPC/CHOL-LUVs⊃MgG Vesicles

As per the previously mentioned procedure, liposomes containing MgG dye were prepared.[22] Suprasomes with 500 µM of CQE were treated with 400 µM of $Zn^{2+}$ and kept under stirring conditions. The addition of $Zn^{2+}$ triggers the generation of supracube from the suprasome that continues the ester hydrolysis, releasing active ionophore (CQ) into the solution. For the MgG-

based ion transport assay, in a clean and dry fluorescence cuvette (3 mL), 10 mM HEPES buffer containing 100 mM NaCl and 100 μM EDTA, pH 7.0 (1930 μL), EYPC/CHOL-LUV⊃MgG (40 μL), and $ZnCl_2$ (final concentration 1 mM) were added. The cuvette was placed under slow stirring conditions in a fluorescence spectrophotometer for about 3 minutes to equilibrate. The fluorescence was evaluated as a function of time ($\lambda_{em}$ = 531 nm, $\lambda_{ex}$ = 506 nm). At 50 s, the $Zn^{2+}$ treated suprasome solution containing CQE was introduced into the cuvette solution containing liposome to initiate the transport studies (Final working concentration of CQE 30 nM). Finally, the vesicles were completely lysed at 450 s by adding 20 μL of 20% Triton X-100. The fluorescence intensity measurement was continued for a further 50 s. The normalized % transport efficiency (%EE) at t = 450 s was considered for the particular transport efficiency of the compounds. The increase in transport activity can be attributed to the in-situ ester hydrolysis activity of the supracube, which releases active ionophore CQ from CQE.

Transport activity, $T_{MgG} = (\frac{F_t - F_0}{F_\infty - F_0} \times 100)$ %

Where, $F_t$ = fluorescence intensity at 450 s, $F_0$ = Initial fluorescence intensity, $F_\infty$ = fluorescence intensity after Triton X-100 addition.

### 4.4.8 NMR and HRMS Spectra of the Synthesised Compounds

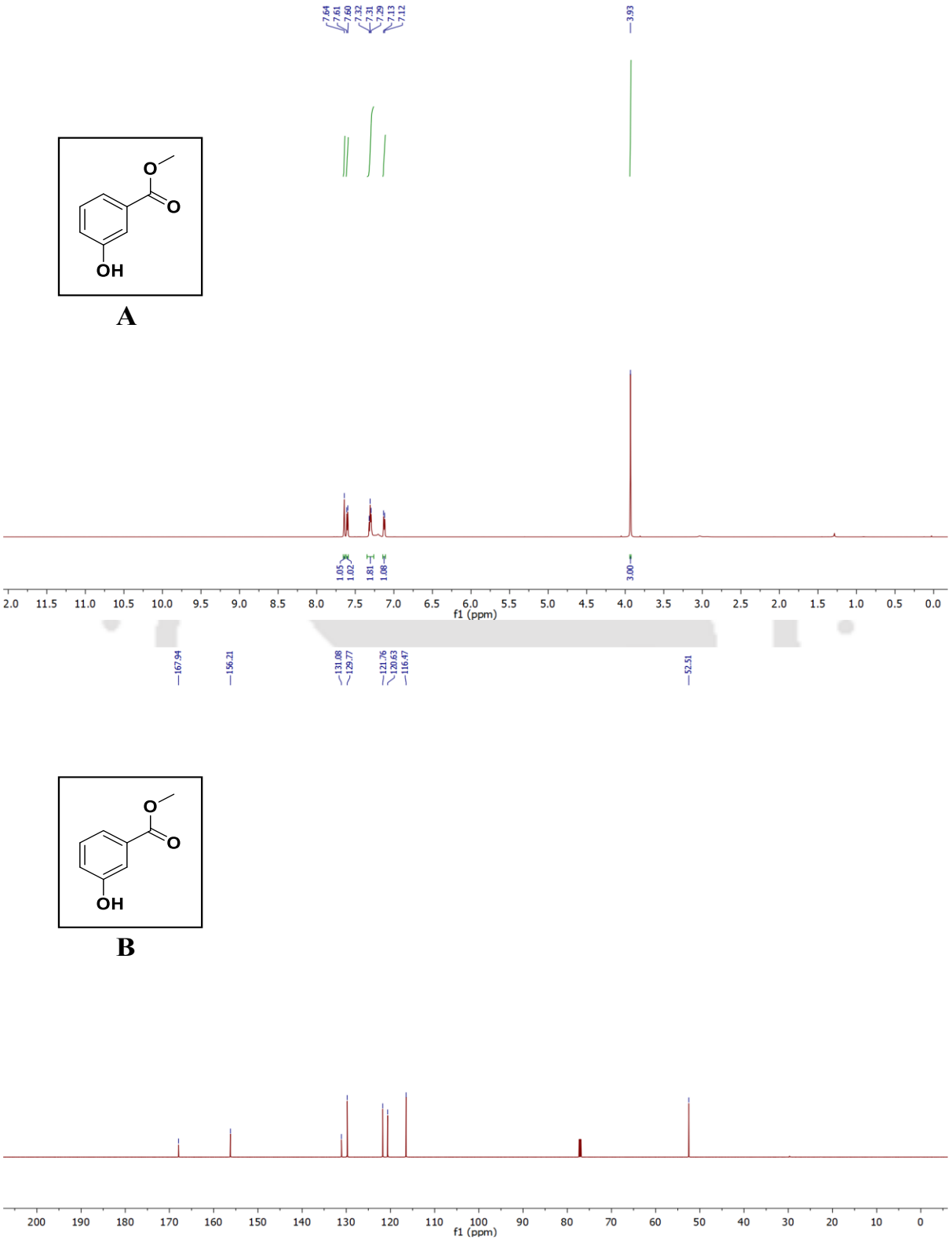


**Figure 4.30** (A) $^{1}$H NMR and (B) $^{13}$C NMR spectra of 3-hydroxybenzoate in the Chloroform-*d* solvent.

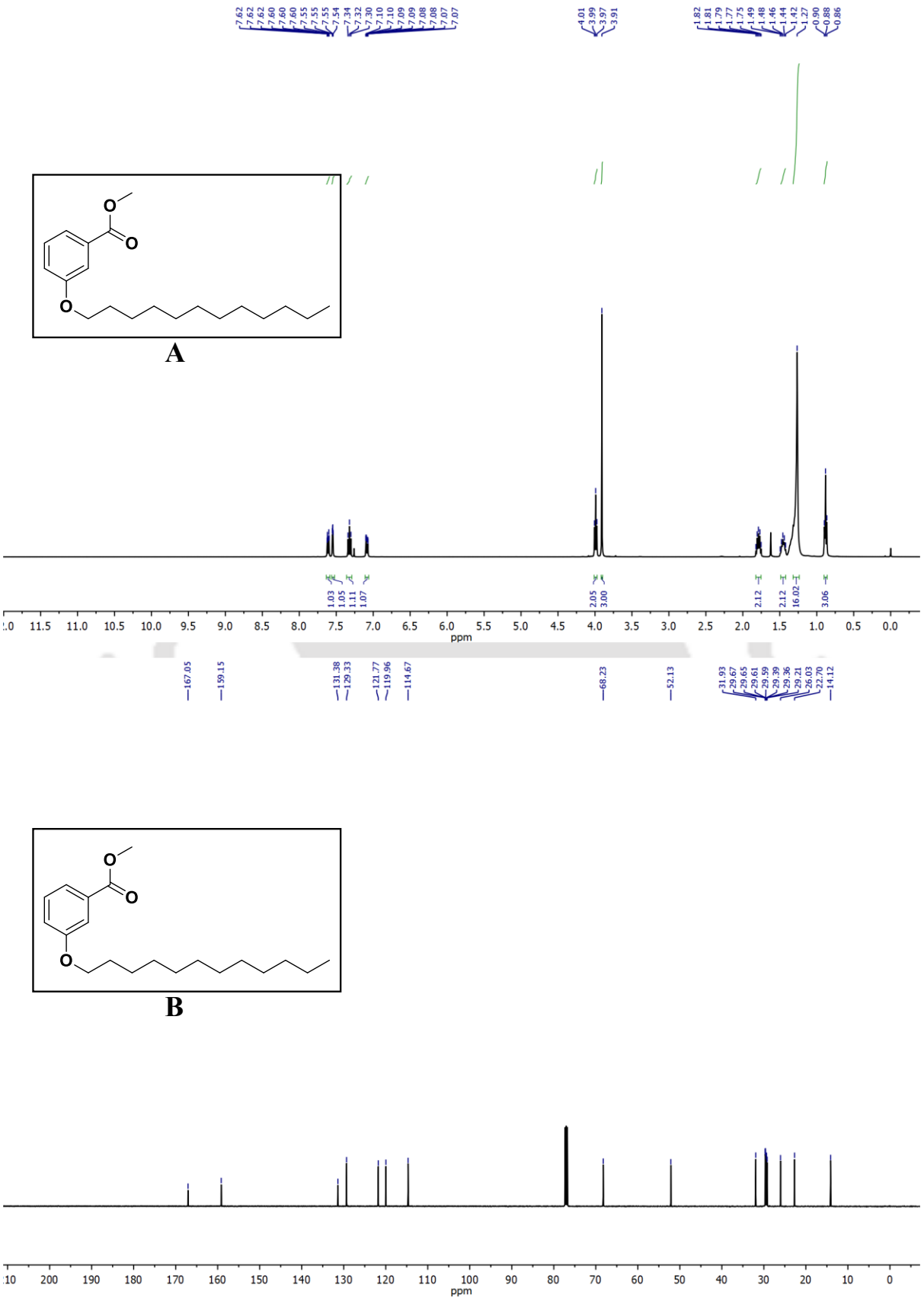


**Figure 4.31** (A) $^{1}$H NMR and (B) $^{13}$C NMR spectra of methyl 3-(dodecyloxy)benzoate in the Chloroform-*d* solvent.

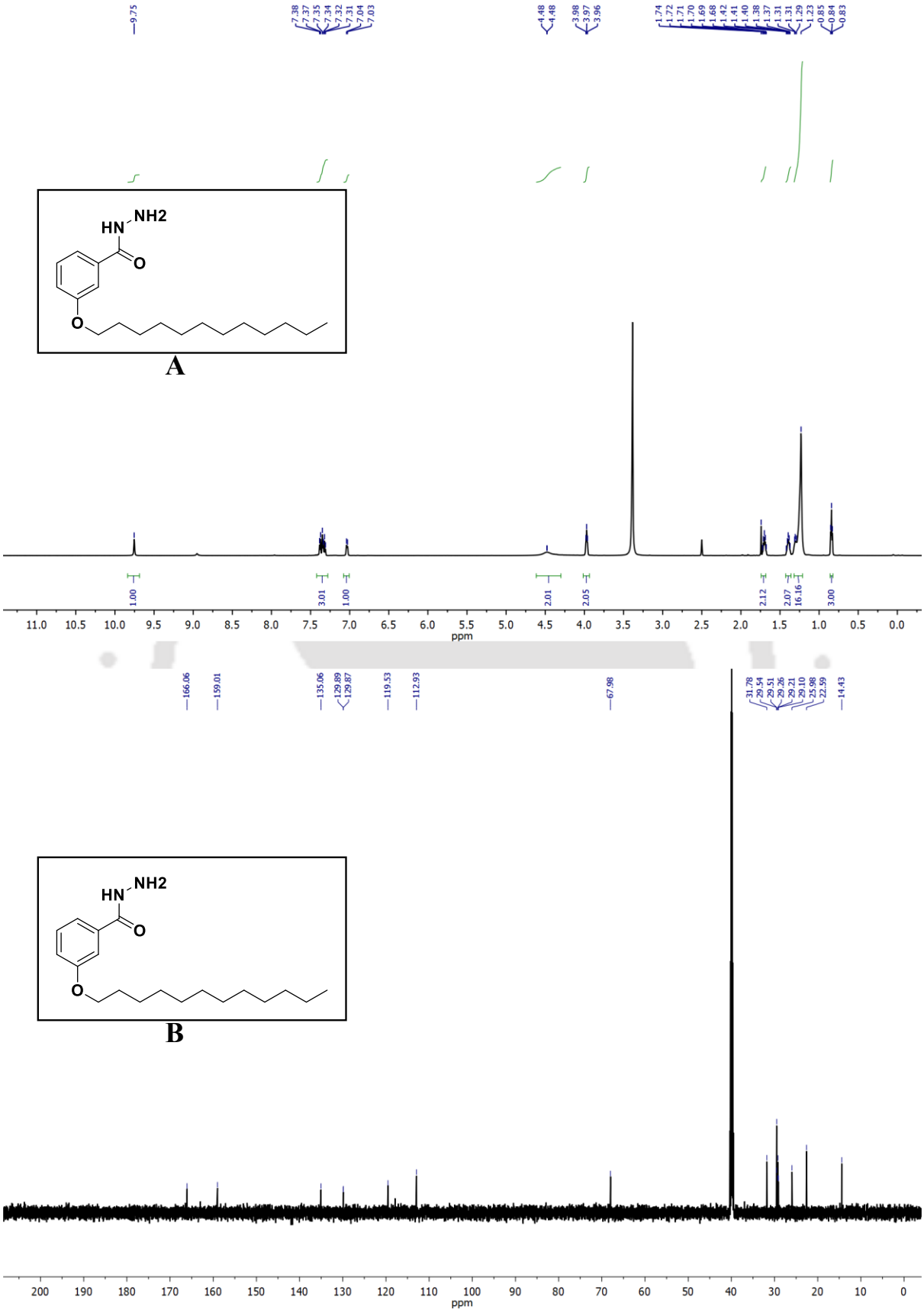


**Figure 4.32** (A) $^{1}$H NMR and (B) $^{13}$C NMR spectra of 3-(dodecyloxy)benzo hydrazide in the DMSO-$d_6$ solvent

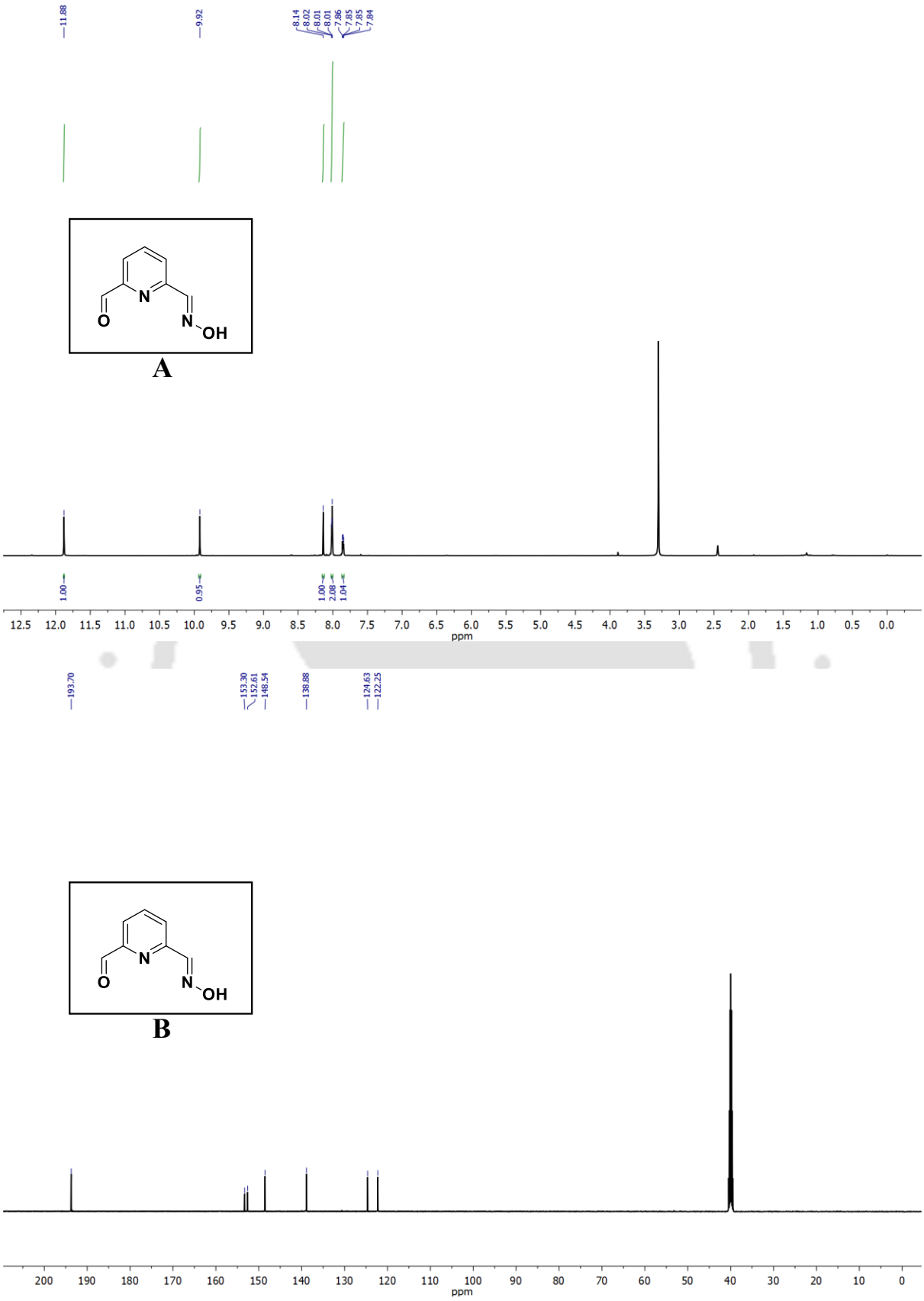


**Figure 4.33** (A) $^{1}$H NMR and (B) $^{13}$C NMR spectra of (E)-6-((hydroxyimino)methyl)picolinaldehyde in the DMSO-$d_6$ solvent.

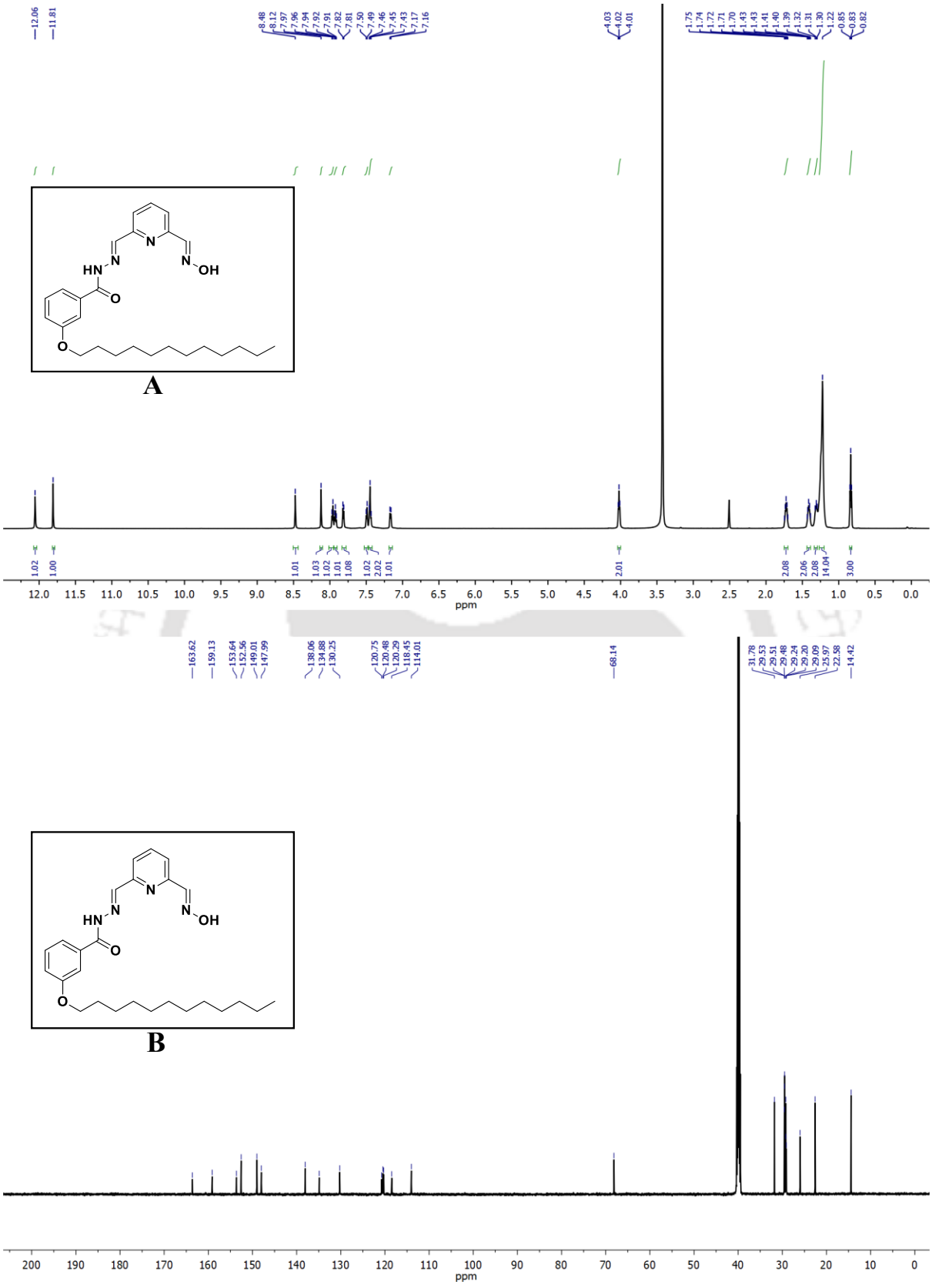


**Figure 4.34** (A) $^{1}$H NMR and (B) $^{13}$C NMR spectra of 3-(dodecyloxy)-N'-((E)-(6-((E)-(hydroxyimino)methyl)pyridin-2-yl)methylene)benzohydrazide in the DMSO-$d_6$ solvent.

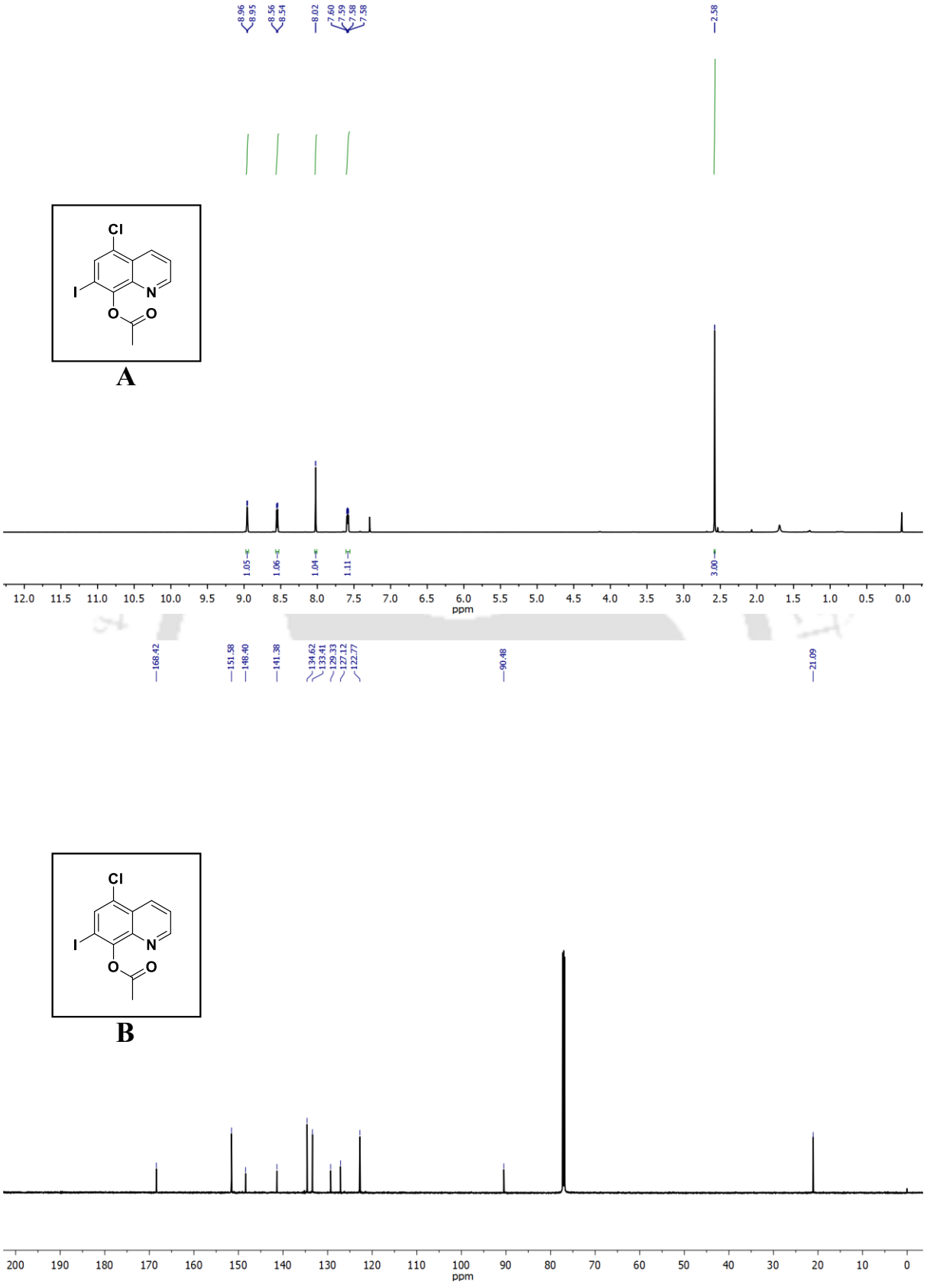


**Figure 4.35** (A) $^{1}$H NMR and (B) $^{13}$C NMR spectra of 5-chloro-7-iodoquinolin-8-yl acetate in the Chloroform-*d* solvent.

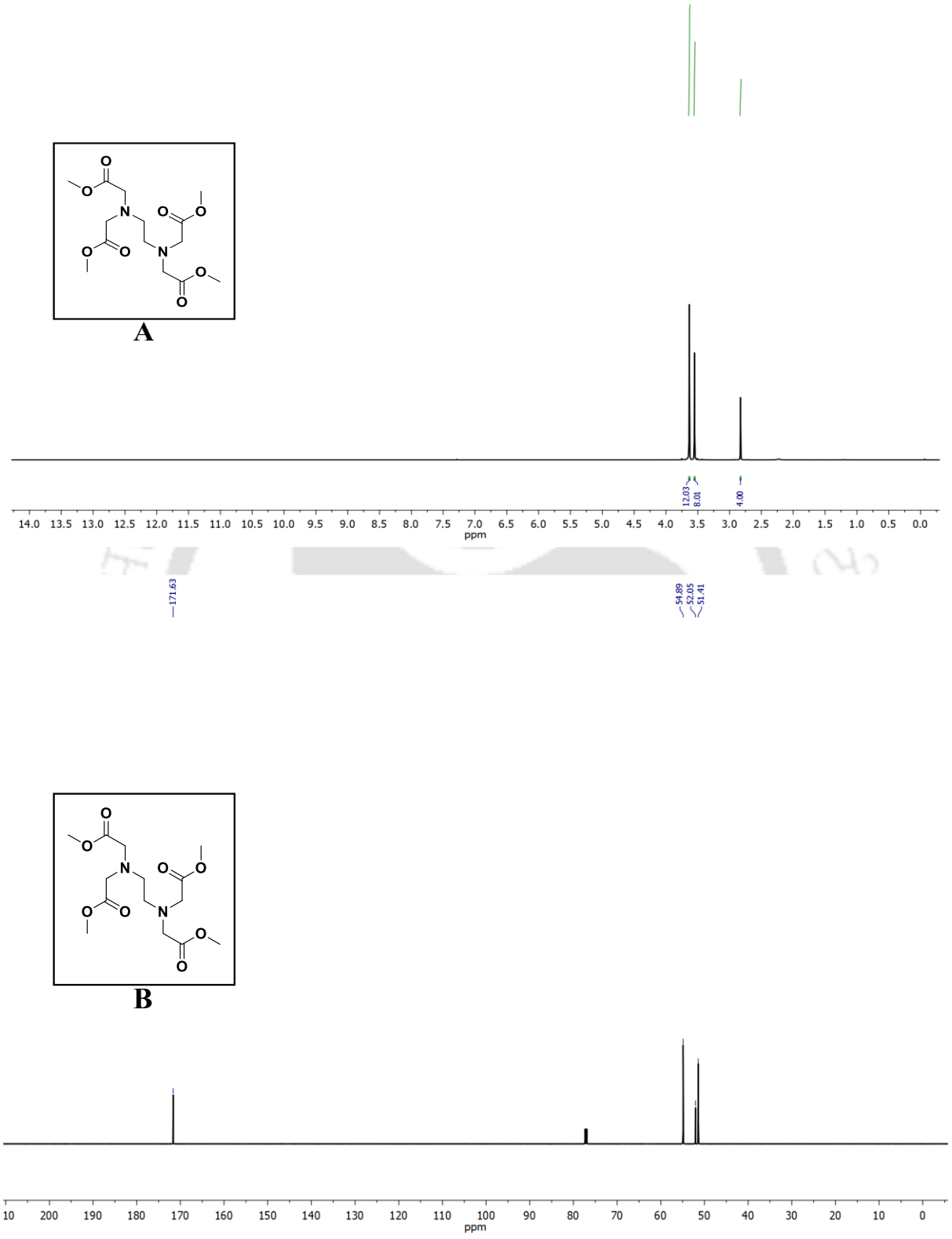


**Figure 4.36** (A) $^{1}$H NMR and (B) $^{13}$C NMR spectra of tetramethyl 2,2',2",2"'-(ethane-1,2-diylbis(azanetriyl))tetraacetate in the Chloroform-*d* solvent.

**HRMS analysis of the synthesised compounds:**

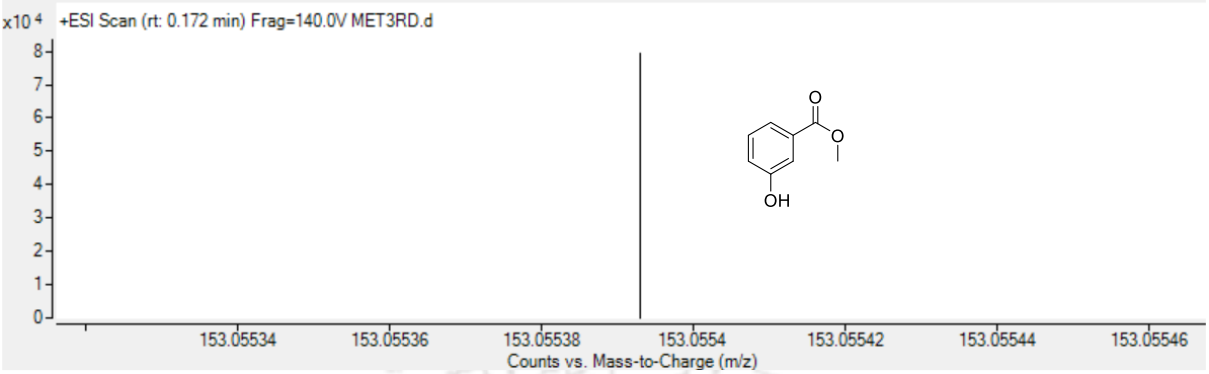


**Figure 4.37** HRMS spectra of methyl 3-hydroxybenzoate.

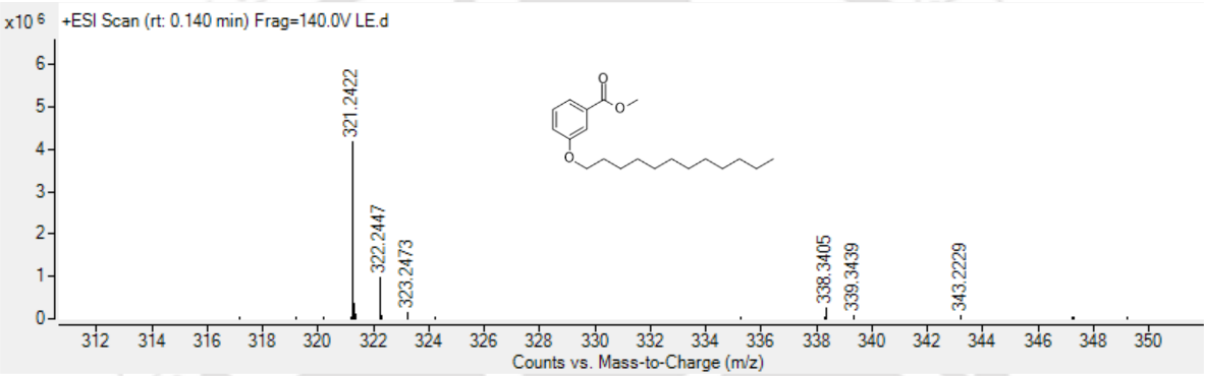


**Figure 4.38** HRMS spectra of methyl 3-(dodecyloxy)benzoate.

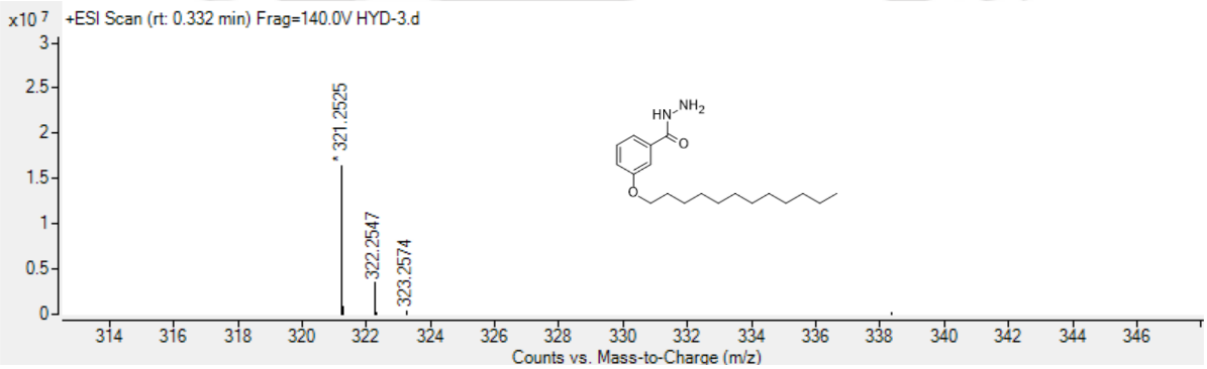


**Figure 4.39** HRMS spectra of 3-(dodecyloxy)benzo hydrazide.

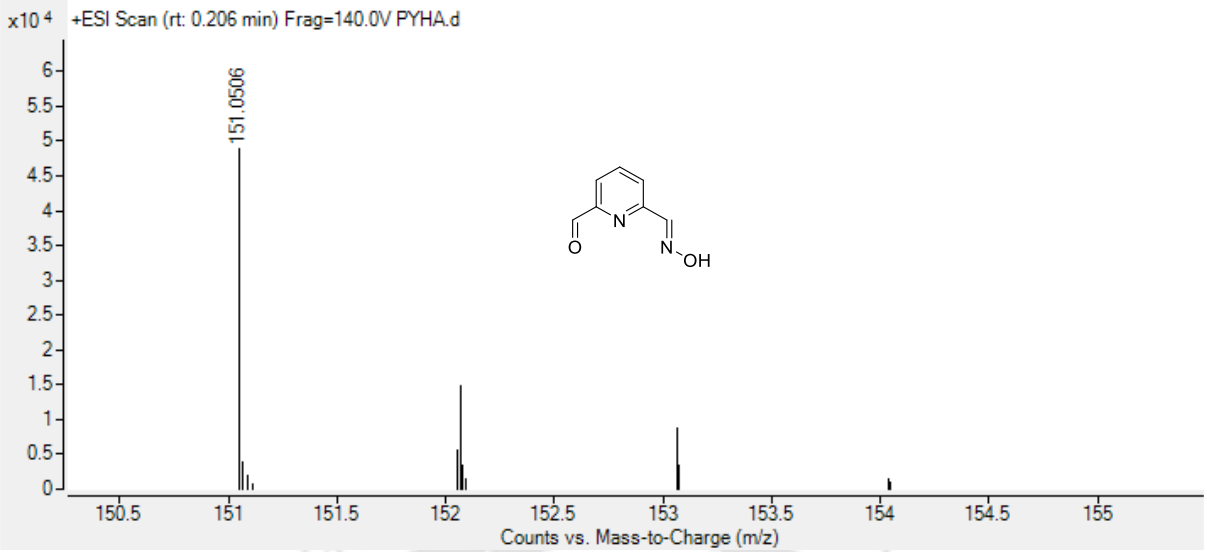


**Figure 4.40** HRMS spectra of (E)-6-((hydroxyimino)methyl)picolinaldehyde.

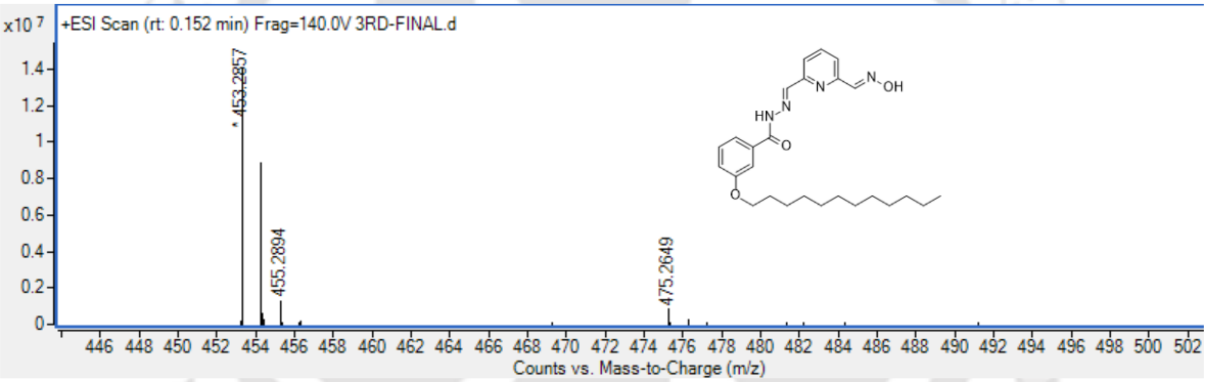


**Figure 4.41** HRMS spectra of 3-(dodecyloxy)-N'-((E)-(6-((E)-(hydroxyimino)methyl)pyridin-2-yl)methylene)benzohydrazide.

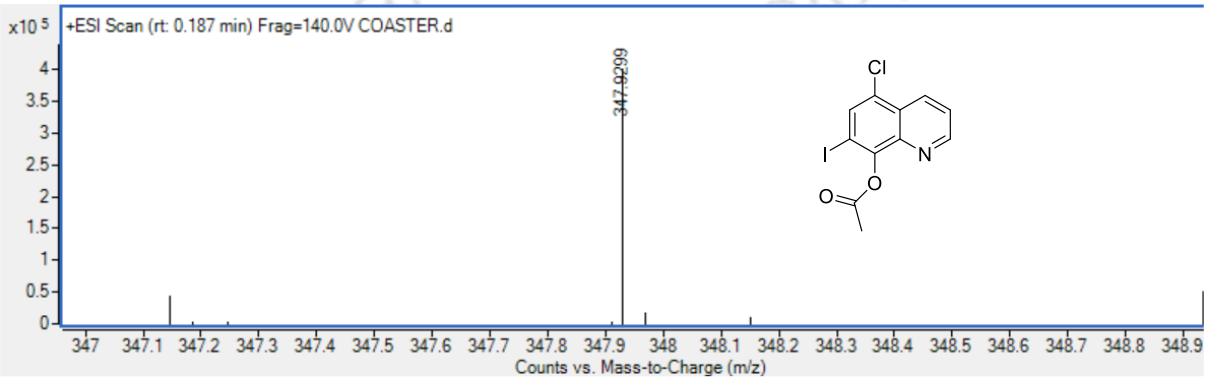


**Figure 4.42** HRMS spectra of 5-chloro-7-iodoquinolin-8-yl acetate.

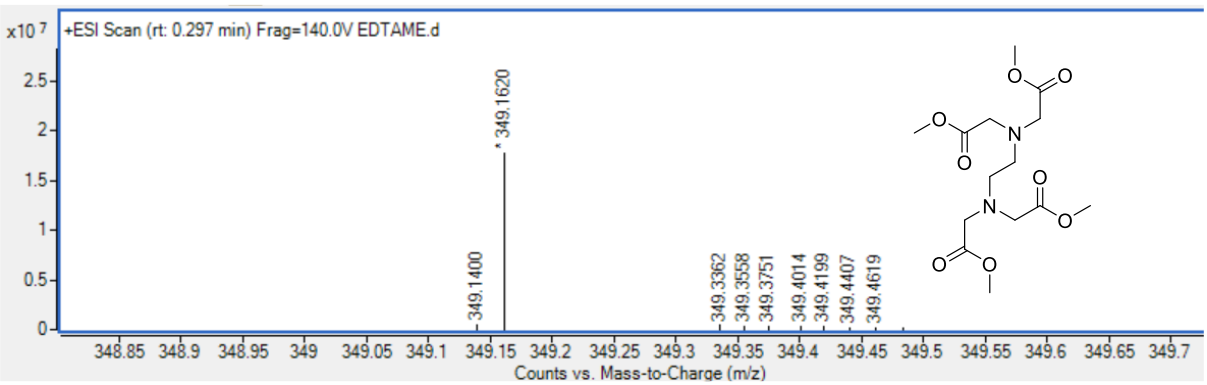


**Figure 4.43** HRMS spectra of tetramethyl 2,2',2",2"'-(ethane-1,2-diylbis(azanetriyl))tetraacetate.

## 4.5 Reference

1. Singh, A.; Parvin, P.; Saha, B.; Das, D., Non-equilibrium self-assembly for living matter-like properties. *Nat. Rev. Chem.* **2024,** *8* (10), 723-740.

2. Zambrano, P.; Chen, X.; Kriebisch, C. M.; Kriebisch, B. A.; Zozulia, O.; Boekhoven, J., Chemically driven division of protocells by membrane budding. *J. Am. Chem. Soc.* **2024,** *146* (49), 33359-33367.

3. Zozulia, O.; Kriebisch, C. M.; Kriebisch, B. A.; Soria-Carrera, H.; Ryadi, K. R.; Steck, J.; Boekhoven, J., Acyl Phosphates as Chemically Fueled Building Blocks for Self-Sustaining Protocells. *Angew. Chem. Int. Ed.* **2024,** *63* (30), e202406094.

4. Qi, C.; Ma, X.; Zeng, Q.; Huang, Z.; Zhang, S.; Deng, X.; Kong, T.; Liu, Z., Multicompartmental coacervate-based protocell by spontaneous droplet evaporation. *Nat. Commun.* **2024,** *15* (1), 1107.

5. Mann, S., The origins of life: old problems, new chemistries. *Angew. Chem. Int. Ed.* **2013,** *52* (1), 155-162.

6. Slootbeek, A. D.; van Haren, M. H.; Smokers, I. B.; Spruijt, E., Growth, replication and division enable evolution of coacervate protocells. *Chem. Commun.* **2022,** *58* (80), 11183-11200.

7. Penocchio, E.; Bachir, A.; Credi, A.; Astumian, R. D.; Ragazzon, G., Analysis of kinetic asymmetry in a multi-cycle reaction network establishes the principles for autonomous compartmentalised molecular ratchets. *Chem.* **2024,** *10* (12), 3644-3655.

8. Mukwaya, V.; Mann, S.; Dou, H., Chemical communication at the synthetic cell/living cell interface. *Commun. Chem.* **2021,** *4* (1), 161.

9. Bal, S.; Gupta, S.; Mahato, C.; Das, D., Catalytically Active Coacervates Sustained Out-of-Equilibrium. *Angew. Chem. Int. Ed.* **2025**, e202505296.

10. Buddingh', B. C.; van Hest, J. C., Artificial cells: synthetic compartments with life-like functionality and adaptivity. *Acc. Chem. Res.* **2017,** *50* (4), 769-777.

11. Koppayithodi, S.; Singh, N., Chemically Triggered Reactive Coacervates Show Life-Like Budding and Membrane Formation. *J. Am. Chem. Soc.* **2025,** *147* (6), 5293-5299.

12. Roy, S.; Laha, J.; Reja, A.; Das, D., Allosteric control of the catalytic properties of dipeptide-based supramolecular assemblies. *J. Am. Chem. Soc.* **2024,** *146* (32), 22522-22529.

13. Jalani, K.; Dhiman, S.; Jain, A.; George, S. J., Temporal switching of an amphiphilic self assembly by a chemical fuel-driven conformational response. *Chem. Sci.* **2017,** *8* (9), 6030-6036.

14. Solís Muñana, P.; Ragazzon, G.; Dupont, J.; Ren, C. Z. J.; Prins, L. J.; Chen, J. L. Y., Substrate-induced self-assembly of cooperative catalysts. *Angew. Chem.* **2018,** *57* (50), 16469-16474.

15. Chen, R.; Das, K.; Cardona, M. A.; Gabrielli, L.; Prins, L. J., Progressive local accumulation of self-assembled nanoreactors in a hydrogel matrix through repetitive injections of ATP. *J. Am. Chem. Soc.* **2022,** *144* (4), 2010-2018.

16. Pramanik, S.; Aprahamian, I., Hydrazone switch-based negative feedback loop. *J. Am. Chem. Soc.* **2016,** *138* (46), 15142-15145.

17. Yang, K.; Hua, B.; Qi, S.; Bai, B.; Yu, C.; Huang, F.; Yu, G., Suprasomes Based on Host-Guest Molecular Recognition: An Excellent Alternative to Liposomes in Cancer Theranostics. *Angew. Chem.* **2022,** *61* (52), e202213572.

18. Prusty, B. M.; Karn, R.; Patel, A.; Mazumder, P.; Kumar, S.; Manna, D., Stimuli-responsive assembly and disassembly of anionic suprasomes with tunable antibacterial activity. *Chem. Commun.* **2023,** *59* (71), 10624-10627.

19. Ding, W. Q.; Yu, H. J.; Lind, S. E., Zinc-binding compounds induce cancer cell death via distinct modes of action. *Cancer Lett.* **2008,** *271* (2), 251-259.

20. Nyborg, J. K.; Peersen, O. B., That zincing feeling: the effects of EDTA on the behaviour of zinc-binding transcriptional regulators. *Biochem. J.* **2004,** *381* (Pt 3), e3-4.

21. Langton, M. J.; Keymeulen, F.; Ciaccia, M.; Williams, N. H.; Hunter, C. A., Controlled membrane translocation provides a mechanism for signal transduction and amplification. *Nat. Chem.* **2017,** *9* (5), 426-430.

22. Prusty, B. M.; Srimayee, S.; Karn, R.; Haloi, N.; Singh, S. K.; Winterhalter, M.; Manna, D., Supramolecular Nanochannels: Suprasome-Mediated Delivery of Ionophore to Regulate Transmembrane $Zn^{2+}$ Ion Transport. *Chem. Eur. J.* **2025,** *31* (31).

23. Han, Y.; Jia, F.; Bai, S.; Xiao, Y.; Meng, X.; Jiang, L., Effect of operating conditions on size of catechin/β-cyclodextrin nanoparticles prepared by nanoprecipitation and characterization of their physicochemical properties. *LWT* **2022,** *153*, 112447.

24. Srimayee, S.; Prusty, B. M.; Kar, M. K.; Winterhalter, M.; Manna, D., Supramolecular Ion Channels to Engineer Zn(2+) Ion Transport Mediated Chemical-to-Optical Signal Transduction. *Angew. Chem.* **2025,** *64* (28), e202501634.

# Chapter 5

## Stimuli-Responsive Dynamic Supramolecular Assemblies: Temporally Gated Catalysis for Photonic Memory Formation and Inter-vesicle Communication

### 5.1 Background and Objective of Current Work

Cellular systems operate through intricate networks of events that require precise spatial and temporal control for optimal performance.[1] Physiological processes such as signal transduction, enzyme activation and neurotransmitter release depend on spatial localisation and meticulously timed activation windows.[2] One such example of a temporally gated response is spike-timing-dependent plasticity (STDP), which demonstrates how the timing between two stimuli influences long-term memory formation.[3] In STDP, an initial presynaptic signal (glutamate) can activate $Mg^{2+}$-blocked NMDA receptors (NMDAR) on the postsynaptic neuron, but this activation only occurs if a second input (postsynaptic depolarisation) arrives within this brief time window. This organised and coherent communication process instigates the long-term potentiation (LTP), which is crucial for creating long-lasting memories.[3, 4] This natural time-gated logic system inspired researchers to design stimuli-responsive time-gated supramolecular systems. In recent years, self-assemblies like micelles, liposomes, and suprasomes have been developed to demonstrate responsiveness to various external stimuli, including redox environment, pH changes, light, temperature, and metal ions. Photo-responsive systems, especially those utilising photochromic switches like azobenzene[5] or spiropyran,[6] offer excellent remote and reversible control while achieving high spatial and temporal precision.

Considerable advancement has been achieved in designing stimuli-responsive compartmentalised structures for applications such as drug delivery, catalysis, and signal processing.[7] These systems face several limitations: they are primarily regulated by a single stimulus or display irreversible responses. This confines their ability for precise temporal regulation by multiple stimuli. Recently, a few studies have attempted to combine stimuli for AND/OR logic gate operations; however, these approaches often lead to irreversible chemical changes (such as bond cleavage) or the permanent disassembly of the supramolecular structure.[8-10] The temporal correlation between the first and second stimuli is often overlooked. Meanwhile, natural systems precisely integrate multiple stimuli and/or inputs to selectively activate processes in specific locations and within short timeframes. Replicating this behaviour in synthetic systems remains a significant challenge. The preliminary step towards achieving such complexity is to develop single stimuli-triggered transient supramolecular assembly. However, efforts to imitate such preliminary complexity have already started. For example, transient assembly driven by ATP-fueled dissipative systems[11, 12] and chemical fuel-driven[13] supramolecular assembly and disassembly have resulted in materials within designated time

domains. Even fewer reports address the concept of transient supramolecular states acting as temporal gates for downstream responses.[14] However, almost no exploration has been done to develop a synthetic supramolecular construct where a temporal gating between multiple stimuli based on their relative input timing decides their downstream future outputs for optical, temporal information storage and vesicle-to-vesicle communication. Such reversible compartmentalised systems that can change in size, shape, or activity and be restored or disrupted in response to specific, time-gated inputs are not well documented.

Herein, we present a temporally gated suprasomal system that integrates reversible photoisomerisation with metal-ion coordination to facilitate time-confined structural and functional transformations (Figure 5.1). The system was developed using a 1:1 mixture of an amphiphilic spiropyran (ASP) derivative and Tween 20, which led to the formation of spherical nanoassemblies in an aqueous medium. In the presence of β-cyclodextrin (β-CD), these nanoassemblies reorganised into larger suprasome-like architectures through the host–guest interactions. Upon photo-irradiation, the conversion from spiropyran (closed form) to merocyanine (open form) results in the shrinkage in the size of the suprasomal assemblies. This process results in a metastable state that reverts to its original form in approximately 45 minutes. During this short-lived phase, the coordination of $Zn^{2+}$ with the merocyanine form of the amphiphile results in a non-equilibrium morphological change into a planar, sheet-like assembly. Additional studies showed that the generation of this metastable state requires the simultaneous influence of both stimuli. This temporally confined dual-input logic gate (light and $Zn^{2+}$) facilitates functional outputs such as the release of encapsulated nonfluorescent substrate, acyl-8-hydroxy-1,3,6-pyrene-trisulfonic acid (AHPTS) and the precatalyst, (1E,1E)-6-((E)-(hydroxyimino)methyl) picolinaldehyde oxime (HMPO) from the suprasomes. The coordination of $Zn^{2+}$ with HPMO catalyses the hydrolysis of AHPTS to fluorescent HPTS. Notably, this functional output was observed only when both stimuli coincided within the transient activation window. This system also demonstrates a time-gated inter-vesicular signalling process, where the $Zn^{2+}$-induced release of clioquinol ester (CQE) from the sender suprasome and HMPO-$Zn^{2+}$-mediated hydrolysis of CQE to CQ facilitate the transport of $Zn^{2+}$ into a receiver liposome. Furthermore, the combination of HMPO and EDTA ester (EDTAE) ascertains the temporary presence of free $Zn^{2+}$, allowing the system to capture both optical and temporal information. Collectively, this supramolecular system provides a minimalistic functional platform to enhance our understanding of intercellular communication and memory formation through a temporally controlled stimuli-responsive process.

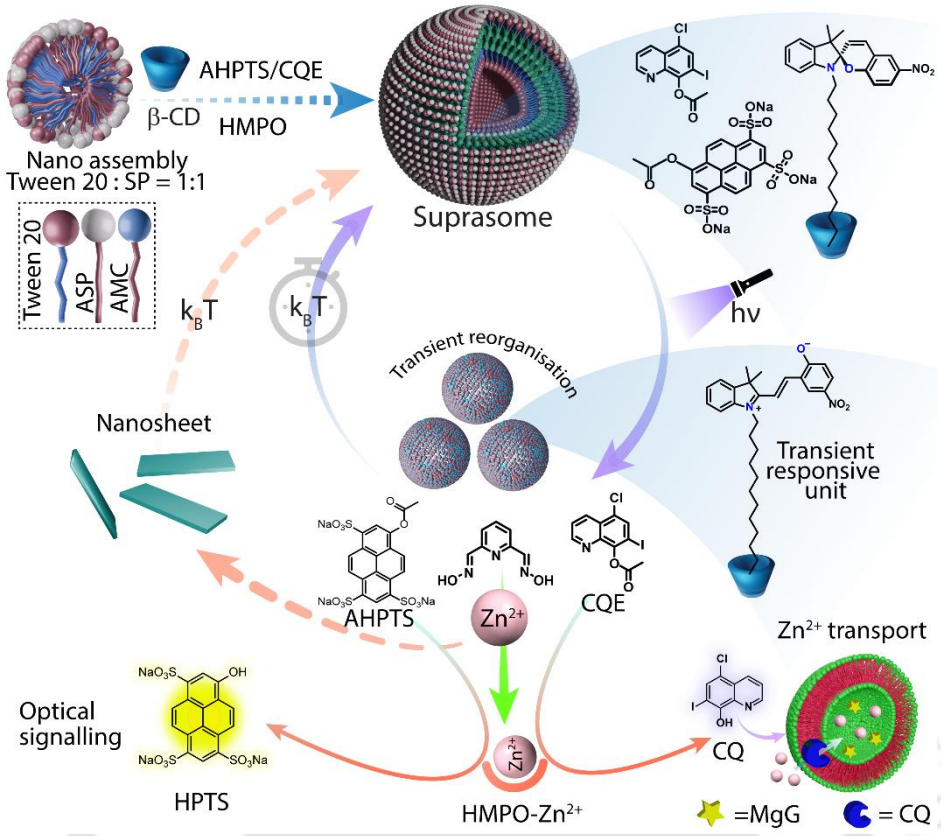


**Figure 5.1** Schematic representation of dual (light and $Zn^{2+}$) stimuli-responsive transition in supramolecular assemblies with temporally gated catalytic activities.

## 5.2 Results and Discussion

### 5.2.1 Synthetic Procedure of Photo-Responsive Amphiphile

To develop stimulus-responsive supramolecular self-assembled structures, we designed and synthesised an amphiphilic molecule, 1'-dodecyl-3',3'-dimethyl-6-nitrospiro[chromene-2,2'-indoline]. This photo-responsive amphiphile features a hydrophobic dodecyl moiety that could facilitate its incorporation into the membrane and a spiropyran (SP) scaffold that can undergo reversible photoisomerisation to the merocyanine (MC) form when exposed to light.

### 5.2.2 Self-Assembly of Photo-Responsive Amphiphile

The amphiphilic derivative of SP (ASP) was co-assembled with Tween 20 in a 1:1 molar ratio in aqueous media. The Tween 20 was used to enhance the aqueous solubility of ASP. The hydrophobic dodecyl moiety of ASP interacts favorably with the alkyl chains of Tween 20, resulting in the formation of a nanoassembly in aqueous medium. Dynamic Light Scattering (DLS) measurements revealed that the hydrodynamic diameters ($D_H$) of these assemblies are approximately 185 nm (Figure 5.2A). Additional morphological analyses of spherical

nanoassembly were performed using field emission scanning electron microscopy (FESEM) (Figure 5.2B). The addition of β-CD (0-14 mM) with increasing concentration resulted in a transition from a clear solution to a cloudy one, indicating the formation of suprasomes (Figure 5.6). The observed suprasomes showed an average $D_H$ value of 1000-1500 nm and showed spherical morphologies in FESEM images (Figure 5.2C and 5.7). The control experiments showed that Tween 20 (1 mM) with β-CD formed suprasomes, while amphiphilic AMC derivative (AMC; 1 mM) with β-CD did not, confirming the essential role of Tween 20 in suprasome assembly (Figure 5.8). To further investigate the interaction between host and guest molecules and their roles in suprasome assembly, we performed isothermal titration calorimetry (ITC) measurements. The thermodynamic parameters obtained from the ITC measurements (ΔS = +ve, ΔH = -ve) confirmed a favorable interaction between β-CD and Tween 20 and the mixed solution (1:1) of ASP and Tween 20 (Figure 5.2D, 5.9). This entropy-

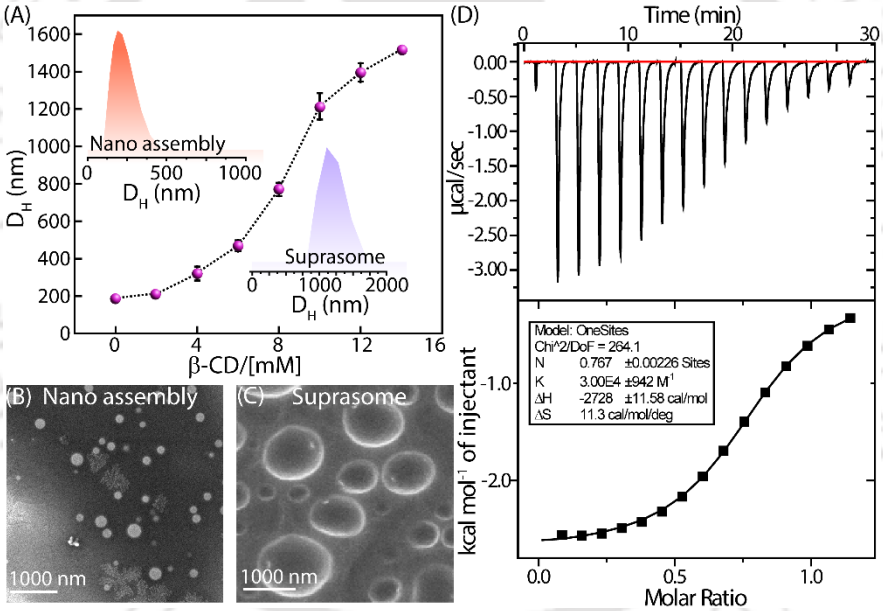


**Figure 5.2** (A) Variation in DH values during the β-CD-mediated conversion of nanoassemblies into suprasomes. Inset: DLS distribution curve of nanoassembly and suprasome. Representative FESEM images of (B) nanoassembly and (C) suprasomes. (D) ITC profile of Tween 20:ASP (1:1) with β-CD.

driven process is primarily governed by the hydrophobic interaction of the alkyl chain with the β-CD, along with the release of structured water molecules from the hydrophobic long tail surface upon complex formation.[15] Therefore, the host-guest interaction of β-CD with a mixture (1:1) of ASP and Tween 20 transforms smaller assemblies into suprasomes.

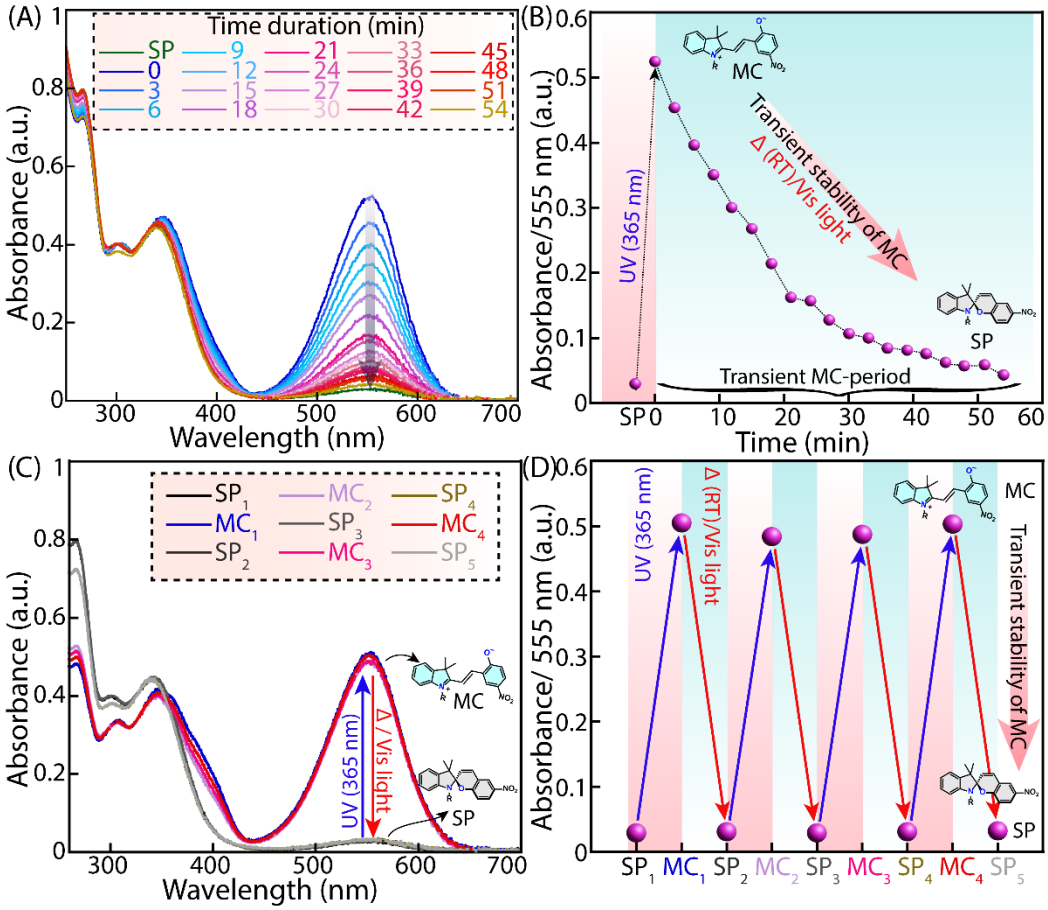


**Figure 5.3** (A) UV-Vis absorbance spectra demonstrating the conversion of AMC to ASP under dark and ambient conditions in aqueous medium. (B) Time-dependent absorbance decay during conversion of AMC to ASP. (C) Absorbance changes during ASP to AMC photoisomerisation under UV light and reversal under dark and ambient conditions in aqueous medium. (D) Reversible ASP-AMC conversion for multiple cycles in aqueous medium.

### 5.2.3 Photoinduced Isomerisation and Morphology Changes

Initially, we investigated the photo-responsive conversion of only ASP to AMC in aqueous medium. Upon photo irradiation ($\lambda_{ex}$ = 365 nm; for 2 minutes), we observed a significant absorption band around 555 nm, which indicates the Isomerisation of ASP to its conjugated planar amphiphilic AMC derivative (Figure 5.10). However, under dark and ambient conditions, the absorbance peak at 555 nm gradually diminished over time, which indicates the spontaneous conversion of AMC to ASP isomer (Figure 5.3A and 5.3B). This photoinduced reversibility of SP-MC forms was also investigated for multiple cycles (Figure 5.3C and 5.3D). Meanwhile, similar photoisomerisation and thermal Isomerisation of AMC to ASP and vice versa were observed with Tween 20 in suprasomal assembly (Figure 5.11 and 5.12).

A substantial morphological alteration in the suprasomal assemblies was observed upon photoirradiation, resulting in a reduction in $D_H$ values from ~1200 nm to ~600 nm. The photo-irradiated transformation of ASP to AMC enhances planarity, polarity and dipole moment.[16-18] This observation suggests a stronger interaction of the MC moiety with the polar moieties of Tween 20 and tighter molecular packing, which could convert suprasomes into smaller and more compact nanostructures.[18] However, over 1 h, under dark and ambient conditions, the suprasomes gradually regained their original size of ~1200 nm. This reversible spherical size alternation (contraction–expansion) was observed for multiple cycles under pulsed light irradiation (Figure 5.4A). Notably, the contraction in spherical shape was observed for ~45 minutes during the existence of the MC state of the amphiphile. This creates a kinetic window in which the assemblies displayed a metastable state of compact morphology. These temporal morphological changes were further validated with FESEM images, revealing smaller spherical assemblies after photoirradiation, while larger spherical assemblies were under dark and ambient conditions (Figure 5.4B). This reversible morphological alternation was further investigated by fluorescence measurements using polarity-sensitive Nile red (NR) dye. Photo irradiation led to the fluorescence quenching of NR, indicating the release of hydrophobic NR dye to the aqueous media due to structural transformation of the suprasomal assemblies (Figure 5.13A). The fluorescence intensity of NR dye increased over time (under dark and ambient conditions), which could be due to the structural reorganisation of the ASP molecule and formation of larger suprasomal assemblies (Figure 5.13B). Interestingly, this time-dependent assembly of smaller suprasomal assemblies create a sensitive state due to the formation of the AMC isomer. In this state, other stimuli, such as metal ions, can facilitate further structural transformation, which has potential applications in cargo delivery and catalysis. Such time-dependent transformation of compartmentalised structures resembles biological transient states, providing a foundation for more complex and temporally gated responses in subsequent biochemical reactions.[2, 4]

### 5.2.4 Time-Gated Orthogonal Stimuli-Induced Transformation

Simultaneous photoirradiation and addition of $Zn^{2+}$ significantly increase $D_H$ values from ~600 nm to ~3500 nm, indicating a collapse of the spherical suprasomal assemblies and reorganisation into different supramolecular assemblies. The FESEM images of the samples after photoirradiation and $Zn^{2+}$ treatment demonstrated the transformation of smaller suprasomes into rectangular sheet-like aggregates (Figure 5.5A). However, this change in self-assembly pattern was not observed without photoirradiation, even in the presence of $Zn^{2+}$. The

DLS measurement confirmed the requirement of both stimuli for this transformation (Figure 5.14). Responsiveness to other metal ions along with light has also been investigated using DLS measurements (Figure 5.14). The FESEM images of only ASP, AMC, and AMC along with $Zn^{2+}$ and a few other control studies suggest that the rectangular self-assembly is most probably due to the interaction of AMC with $Zn^{2+}$ (Figure 5.15). This highlights the crucial role of the open-ring MC isomer in facilitating this transformation in supramolecular structures. It is important to mention that $Zn^{2+}$ was selected in this study for its biologically relevant and redox-inactive properties. $Zn^{2+}$ complexes exhibit esterase-like enzymatic activity in various pre-catalysts without undergoing unwanted redox transformations.[19] DLS measurements also showed that $Zn^{2+}$ significantly alters the suprasomal structures compared to other tested cations (Figure 5.14). The absorbance study revealed a red shift in the characteristic absorbance peak of the MC form, changing from 555 nm to 610 nm, with the addition of $Zn^{2+}$ ions. This shift in absorbance peak indicates a direct interaction between $Zn^{2+}$ and the phenolate oxygen of the MC form, which facilitates structural alteration and reorganisation (Figure 5.16A).

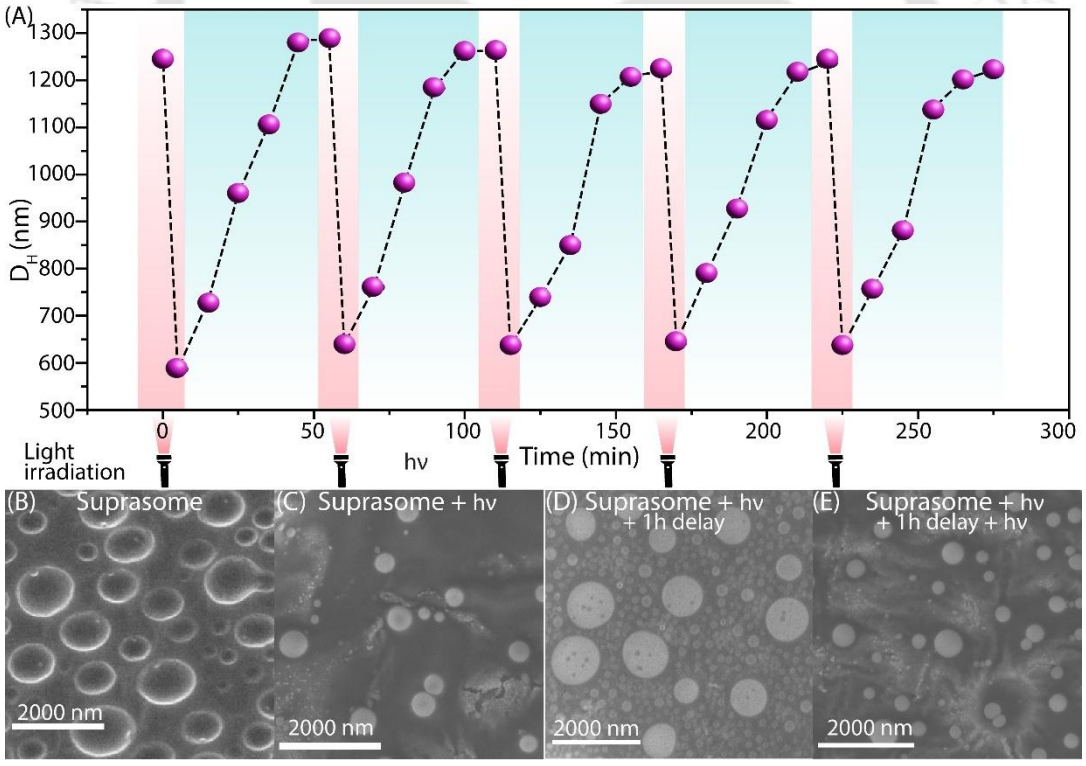


**Figure 5.4** (A) DLS measurements showing a rapid decrease in DH upon light exposure (365 nm, 5 min), followed by a gradual increase over 1 h post-irradiation at rt. DLS data were recorded every 10 minutes at rt. (B) Representative FESEM images showing size reduction after light treatment and gradual recovery after 1 h.

Absorbance studies revealed that the AMC $Zn^{2+}$ progressively dissociates as AMC thermally reverts to the ASP isomer, pointing toward morphological reversal to the prior spherical suprasomal assemblies (Figure 5.16B). The FESEM analysis further confirmed the reappearance of spherical suprasomal suprasomes upon prolonged thermal relaxation of the planar sheet-like assembly (Figure 5.17).

These observations indicate that two orthogonal stimuli (light and $Zn^{2+}$) must coincide within a specific temporal window to induce suprasome disassembly, leading to morphological transformation of the compartmentalised structures. The temporally confined stimuli-responsive nature of these suprasomal assemblies could be further exploited to develop biomimetic strategies. One such application could be the construction of a photonic memory module for information storage and retrieval, analogous to memory formation in neurons. Secondly, inter-vesicular communication via a temporally gated signalling process analogous to inter-neuron communication at the synaptic cleft.

To develop a photonic memory module via temporally controlled esterase activity, HMPO (precatalyst) and AHPTS (nonfluorescent substrate) were co-encapsulated within suprasomes. The HMPO is known to exhibit esterase-like activity upon complexation with $Zn^{2+}$.[20] The catalytic activity of the HMPO-$Zn^{2+}$ complex was confirmed through fluorescence and HPLC studies using AHPTS and CQE as the desired substrates (Figure 5.18-5.20). Interestingly, we observed that fluorescent HPTS was generated as a photonic output only when both orthogonal stimuli (light and $Zn^{2+}$) were applied within a specific temporal window. While other control experiments did not produce a similar effect, as shown in the truth table (Table 5.1, Figure 5.5B and 5.21). This time-dependent response resulted from the HMPO-$Zn^{2+}$ complex facilitating the AHPTS ester hydrolysis, which occurs exclusively after the disassembly of the suprasome and the subsequent release of its components, HMPO and AHPTS.

Based on these findings, we developed a time-dependent inter-vesicle communication system utilising chemical activation. In this system, the HMPO and an ester derivative of clioquinol (CQE) were encapsulated within suprasomes that serve as signal senders. The pentapotassium salt of magnesium green (MgG)-encapsulated vesicles composed of EYPC and cholesterol were used as signal receivers. CQ is a known $Zn^{2+}$ transporter,[21] and CQE serves as its inactive pro-ionophore (Figure 5.22). We observed that the addition of suprasome-containing solution to a liposome-containing solution led to the transport of $Zn^{2+}$ only under simultaneous exposure to light and $Zn^{2+}$ within a defined temporal window (Figure 5.23, 5.24 and 5.25). We

hypothesise that the $Zn^{2+}$-mediated morphological change in suprasomal assembly led to the release of HMPO and CQE from the suprasomes to the extravesicular environment. This release facilitated the complexation of $Zn^{2+}$ with HMPO, which catalytically converted CQE to CQ, which facilitates the efficient transport of $Zn^{2+}$ (~80%) to the MgG-encapsulated liposomes (Figure 5.5B and 5.24). In contrast, control experiments that were devoid of either stimulus or the required temporal confinement failed to induce significant $Zn^{2+}$ influx into the receiver vesicle. We hypothesise that the gated optical responses, whether caused by the hydrolysis of AHPTS to fluorescent HPTS or by the conversion of CQE to CQ, followed by the transport-mediated enhancement of MgG fluorescence within liposomes, could serve as a functional analogy of memory formation. In our synthetic model, the simultaneous application of light and $Zn^{2+}$ to the suprasome (signal sender) triggers HMPO-$Zn^{2+}$ complexation and subsequent CQE hydrolysis, generating the active ionophore CQ. This initiates $Zn^{2+}$ transport into an effector liposome, where fluorescence enhancement from the encapsulated MgG dye serves as a photonic output (Figure 5.25). Hence, this synthetic model offers a minimalistic framework that emulates selected features of the neural signalling process, such as coincident signalling and temporally regulated inter-vesicular communication, without replicating the full biological intricacy of neuronal networks. The results from these gated optical response studies indicate that this modular system functions as a temporal three-input AND logic gate, and its input-output relationship can be visualised as a logic cube where each axis represents an orthogonal control input, and temporal control is key to the functionality of the system. (Figure 5.5B, inset).

The temporally confined fluorescent signalling due to the generation of HPTS can be utilised as a functional memory unit for uniquely storing both optical and temporal information that can be retrieved when needed. However, both stimuli should be transient to capture optical and temporal information within a specific time frame. While the photoinduced formation of AMC isomer is inherently short-lived, any pre-existing $Zn^{2+}$ in solution would negate temporal control, as light alone would suffice to induce suprasome disassembly and downstream signalling. To maintain the limited availability of $Zn^{2+}$ and ensure temporal gating, the availability of $Zn^{2+}$ should also be transient. In this regard, AHPTS-encapsulated suprasomes with external HMPO and EDTAE were used for the assay (Figure 5.26). Upon $Zn^{2+}$ addition, the HMPO–$Zn^{2+}$ complex catalyses the EDTAE hydrolysis, resulting in the release of EDTA. The released EDTA rapidly chelates $Zn^{2+}$, quenching both $Zn^{2+}$ availability and HMPO-mediated catalysis. This design renders both $Zn^{2+}$ activity and esterase function transient. The

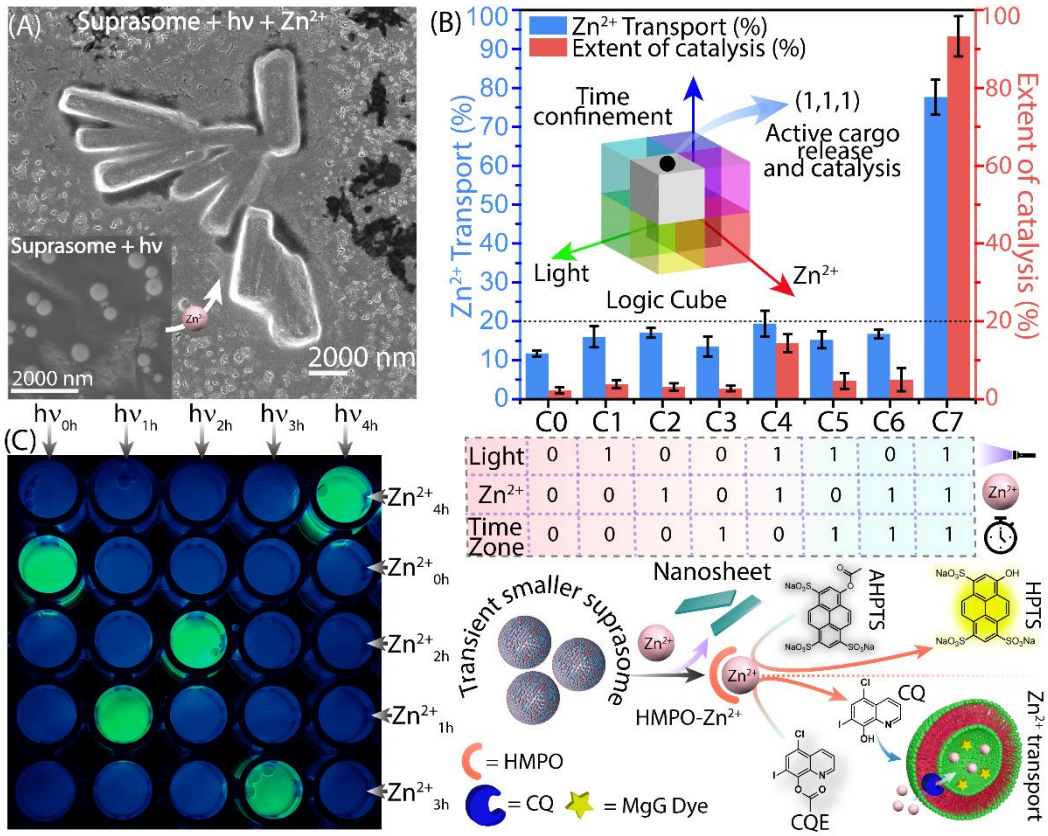


**Figure 5.5** (A) Representative FESEM images of the morphological transition of suprasomes upon simultaneous light irradiation and $Zn^{2+}$ addition during the transient metastable state. Inset: Photo-irradiated suprasome (smaller size). (B) Extent of hydrolysis of AHPTS to HPTS (right Y-axis) and $Zn^{2+}$ transport activity to the MgG encapsulated vesicles (left Y-axis) against different stimulus combinations. Inset: The logic cube represents a time-gated logic system, where $Zn^{2+}$ and light treatment under a temporal window are essential for downstream esterase activity regulating HPTS, CQ release and $Zn^{2+}$ transport activity in liposomes. The truth table shows different conditions (C0-C7) applied to the suprasomal solution. Schematic representation of a time-confined light and $Zn^{2+}$-triggered cascade involving HMPO release and subsequent ester hydrolysis leading to HPTS generation and $Zn^{2+}$ transport in liposomes. (C) Photonic memory (output) generation was observed only when the transient AMC isomer (light trigger) and the transient $Zn^{2+}$ triggered esterase activation coincide on the time axis. HMPO and EDTAE are used for the transience of the $Zn^{2+}$ trigger.

EDTA release from EDTAE and subsequent removal of free $Zn^{2+}$ from solution in the presence of HMPO-$Zn^{2+}$ was confirmed through a $Zn^{2+}$ sensing arsenazo-III dye-based experiment (Figure 5.27 and 5.28). A blue shift was observed only when both EDTAE and HMPO were

added to the arsenazo III + $Zn^{2+}$ system in the solution, indicating the controlled availability of $Zn^{2+}$ within the system.

To demonstrate the potential of this modular system in retaining both optical and temporal information, a 5×5 section of a 96-well plate was used. Each well contained AHPTS encapsulated suprasomes, with HMPO and EDTAE present in the extravesicular solution. UV light was irradiated (for 2 min) to each column sequentially at 1h interval, while $Zn^{2+}$ was blindly added to different rows at randomised hourly time points. After 5 h, fluorescence was observed only in the wells where light exposure and $Zn^{2+}$ addition coincided temporally. This HPTS fluorescence signal was generated by changes in suprasomal arrangements, release of AHPTS, and HMPO–$Zn^{2+}$-mediated hydrolysis of AHPTS to HPTS (Figure 5.5C and 5.27). Therefore, the fluorescence signal from these specific wells represents optical output exclusively at the temporal intersection of both stimuli, enabling temporal information capture. In this system, $Zn^{2+}$ and the light-induced MC state are transient, requiring precise temporal overlap for signal generation, unlike previous systems where $Zn^{2+}$ was persistently available (Figure 5.27).[22] Consequently, the fluorescence output represents both binary logic and the timing of input events. Hence, these observations from our model system provide a functional analogy to biological memory formation, where photonic output is generated only when stimuli coincide within a brief time window.

### 5.3 Summary

This study demonstrates the development of a dynamic suprasomal system where photo-induced metastable state produces a temporally confined window during which $Zn^{2+}$ can trigger structural transitions and functional outputs. By combining Tween 20 and photo-switchable ASP amphiphiles with β-CD, we created suprasomal assemblies that can undergo reversible photoinduced breathing, resulting in a time-dependent metastable state. During this specifically defined time frame, $Zn^{2+}$ coordination to the AMC triggers a non-equilibrium transformation into a planar sheet-like assembly, a transition that is not achievable without photo-stimulation or beyond the transient activation phase. This dual-input (light and $Zn^{2+}$) logic gate, which is temporally confined, enabled the conditional release of both the encapsulated precatalyst (HMPO) and the substrate (AHPTS) from suprasomes. This process initiated HMPO-$Zn^{2+}$ mediated AHPTS hydrolysis, resulting in a self-recording optical output (HPTS). Additionally, this time-gated esterase activity was further utilised for temporally restricted inter-vesicular

communication, employing CQE-encapsulated suprasomes as the sender vesicle and MgG dye encapsulated liposomes as the receiver vesicle. A transport of $Zn^{2+}$ in the receiver liposome was observed only when both $Zn^{2+}$ and light treatment occurred simultaneously. Additionally, by utilising AHPTS-encapsulated suprasomes along with EDTAE and HMPO in the external solution, we demonstrated that the system can encode both optical and temporal information of input events. This capability arises from the temporary availability of both free $Zn^{2+}$ ions and the AMC isomer, which requires precise timing to overlap for the optical output, thereby revealing the photonic memory of the inputs. The synthetic system, while not replicating the full complexity of neuronal function, emulates key features of synaptic processing during LTP, such as coincident-stimuli-responsive output generation and inter-compartmental communication, and offers a minimalistic analogue of time-gated synaptic potentiation. This unique system presents a conceptually versatile strategy for constructing artificial systems with precise spatiotemporal control and optical and temporal memory-output behaviour, providing exciting opportunities for the development of synthetic biology and artificial cell engineering.

## 5.4 Experimental Section

### 5.4.1 General Information

The reagents and solvents used in the experiment were purchased from commercial sources such as Sigma-Aldrich, TCI and Thermo Fisher Scientific. These were used without undergoing additional purification unless explicitly indicated. The monitoring of reactions was conducted through thin-layer chromatography (TLC) on silica gel 60 F254 (0.25 mm). Silica gel with a mesh size of 120-200 was utilised for the execution of column chromatography. The Bruker spectrometer was used to record the 1H NMR and 13C NMR at 600 MHz and 151 MHz, respectively. The chemical shifts were determined using internal solvents DMSO-$d_6$ and $CDCl_3$ and were expressed in parts per million (ppm). The values of the coupling constant (J) were expressed in hertz, and the corresponding abbreviations were provided as follows: s (representing singlet), d (representing doublet), t (representing triplet), q (representing quartet), m (representing multiple), and br (representing broadened). High-resolution mass spectra (HRMS) were acquired using an Agilent Q-TOF mass spectrometer equipped with a Z-spray source. The obtained mass data were analysed using the software integrated into the instrument. The chemical compounds utilised in the study, namely β-cyclodextrin (β-CD), Tween 20, Clioquinol (CQ), Ethylenediaminetetraacetic acid (EDTA), Nile Red (NR), Sodium 8-

acetoxypyrene-1,3,6-trisulfonate (AHPTS), were procured from commercial sources (Sigma Aldrich, TCI India and BLD Pharma India).

### 5.4.2 Synthesis and Characterization:

#### 5.4.2.1 Synthesis of 1'-dodecyl-3',3'-dimethyl-6-nitrospiro[chromene-2,2'-indoline] (ASP)

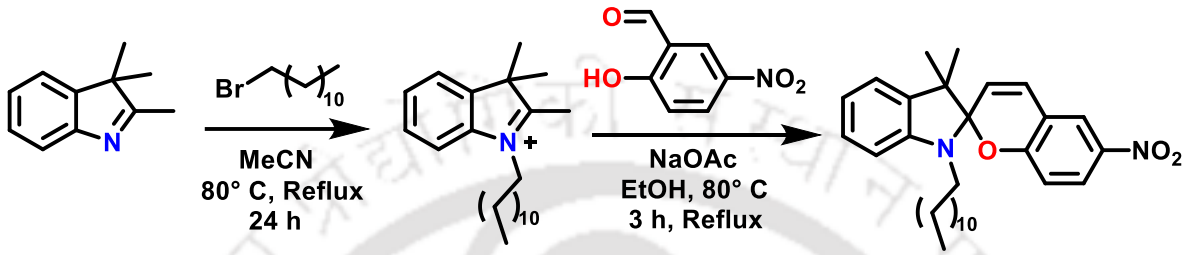


**Scheme 5.1.** Synthetic routes to 1'-dodecyl-3',3'-dimethyl-6-nitrospiro[chromene-2,2'-indoline].

The synthesis of the target compound **ASP** commenced with the alkylation of 2,3,3-trimethylindoline (1 mmol) by refluxing it with 1-bromododecane (2 mmol) in acetonitrile. After completion, the solvent was evaporated under reduced pressure, and the resulting residue was washed with diethyl ether to afford the crude product, 1-dodecyl-2,3,3-trimethyl-3H-indol-1-ium. This crude intermediate (1 mmol) was directly used in the subsequent step without further purification. It was stirred with sodium acetate (1 mmol) and 2-hydroxy-5-nitrobenzaldehyde (1 mmol) in ethanol under reflux at 80 °C for 3 hours. The progress of the reaction was monitored by thin-layer chromatography (TLC). Upon completion, the final product was purified by column chromatography using a 20:80 ethyl acetate/hexane solvent system to yield the desired 1'-dodecyl-3',3'-dimethyl-6-nitrospiro[chromene-2,2'-indoline] (**SP1**) in 59% yield. The product was characterized by high-resolution mass spectrometry (HRMS) and nuclear magnetic resonance (NMR) spectroscopy. **$^1$H NMR (600 MHz, Chloroform-*d*)**: $\delta_{ppm}$ 8.04 (dd, $J$ = 12.2, 3.2 Hz, 2H), 7.21 (t, $J$ = 7.7 Hz, 1H), 7.11 (d, $J$ = 7.2 Hz, 1H), 6.96 – 6.83 (m, 2H), 6.77 (d, $J$ = 8.8 Hz, 1H), 6.60 (d, $J$ = 7.8 Hz, 1H), 5.89 (d, $J$ = 10.4 Hz, 1H), 3.24 – 3.10 (m, 2H), 1.71 – 1.52 (m, 6H), 1.31 (s, 2H), 1.29 – 1.27 (m, 10H), 1.26 (s, 6H), 1.21 (s, 2H), 0.91 (t, 3H). **$^{13}$C NMR (151 MHz, $CDCl_3$)**: $\delta_{ppm}$ 159.75, 147.19, 140.86, 135.93, 128.04, 127.74, 125.87, 122.70, 122.11, 121.66, 119.23, 118.51, 115.55, 106.79, 106.67, 52.65, 43.77, 31.93, 29.72, 29.66, 29.63, 29.62, 29.60, 29.42, 29.35, 28.96,

27.33, 26.04, 22.71, 19.86, 14.14. **HRMS** (ESI) m/z: calculated for C30H40N2O3 $[M+H]^+$ : 437.3112, found 437.3110.

### 5.4.2.2 Synthesis of 5-chloro-7-iodoquinolin-8-yl acetate (CQE)

The 5-chloro-7-iodoquinolin-8-ol (3.04 g, 10 mmol, 1.0 equiv.) was refluxed in 10 mL acetic anhydride ($Ac_2O$) for 1h. The reaction mixture was brought to room temperature. The mixture was evaporated, and the residue was dissolved in dichloromethane. Then it was washed with aqueous $NaHCO_3$ and dried over $MgSO_4$. Further, the solvent was evaporated to obtain the final compound in 92% yield. Characterization was done according to the reported procedure.[23]

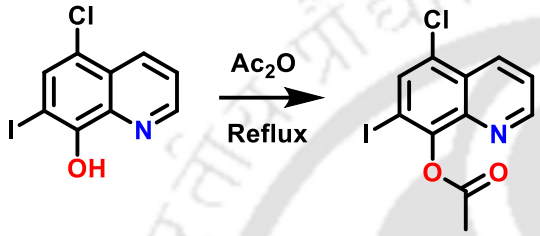


**Scheme 5.2.** Synthesis of 5-chloro-7-iodoquinolin-8-yl acetate.

### 5.4.2.3. Synthesis of tetramethyl 2,2',2'',2'''-(ethane-1,2-diylbis(azanetriyl))tetraacetate (EDTAE)

To the stirring solutions of ethylenediaminetetraacetic acid (EDTA) (2.92 g, 10 mmol, 1.0 equiv.) in 10 mL MeOH, $H_2SO_4$ 500 µl was added. The reaction mixture was refluxed at 80 °C for 8 hours. The reaction mixture was brought to room temperature, and the solvents were evaporated under reduced pressure. The compound was extracted with dichloromethane and washed with bicarbonate solution. The organic layer was dried over $MgSO_4$ and evaporated under reduced pressure, yielding 85%. Characterization was done according to the reported procedure.[24]

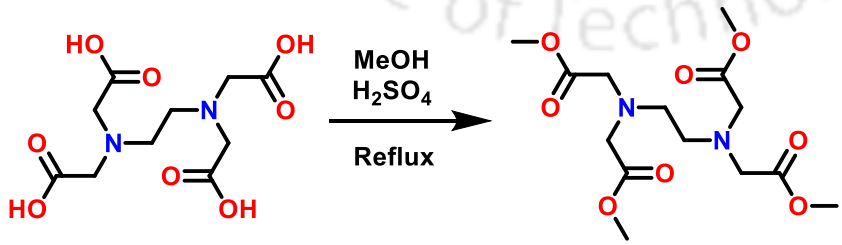


**Scheme 5.3.** Synthesis of tetramethyl 2,2',2'',2'''-(ethane-1,2-diylbis(azanetriyl))tetraacetate.

### 5.4.2.4 Synthesis of (1E,1'E)-pyridine-2,6-dicarbaldehyde dioxime (HMPO)

To a stirring solution of 2,6-pyridinedicarboxaldehyde (0.15 g, 1.11 mmol) and hydroxylamine hydrochloride (0.31 g, 4.44 mmol) in EtOH (50 mL), sodium hydroxide (0.178 g, 4.44 mmol) was added. The reaction mixture was stirred at 75 °C for 3 h, after which the resulting suspension was filtered, and the solid residue was washed with EtOH (2 × 20 mL). The filtrate was concentrated to dryness, affording the bis-oxime (0.176 g, 96%). Characterization was done according to the reported procedure.[25]

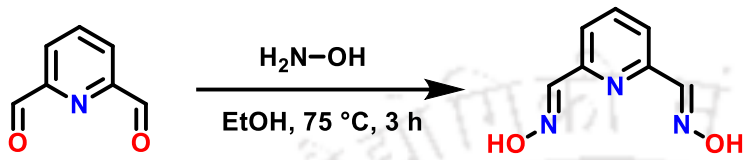


**Scheme 5.4.** Synthesis of (1E,1'E)-pyridine-2,6-dicarbaldehyde dioxime.

### 5.4.3 Sprasome Formation and Characterization

Initially, micelles out of SP and Tween 20 were prepared to develop suprasomes. For this, ASP (1 mM) and Tween 20 (Tween 20, 1 mM) were mixed into 1 mL of deionized water and subjected to sonication (10 min) followed by vortexing for 10-15 minutes to enable self-assembly into micelles. Thereafter, β-CD was introduced into the solution at varying concentrations (0-14

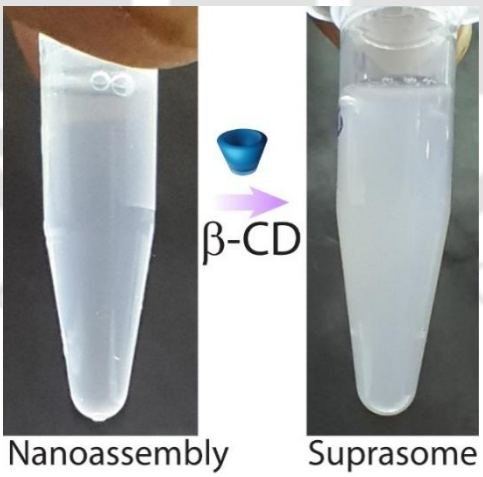


**Figure 5.6.** Visual observation showing increased cloudiness during the transition from nanoassembly to suprasome formation.

mM), and the mixture was vortexed for 5 minutes and then kept in a shaker incubator at 180 rpm for 1 hour to promote the transition from micelles to suprasomal assemblies, which can be observed visually due to increased cloudiness.

### 5.4.3.1 Measurements of Hydrodynamic Diameter by Dynamic Light Scattering (DLS)

Following the method mentioned above, suprasome were prepared with different β-CD concentrations. The $D_H$ values were recorded using a DLS instrument (Zetasizer Nano ZS90, Malvern, Westborough, MA) at 25 °C. These measurements were performed for all different β-CD concentrations as mentioned in the above-mentioned experiment.

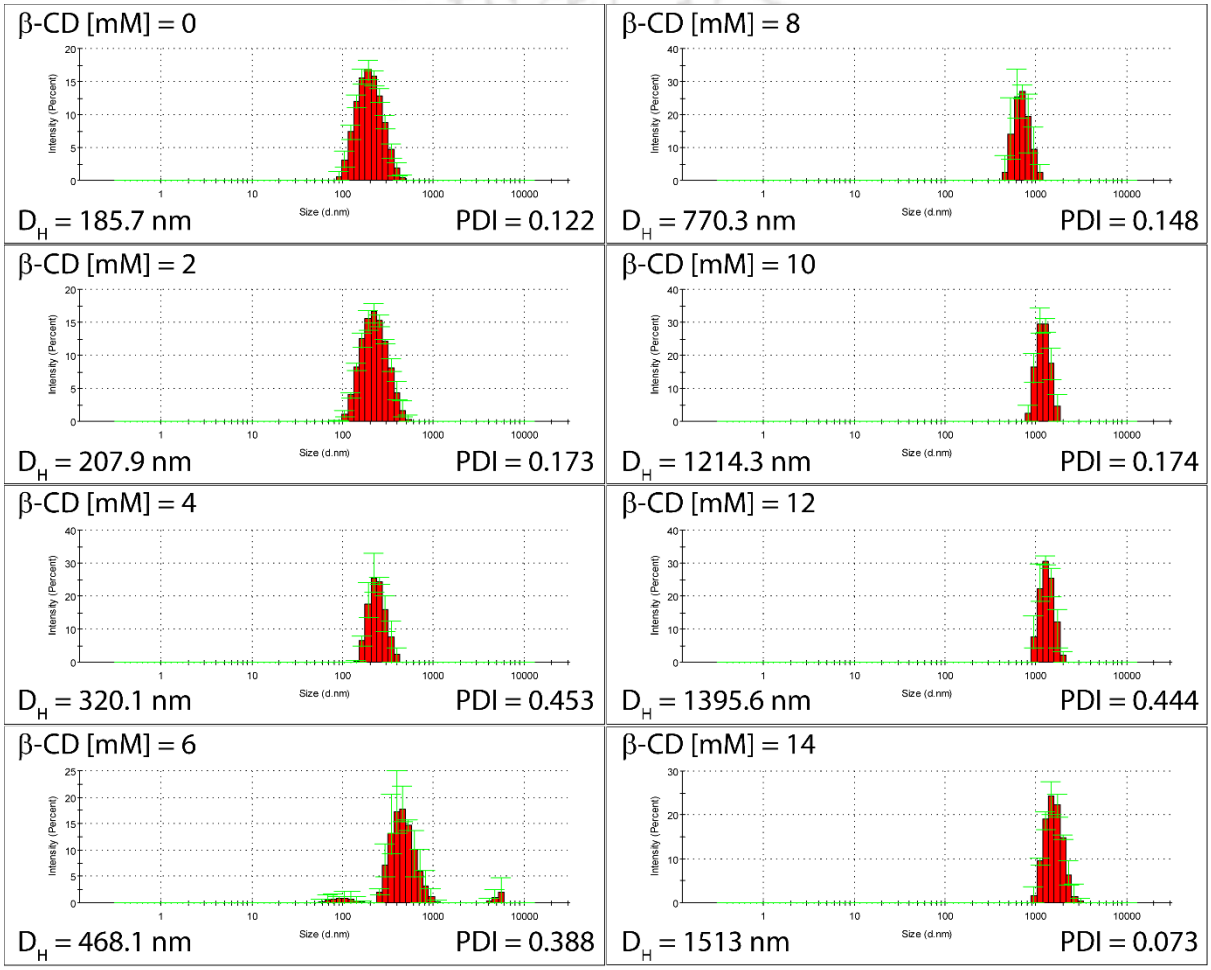


**Figure 5.7.** Variation of hydrodynamic diameter ($D_H$) distribution of suprasomes of Tween 20 (1 mM) and ASP (1 mM) at different concentrations of β-CD (0-14 mM).

Control experiments for suprasome formation revealed that mixing only Tween 20 (1 mM) with β-CD led to suprasome assembly, whereas mixing AMC (1 mM) with β-CD failed to form suprasomes. These results indicate that Tween 20 is essential for suprasome assembly, while AMC alone is insufficient.

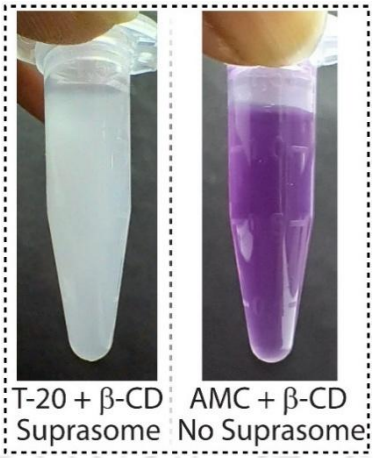


**Figure 5.8**. Control studies: Visual observation of (Tween 20 + β-CD) showing suprasome formation with increased cloudiness, whereas (AMC + β-CD) showcase no suprasome formation.

### 5.4.3.2 Morphology of Nanoassembly and Suprasome

Nanoassembly (ASP = 1mM, AMC = 1mM) and suprasome (ASP = 1mM, AMC = 1mM, β-CD = 10 mM) were prepared following the previously mentioned method and were drop-casted to investigate the morphology of both nanoassembly and suprasome using FESEM. The samples were dried at room temperature. Before analysis, the samples were stacked onto the FESEM grid and coated with gold.

### 5.4.3.3 ITC-based Host-Guest Interaction Study with Amphiphiles

The host-guest interaction of β-CD with Tween 20 and (Tween 20 + ASP) 1:1 mixture was investigated by isothermal titration calorimetry (ITC) measurements. The heat change induced by the host-guest interactions was measured at 25 °C (301 K) and 300 rpm stirring speed using a Microcal PEAQ-ITC. A 1 mM solution of Tween 20 was titrated against a β-CD (10 mM) solution. The titration method followed 16 injections (2 μL of each) of titrant (β-CD) into the sample cell containing Tween 20 (300 μL) at 2-minute intervals with continuous stirring. The enthalpy change (ΔH) and entropy (ΔS) values were calculated using a nonlinear least-square fit analysis. Gibbs free energy (ΔG) was calculated by using the Gibbs equation: $\Delta G = \Delta H - T\Delta S$. The ΔH and ΔS values suggested that the interaction of Tween 20 with β-CD is an enthalpy-driven process. Similar measurements were performed for a mixture of Tween 20 and SP (1:1) with β-CD.

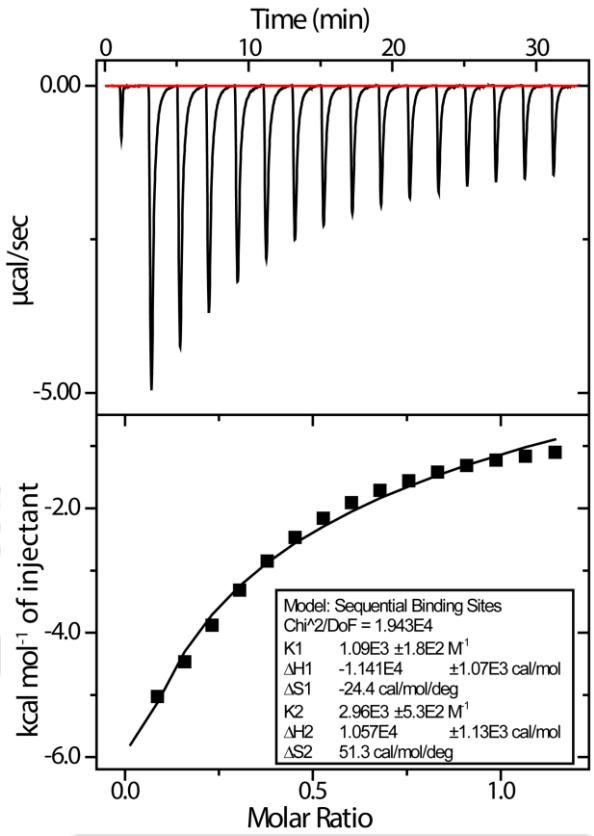


**Figure 5.9.** ITC profile of Tween 20 titrated against β-CD.

### 5.4.4 Photophysical Property and Photoinduced Isomerisation of Spiropyran to Merocyanine

#### 5.4.4.1 Absorbance Study of SP and MC

Spiropyran derivative (ASP) was dissolved in a 1:1 (v/v) acetonitrile/water mixture to a final concentration of 60 µM. The UV–vis absorbance spectrum was recorded (300–700 nm) in a

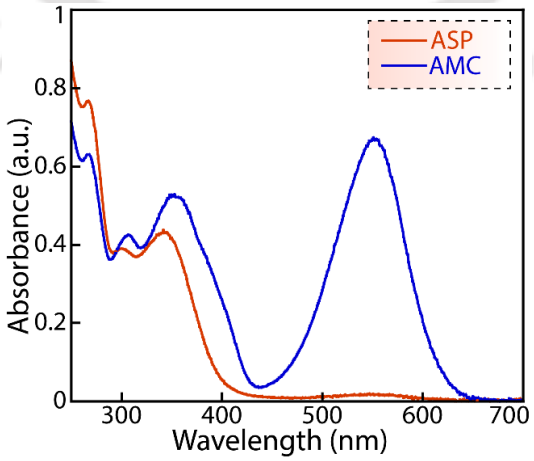

**Figure 5.10.** UV–Vis absorbance spectra demonstrating SP to MC photoisomerisation upon UV light exposure.

1 cm quartz cuvette. The solution was then irradiated with 365 nm UV light for 5 min at room temperature, and the spectrum was re-recorded to confirm conversion to the merocyanine (MC) form.

### 5.4.4.2 Reversibility Cycle of Spiro-Mero Interconversion

The aforementioned method converted SP to MC, and the absorbance was recorded. Furthermore, the MC solution was kept in the dark at room temperature, and absorbance spectra were recorded at 3-minute intervals for 1 hour, which demonstrated the complete thermal reversal of MC to SP. This process was conducted for multiple cycles to demonstrate reversibility.

### 5.4.4.3 Photophysical and Photoisomerisation Property of Suprasome

Suprasomes were prepared following the previously mentioned method. Their photophysical and photoisomerisation property were subsequently studied using a UV-Vis spectrophotometer. Suprasome was diluted to reduce light scattering, and suprasome was subjected to UV irradiation (365 nm, 5 min) to induce Isomerisation of the photo-responsive component, i.e., ASP. The UV–Vis absorption spectra were recorded before and after

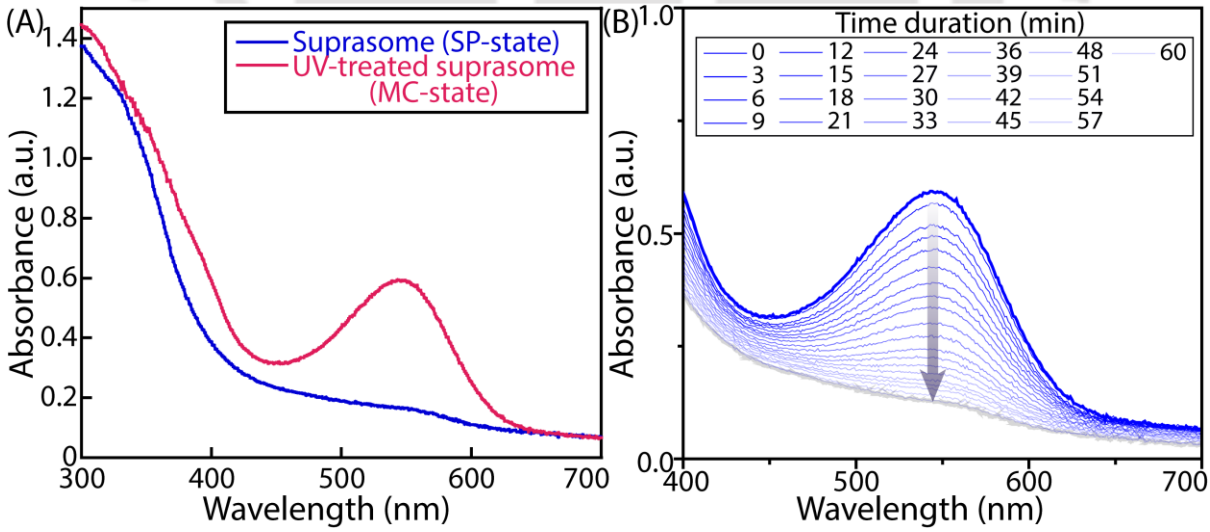


**Figure 5.11.** UV–Vis spectra showing (A) ASP-to-AMC photoisomerisation of suprasome under 365 nm irradiation (5 min). (B) Thermal AMC-to-ASP relaxation of suprasome in the dark.

irradiation to monitor the conversion from the spiro to merocyanine form. The change in absorbance confirmed successful photoisomerisation within the suprasomal assembly. Reversibility was examined by keeping the irradiated sample in the dark at room temperature, and the absorbance was recorded at regular intervals. The observed spectral changes indicated that the suprasome retained their ability to undergo reversible Isomerisation under light and dark conditions.

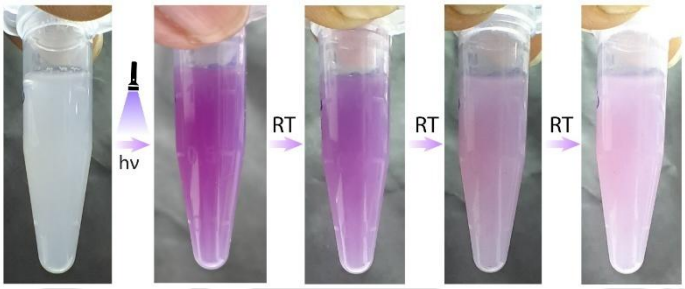


**Figure 5.12.** Visual observation reveals photoisomerisation of ASP to AMC under suprasomal conditions, followed by thermal reversal to the ASP form, thereby creating a transient AMC-suprasome state.

### 5.4.5 Stimuli Responsiveness of Suprasome

#### 5.4.5.1 Effect of Photo-Induced Isomerisation on Suprasome Size and Morphology

To investigate the effect of photo-induced Isomerisation on suprasome architecture, samples were irradiated with UV light (365 nm, 5 min) to induce conversion of the photo-responsive component SP. DLS measurements were performed at 10-minute intervals post-irradiation to monitor time-dependent changes in hydrodynamic diameter ($D_H$). The light-dark cycle was repeated multiple times to assess the reversibility, and DLS data were recorded for each cycle. Morphological alterations were further examined using field emission scanning electron microscopy (FESEM). Considering the transient nature of the MC-state, only 2 µL of sample was drop-casted onto the sample grid and kept under constant 365 nm light irradiation until it dried completely. The results indicated reversible changes in suprasome size, suggesting light-triggered dynamic restructuring within the assemblies.

#### 5.4.5.2 Nile Red-based Study of Photoinduced Suprasome Reorganisation and Recovery

Nile Red (NR, 100 µM final concentration) was co-encapsulated within the suprasomal dispersion (prepared as per the previously mentioned protocol) and subjected to photoirradiation using a 365 nm UV lamp for 5 minutes. The fluorescence intensity of NR ($\lambda_{ex}$ = 550 nm, $\lambda_{em}$ = 640 nm) was recorded before and immediately after irradiation, which showed

a significant quenching, indicating the release of NR into the aqueous medium due to suprasome reorganisation. The sample was then kept in the dark at room temperature (RT), and the fluorescence emission of NR was recorded at regular intervals over 1 hour. A gradual increase in fluorescence was observed, supporting the reassembly of the smaller disassembled units into larger suprasome, allowing NR re-partitioning into the hydrophobic membrane environment.

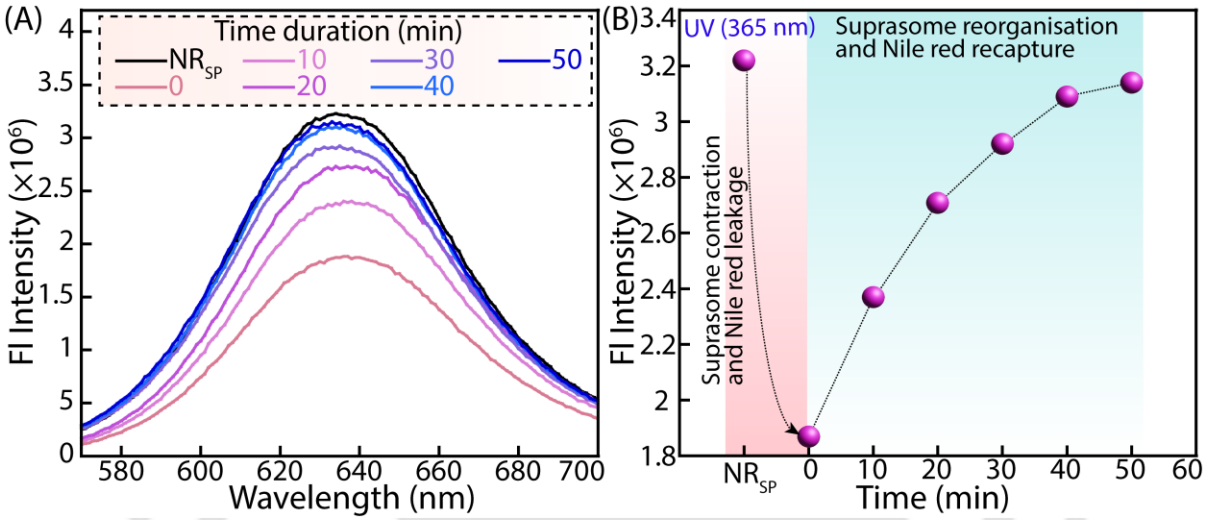


**Figure 5.13.** (A) Fluorescence spectra of Nile red-loaded suprasome before and after light irradiation, showing disassembly-induced quenching and subsequent fluorescence recovery upon reassembly. (B) Time-dependent fluorescence intensity of Nile red has been presented as discrete points before and after light irradiation, showing initial quenching followed by gradual fluorescence increase due to suprasome reassembly.

### 5.4.5.3. Effect of $Zn^{2+}$ on Light-Treated and Untreated Suprasome Sizes (DLS-based $D_H$ Measurements)

Light irradiation of the suprasome induced a reversible transformation into a transient MC-suprasome, with a reduced size of ~600–700 nm as observed by DLS, indicating structural rearrangement and compaction. Upon treatment with $Zn^{2+}$ (1 mM) and incubation in a shaker incubator for 5 minutes, the particle size dramatically increased to ~3500–4000 nm (DLS), suggesting $Zn^{2+}$-induced disassembly accompanied by increased aggregation and probable morphological alterations. In contrast, control studies with the native SP-suprasome showed no such increase in size upon $Zn^{2+}$ addition. Additionally, SP-suprasome that reformed after a 1-hour incubation following photoirradiation also exhibited negligible changes in size upon $Zn^{2+}$ treatment, as confirmed by DLS measurements. These findings underscore the critical role

of the transient MC form in coordinating with $Zn^{2+}$ to drive suprasomal destabilisation and structural reorganisation.

### 5.4.5.4 Effect of Different Metal Ions on Light-Treated Suprasome Sizes (DLS-based $D_H$ Measurements)

The photo-irradiated suprasomes (365 nm, 5 min) were treated with different metal ions ($Na^+$, $K^+$, $Zn^{2+}$, $Mg^{2+}$, $Ca^{2+}$, $Cu^{2+}$, $Mn^{2+}$, $Fe^{3+}$, 1 mM), and the hydrodynamic diameter ($D_H$) was immediately measured

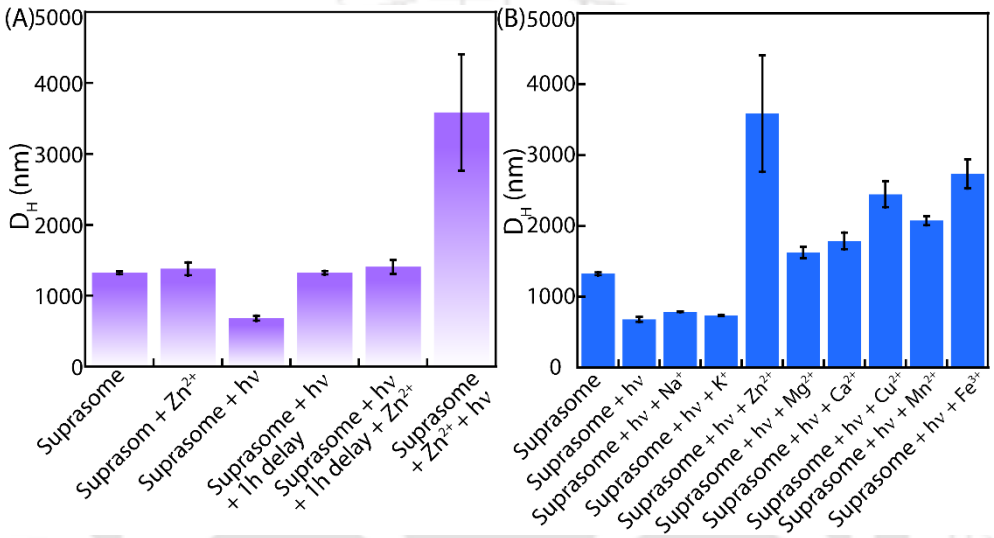


**Figure 5.14.** (A) DLS analysis shows an increase in suprasome $D_H$ only upon simultaneous $Zn^{2+}$ addition and light irradiation, indicating photoactivated $Zn^{2+}$-induced disassembly. Other controls—including $Zn^{2+}$ treatment alone and $Zn^{2+}$ treatment after 1 h light pre-irradiation showed no significant change in DH. (B) DLS analysis of suprasomes along with simultaneous photo-irradiation and different metal ion treatment ($Na^+$, $K^+$, $Zn^{2+}$, $Mg^{2+}$, $Ca^{2+}$, $Cu^{2+}$, $Mn^{2+}$, $Fe^{3+}$; 1 mM).

### 5.4.5.5 Morphology Analysis of Simultaneous Dual Stimuli (UV-irradiation and $Zn^{2+}$) Treated Suprasome

The suprasome was prepared using the previously mentioned method and simultaneously treated with UV-irradiation (365 nm) and $Zn^{2+}$ for 5 minutes. Furthermore, 2–3 µL of the sample was drop-casted and kept under UV light to prevent thermal reversal until it was completely dried, to investigate the morphological changes. Several other control samples were also examined for their morphology to identify the factors contributing to the suprasome morphology changes. These controls included only ASP, only AMC, (AMC + $Zn^{2+}$), (AMC +

β-CD), and (AMC + β-CD + $Zn^{2+}$). The samples were dried at room temperature. Before analysis, the samples were stacked onto the FESEM grid and coated with gold.

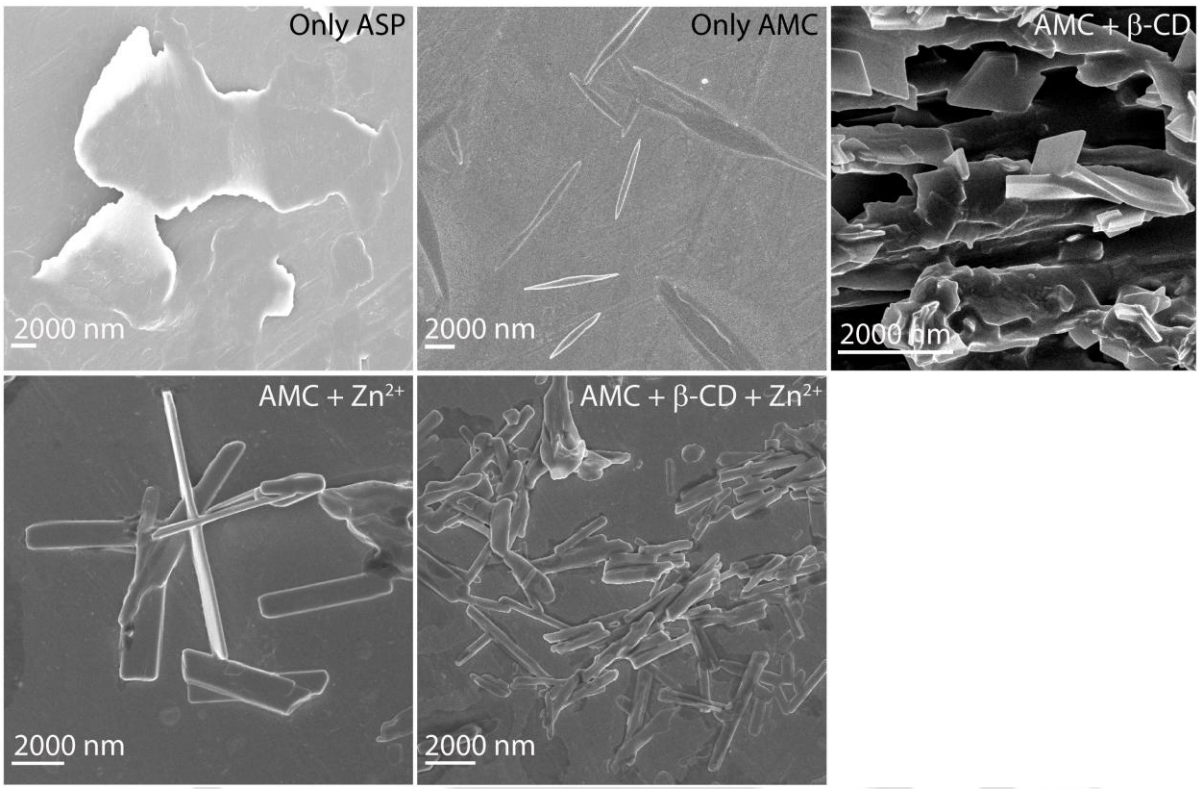


**Figure 5.15.** Representative FESEM images of different controls, such as only ASP, only AMC, (AMC + β-CD), (AMC + $Zn^{2+}$), and (AMC + β-CD + $Zn^{2+}$), in aqueous media.

### 5.4.5.6 UV–Vis Absorbance Study of AMC and $Zn^{2+}$ Interaction and Thermal Decay Behaviour of AMC–$Zn^{2+}$ Complex

ASP (30 μM) was exposed to only UV light treatment (365 nm) for AMC generation and simultaneous treatment with UV light and $Zn^{2+}$ (100 μM) to generate the (AMC + $Zn^{2+}$) coordinated state. The absorbance study of these samples was undertaken to investigate any interaction between AMC and $Zn^{2+}$. Further, the thermal decay (reversal) behaviour of the same (AMC + $Zn^{2+}$) coordinated state was also observed through an absorbance study. UV–vis absorbance spectra were then recorded at fixed time intervals (5 min intervals) to monitor changes in absorbance corresponding to the thermal reversal of the AMC–$Zn^{2+}$ complex.

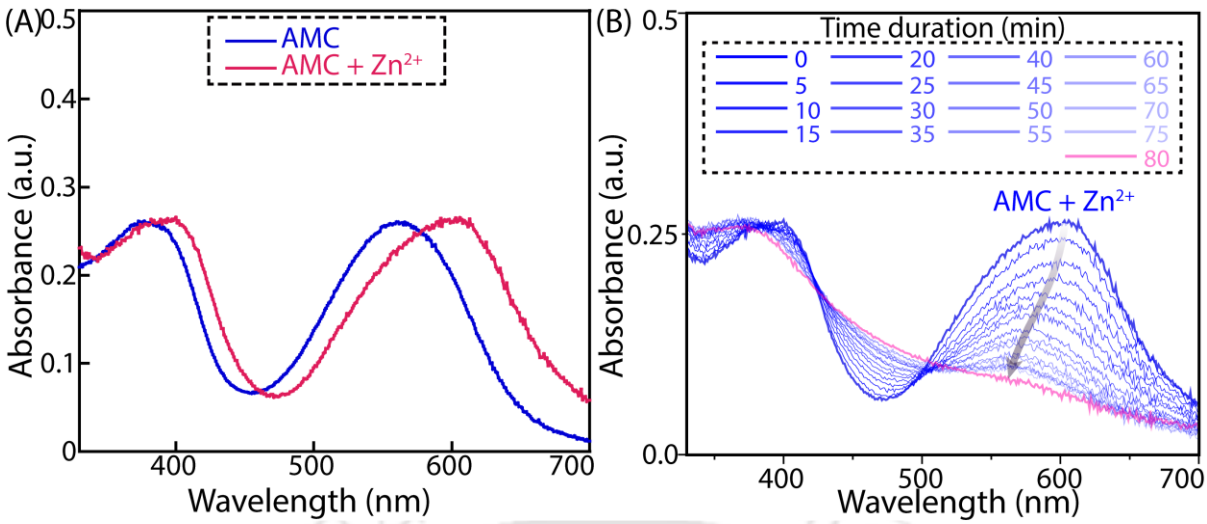


**Figure 5.16.** UV–vis absorbance study showing (A) the interaction between AMC and $Zn^{2+}$, and (B) the thermal decay (reversal) of the AMC–$Zn^{2+}$ complex over time.

### 5.4.5.7 Morphological Changes in Nanosheets Upon Long-Term Ambient Storage

UV-absorbance studies revealed that the AMC–$Zn^{2+}$ complex undergoes thermal relaxation at room temperature, reverting back to the ASP (SP) state. Accordingly, after nanosheet formation induced by combined light and $Zn^{2+}$ treatment, the resulting solutions were stirred at room temperature for 2-3 hours to investigate morphological evolution under ambient relaxation conditions. Subsequently, 5 µL of the sample was drop-cast onto a substrate to investigate any morphological changes in the nanosheets using FESEM. The samples were dried at room

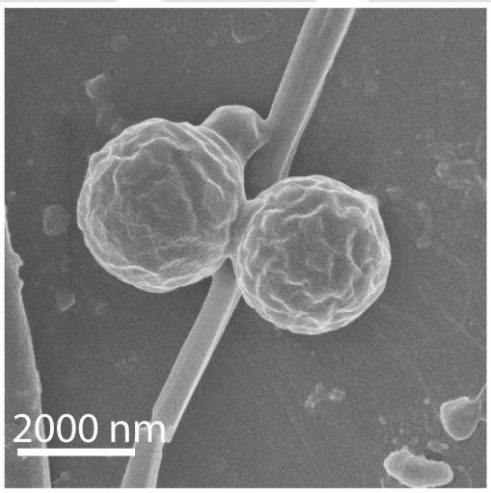


**Figure 5.17.** Representative FESEM images showing the morphological reversal of nanosheets into suprasome-like structures after prolonged exposure to ambient conditions.

temperature, mounted onto FESEM grids, and coated with a thin layer of gold prior to imaging. We observed the formation of spherical structures, indicative of a prior suprasome being

formed, which showcases a probable thermal reversal of the nanosheet back into a spherical suprasome.

### 5.4.6 Development of Conditional Suprasome for Optical Output and $Zn^{2+}$ Transport

#### 5.4.6.1 $Zn^{2+}$-Mediated Esterase Activity of HMPO on AHPTS and CQE Substrates

In 2 ml HEPES buffer (pH 7.0), HMPO (20 μM) was incubated with $Zn^{2+}$ (40 μM) under slow stirring in the presence of either AHPTS (100 μM) or CQE (100 μM) in two separate experimental sets. For CQE, the buffer also contained 25% DMSO. In the first set, the

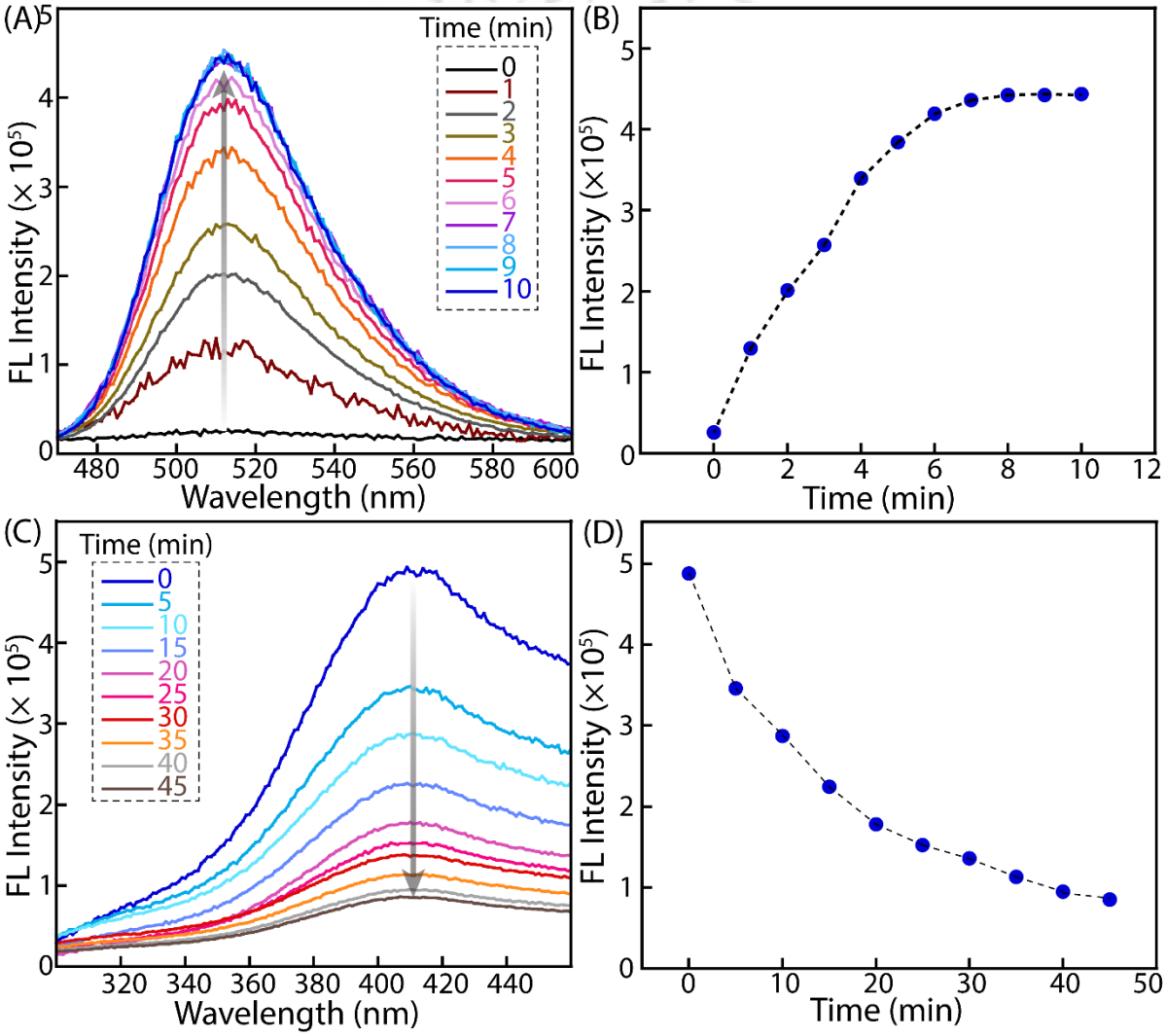


**Figure 5.18.** (A) Fluorescence emission spectra of HPTS generated through hydrolysis of AHPTS catalysed by the HMPO–$Zn^{2+}$ complex and (B) corresponding kinetics. (C) Fluorescence decay profile of CQE upon conversion to CQ, facilitated by the HMPO–$Zn^{2+}$ complex (D) corresponding kinetics.

hydrolysis of AHPTS to HPTS was monitored using fluorescence spectroscopy ($\lambda_{ex}$ = 450 nm, $\lambda_{em}$ = 510 nm). Due to the rapid nature of AHPTS hydrolysis, measurements were recorded at 1-minute intervals over 10 minutes. In the second set, the hydrolysis of CQE to CQ was tracked by observing the fluorescence decay of CQE ($\lambda_{ex}$ = 240 nm, $\lambda_{em}$ = 410 nm). As CQE is converted to the non-fluorescent product CQ, a progressive decrease in fluorescence indicated substrate consumption and product formation. Measurements were recorded at 5-minute intervals over 45 minutes.

CQE to CQ conversion was also observed through HPLC upon HMPO-$Zn^{2+}$ treatment. At time intervals of 0 min, 10 min, 20 min, 30 min, 40 min, and 50 min, incubated samples were recorded. For the HPLC-based study of proionophore (CQE) to ionophore (CQ) release, the samples were filtered using a 0.22 µm PTFE syringe filter. Another control HPLC of CQE in presence of only $Zn^{2+}$ was performed for similar time duration. Column used: Ascentis® express C18, 2.7 µm HPLC column, flow rate: 0.5 mL/min, mobile phase used: gradient of acetonitrile/water.

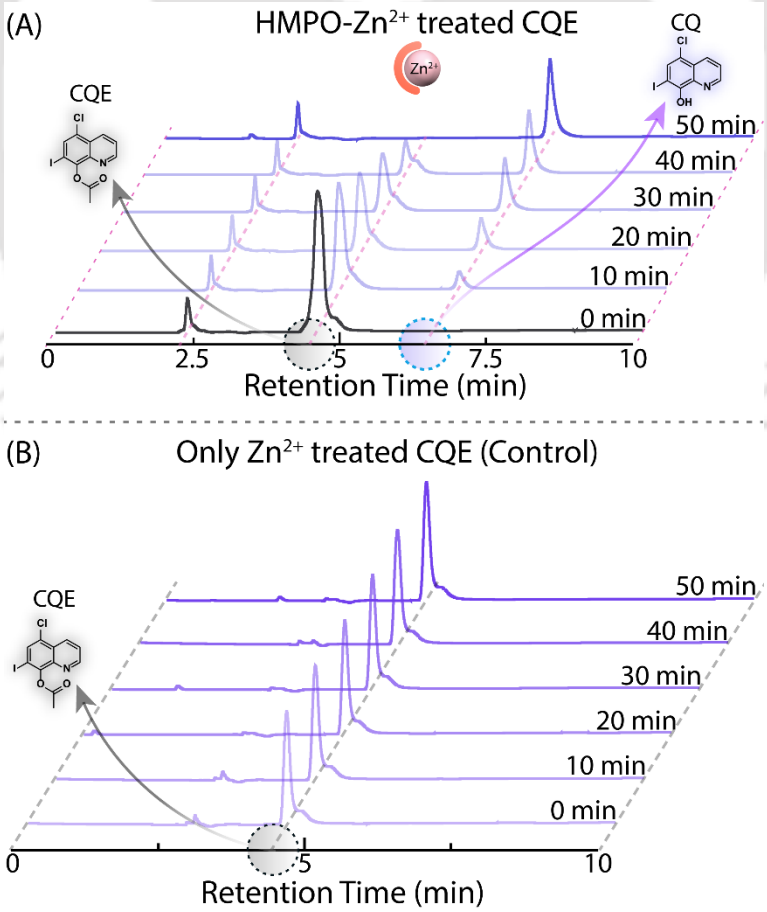

**Figure 5.19.** HPLC-based measurement of CQE hydrolysis and active ionophore (CQ) release upon treatment with HMPO-$Zn^{2+}$ complex and only $Zn^{2+}$ as a control. Chromatograms of CQE in the presence (A) HMPO-$Zn^{2+}$ and (B) $Zn^{2+}$.

The UV-Vis absorbance studies in aqueous media indicate that CQE exhibits a distinct absorbance peak at 240 nm, which is absent in CQ. This enables selective excitation of CQE, allowing its concentration to be monitored via fluorescence. The observed fluorescence decay thus reflects a decrease in CQE concentration, while the concurrent formation of CQ, which lacks absorbance at 240 nm, results in a decrease in fluorescence emission.

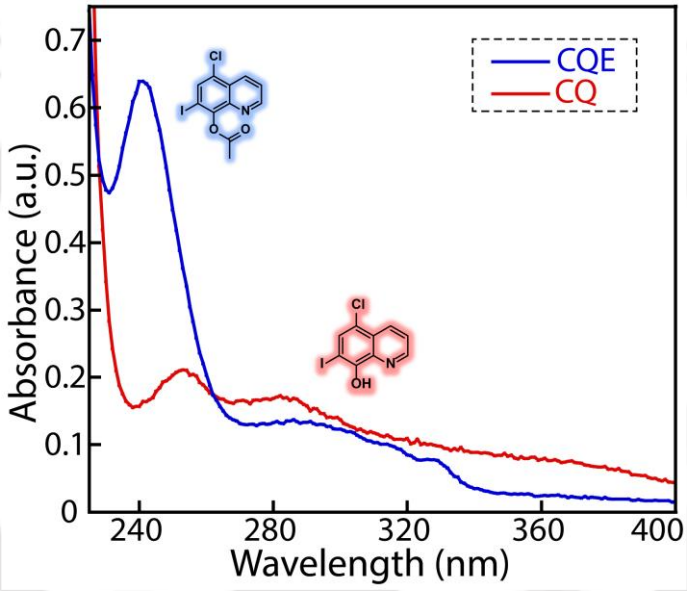


**Figure 5.20.** UV-Vis absorbance spectra of CQ (10 µM) and CQE (10 µM) in aqueous media.

### 5.4.6.2 Conditional Suprasome Disassembly and Subsequent Ester Hydrolysis of AHPTS and CQE for Optical Output and $Zn^{2+}$ Transport

To establish the transient, logic cube–like conditional behaviour of the suprasome, we conducted experiments in which suprasomes were subjected to different input conditions (C0–C7) as defined in the truth table below.

**Table 5.1.** Truth table illustrating various combinations of stimuli and their corresponding outputs in terms of $Zn^{2+}$ transport efficiency (%) and optical signal generation via fluorescent HPTS formation.

| Condition | Light | $Zn^{2+}$ | Time Confinement | Transport (%) | HPTS generation (%) |
|---|---|---|---|---|---|
| C0 | 0 | 0 | 0 | 11.7 | 2.2 |
| C1 | 1 | 0 | 0 | 16.0 | 3.8 |
| C2 | 0 | 1 | 0 | 17.0 | 3.1 |
| C3 | 0 | 0 | 1 | 13.5 | 2.7 |
| C4 | 1 | 1 | 0 | 19.3 | 14.3 |
| C5 | 1 | 0 | 1 | 15.2 | 4.6 |
| C6 | 0 | 1 | 1 | 16.7 | 5.0 |
| C7 | 1 | 1 | 1 | 77.6 | 93.2 |

(Light- 0: no UV light treatment (365 nm), 1: UV light treatment (365 nm) for 5 min

$Zn^{2+}$- 0: no $Zn^{2+}$ treated to suprasome, 1: $Zn^{2+}$ (1mM) treated to suprasome.)

(Time confinement- 0: all the treated stimuli outside the confined time window, 1: all the treated stimuli within the confined time window.)

Simultaneously, two distinct suprasome formulations were prepared: one containing AHPTS and HMPO, and the other containing CQE and HMPO. During suprasome assembly, aqueous solutions were supplemented with HMPO (200 µM) and AHPTS (200 µM) for the first set, and with HMPO (200 µM) and CQE (200 µM) for the second set. Following suprasome formation, the solution was passed multiple times through an ultracentrifuge filtration tube to remove excess, unencapsulated HMPO, AHPTS, and CQE from the external medium, and then resuspended in an aqueous solution containing a similar concentration of β-CD as previously.

The first set of suprasomes was subjected to different input conditions (C0–C7), and optical output was monitored by tracking the fluorescence signal of HPTS ($\lambda_{ex}$ = 450 nm, $\lambda_{em}$ = 510 nm). The HMPO–$Zn^{2+}$ complex forms only under the (1,1,1) input condition, which catalyses the hydrolysis of AHPTS to fluorescent HPTS, thereby generating a detectable optical signal. Similarly, the second set of suprasomes was treated under the same conditions (C0–C7) and subsequently introduced to liposomal solutions containing the $Zn^{2+}$-sensitive dye Magnesium Green (MgG) (EYPC/CHOL-LUVs⊃MgG vesicles). The detailed procedure for this is explained in the ion transport section. This setup enabled the observation of triggered $Zn^{2+}$

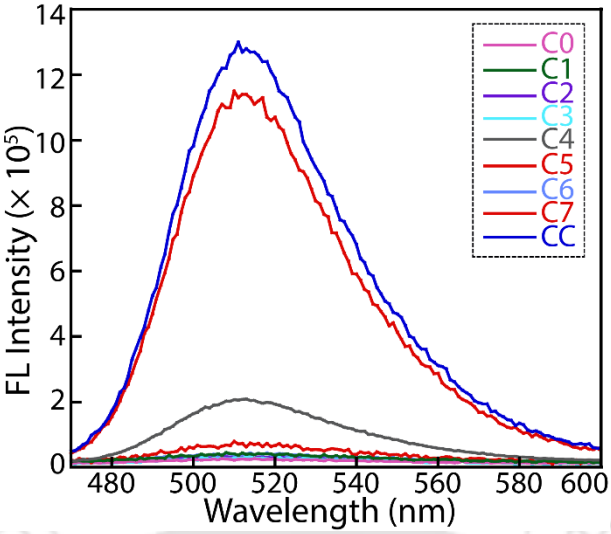


**Figure 5.21.** AHPTS hydrolysis leading to fluorescent HPTS generation under different conditions (C0-C7).

transport into the secondary liposomes, representing a form of sacrificial, transient communication where the disassembly of the suprasome facilitates ion transfer, highlighting the system's potential as a conditional molecular communication strategy. This phenomenon parallels the previously discussed neural model, in which the coincident transient excitation of two neurons enables $Ca^{2+}$ influx into a downstream (secondary) neuron. Similarly, in our system, synchronized transient stimuli promote $Zn^{2+}$ transport into a secondary liposome, highlighting an analogous mechanism of stimulus coincidence-dependent signalling.

### 5.4.6.3 Ion Transport Studies

The CQ is a known transmembrane transporter of $Zn^{2+}$. Upon simultaneous dual-stimuli treatment (light and $Zn^{2+}$) of the HMPO and CQE loaded suprasome, it disassembles and an HMPO–$Zn^{2+}$ complex is formed. This complex then facilitates in situ ester hydrolysis of CQE (esterified precursor of CQ) and release of the $Zn^{2+}$ transporter CQ, thereby promoting $Zn^{2+}$ transport across the lipid bilayer of a secondary liposome. This transport was monitored using the $Zn^{2+}$-sensitive dye Magnesium Green (MgG), encapsulated within the secondary liposome, via fluorescence kinetics measurements.

#### 5.4.6.3.1 Preparation of EYPC/CHOL-LUVs⊃MgG Vesicles

Phosphatidylcholine (PC) and cholesterol (CHOL) are the two most abundant lipids in mammalian cell membranes; hence, both these lipids were used to prepare model large unilamellar vesicles (LUVs). To conduct the MgG fluorescence-based ion-transport studies,

we took EYPC (50 mg/mL in deacidified $CHCl_3$) and cholesterol (CHOL; 25 mg/mL in deacidified $CHCl_3$) in a clean, dry glass vial in a molar ratio of 8:2. The solution was evaporated for 6 hours under reduced pressure to form a thin lipid film. After that, we rehydrated the film with 10 mM HEPES buffer containing 100 mM NaCl, 100 µM EDTA and 50 µM MgG dye at pH 7.0. The resulting suspension was vortexed six to seven times over 1 hour. Next, we

performed 6-7 freeze-thaw cycles followed by 10 minutes of constant vortexing. We then extruded the lipid suspension 15–17 times using a mini extruder with a 200 nm pore size to achieve a uniform liposome size of 200 nm. Finally, we removed the unencapsulated MgG dye using the gel filtration technique (Sephadex G-50) and 10 mM HEPES buffer containing 100 mM NaCl, 100 µM EDTA at pH 7.0 as the eluting solution. This process yielded a final lipid concentration of 25 mM (assuming 100% lipid regeneration).

#### 5.4.6.3.2 Ion Transport Studies using EYPC/CHOL-LUVs⊃MgG Vesicles

For the MgG-based ion transport assay, in a clean and dry fluorescence cuvette (3 mL), 10 mM HEPES buffer containing 100 mM NaCl and 100 µM EDTA, pH 7.0 (1930 µL), EYPC/CHOL-LUV⊃MgG (40 µL), and $ZnCl_2$ (final concentration 1 mM) were added. The cuvette was placed under slow stirring conditions in a fluorescence spectrophotometer for about 3 minutes to equilibrate. The fluorescence was evaluated as a function of time ($\lambda_{em}$ = 531 nm, $\lambda_{ex}$ = 506 nm). At 50 s, the compound (stock solution of CQ and CQE in DMSO) was added to the cuvette solution to initiate the transport activity (Final working concentration 50 nM). Finally, the vesicles were completely lysed at 450 s by adding 20 µL of 20% Triton X-100. The fluorescence intensity measurement was continued for a further 50 s. The normalized % transport efficiency (%EE) at t = 450 s was considered for the particular transport efficiency of the compounds.

Transport activity, $T_{MgG} = (\frac{F_t - F_0}{F_\infty - F_0} \times 100)$ %

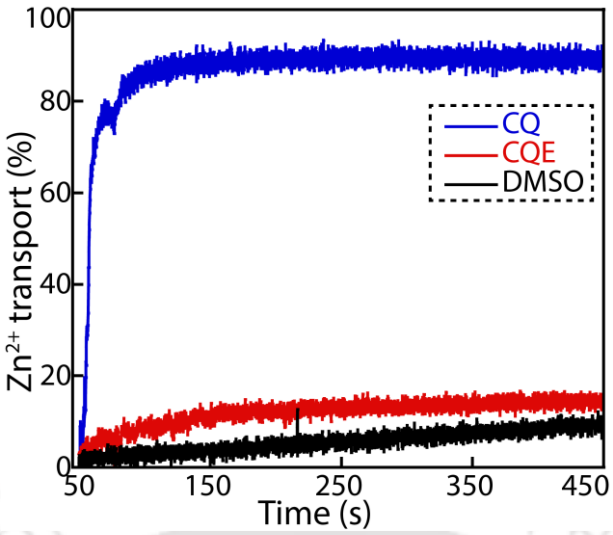


**Figure 5.22.** $Zn^{2+}$ transport activity of CQ and CQE (50 nM) across the bilayers of EYPC/CHOL-LUV⊃MgG. (5 µl DMSO as a control).

#### 5.4.6.3.3 Ion Transport Activity of CQE Exposed to Light and $Zn^{2+}$ Treated Suprasome (Loaded with HMPO and CQE) using EYPC/CHOL-LUVs⊃MgG Vesicles

As per the previously mentioned procedure, liposomes containing MgG dye were prepared. Suprasomes were prepared with an aqueous solution containing 200 µM HMPO and 200 µM CQE. Further, the suprasomes were filtered through an ultracentrifugation tube a few times in order to remove any unencapsulated HMPO or CQE and resuspended in an aqueous solution containing a similar concentration of β-CD as previously. These suprasomes were treated to different conditions as mentioned in the truth table (C0-C7) and kept under stirring for 5 min. Simultaneous dual stimuli (condition C7: (1,1,1)) triggers suprasome disassembly, nanosheet generation and subsequent release of HMPO and CQE. HMPO combines with $Zn^{2+}$ to generate HMPO-$Zn^{2+}$-complex that continues in-situ ester hydrolysis, releasing active ionophore (CQ) into the solution.

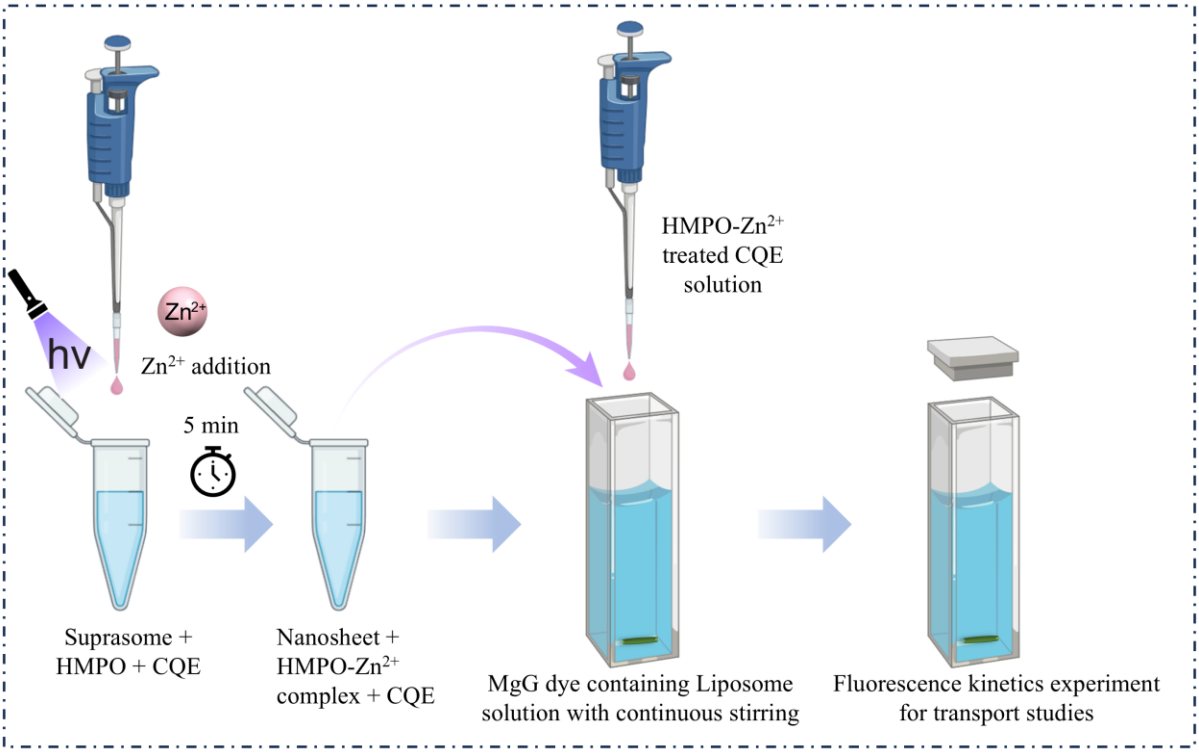


**Figure 5.23.** Schematic representation of the in-situ ester hydrolysis of CQE to CQ via HMPO-$Zn^{2+}$ complex and subsequent $Zn^{2+}$ transport activity assay using the EYPC/CHOL-LUVs⊃MgG vesicles.

For the MgG-based ion transport assay, in a clean and dry fluorescence cuvette (3 mL), 10 mM HEPES buffer containing 100 mM NaCl and 100 µM EDTA, pH 7.0 (1930 µL), EYPC/CHOL-LUV⊃MgG (40 µL), and $ZnCl_2$ (final concentration 1 mM) were added. The cuvette was placed under slow stirring conditions in a fluorescence spectrophotometer for about 3 minutes to equilibrate. The fluorescence was evaluated as a function of time ($\lambda_{em}$ = 531 nm, $\lambda_{ex}$ = 506 nm). At 50 s, the dual stimuli-treated suprasome solution containing HMPO-$Zn^{2+}$ and CQE was introduced into the cuvette solution containing liposome to initiate the transport studies (Final working concentration of CQE 200 nM, assumption: 100% encapsulation efficiency of CQ via suprasome, hence actual concentration of CQE introduced will be much less). Finally, the vesicles were completely lysed at 450 s by adding 20 µL of 20% Triton X-100. The fluorescence intensity measurement was continued for a further 50 s. The normalized % transport efficiency (%EE) at t = 450 s was considered for the particular transport efficiency of the compounds. The increase in transport activity can be attributed to the in-situ ester hydrolysis activity of HMPO-$Zn^{2+}$-complex, which releases active ionophore CQ from CQE.

Transport activity, $T_{MgG} = (\frac{F_t - F_0}{F_\infty - F_0} \times 100)$ %

Where, $F_t$ = fluorescence intensity at 450 s, $F_0$ = Initial fluorescence intensity, $F_\infty$ = fluorescence intensity after Triton X-100 addition.

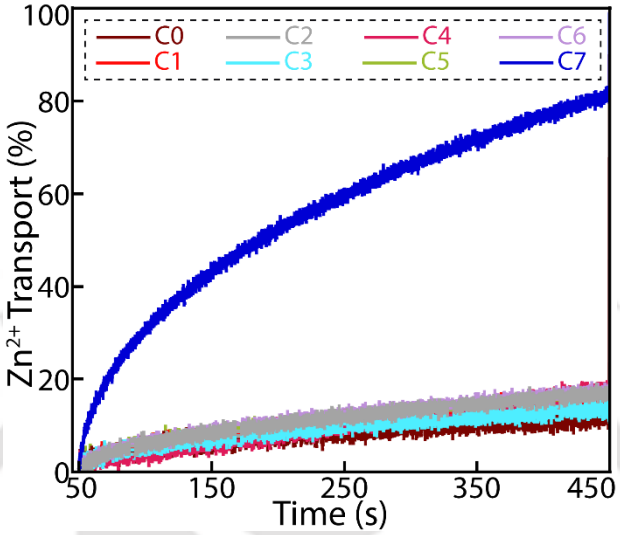


**Figure 5.24.** $Zn^{2+}$ transport activity of CQ, released via conditional ester hydrolysis from suprasomes treated under different conditions (C0–C7), was evaluated across EYPC/CHOL-LUV⊃MgG.

The designed suprasome construct functionally replicates key features of biomimetic signalling pathway inspired by neuronal synaptic communication. The suprasome serves as a signalling unit (initiator) in this system that is responsive solely to the simultaneous application of light and $Zn^{2+}$, conceptually analogous to the requirement of coincident pre- and postsynaptic activation during long-term potentiation (LTP). Stimulation causes HMPO to be released, thereby triggering hydrolysis of CQE via HMPO-$Zn^{2+}$ complexation, leading to $Zn^{2+}$ transport into a signal-receiving effector liposome, wherein enhanced fluorescence from the encapsulated dye (MgG) serves as a downstream optical output. This model, while inspired by neural communication, does not attempt to reproduce the entire complexity of neuronal function and hence provides a simplified, synthetic framework that mimics key features of temporally gated signal transduction and inter-vesicular communication.

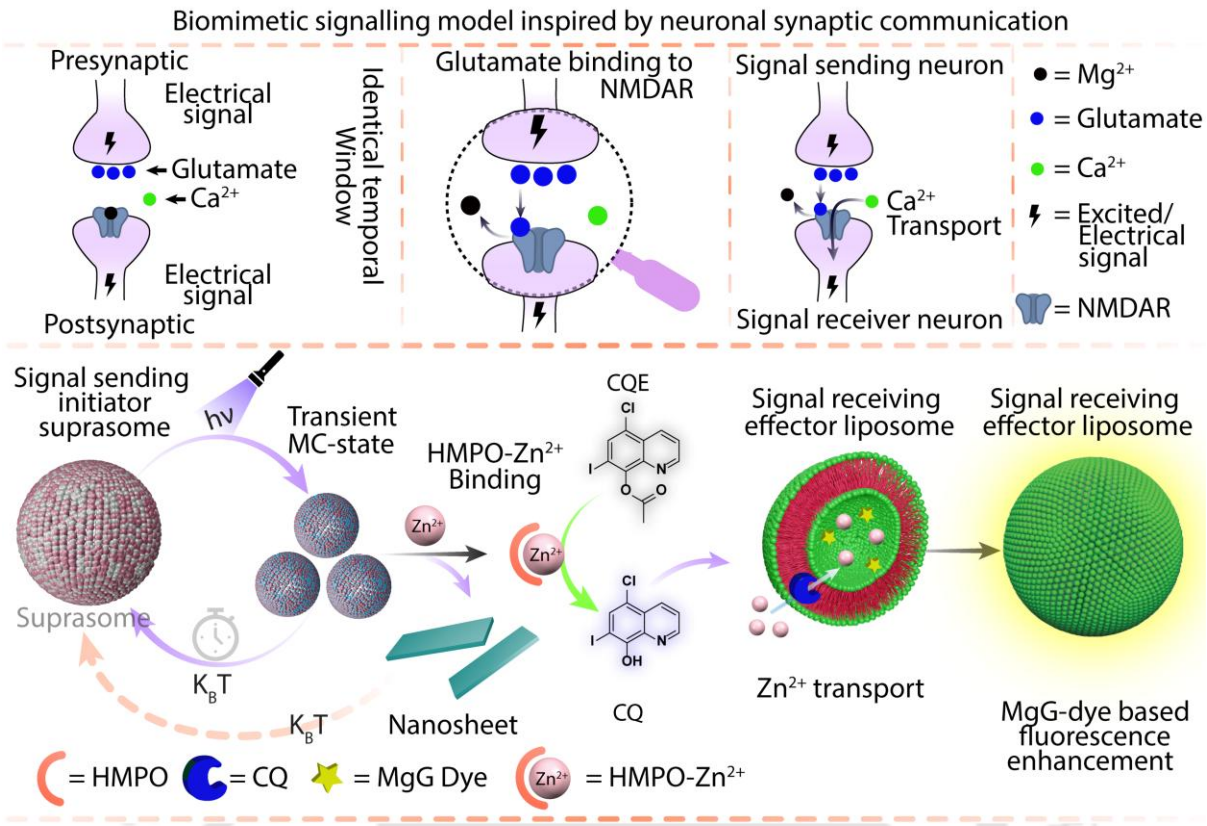


**Figure 5.25.** Schematic comparison between natural neuronal signalling and the biomimetic vesicle system. The sender–receiver neuron pair is functionally replicated by an initiator vesicle (suprasome) responding to dual stimuli (light + $Zn^{2+}$) and triggering $Zn^{2+}$-transport fluorescence in a spatially separated effector vesicle (MgG containing liposome).

### 5.4.6.4.1 Photonic Memory Generation via Coincident Dual Stimuli: A Supramolecular Analogue of Long-Term Memory Consolidation

To establish the effect of transient, time-overlapping stimuli, we demonstrate a scenario where an optical output is generated only within a narrow temporal window, mimicking the mechanism of long-term potentiation (LTP) in the brain. In biological systems, LTP, a foundational process in memory formation, occurs only when two adjacent neurons are activated simultaneously, reinforcing their synaptic connection. Similarly, if one has to remember and later recall an image, this process involves LTP, where the coincidence of transient neural stimuli leads to persistent synaptic strengthening. These strengthening forms a memory trace, enabling recall of the image through reactivation of the associated neural network. By analogy, our system functions as a photonic memory, where temporally confined inputs produce a stable optical output, much like LTP-driven memory encoding in neural

circuits. Thus, transient stimulus overlap in our system serves as the synthetic counterpart to biological coincidence detection underlying memory formation.

To achieve temporally gated optical output, we prepared a suprasome system encapsulating AHPTS (500 μM), introduced during suprasome formation. The solution was passed multiple times through an ultracentrifuge filtration tube to remove excess, unencapsulated AHPTS from the external medium and resuspended in aqueous solution containing similar concentration of β-CD as previous. Further, HMPO (500 μM) was added externally to the suprasome dispersion, along with an excess of EDTAE (1100 μM). The role of EDTAE is critical as it enables $Zn^{2+}$-activated esterase activity of HMPO to remain transient, as $Zn^{2+}$ availability is curtailed over time by the formation of EDTA, which strongly chelates $Zn^{2+}$ and deactivates the HMPO– $Zn^{2+}$ complex. Thus, optical output is generated only under temporally confined co-presence of $Zn^{2+}$ and light stimuli.

The resulting AHPTS-encapsulated suprasome solution, containing HMPO and EDTAE externally, was aliquoted (200 μL) into a 5×5 grid on a 96-well plate. Columns were exposed to 365 nm UV light for 5 min at 1-hour intervals, one column at a time, while shielding the rest. Meanwhile, $Zn^{2+}$ was added blindly (final concentration 1mM) to different rows at 1-hour intervals in a randomised order, such that the intersection points between UV treatment and $Zn^{2+}$ addition occurred at different times across the grid. After 5 hours, the entire plate was irradiated at 450 nm ($\lambda_{ex}$ of HPTS), and optical output was recorded. Remarkably, only those wells where UV irradiation and $Zn^{2+}$ addition occurred simultaneously (the cross-wells) displayed a fluorescent signal, confirming successful time-gated activation of esterase-like activity and AHPTS hydrolysis. Thus, it revealed the binary input and the temporal information along with the optical output, suggesting that such a system can act as a memory device that uniquely stores optical data along with its time coordinates.

Another control experiment with similar set up, only without EDTAE was also performed, where the wells where $Zn^{2+}$ was added prior to photo-irradiation also showcased optical signalling. This demonstrated that the existence of $Zn^{2+}$ and permanent generation of HMPO-$Zn^{2+}$ leads to inability to capture the temporal information.

This setup effectively partitions the 25 wells into three categories, based on the temporal overlap (or lack thereof) between the two stimuli:

**Category 1**: When $Zn^{2+}$ and light are applied concurrently, the suprasome undergoes a transition into its MC-state and subsequent disassembly: In this case, the suprasome

disassembles due to AMC-$Zn^{2+}$ interaction and the AHPTS is released into solution, resulting in HPTS release through HMPO-$Zn^{2+}$ complex before the catalytic complex is dismantled by EDTA released via ester hydrolysis of EDTAE. These are the cross wells where we observed an optical output generation. These reactions occur specifically in cross-well conditions where both stimuli are applied concurrently, leading to spatially and temporally gated fluorescent output, analogous to coincidence-detection mechanisms in long-term potentiation.

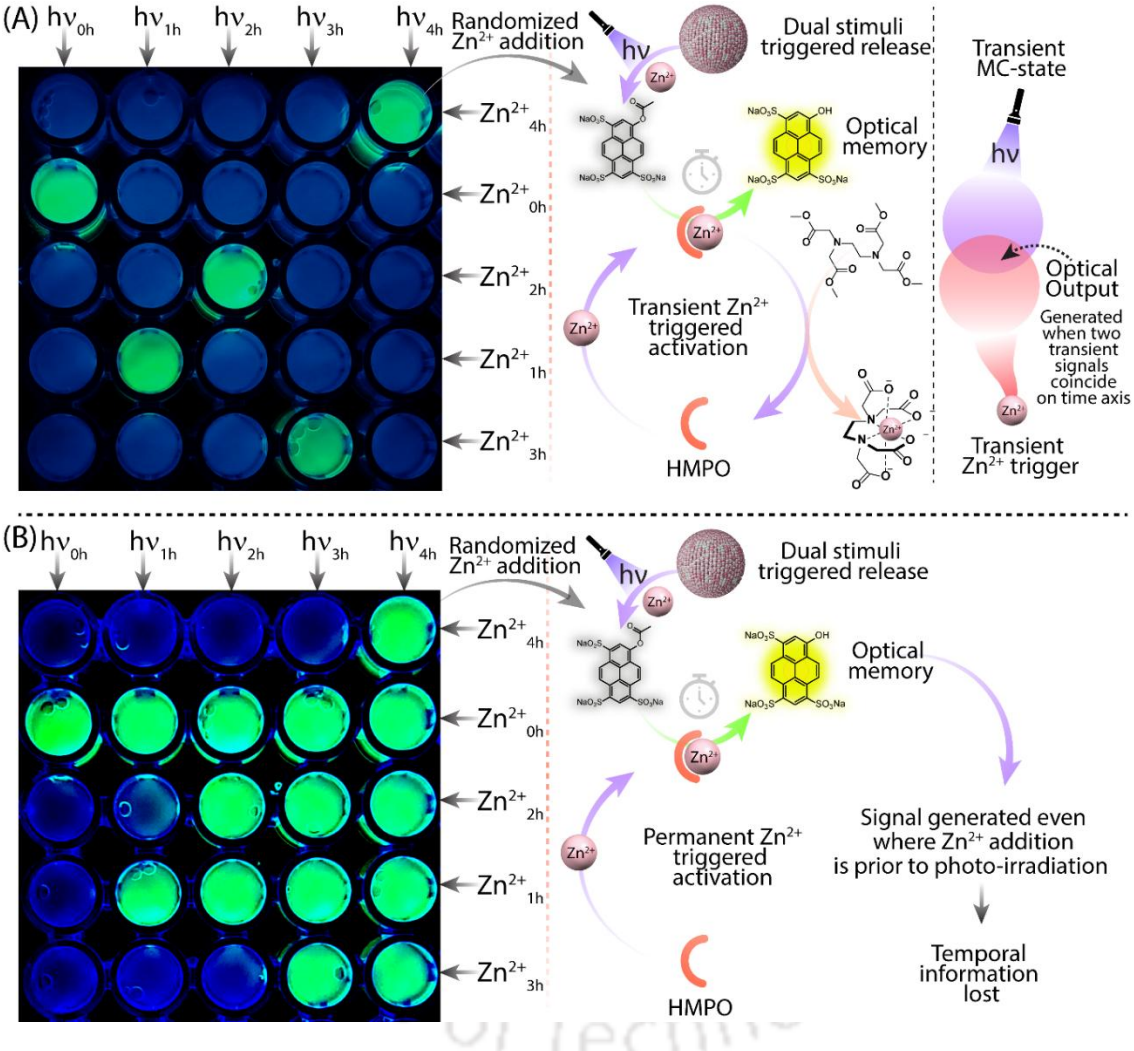


**Figure 5.26.** Photonic output (memory) generation experiment: (A) Coincidence of dual transient stimuli mimicking long-term photonic memory formation, analogous to memory consolidation processes in the brain (System with EDTAE, showcasing temporal information capture). (B) Photonic output generation (Control experiment: without EDTAE, showcasing loss of temporal information.

**Category 2**: When $Zn^{2+}$ is introduced 1 hour or more prior to light stimulation, mediated system transitions into the MC-state suprasome: In this scenario, $Zn^{2+}$ initially activates the HMPO–

$Zn^{2+}$ complex, which exhibits esterase-like activity and catalyses the hydrolysis of EDTAE to EDTA. The newly formed EDTA captures $Zn^{2+}$ in solution, thereby dismantling the HMPO–$Zn^{2+}$ complex and halting further esterase activity. As a result, $Zn^{2+}$-induced esterase activation becomes a transient event, limited to the time window before EDTA accumulates. This built-in negative feedback mechanism ensures that $Zn^{2+}$ availability and hence esterase activity is temporally constrained, even though $Zn^{2+}$ was introduced earlier. Light activation at a later time thus fails to release AHPTS and regenerate the active HMPO–$Zn^{2+}$ complex, making the system dependent on precise temporal coordination of stimuli.

**Category 3**: When $Zn^{2+}$ is introduced 1 hour or more after light irradiation: In this case, suprasome has already reverted from its photoinduced MC-state back to the thermodynamically stable SP-state. As a result, the $Zn^{2+}$ trigger alone is insufficient to induce suprasome disassembly or to facilitate the release of encapsulated AHPTS. Consequently, the HMPO–$Zn^{2+}$ complex cannot access its substrate, and no hydrolysis to HPTS occurs. These wells therefore fail to generate any fluorescent signal or optical output, confirming that temporal coordination of stimuli is essential for productive response.

**5.4.6.4.2 Evaluation of EDTA Release Using Arsenazo-III Dye: HMPO–$Zn^{2+}$ Complex**

Arsenazo-III dye is recognised for its capability to detect divalent metal ions like $Zn^{2+}$, exhibiting distinct spectral changes depending on whether free $Zn^{2+}$ ions are present or absent in the solution.[26] To a solution of arsenazo-III dye (20 μM) in distilled water, $Zn^{2+}$ (2 mM) was added till the spectral red-shift got saturated in absorption spectra.

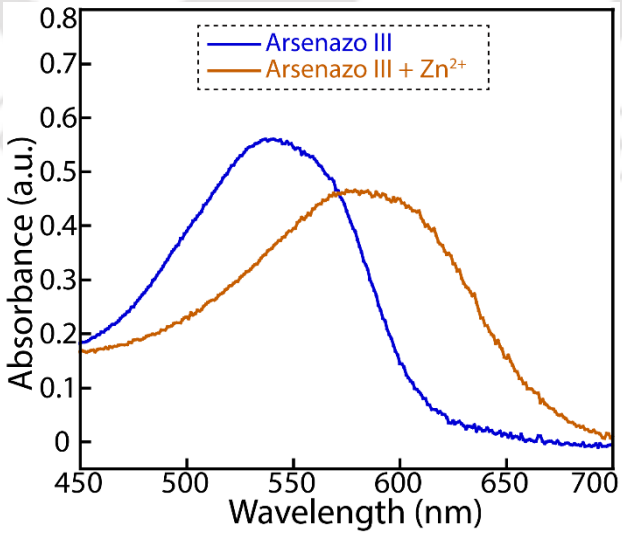


**Figure 5.27.** UV-Vis absorbance spectra of arsenazo-III dye (20 μM) in the absence and presence of $Zn^{2+}$ (2 mM).

In a separate time-dependent experiment, the prepared solution containing arsenazo-III (20 μM) and $Zn^{2+}$ (2 mM) was treated with either EDTAE (2 mM) alone, EDTAE (2 mM) combined with HMPO (500 μM), which will complex with $Zn^{2+}$ to form HMPO-$Zn^{2+}$ complex, causing ester hydrolysis. The absorption spectra were recorded every 10 min thereafter. Only the EDTAE addition did not reverse the red shift, confirming no generation of EDTA in the solution. This ruled out any possibility of EDTAE ester hydrolysis to EDTA by only $Zn^{2+}$. On the contrary, the HMPO treated EDTAE successfully reversed the red shift of arsenazo-III in a period of 50 min. It is noteworthy that the HMPO converts to HMPO-$Zn^{2+}$ in solution due to excess $Zn^{2+}$ presence, which hydrolyses EDTAE to EDTA that preferably captures the free $Zn^{2+}$ present in solution, hence reversing the red-shift of $Zn^{2+}$ sensitive arsenazo-III dye.

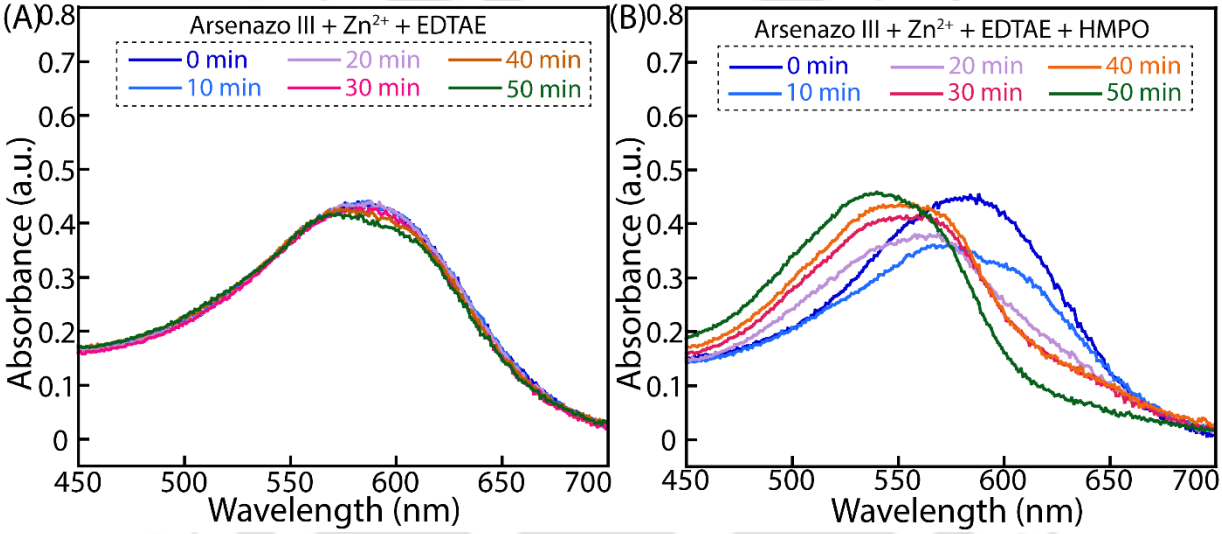


**Figure 5.28.** Time-dependent UV-Vis absorbance spectra of arsenazo-III dye (20 μM) with $Zn^{2+}$ in the presence of (A) EDTAE, (B) HMPO-treated EDTAE.

### 5.4.7 NMR and HRMS Spectra of the Synthesised Compounds

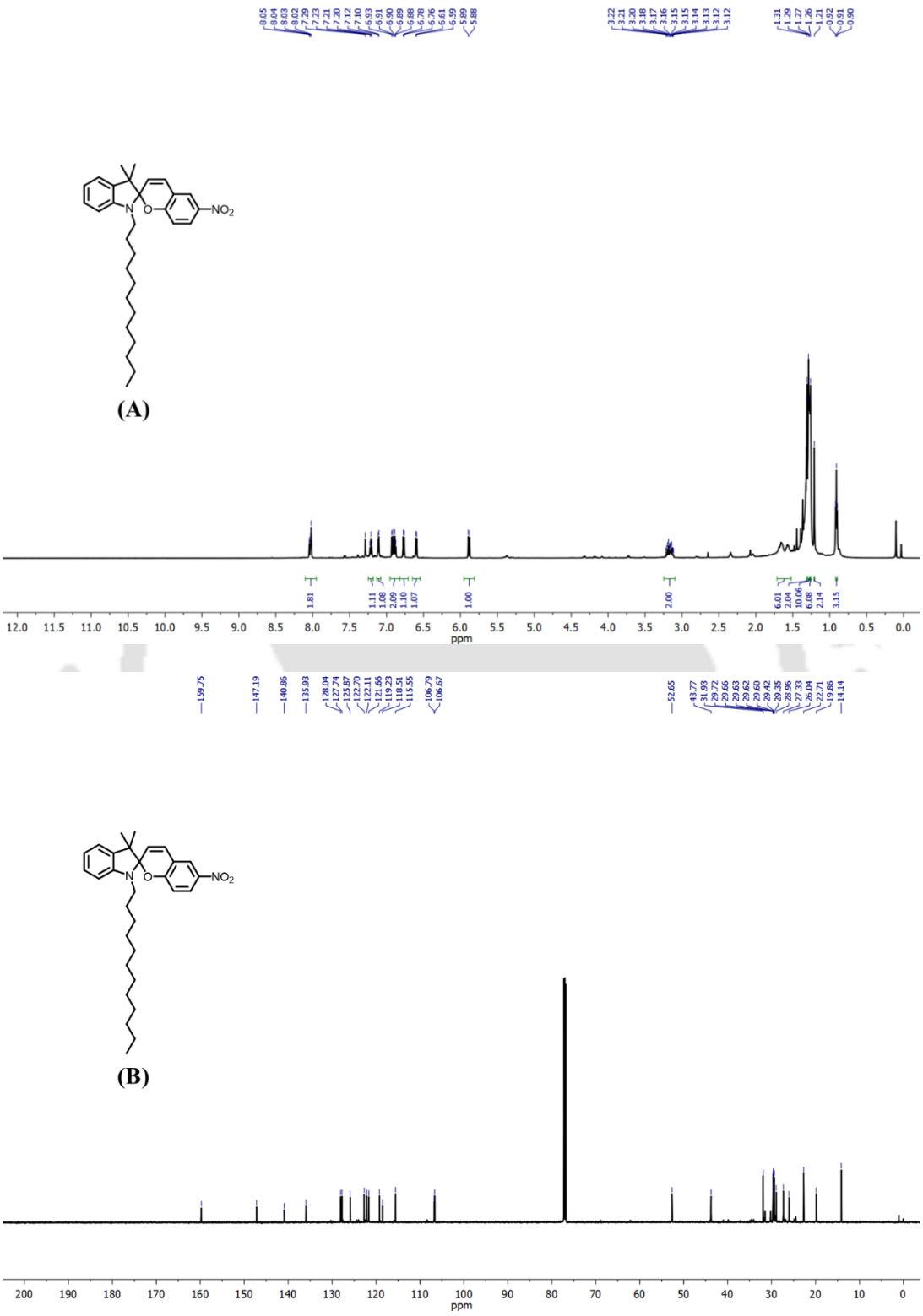


**Figure 5.29.** $^{1}H$ NMR (A) and $^{13}C$ NMR (B) spectra of 1'-dodecyl-3',3'-dimethyl-6-nitrospiro[chromene-2,2'-indoline] in $CDCl_3$ solvent.

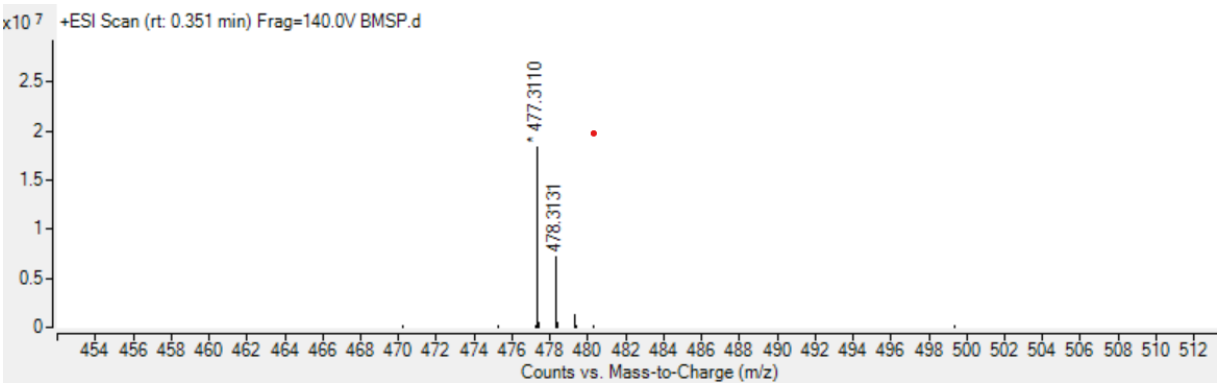


**Figure 5.30.** HRMS spectra of 1'-dodecyl-3',3'-dimethyl-6-nitrospiro[chromene-2,2'-indoline].

## 5.5 References

1. Yang, X.; Lu, H.; Tao, Y.; Zhou, L.; Wang, H., Spatiotemporal Control over Chemical Assembly in Living Cells by Integration of Acid-Catalysed Hydrolysis and Enzymatic Reactions. *Ang. Chem.* **2021,** *133* (44), 23990-23997.

2. Rodrigues, S.; Desroches, M.; Krupa, M.; Cortes, J. M.; Sejnowski, T. J.; Ali, A. B., Time-coded neurotransmitter release at excitatory and inhibitory synapses. *Proc. Natl. Acad. Sci. U.S.A.* **2016,** *113* (8), E1108-E1115.

3. Bliss, T. V.; Collingridge, G. L., A synaptic model of memory: long-term potentiation in the hippocampus. *Nature* **1993,** *361* (6407), 31-39.

4. Malenka, R. C.; Bear, M. F., LTP and LTD: an embarrassment of riches. *Neuron* **2004,** *44* (1), 5-21.

5. Lee, Y.; Fracassi, A.; Devaraj, N. K., Light-driven membrane assembly, shape-shifting, and tissue formation in chemically responsive synthetic cells. *J. Am. Chem. Soc.* **2023,** *145* (47), 25815-25823.

6. Ye, N.; Pei, Y.-r.; Han, Q.; Jin, L. Y., Photoresponsive reversible self-assembly of rod-coil amphiphiles containing spiropyran groups. *Soft Matter* **2023,** *19* (8), 1540-1548.

7. Sun, Z.; Xu, Z.; Ding, M.; Wang, L.; Zhao, L.; Sui, P.; Li, G.; Jin, H.; Zhou, Y.; Lin, S., Ultrathin Polymersomes with Controllable Light-Responsivity via Adjusting the Electronic Effect from Para-Substituents of Azobenzene. *Angew. Chem. Int. Ed.* **2025,** *64* (20), e202503104.

8. Huang, Q.; Ding, C.; Wang, W.; Yang, L.; Wu, Y.; Zeng, W.; Li, Z.; Shi, Z.; Mei, L.; Zeng, X., An "AND" logic gate–based supramolecular therapeutic nanoplatform for combatting drug-resistant non–small cell lung cancer. *Sci. Adv.* **2024,** *10* (39), eadp9071.

9. Guo, J.; Zhuang, J.; Wang, F.; Raghupathi, K. R.; Thayumanavan, S. J. J. o. t. A. C. S., Protein AND enzyme gated supramolecular disassembly. *J. Am. Chem. Soc.* **2014,** *136* (6), 2220-2223.

10. Yan, C.; Guo, Z.; Liu, Y.; Shi, P.; Tian, H.; Zhu, W.-H., A sequence-activated AND logic dual-channel fluorescent probe for tracking programmable drug release. *Chem. Sci.* **2018,** *9* (29), 6176-6182.

11. Mishra, A.; Korlepara, D. B.; Kumar, M.; Jain, A.; Jonnalagadda, N.; Bejagam, K. K.; Balasubramanian, S.; George, S. J., Biomimetic temporal self-assembly via fuel-driven controlled supramolecular polymerization. *Nat. Commun.* **2018,** *9* (1), 1295.

12. Maiti, S.; Fortunati, I.; Ferrante, C.; Scrimin, P.; Prins, L. J., Dissipative self-assembly of vesicular nanoreactors. *Nat. Chem.* **2016,** *8* (7), 725-731.

13. Wang, H.; Wang, Y.; Shen, B.; Liu, X.; Lee, M., Substrate-driven transient self-assembly and spontaneous disassembly directed by chemical reaction with product release. *J. Am. Chem. Soc.* **2019,** *141* (10), 4182-4185.

14. Van Der Helm, M. P.; Li, G.; Hartono, M.; Eelkema, R., Transient host–guest complexation to control catalytic activity. *J. Am. Chem. Soc.* **2022,** *144* (21), 9465-9471.

15. Metherell, A. J.; Cullen, W.; Williams, N. H.; Ward, M. D., Binding of hydrophobic guests in a coordination cage cavity is driven by liberation of "high-energy" water. *Chem. Eur. J.* **2018,** *24* (7), 1554-1560.

16. Sharma, D.; Goyal, S.; Kumar, K.; Sharma, A. L., Advanced Functional Spiropyran-Based Smart Materials with Rapid and Reversible Photochromic Response for Optical Sensing Applications. *Adv. Mater. Technol.* **2025,** *10* (10), 2401288.

17. Barsi, D.; Buratti, E.; Tarantino, A.; Dinelli, F.; Castelvetro, V.; Bertoldo, M., Effect of grafted Spiropyran on the solubility and film properties of photochromic amylose. *Macromol. Chem. Phys.* **2023,** *224* (15), 2300092.

18. Min, Y.; Zhang, R.; Dong, X.; Zhang, L.; Qi, D.; Hua, Z.; Chen, T., Spiropyran-based polymeric micelles in aqueous solution: light-regulated reversible size alterations and catalytic characteristics. *Polym. Chem.* **2023,** *14* (7), 888-897.

19. Ding, Y.; Williams, N. H.; Hunter, C. A., A synthetic vesicle-to-vesicle communication system. *J. Am. Chem. Soc.* **2019,** *141* (44), 17847-17853.

20. Langton, M. J.; Keymeulen, F.; Ciaccia, M.; Williams, N. H.; Hunter, C. A., Controlled membrane translocation provides a mechanism for signal transduction and amplification. *Nat. Chem.* **2017,** *9* (5), 426-430.

21. Gartland, S. A.; Johnson, T. G.; Walkley, E.; Langton, M. J., Inter-Vesicle Signal Transduction Using a Photo-Responsive Zinc Ionophore. *Angew. Chem. Int. Ed.* **2023,** *62* (38), e202309080.

22. Srimayee, S.; Prusty, B. M.; Kar, M. K.; Winterhalter, M.; Manna, D., Supramolecular Ion Channels to Engineer $Zn^{2+}$ Ion Transport Mediated Chemical-to-Optical Signal Transduction. *Angew. Chem. Int. Ed.* **2025**, e202501634.

23. Cironi, P.; Tulla-Puche, J.; Barany, G.; Albericio, F.; Álvarez, M., Solid-phase syntheses of furopyridine and furoquinoline systems. *Org. Lett.* **2004,** *6* (9), 1405-1408.

24. Keana, J. F.; Mann, J. S., Chelating ligands functionalized for facile attachment to biomolecules. A convenient route to 4-isothiocyanatobenzyl derivatives of diethylenetriaminepentaacetic acid and ethylenediaminetetraacetic acid. *J. Org. Chem.* **1990,** *55* (9), 2868-2871.

25. Goyard, D.; Telligmann, S. M.; Goux-Henry, C.; Boysen, M. M.; Framery, E.; Gueyrard, D.; Vidal, S., Carbohydrate-based spiro bis (isoxazolines): synthesis and evaluation in asymmetric catalysis. *Tetrahedron Lett.* **2010,** *51* (2), 374-377.

26. Srimayee, S.; Prusty, B. M.; Kar, M. K.; Winterhalter, M.; Manna, D., Supramolecular Ion Channels to Engineer Zn(2+) Ion Transport Mediated Chemical-to-Optical Signal Transduction. *Angew. Chem.* **2025,** *64* (28), e202501634.

**Conclusions**

In this thesis, suprasomes were established as a versatile supramolecular platform that can cater to the needs of multiple fields of research. Although it initially served as a facile, flexible 3rd-generation DDS, it has tremendous potential to be a key player in new areas of research, such as signal transduction, intervesicle communication, and systems chemistry. Similar to its multifaceted progress in the scientific world, we have demonstrated the utility of suprasome in diverse and modern research arenas as we go through the progressive chapters. To understand, design, and develop suprasomal platforms with desired functionalities, it's crucial to have in-depth knowledge of noncovalent interactions and their key attributes, as well as their natural activities. Keeping this in mind, Chapter 1 comprehensively discusses supramolecular assembly, noncovalent interactions, and inspirations from nature to design and develop principles of the suprasome. **Chapter 2** illustrates how the simple integration of anionic and cationic amphiphiles, along with β-CD as a host, can deliver antibiotics in a $Zn^{2+}$-responsive manner. Additionally, it highlighted a key concept of masking and stimulus-triggered unmasking of antibacterial activity by the suprasome. This highlights the importance of such a vesicular platform in therapeutic research, which shows an undemanding medicinal property. In **Chapter 3**, we developed a suprasome with a $Zn^{2+}$ ionophore, which solved multidirectional challenges. Not only did it resolve the issue of stimulus-triggered ionophore delivery, but it also displayed reassembly of ionophores in the bacterial membrane to cause excess $Zn^{2+}$ influx-mediated killing. As the 2$^{nd}$ and 3$^{rd}$ chapters explored the therapeutic aspect of suprasome, we wanted to explore beyond this. Hence, in **Chapter 4**, our exploration led to the development of a suprasome-supracube-based reversible interconversion with $Zn^{2+}$ as a stimulus. This chemical system, along with EDTAE, displayed temporal conversion to supracube, which catalysed ester hydrolysis. This transient activity was utilised to further control proionophore-to-ionophore release that helped $Zn^{2+}$ influx in another secondary liposome. This study provided proof-of-concept evidence for vesicle-to-vesicle communication. In **Chapter 5**, we took a step further by developing a dual stimuli-responsive suprasome, where the relative timing of stimulus treatment holds the key to further activity that leads to optical output generation and intervesicle communication. Such temporally gated, multistimuli-responsive suprasome are stepping stones for next-generation smart artificial cells that have the ability to make smart decisions. This chapter highlights the utility of suprasomes for developing time-gated photonic memory generation, which mimics key fundamental concepts of neuronal signal transmission and memory formation. Collectively, this thesis revolves around the design,

development, and utility of suprasome as its central theme and covers its multifaceted applications ranging from drug delivery to temporal catalysis, photonic memory storage, and inter-vesicle communication.

**Future Scope**

This thesis explores the various possibilities made attainable by stimuli-responsive suprasomes. Our work has examined targeted treatments, ionophore delivery, the development of supramolecular ion channels, stimuli-triggered temporal catalysis, and temporally gated photonic memory storage. Nonetheless, our little endeavour has just scratched the surface of the issue. The core principle of suprasome may be utilised for the progression of synthetic chemical biology, artificial cells, communication networks, and biomedical applications, among others.

To develop an artificial cellular network and an advanced synthetic cellular system, it is essential to integrate knowledge from multiple scientific fields. This thesis presents a preliminary effort to achieve this objective by integrating ion transport with suprasome-based stimuli-responsive construction, disassembly, and reassembly techniques, facilitating intervesicle communication and temporally controlled photonic memory storage. These creative advancements signify preliminary, however significant achievements in the progression of next-generation artificial cells. Future developments rely on continuous discoveries through strong interdisciplinary collaboration across several fields, including supramolecular and systems chemistry, synthetic ion channels, signal transduction, and intervesicle communication. This discipline is evolving into a comprehensive platform capable of addressing challenges in medicine, catalysis, energy, environmental sustainability, and the fundamental knowledge of life's origins.

# Stimuli-responsive assembly and disassembly of anionic suprasomes with tunable antibacterial activity

B. M. Prusty, R. Karn, A. Patel, P. Mazumder, S. Kumar and D. Manna, *Chem. Commun.*, 2023, **59**, 10624 **DOI:** 10.1039/D3CC02729E

CrossMark

**Document is current**

Any future updates will be listed below

Supramolecular Nanochannels: Suprasome-Mediated Delivery of Ionophore to Regulate Transmembrane Zn<sup>2+</sup> Ion Transport

Crossref DOI link: https://doi.org/10.1002/chem.202501013

Published Online: 2025-04-27

Published Print: 2025-06-03

Update policy: https://doi.org/10.1002/crossmark_policy

› Authors

› Funding

**Publications**

1. Prusty, B. M.; Srimayee, S; Karn, R.; Haloi, N.; Singh, K.S.; Winterhalter, M; Manna, D., Supramolecular Nanochannels: Suprasome Mediated Delivery of Ionophore to Regulate Transmembrane $Zn^{2+}$ Ion Transport, Chemistry–A European Journal, 2025, 31 (31).

2. Srimayee, S.†; Prusty, B. M.†; Kar, M. K.; Winterhalter, M.; Manna, D., supramolecular ion channels to engineer $Zn^{2+}$ ion transport mediated chemical-to-optical signal transduction. Angew. Chem. Int. Ed. 2025, e202501634.

3. Das, N. M.; Prusty, B. M.; Sahoo, A.; Mazumder, P.; Chauhan, S.; Hazarika, G.; Kumar, S.; Dhabal, D.; Manna, D., Photoresponsive prodrug for regulated inhibition of indoleamine 2, 3-dioxygenase 1 enzyme activity. RSC med. chem. 2025.

4. Das, N. M.†; Prusty, B. M.†; Pradhan, N.; Gupta, A.; Carmena-Bargueño, M.; Karn, R.; Pérez-Sánchez, H.; Kumar, S.; Manna, D., Evaluation of mode of indoleamine 2, 3-dioxygenase 1 inhibition by 4, 7-dichloroquinolines. Eur. J. Med. Chem. Rep. 2023, 9, 100110.

5. Dey, S.; Patel, A.; Haloi, N.; Srimayee, S.; Paul, S.; Barik, G. K.; Akhtar, N.; Shaw, D.; Hazarika, G.; Prusty, B. M., Quinoline thiourea based zinc ionophores with antibacterial activity. J. Med. Chem. 2023, 66 (16), 11078-11093.

6. Kumar, S.; Dhar, M.; Prusty, B. M.; Sarkar, D.; Das, A.; Manna, D.; Manna, U., Amidation reaction to derive waterborne, tolerant, and optically transparent solid slippery and superhydrophobic coatings. Chem. Eng. J. 2023, 465, 142776.

7. Choudhary, S. A.; Patra, D.; Sinha, A.; Mazumder, S.; Pant, R.; Chouhan, R.; Jha, A. N.; Prusty, B. M.; Manna, D.; Das, S. K., A small molecule potent IRAK4 inhibitor abrogates lipopolysaccharide-induced macrophage inflammation in-vitro and in-vivo. Eur. J. Pharmacol 2023, 944, 175593.

8. Mazumder, S.; Sinha, A.; Ghosh, S.; Sharma, G. C.; Prusty, B. M.; Manna, D.; Pal, D.; Pal, C.; Dasgupta, S.; Disease, Leishmania LPG interacts with LRR5/LRR6 of macrophage TLR4 for parasite invasion and impairs the macrophage functions. Pathogens 2023, 81, ftad019.

9. Prusty, B. M.; Karn, R.; Patel, A.; Mazumder, P.; Kumar, S.; Manna, D., Stimuli-responsive assembly and disassembly of anionic suprasomes with tunable antibacterial activity. Chem. Commun. 2023, 59 (71), 10624-10627.

10. Dey, S., Dey, S.; Sen, P.; Patel, A.; Prusty, B. M.; Ghosh, S. S.; Manna, D., A photo-responsive fluorescent amphiphile for target specific and image-guided drug delivery applications. Org. Biomol. Chem. 2022, 20 (39), 7803-7813.

(† = equal contribution)